



University of Crete  
School of Sciences  
Department of Physics

Postgraduate Course in Microelectronics and Optoelectronics

Master Thesis

2D AND 3D DEPOSITION OF  
BIOCOMPATIBLE AND BIOLOGICAL  
MATERIALS BY LASER BASED  
TECHNIQUES

Areti Mourka

Supervisor: Prof. C. Fotakis  
Advisor: Dr. M. Farsari

Heraklion, Crete  
March 2009



Πανεπιστήμιο Κρήτης  
Σχολή Θετικών Επιστημών  
Τμήμα Φυσικής

ΜΕΤΑΠΤΥΧΙΑΚΟ ΠΡΟΓΡΑΜΜΑ ΟΠΤΟΗΛΕΚΤΡΟΝΙΚΗΣ - ΜΙΚΡΟΗΛΕΚΤΡΟΝΙΚΗΣ

## Μεταπτυχιακή Εργασία

ΔΙΣΔΙΑΣΤΑΤΗ ΚΑΙ ΤΡΙΣΔΙΑΣΤΑΤΗ  
ΕΝΑΠΟΘΕΣΗ ΒΙΟΣΥΜΒΑΤΩΝ ΚΑΙ  
ΒΙΟΛΟΓΙΚΩΝ ΥΛΙΚΩΝ  
ΧΡΗΣΙΜΟΠΟΙΩΝΤΑΣ  
ΤΕΧΝΙΚΕΣ ΛΕΙΖΕΡ

Αρετή Μούρκα

Υπεύθυνος καθηγητής: Καθ. Κ. Φωτάκης  
Επιβλέπουσα: Δρ. Μ. Φαρσάρη

Ηράκλειο Κρήτης  
Μάρτιος 2009



## Acknowledgements – Ευχαριστίες

Η παρούσα εργασία είναι αποτέλεσμα συνεργασίας πολλών ανθρώπων τους οποίους θα ήθελα να ευχαριστήσω για την ευγενική προσφορά τους. Καταρχήν θα ήθελα να ευχαριστήσω τον υπεύθυνο καθηγητή της εργασίας αυτής, κ. Κωνσταντίνο Φωτάκη, διευθυντή του Ι.Η.Δ.Α. του Ι.Τ.Ε ,ο οποίος μου έδωσε την ευκαιρία να εργαστώ στα εργαστήρια λέιζερ κατά τη διάρκεια διεκπεραίωσης των πειραμάτων.

Στη συνέχεια θα ήθελα να ευχαριστήσω ιδιαίτερα την επιβλέπουσα της εργασίας αυτής, κα. Μαρία Φαρσάρη ερευνήτρια του Ι.Η.Δ.Α., για την πολύτιμη συνεργασία της, γιατί υποστήριξε υλικά και επιστημονικά την εργασία αυτή. Ακόμη, θα ήθελα να ευχαριστήσω τον κ. Παναγιώτη Τζανετάκη αναπληρωτή καθηγητή του τμήματος Φυσικής του Πανεπιστημίου Κρήτης και τον κ. Κώστα Καλπούζο ερευνητή του Ι.Η.Δ.Α., που δέχτηκαν μαζί με τον κ. Κωνσταντίνο Φωτάκη να συμμετέχουν στην τριμελή επιτροπή του μεταπτυχιακού μου διπλώματος.

Ευχαριστώ θερμά τον καθηγητή κ. Boris Chichkov, διευθυντή του γκρουπ νανοτεχνολογίας (Head of Nanotechnology group) του Ινστιτούτου Λείζερ του Αννοβέρου (Laser Zentrum Hannover, L.Z.H.), στο Αννόβερο της Γερμανίας, και τον Dr.Lothar Koch και τον Dipl. Martin Grune για την πολύ καλή συνεργασία που είχαμε, στα πλαίσια της οποίας μου δόθηκε η ευκαιρία να βρεθώ στα εργαστήρια του L.Z.H. και να πραγματοποιήσω κάποια από τα πειράματα που παρουσιάζονται στην εργασία αυτή.

Επίσης να ευχαριστήσω την κα. Άννα Μητράκη, καθηγήτρια του τμήματος Επιστήμης και Τεχνολογίας Υλικών του Πανεπιστημίου Κρήτης για την πολύ καλή συνεργασία που είχαμε στο πρώτο μέρος της εργασίας αυτής, που μας απασχόλησε η εναπόθεση πεπτιδίων. Να ευχαριστήσω θερμά τους Ανθή Ρανέλλα, Valentina Dinca, Μανώλη Κασωτάκη, Julien Catherine για την συνεργασία και την πολύτιμη βοήθειά τους. Να ευχαριστήσω ακόμα τους Βάσω Μελισσινάκη, Ραφαέλο Ελ Μποργκίνι για τον σχεδιασμό των τρισδιάστατων σχεδίων που χρησιμοποιήθηκαν στην εργασία αυτή. Τέλος θα ήθελα να ευχαριστήσω τους Στράτο Στυλιανό, Γιώργο Παπαιωάννου, Μιχάλη Γαλανάκη για την πολύτιμη βοήθειά τους σε θέματα προγραμματισμού.

Ακόμη να ευχαριστήσω θερμά τις Αλέκα Μανουσάκη, Αλεξάνδρα Σιακούλη για την βοήθειά τους για την μελέτη των δειγμάτων με χρήση του Ηλεκτρονικού Μικροσκοπίου. Ευχαριστώ τον Αποστόλη Εγγλέζη για την πολύτιμη βοήθειά του στον χειρισμό του femtosecond λέιζερ.

Επίσης θα ήθελα να ευχαριστήσω τις Αναστασία Γιακουμάκη και Αργυρώ Κλίνη για την βοήθειά τους στην επιμέλεια της παρουσίασης της εργασίας αυτής και για την υποστήριξή τους.

Βέβαια, πριν κλείσω το μέρος αυτό, ευχαριστώ θερμά τους ανθρώπους του meeting room, που έκαναν τόσο ευχάριστο το περιβάλλον εργασίας και ιδιαίτερα την Μερóπη Μαρή και την Gabriella Kecskemeti για την ηθική υποστήριξή τους.

Τέλος το μεγαλύτερο ευχαριστώ νιώθω την ανάγκη να το πω στην οικογένειά μου, που μπορεί να μη βοήθησαν στα πειράματα αλλά με στήριξε και με στηρίζει με υπομονή και κατανόηση όλα αυτά τα χρόνια.

Σας Ευχαριστώ όλους

## Abstract

In the first part of this thesis, we demonstrate a novel method for the precise, three-dimensional patterning of beta amyloid self-assembled peptide fibrils, on 3D structures of Ormocer by using the multi-photon polymerization method. The technique which combines femtosecond laser technology and biotin avidin mediated assembly on a polymeric matrix, can be applied in a wide variety of fields, from molecular electronics to tissue engineering.

Molecular self-assembly is emerging as a viable “bottom-up” approach for fabricating nanostructures. Self-assembled biomolecular structures are particularly attractive, due to their versatile chemistry, molecular recognition properties, and biocompatibility. Among them, amyloid protein and peptide fibrils are self-assembled nanostructures with unique physical and chemical stability, formed from quite simple building blocks; their ability to work as a template for the fabrication of low resistance, conducting nanowires has already been demonstrated. The precise positioning of peptide-based nanostructures is an essential part of their use in technological applications, and their controlled assembly, positioning, and integration into microsystems is a problem of considerable current interest. To date, their positioning has been limited to their placement on flat surfaces or to the fabrication of peptide arrays by L.I.F.T. technique.

Over the last few years, there has been a lot of interest and progress in the direct laser writing of biological molecules. Laser induced forward transfer (L.I.F.T.) is a direct-write non contact method, which offers an interesting and versatile alternative to conventional arraying techniques, since it does not require the use of expensive photolithographic equipment, and it does not suffer from clogging and contamination problems, as pin deposition and ink-jet printing do. It is the long transfer distances, the precise and high focusing ability of lasers and the laser directionality, which gives flexibility to the L.I.F.T. method. In the second part of this thesis, patterns of different kind of cells were created by using L.I.F.T. method. By using again L.I.F.T. followed the 3D structuring of calcium alginate gel, those structures can be used as a scaffold for tissue engineering. Tissue engineering refers to a special group of radically new procedures and techniques developed for the treatment of various diseases and injuries.

# TABLE OF CONTENTS

<b>Acknowledgement-Ευχαριστίες</b> .....	<b>5</b>
<b>Abstract</b> .....	<b>7</b>
<b>Chapter 1 INTRODUCTION</b> .....	<b>11</b>
1.1. Overview .....	13
1.2. Chapter content.....	14
<b>Chapter 2 METHODS</b> .....	<b>15</b>
2.1. 2D Patterning Methods.....	17
2.1.1 Introduction .....	17
2.1.2 Contact printing techniques .....	19
2.1.3 Microstamping.....	22
2.1.4 Non-Contact printing techniques.....	24
2.1.5 Interaction of the laser radiation with the solids .....	26
2.1.6 Laser Induced Forward Transfer (L. I. F. T.) Method.....	29
2.2. 3D Patterning Methods.....	32
2.2.1 Material processing with femtosecond lasers.....	33
2.2.2 Two-photon polymerization .....	38
2.2.3 Advanced techniques in two-photon micro-fabrication .....	43
2.2.4 Three-photon polymerization .....	46
<b>Chapter 3 MATERIALS</b> .....	<b>57</b>
A. Materials that were used for the 2D deposition by L.I.F.T. Method .....	59
3.1 Self-Assembled Peptide Fibrils .....	59
3.2 Alginate Gel.....	70
3.3 Cells.....	76
B. Materials that were used for the 3D deposition by Multi-Photon Polymerization Method.....	80
3.4 Ormocer Polymer .....	80
<b>Chapter 4 EXPERIMENTAL</b> .....	<b>89</b>
4.1. Experimental Set-ups.....	91
4.2. Techniques of Characterizations .....	96

<b>Chapter 5 RESULTS .....</b>	<b>99</b>
A. Results after the 2D deposition by using L.I.F.T. method.....	101
5.1 Optimization of the process.....	101
5.1.1 Distance between target-substrate .....	102
5.1.2 Laser pulse duration.....	102
5.1.3 Distance between target-substrate .....	103
5.1.4 Film Thickness .....	104
5.2 Apply the optimized conditions to transfer peptides, alginate gel, cells .....	105
5.2.1 2D deposition of self-assembled peptides fibrils.....	105
5.2.2 Fabrication of amyloid peptide micro-arrays using laser-induced forward transfer and avidin-biotin mediated assembly .....	111
5.2.3 3D deposition of alginate gel.....	116
5.2.4 2D deposition of cells.....	145
5.2.5 Construction of calcium alginate gel scaffolds.....	157
B. Results after the using the Multi-Photon Polymerization technique.....	159
5.3 3D structures of Ormocer by three photon polymerization.....	160
5.3.1 Directed three-dimensional patterning of self-assembled peptide fibrils .....	163
5.3.2 Conclusions .....	172
<b>Publications .....</b>	<b>174</b>



CHAPTER 1  
INTRODUCTION



## 1.1 Overview

Bio-inspired fibrous materials such as self-assembling peptides have potentially broad applications in biotechnology, such as scaffolds in three dimensional cell culture and tissue engineering and as templates for the assembly of polymeric and inorganic materials. Peptides, which were used in the first part of this thesis, have some very interesting features as capture ligands: they can mimic biological activities of proteins, they are easy to synthesize and manipulate, and they are usually highly stable and relatively inexpensive. Their potential use as biomaterials, such as filaments, fibrils and hydrogels has recently started to be exploited. They offer attractive features, principally because of their ability to fold into specific structures, and the rich chemistry with which their structure and function can be manipulated for environmental response. Over the last few years, there has been a lot of interest and progress in the direct laser writing of biological molecules. Laser induced forward transfer (L.I.F.T.) is a direct-write, non-contact method, which offers an interesting and versatile alternative to conventional arraying techniques, since it does not require the use of expensive photolithographic equipment, and it does not suffer from clogging and contamination problems, as pin deposition and ink-jet printing do. At L.I.F.T., a single pulse from a focused laser beam is used to transfer a thin film from a donor-coated surface to an acceptor surface. The laser beam is firstly focused onto a metallic layer which coats the transparent donor surface- the target; this acts as an energy conversion material, converting the laser energy via absorption and conduction into heat used to expel the target material. The transferred material is collected on a substrate, placed in close proximity and parallel to the donor surface. The advantage of L.I.F.T. over other techniques is its ability to provide high resolution, noncontact, direct, flexible and parallel transfer of more than one type of materials while not mixing them, as different targets can be used.

In this thesis, we created 2D patterns of peptides and 2D patterns of different kind of cells by using the L.I.F.T. technique. The 3D deposition of calcium alginate gel followed, which can be used as a scaffold for tissue engineering. A systematic study has been made by irradiating the target surface with the thin film of cells at different laser fluencies, in order to examine the viability of the cells.

Finally, we propose a new method for the precise, three dimensional patterning of beta amyloid peptide fibrils. The technique, which combines laser technology and avidin-biotin mediated patterning of the self-assembling peptide fibers, could potentially be applied in a wide variety of fields, from molecular electronics to tissue engineering.

The technique is based on the selective attachment of photosensitive biotin (photobiotin) on surfaces and 3D structures and exploits thiol chemistry and self-assembly of peptide fibrils.

These structures consist of ORMOCER, a photostructurable organic-inorganic hybrid, on which photobiotin can be irreversibly attached when exposed to UV light from a laser or a lamp. However, the technique is not limited to ORMOCER; photobiotin can be photolytically attached on a variety of organic and inorganic materials such as silicon, glass, and PDMS; this gives this technique a large flexibility and applicability. Once biotin has been immobilized on ORMOCER, then it is first incubated with avidin and subsequently with the iodoacetamidofunctionalized biotin *N*-(biotinoyl)-*N*ϵ-(iodoacetyl) ethylenediamine. Finally, the 3D structures are immersed in an aqueous solution of peptides that contain a cysteine residue. The peptide solutions have been “aged” so that self assembled fibrils are already formed in solution. The 3D structures that were used in this part were made by using the Multi-photon polymerization technique.

## 1.2 Chapter content

In **chapter 2** we will briefly summarize the theory of the interaction of laser radiation with a matter and the methods that were used in this thesis will be analyzed too. In **chapter 3** we will briefly describe the materials that were used in this thesis. In **chapter 4** follows in details the description of experimental techniques that were used in the frames of experiments and of the set-ups, too. In **chapter 5** we present the results of the 2D deposition of different kind of cells by using the L.I.F.T. technique, the 3D deposition of alginate gel by using the L.I.F.T. technique and finally the 2D deposition of peptides by using the L.I.F.T. technique and their 3D deposition by using the Multi-photon polymerization technique, too.

# CHAPTER 2

## METHODS



In this chapter the methods that were used in this study are being explained. This chapter is separated in two parts. In the first part we focus in presentation of 2D patterning methods. Then it is described the interaction of laser radiation with a matter, which is separated in primary and secondary activities. Finally, follows the analytic description of the Laser Induced Forward Transfer-LIFT method, which was used in the first part of this study. In the second part are described the 3D patterning methods. The method of Multi-Photon Polymerization that was used in this second part of this thesis is being explained. Firstly, the material processing with femtosecond lasers is been presented and then the descriptions of the two photon and three photon polymerizations are taken place. Finally the applications of the 3D structures made by three photon polymerization are mentioned.

## **2.1 2D Patterning Methods**

Two dimensional patterns with biomolecules (e.g., DNA and proteins), cells, and tissues immobilized on solid substrates are important tools for biological research, including genomics, proteomics, and cell analysis. According to spot formation techniques, methods are categorized as “contact printing” and “non-contact printing.” Contact printing is a widely used technology, comprising methods such as contact pin printing and microstamping. These methods have many advantages, including reproducibility of printed spots and facile maintenance, as well as drawbacks, including low-throughput fabrication of arrays. Non-contact printing techniques are newer and more varied, comprising photochemistry-based methods, laser writing, electrospray deposition, and inkjet technologies. These technologies emerged from other applications and have the potential to increase microarray fabrication throughput; however, there are several challenges in applying them to microarray fabrication, including interference from satellite drops and biomolecules denaturation.

### **2.1.1 Introduction**

Deoxyribonucleic acid (DNA) and protein microarrays, also called biochip microarrays, have accelerated the process of understanding gene and protein function in living organisms. Microarrays provide molecular signatures for cells, tissues and disease states that can be used for disease diagnosis, prediction, prevention, and drug discovery. A microarray is a two-dimensional pattern of specific biological probes (e.g., DNA or protein molecules) deposited in an addressable fashion on a glass slide or other substrates (e.g., polymer-coated glass, plastics, nitrocellulose).

Cell microarrays combine well-established methods for cellular investigation with the high-throughput screening capabilities of microarrays. They can be used in drug screening, *in vitro* toxicology testing and in functional genomics studies.

Tissue microarrays, formed by embedding biopsies of donor tissue blocks on a substrate, are used for phenotypic analyses (e.g., immunohistochemistry). By monitoring the expression of molecular markers in these arrays, many pathological characteristics can be determined (stage and progression of the disease). Although there are several general reviews of biochip microarrays,<sup>8,9,10</sup> we focus here on the fabrication (or printing) techniques used to form two-dimensional patterns of probe molecules (DNA and proteins). Microarray fabrication is inherently a biological fluid dispensing process.<sup>11</sup> Nanoliter drops of biological solutions are deposited in an addressable arrangement of spots on a substrate surface. The spots must be homogeneous and dense, yet spatially discrete. Table 1 summarizes the types of printing techniques and presents the organization of this review. Printing methods can be broadly categorized into contact and non-contact printing methods. During contact printing, a printing device comes in physical contact with the substrate while depositing biological samples. In contrast, non-contact printing involves no physical contact between the device and the substrate (e.g., photolithography, ink-jet printing, and laser writing). Each of these array fabrication techniques can be sub-classified as serial or parallel. In serial deposition, serially repeated movements of the printing device limit fabrication throughput. Hence, parallel deposition techniques are a better choice for large-scale fabrication; however, most of the parallel techniques for depositing biomolecules are newer and thus, less developed than serial techniques.<sup>12</sup> All microarray fabrication techniques target the same objective: efficient deposition of uniform, dense arrays of small droplets of probe molecules.

In addition, a technique should minimize cost and the required volume of solution, while preventing solution contamination and biomolecular damage. This review analyzes the capabilities and limitations of conventional and emerging technologies for microarray fabrication.

**TABLE 1** Microarray printing techniques

Contact		Non-Contact	
Serial	Parallel	Serial	Parallel
Solid/Split Contact Pins		Dynamic Controlled Pins	Photochemical Printing Electro-Printing
Nano-Tips	Microstamps	Laser Writing	Inkjet/Nozzle Printing Electrospray Deposition

## 2.1.2 Contact printing techniques

Contact printing methods are used to form arrays by means of direct contact between the printing device and the substrate. As shown in Table 1, contact printing technologies employ solid pins, split pins, nanotips, and microstamps. One of the first approaches used for microarray fabrication was contact printing with a single pin, which evolved into methods relying on an array of pins. While pin printing is a serial deposition method, microstamps are used for depositing a large number of proteins or DNA molecules in a parallel fashion. Nanotip printing is the most recent technology based on Scanning Probe Microscopy (SPM) and yields arrays with submicron spots.

### 2.1.2.1 Pin Printing

Pin printing is a widely used technique for microarray fabrication. Accurate quantitative analysis of printed microarrays is only possible if spot uniformity (i.e., spot-to-spot size and shape repeatability) and positional accuracy are achieved.<sup>13</sup> Spot uniformity is primarily determined by the sample viscosity, pin contact area, pin surface properties, substrate surface properties, and substrate planarity. Additional factors include pin velocity, the precision of robotic controls, and environmental control of humidity, temperature, and contamination. A high pin velocity (>2 cm/s) can induce high inertial forces that drive large sample volumes out of the pin, making the size of spots very large.<sup>14</sup> However, inertia typically does not play a large role in pin printing. Pin printing is governed by the surface tension of the solution, and the wet ability of the solution on the substrate. Maintaining a high, stable humidity prevents the sample from evaporating from the wells and pin channels. Temperature affects the sample viscosity and therefore, the dispensed volume. Contamination and dust must be controlled if high-quality arrays are to be produced with minimal risk of split pin clogging.

#### 2.1.2.1.a Solid pins

The simplest method of microarray printing is solid pin contact printing. In this method, a solid pin is dipped into a reservoir to load the sample on the tip of the pin (Figure 1.a). The pin then touches to the substrate surface to deposit the sample (Figure 1.b). A single sample load is usually sufficient for printing a few spots.

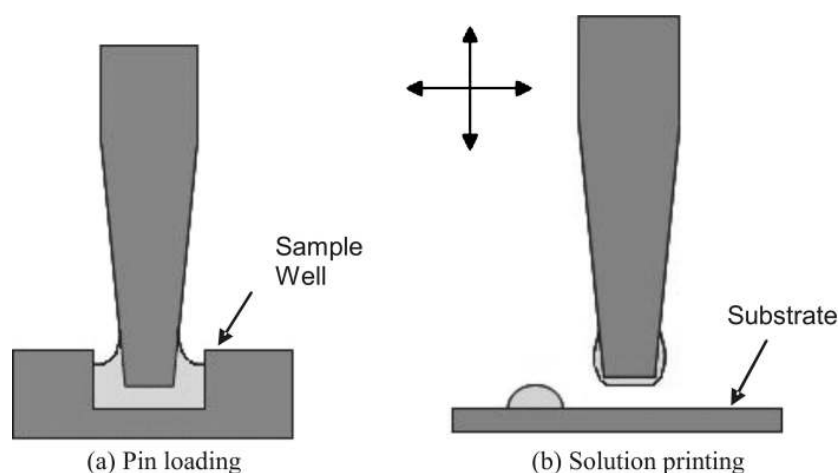


FIGURE 1: Solid pin printing process. a) Solid pin is loaded with solution from well plate by capillary force action, b) Spot printing with a single load.

Much of the innovation in solid pin designs has been to develop different tip shapes to improve spot uniformity.

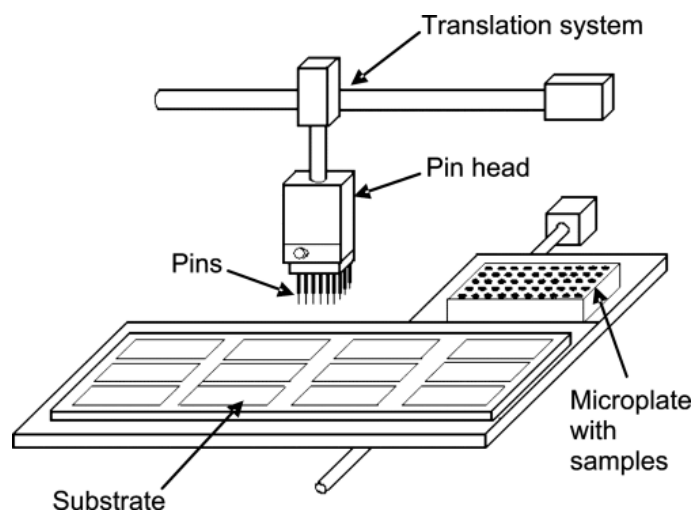
#### 2.1.2.1.b Pin Printing System

Figure 2 shows an example of a microarray printing system. Pins are carried by a pin head as it transfers samples from the microplate to the substrate. The pins float under their own weight and are free to move in the vertical direction in the pin head when in contact with the substrate. There are usually 16, 64, or 96 pins in one pin head.<sup>16</sup> The usual pin spacing of 4.5 mm or 9 mm is determined by the commercial microplate configuration 384 or 96 wells, respectively.

Microarrays do not exactly map the source plate; in fact, spot distance on microarrays is much smaller than the distance between the source plate wells.

A typical density of spots with 75-360  $\mu\text{m}$  diameters is 400-10000 spots/ $\text{cm}^2$ . As described, the pins are dipped into the wells, and the solution is held by surface tension on the outside of solid pins or driven into the slit/channel in split pins by capillary forces. Dipping split pins in a larger sample volume results in spot inconsistency in the first few spots due to the draining of the excess sample solution from the pin sidewalls; therefore, preprinting is necessary until uniform printing is achieved.<sup>16</sup> The typical substrates for microarray printing are microscope slides. Prior to spotting, the slides are treated with poly lysine, amino silanes or amino-reactive silanes that enable DNA or protein to bind to the surface and prevent the sample from being washed away during the hybridization process. In addition, the dispensed sample spot spreads less if the surface is hydrophobic, allowing higher array densities.

Other materials, such as polymer-coated glass or plastics, are also used as substrates for microarray printing. Accurate quantitative analysis of printed microarrays is only possible if spot uniformity (i.e., the spot size and shape is consistent and reproducible) and positional accuracy are achieved.<sup>13</sup>



*FIGURE 2: System for microarray printing. Print head mounted on translation system carries printing devices (pins) from the source microplate to the substrate, where it deposits sample. Adapted from Ito and Tachibana<sup>17</sup>*

As discussed above, spot uniformity is affected by the sample viscosity, pin contact area, pin surface properties, substrate surface properties, and substrate planarity. Additional factors that define spot sizes are pin velocity, the precision of robotic controls, environmental control of humidity, temperature, and contamination. A high pin velocity ( $>2$  cm/s) can induce high inertia forces that drive large sample volumes out of the pin, making the size of spots very large.<sup>16</sup> Setting a high, stable humidity level prevents the sample from evaporating from the wells and pin channels. Temperature affects sample viscosity and therefore, dispensed volume. Contamination and dust must be controlled if high-quality arrays are to be produced with minimal risk of split pin clogging. Pin printing is probably the most popular method for microarray fabrication. However, the primary reason for the development of other printing methods is the tedious, time-consuming nature of pin printing. Rose<sup>16</sup> reported that typical printing time for an Arrayit ChipMaker<sup>TM</sup> microprinting system (TeleChem International, Inc., Sunnyvale, CA), including loading, preprinting, printing, and washing of pins, was 0.2 h for a 384-well microplate using 32 pins, and 6.4 h for a 384-well microplate using a single pin. These inherent inefficiencies have spurred the development of other spotting methods.

### 2.1.3 Microstamping

Pin printing is an inherently serial technique in which a single pin or groups of pins are iteratively loaded for spotting. An alternative to pin printing is microstamping. With microstamps, hundreds of spots are printed in parallel, enabling high-throughput microarray fabrication. The microstamping process, depicted in Figure 3, is simple and inexpensive and can be readily conducted in a laboratory. A sample is first adsorbed on the patterned surface of a stamp and then transferred to a substrate by physical contact. In order to obtain good contact, microstamps are generally made from elastomeric materials, such as poly (dimethylsiloxane) (PDMS), which conform to surface roughness under an applied load. Microcontact printing with elastomeric stamps, along with other soft lithographic microfabrication techniques, was developed by Whitesides' group<sup>18,19</sup> and first demonstrated for self-assembled monolayer (SAMs) of alkanethiols on gold.<sup>20</sup> Elastomeric stamps are manufactured by a micromolding technique that requires only a single photolithography step (Figure 4).

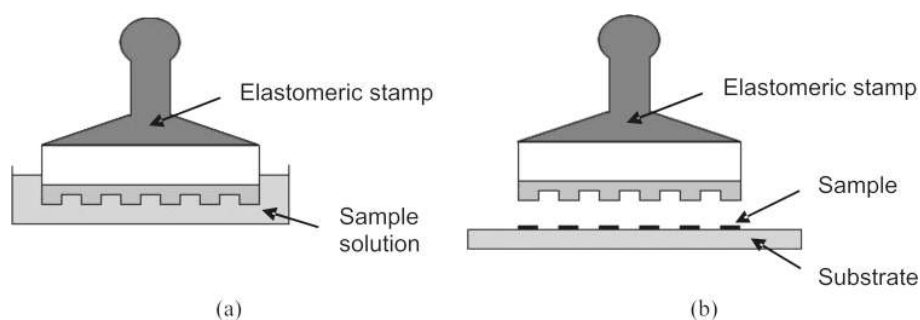


*FIGURE 3: Microstamping process. a) Stamp inking in a sample solution well, b) Transferring sample to the substrate by physical contact between the elastomeric stamp and the substrate.*

Mold masters are fabricated by photolithography to define a pattern of the stamp. Then, an uncured liquid elastomer (e.g., PDMS) is cast on the master. After curing, the stamp is released from the master. This process enables reproducible, low cost batch production, resulting in inexpensive and disposable microstamps. Using disposable stamps minimizes the problems of sample carry-over, cross-contamination, and the time-consuming cleaning processes that are required for pin printing. Hydrogels have also been used as a stamp material for protein patterning.<sup>21</sup>

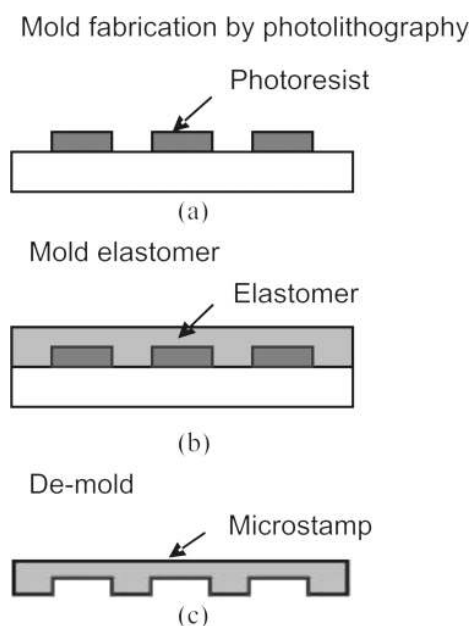


*FIGURE 4: Microstamp fabrication. The master is fabricated by photolithography to define the feature of the stamp. The liquid elastomer is then cast on the master to produce designed patterns. After the curing process, the stamp is released from the master<sup>22</sup>*

Some disadvantages for microstamping are related to the sample volumes transferred. In microstamping, the amount of sample transferred from the stamp to the substrate is not well controlled and depends on both surface and sample properties. Additionally, for the same amount of printed sample, microstamping requires larger initial sample volumes, as only a small amount of solution in a well is adsorbed onto the stamp surface, and only a small fraction of the adsorbed solution is transferred from the stamp to the substrate, due to strong non-specific adsorption to the hydrophobic stamp material. Likewise, if microstamps are to be reused, the washing process is more tedious than for pins because of non-specific adsorption.<sup>12</sup> Microstamping techniques for biomolecules can be categorized into indirect stamping<sup>5,21,23,24</sup> and the more recently developed direct stamping.<sup>25-29</sup> Both categories utilize similar tools but different stamping procedures. In indirect stamping, the SAM is first patterned on the substrate, which is then exposed to the sample solution. In direct microstamping, samples (DNA, proteins) are simply transferred from an inked stamp to the substrate in a single step. Regardless of direct or indirect stamping, the first step in microstamping is “inking” sample onto the stamp surface.

### 2.1.4 Non-contact printing techniques

Contact printing methods include a variety of techniques, but all methods ultimately involve contact between the substrate surface and a stamp or pin. In contrast, non-contact printing techniques vary considerably from photochemistry based methods to laser writing to fluid droplet dispensing. There are two main advantages to non-contact printing: reduced contamination and higher throughput. By keeping the printing device and the substrate separated at all times, the likelihood of contamination is greatly reduced. Hence, the need to constantly clean the printing device between uses is eliminated. Furthermore, non-contact printing methods hold the greatest potential for increasing microarray fabrication throughput. Many non contact methods deposit solutions in parallel, allowing entire arrays to be produced simultaneously.

#### 2.1.4.1 Photochemistry-Based Printing

Photochemistry microarray printing is based on chemical treatment of the substrate and UV light exposure through photomasks. The two main methods are photolithography<sup>30-33</sup> and direct photochemical patterning<sup>30,34,35</sup>. In photolithography, a positive photoresist layer is spin-coated onto the substrate, exposed to UV light through a photomask and then developed to form micrometer sized open regions where adhesion-promoting molecules are bound (Figure 5.a).

The substrate is then immersed in solvent to remove the remaining photoresist, and adhesion-resistant molecules are bound to the exposed glass surfaces. Direct photo-chemical patterning is very similar to photolithography except that it does not require a photoresist layer. A substrate is coated with photochemical molecules and exposed to UV light through a photo mask, as illustrated in Figure 5(b). UV-exposed molecules are either activated or deactivated to bind biological molecules of interest. Photochemistry-based fabrication methods are mainly applied to protein and DNA arrays although cell adhesion regions can also be fabricated in this way.<sup>36,37,25,31</sup> Similar to all parallel patterning methods, photochemistry features high throughput. The disadvantages include the risk of biomolecule denaturation by photoresist solvents and the difficulty in patterning different samples in a single step.<sup>22</sup> Photolithographic printing is commonly used in generating DNA microarrays of *in situ* synthesized oligonucleotides.<sup>38,39</sup> For example, the Affymetrix Inc., Santa Clara, CA, process comprises serial light exposures through different photolithographic masks followed by the chemical synthesis of DNA bases at the exposed/activated sites.

After each exposure a single DNA base is coupled to the activated sites and the process is repeated until the sequences are generated. As a serial process, this method can be time consuming for longer sequences of oligonucleotides, but it provides high-density arrays. The GeneChip® (Affymetrix Inc.), a high-density-oligonucleotide array, is generated on fused silica substrates that carry 50 to 400 replicate arrays. Each has up to 400,000 probes on a 1.6 cm<sup>2</sup> area.<sup>10</sup> A recent innovation is to use a virtual mask created on a computer and projected onto the substrate with a digital micromirror array<sup>40,41</sup>. Microfeatures measuring 16 μm<sup>2</sup> were created in this way.<sup>41</sup>

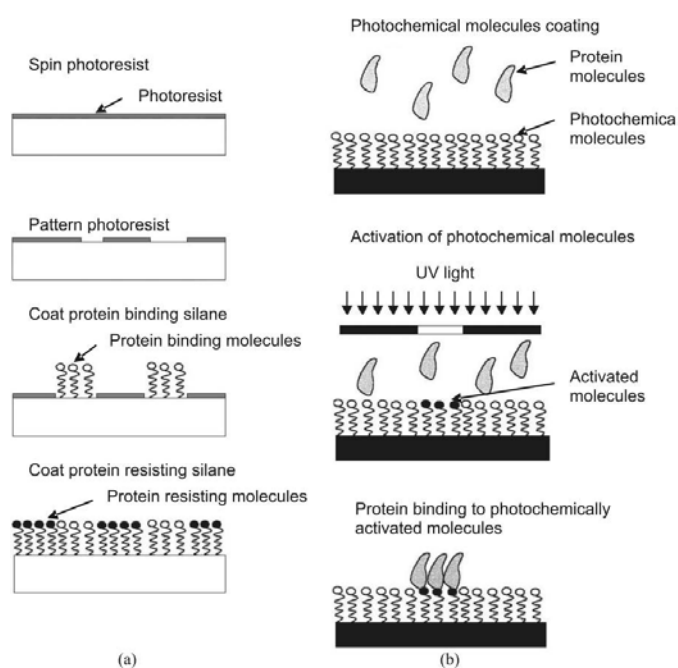


*FIGURE 5: Schematic illustrations of photochemistry based manufacturing procedures: a) Photolithography applied to silane self-assembled monolayers (SAMs), b) Direct photochemical protein patterning by activation of a photochemical coupling species<sup>22</sup>*

### 2.1.5 Interaction of the laser radiation with the solids

The treatment of the solid materials by using laser as cutting, welding, incision constitutes one very active inquiringly field and exist a big number of bibliography around from this<sup>45,46,41,5</sup>. The interaction's mechanisms of the directional laser radiation with the materials depend from the following parameters<sup>47</sup>

- Source of irradiation (e.g. wavelength, duration of pulse, space and time agreement, polarisation)
- Physical properties of the material that we radiate (these properties are expressed from the optical absorption's factor, the thermal diffusion factor e.t.c..)
- Environmental conditions (e.g. vacuum conditions)

These parameters also determine the type of the basic excitations and interactions between the laser radiation and the material.

#### 2.1.5.1 Primary Activities

The first stage in each change in the material's structure from laser radiation, is the deposition of a big energy quantity at a very small surface. The total energy, the space and the time change of the exposure determine which type will be the final change in the surface or in the volume of the material.<sup>48</sup> The basic interactions of laser pulses with a solid material emanates from the excitation of electrons. With the absorption of the photons, the electrons excite from their basic situations in not occupied situations. One-photon ionization is the basic activity that takes place while the radiation with short laser pulses (ns), where the passages are proportional of the beam energy that was used, that is to say it dominates the phenomenon of linear absorption. While the radiation with ultrashort laser pulses (ps, fs) the sovereign phenomenon is the multiphoton absorption, where with the increase of laser's energy we are led in more intense processes of not linear absorption.<sup>49</sup> If the number of electrons in the conductivity zone is big, their number can increase itself via the ionization of conflict (impact ionization). If the beam's energy is enough, the multiphoton absorptions and the ionization of conflict (impact ionization) can lead in optical collapse of the material that has as a result the creation of plasma<sup>22</sup>.

### 2.1.5.2 Secondary Activities

The initial electronic passages are followed by a complicated hierarchy of the secondary processes. The excited electrons de-energize and release their energy through a number of processes that finally create a structural change in the material. The table that presents the "chain of" facts that develop depending on the pulse's time appears in figure 8.<sup>50</sup> The primary processes are connected with one very small time of agreement of the material's polarisation. Processes of phase destruction disappear the polarisation in time that corresponds at  $10^{-14}$  sec<sup>51</sup>. The initial distribution of the excited electron's situations very rapidly changes with the interactions institution of - institution, with the result of the creation of a partial balance situation between the electrons in time roughly  $10^{-13}$  sec.

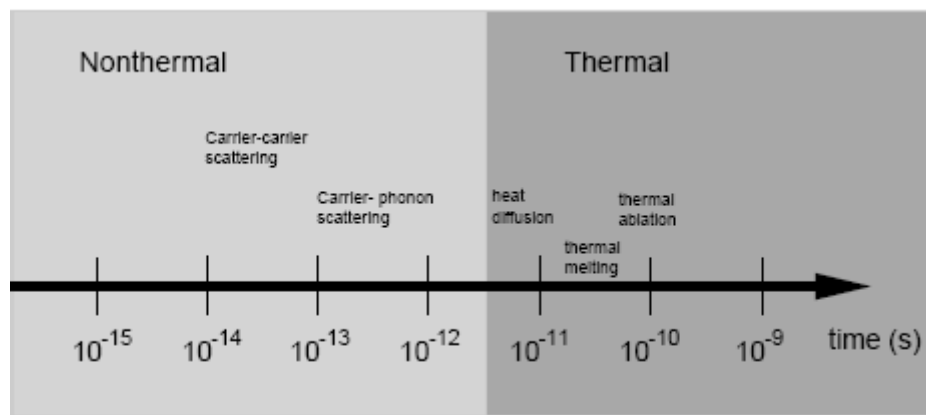


FIGURE 8: Time development of the phenomena that develop depending on the duration of the pulse.

The electrons that are found in the partial balance situation, they lead in their initial situation in time duration between  $10^{-13}$  and  $10^{-12}$  sec emitting phonons (carrier-phonon scattering). The final stage of the thermal process is the redeployment of phonons in entire the Brillouin zone accordingly with the Bose-Einstein distribution.

### 2.1.5.3 Macroscopic Regard

This paragraph describes from a macroscopic side, the phenomena that develop in the solid material while its irradiation with powerful laser radiation. While the material's irradiation, the laser radiation is absorbed in a determined region that is named length of optical absorption  $L_{opt}$ . This quantity (equation 1) is the reverse of the absorption's factor  $\alpha$ , that is presented in Beer-Lambert equation and depends from the radiation's wavelength and the material (equations 1 and 2):

$$\bullet L_{optical} = a^{-1} \quad (1)$$

$$\bullet L_{optical} = \frac{\lambda}{4\pi\kappa} \quad (2)$$

✚  $\lambda$ : the radiation's wavelength

✚  $\kappa$ : the creolic part of the indicator of diffraction that expresses the absorption.

✚

In the end of the laser pulse with time duration  $\tau$ , the energy of radiation is diffused under a form of heat in-depth that is determined from the length of the thermal diffusion<sup>52</sup> (eq. 3).

$$L_{thermal} = \sqrt{2\chi\tau} \quad (3)$$

where:  $\chi$  the factor of thermal diffusion (equation 4):

$$\chi = \frac{\kappa}{\rho C_v} \quad (4)$$

✚  $\kappa$  the factor of thermal conductivity of material,

✚  $\rho$  the density of material,

✚  $C_v$  the special heat respectively of the material that irradiates.

Figure 9 presents the absorption of the electromagnetic radiation and the heating of the material, for the case where the optical absorption length  $L_{opt.}$  is much smaller from the thermal diffusion length  $L_{thermal}$ .

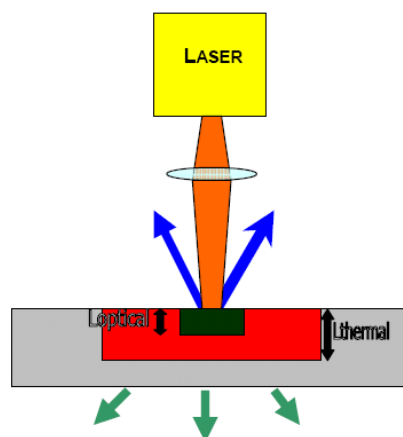


FIGURE 9: Absorption of radiation and heating of the sample in the case where  $L_{thermal} \gg a^{-1}$

According to the equation 3 for pulses with big duration of time  $\tau$  prevail phenomena of thermal diffusion, while by using laser with shorter pulses offers smaller thermal diffusion length during the action of the pulse and accordingly limited thermal volume.

## 2.1.6 Laser Induced Forward Transfer (L.I.F.T.) Method

### 2.1.6.1 Introduction

Apart from the techniques that we reported above, the deposition of materials can be also achieved via methods that use laser. Technical Laser Capture Micro Dissection (LCM)<sup>13,15</sup> is used for the transport and the segregation of concrete cells from a solution, but it cannot be used for the transport of living micro-organisms. The ultraviolet radiation is used for the treatment of biological substrates<sup>3,18,53</sup> and the techniques of guidance with laser (laser guidance)<sup>54,55</sup> can produce structures of limited number of polymers. The 1990, Nelson et. al<sup>19</sup> described the entire transport of molecules DNA from a cold hybrid target by using pulse laser. In this approach that it was characterized as matrix assisted laser desorption /ionization time-of-flight (MALDI-TOF), the material that is transported, is dipped in a solution that shields it from any chance of its destruction from the use of laser. Continuity the ionised material is directed in the pipe of spectrograph of mass of time of flight. The Tsuboi et.al<sup>56</sup> used the technique of deposition via deconstruction with laser, for the transport of protein of silk from a solid target in substrates like hails and ZnSe under vacuum conditions. Via spectrum in infrared it was almost ascertained similar constitution of the transferred material with the initial material at the target, but it was not reported the distribution of its mass. The Phadke et.al<sup>57,58</sup> used a variant of this technique for the creation of thin bacteriophorhodhopsin surfaces and glucose oxidase surfaces too. For the restriction of laser interaction with the protein, they used a complex target that it contained apart from certain biological material and chemical agent that protected the protein from its direct interaction with the laser and accordingly its destruction by this. The disadvantage of this technique is the creation of thin surfaces which except the protein they are contained and certain components of the solution. The Ringeisen et. al.<sup>59,60</sup> created micropatterns of active proteins, viable bacteria E.coli and cells of ovaries of suckling rodents with the technique matrix-assisted pulsed laser evaporation (MAPLE).

In the technique MAPLE is avoided the destruction of biological union by dip the sample in regulating solution that absorbs powerfully the ultra-violet radiation. Also high pressure of evaporation is presented. The complex solution is transferred in optically transparent surface hails. Via suitably selected objective lens the beam laser is focused in the down surface of hails substrates where is found the thin layer of the solution.

Owing to the low concentration of thin film of the material in the target, the photons react initially with the regulating solution, the frozen material is evaporated releasing the biological union, remaining finally intact in the booth of void.

Finally Karaiskou et. al.<sup>61</sup> applied recently the laser induced forward transfer-LIFT method in a line of biological molecules of creating micropatterns of nucleons acids and proteins of 50  $\mu\text{m}$  size. The morphology of the transferred structures was examined with the method of scanning electronic microscopy (SEM), while the constitution of the substrates was examined with the method of electrophoresis proving that the provision of micropatterns is suitable for experiments of hybridization. Even if L.I.F.T. method was initially used for the transport of metals, this technique was extended fast also in the transport of other materials. It has been used also for growth of provisions of microelectronics, as capacitors, resistors, chemical sensors, biosensors, thin transistors (TFTs), organic orders TFT and organic passages of light (OLED). This technique was used in this work and it is described in details below.

#### 2.1.6.2 L.I.F.T. Process

The Laser Induced Forward Transfer-L.I.F.T. is a technique which allows the checked transport of thin coating (film) of some materials for the creation patterns. In most cases, the transport of thin film is achieved with by using pulse lasers, but has also realised with the use of continuous pulse lasers. The beam laser, after it is shaped in dimensions of scale  $\mu\text{m}$ , it is focused in target's surface, which is a thin coating from the material we want to transfer on a transparent substrate in this laser radiation<sup>62</sup> With the effect of radiation is created a shock wave between the surface of the coating and the transparent substrate, with the result of the detachment of radiating spot and its transport in the substrate's surface that has been placed in parallel and very near in the target's surface (Figure 10).

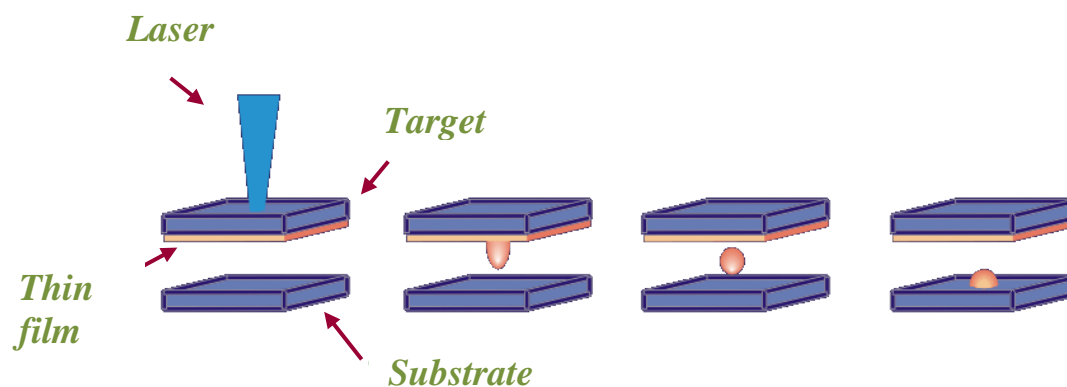


FIGURE 10: Presentation of L.I.F.T process.

The system of target-substrate is placed in a cell where the deposition can take place under air or under vacuum conditions. The repetition of process of the transport in different places of the target and the substrate, under the control of computer and drivers of step engines has as a result the creation extensive shapes, as patterns of elements or located coverings. The dimensions of shaped beam laser are identified with dimensions of the irradiative material and at extension of unit of deposition (pixels). Figure 11, which follows, presents the phenomena that are happening during LIFT process with use of ultra short pulses. The pressure that is developed in the surface of the target under review, owing to its irradiation, it forces the material to be defused in the same time with the incident time of radiation<sup>31</sup>. Due to the fact that the beam meets first the transparent substrate of the target, we have the threshold of intensity for the achievement of deconstruction that is related with the reject of destruction of glass. Therefore the intensity of beam should be of course smaller than the intensity that leads to destruction of glass. Immediately afterwards the end of pulse and owing to the progressive transfer of the material a shock wave is created in between the surface of target-air, which continues propagating itself in air. The same moment, it is created in a material a wave of rarefaction (rarefaction wave) in opposite direction from the direction of distribution of shock waves and with speed equal with the speed of sound in the material, contributing with this way, in the of expansion abrupt increase of pressure that is developed in the target. The surface between the target-air begins to shift the moment where the pressure near in the surface exceeds the atmospheric pressure, while the speed of the transferred material increases progressively with increase of pressure associates the time of vibration.

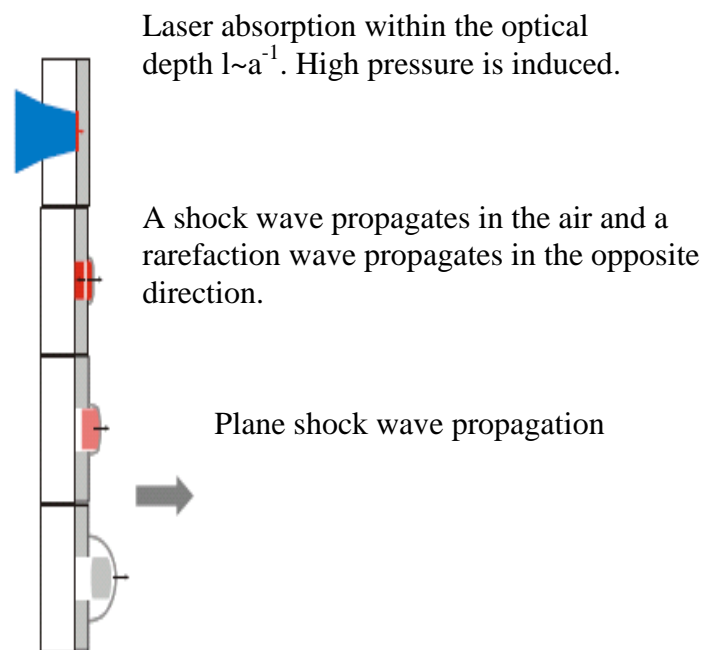


FIGURE 11: Stages of ejection of material during L.I.F.T. process

### 2.1.6.3 Advantages of L.I.F.T. method

Basic advantage of L.I.F.T. method is the simplicity with which the materials can be transferred, without the help of some material of transporting uterus. In comparison with photolithography methods, what were presented very analytically in the previous paragraph, the present method is a "clean" activity of step. Finally, it can be used for the deposition of big variety of materials in various substrates. It has been applied, as we reported also in the import, for the transport of metals (Cr, Au, Al, Cu, Ni), metal oxides, semiconductors (Si, Ge) and recently it is used in the transport of biological materials (Pyrene) as well as organic materials (PMMA).

## 2.2. 3D Patterning Methods

Femtosecond laser interaction with matter differs essentially from those with longer pulses or CW lasers in its significant nonlinearity, ultrafast characteristics and the possibility of highly localization of reaction volume. The multi-photon photopolymerization technology is expected to play a similar role to that played by lithography for planar semiconductor device processing and for micro-nanofabrication of 3D polymer-based optoelectronic devices as well for microelectromechanical systems. The emergence of a new technology in 1997, two-photon polymerization<sup>1</sup> (2PP), has brought the light curable resin into the realm of nanofabrication. As indicated by the name, the resins are polymerized not by absorbing one UV photon, but by simultaneously absorbing two photons at longer wavelength, usually in the red-infrared (IR) spectral region. The two-photon process<sup>67,68</sup> has at least two advantages compared to single-photon absorption used in conventional rapid prototyping. First, common polymers have negligible linear absorption in the red-near-infrared (NIR) region, so the laser penetrates deeply into materials and directly induces polymerization from inside without contaminating outside of the focal volume. Secondly, the quadratic dependence of polymerization rate on the light intensity enables 3D spatial resolution, and the accuracy is better than that achieved in single photon process. In addition three photon polymerization (3PP) is initiated through the non linear process of three-photon absorption of a photoinitiator, and induces several chemical reactions between starter molecules and monomers in a transparent resin. 3PP is a process which allows the fabrication of components of very high resolution. The 3PP was experimentally reported for the first time in 2005 by M. Farsari, G. Filippidis and C. Fotakis<sup>69</sup> for fabrication microstructures with high resolution.

## 2.2.1 Material processing with femtosecond lasers

### 2.2.1.1 Interaction of an organic medium with light

The interaction of an organic medium with light can be regarded within the framework of a dielectric subjected to an electric field. In the dipole approximation, the induced dipole momentum in a molecule due to the applied field is given by the following equation [5]:

$$\mu_{ind} = -er \quad [5]$$

where  $e$  is the electronic charge and  $r$  is the field induced displacement. The bulk polarization resulting from this induced dipole moment is given by:

$$P_{ind} = -Ner \quad [6]$$

where  $N$  is the electron density in the medium. In these cases (where the field strength is low), to a good approximation, the induced polarization  $P_{ind}$  in a medium, due to the applied electric field  $E$  is linear in  $E$  and can be written as:

$$P_{ind} = X^{(1)}E \quad [7]$$

where  $X^{(1)}$  is a susceptibility and is a second rank tensor and has 9 components because it relates all the components of the polarization vector with all components of the electric field vector. The optical response of a medium at an optical frequency  $\omega$  is represented equivalently by the complex refractive index  $n_c$  given by:

$$n_c^2(\omega) = 1 + 4\pi\omega X^{(1)} \quad [8]$$

The complex refractive index can be written as the sum of the real and imaginary part as:

$$n_c = n + ik \quad [9]$$

where  $n$  the real part which corresponds to the dispersion of refractive index, while  $k$  the imaginary part which corresponds to an electronic absorption.

This can be understood by considering the medium to be an assembly of forced harmonic oscillators which are driven by sinusoidal optical field. The oscillators also experience a damping force which can be interpreted as an exchange of energy between the optical field and the medium. Using the harmonic oscillator model, we get the following equation of motion:

$$\frac{d^2x}{dt^2} + 2\Gamma \frac{dx}{dt} + \omega_0^2 x = -\frac{e}{m} E \quad [10]$$

where  $\Gamma$  is the damping constant. Considering a sinusoidal electric field:

$$E(t) = \frac{1}{2} E_0 [e^{i\omega t} + e^{-i\omega t}] \quad [11]$$

The solutions to this differential equation are:

$$n = \text{Re} n_c = 1 - \frac{Ne^2}{m} \frac{2\pi(\omega^2 - \omega_0^2)}{(\omega^2 - \omega_0^2)^2 + (2\Gamma\omega)^2} \quad [12]$$

$$k = \text{Im} n_c = \frac{Ne^2}{m} \frac{4\pi\Gamma\omega}{(\omega^2 - \omega_0^2)^2 + (2\Gamma\omega)^2} \quad [13]$$

The real part of the refractive index corresponds to dispersion while the imaginary part corresponds to absorption.

### 2.2.1.2 Non linear Optical Effects

The treatment of the previous section assumed the medium to be a collection of harmonic oscillators. This assumption is valid only for small displacement from the equilibrium position. If the field is strong enough as in our case, the equation of motion will contain non harmonic terms. Equation [10] must be modified to:

$$\frac{d^2x}{dt^2} + 2\Gamma \frac{dx}{dt} + \omega_0^2 x + ax^2 + bx^3 + \dots = -\frac{e}{m} E \quad [14]$$

If the diversion in harmony is small compared to the linear term, the solution can be approximated as a power series in E. The value of material polarization P can be written as:

$$P = \chi^{(1)} E + \chi^{(2)} E^2 + \chi^{(3)} E^3 + \dots \quad [15]$$

where the quantities of  $\chi^{(1)}$ ,  $\chi^{(2)}$ ,  $\chi^{(3)}$  are first, second and third-rank tensors, representing linear, second-order and third-order optical susceptibilities.  $\chi^{(2)}$  gives rise to second order nonlinear effects such as optical rectification, second harmonic generation, and linear electro-optic effect.  $\chi^{(3)}$  is responsible for third-order effects such as optical Kerr effect, electric field induced second harmonic generation, four wave mixing, third harmonic generation and two photon absorption. In resonant processes, there is no contribution from the even-order susceptibilities like  $\chi^{(2)}$  and  $\chi^{(4)}$ . Therefore, the nonlinear absorption is described by the imaginary parts of  $\chi^{(3)}$ ,  $\chi^{(5)}$  of which typical effects are two-photon and three-photon absorptions, respectively.

Nonlinear processes<sup>70,71</sup>, for example, multiphoton absorption including two-photon absorption (TPA)<sup>71,72</sup>, have come to play a dominant role in nanofabrication. In order to produce a lasting effect on a material, photons must first be absorbed.

The energy and momentum are exchanged between the optical fields and molecules through absorption and emission. In such a process, the imaginary part of nonlinear susceptibility represents the energy transfer from the light field to a medium.

The energy exchanged between the light beam and the medium per unit time and unit volume is:

$$\frac{dW}{dt} = \left\langle \vec{E} \cdot \dot{\vec{P}} \right\rangle \quad [16]$$

where E is the electric field vector and the brackets denote time average over several cycles of the field.

Particularly, for degenerate TPA, that is, the process of photons of identical energy that are simultaneously absorbed, the energy absorption rate is:

$$\frac{dW}{dt} = \frac{8\pi^2\omega}{c^2n^2} I^2 \text{Im}[\chi^{(3)}] \quad [17]$$

It is seen that the TPA rate quadratically depends on the light intensity, which is an important mechanism to improve the spatial resolution in two-photon fabrication. Typical values of intensity are  $10^{69}$  photons/cm<sup>2</sup>\*sec. Something proportional matters in chemical reactions like  $2A + B \rightarrow C$  where the rate of this reaction depends quadratically on the concentration of A.

### 2.2.1.3 Cross section of 2PA

Two photon absorption (TPA) is often described in terms of a cross section  $\sigma_2$ . A high capability of materials to absorb photons via TPA is desired, which is described by TPA cross-section,  $\sigma_2$ , defined by

$$\frac{dn_p}{dt} = \sigma_2 N F^2 \quad [18]$$

where N and  $dn_p/dt$  are the number of absorbing molecules per unit volume and the number of absorbed photons per unit time respectively.  $F=I/h\nu$  denotes photon flux. According to equation [19], the TPA cross-section is:

$$\sigma_2 = \frac{8\pi^2 h\nu^2}{c^2 n^2 N} I^2 \text{Im}[\chi^{(3)}] \quad [19]$$

Two Photon cross-section can also be expressed in terms of the change in intensity of an incident laser beam:

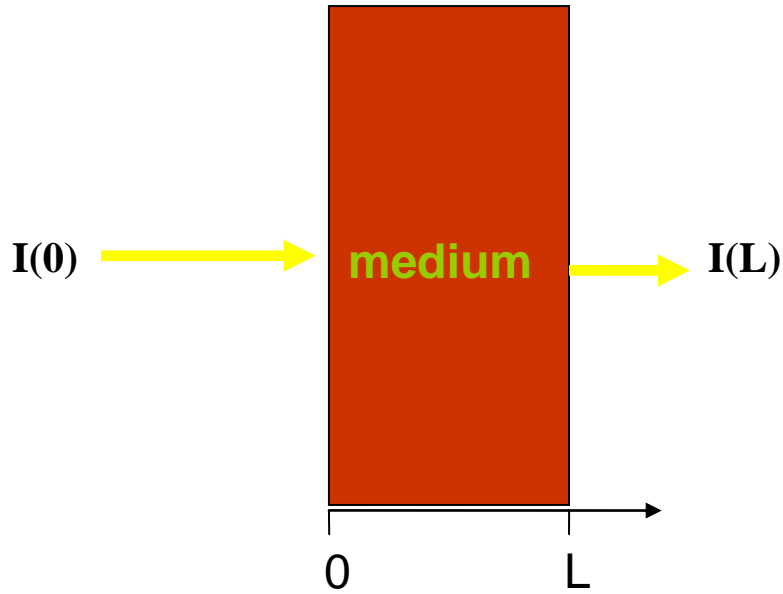


FIGURE 12: Change in intensity of a beam as it propagates through a medium

The change in intensity  $I$  of a beam as it propagates through a medium with linear and two photon absorption is given by:

$$\frac{dI}{dz} = -(a_1 I + a_2 I^2) \quad [20]$$

where  $a_1$  is the linear absorption coefficient and  $a_2$  is the two photon absorption coefficient related to the imaginary part of the third order susceptibility  $\chi^{(3)}$ .

For a beam with a rectangular temporal profile and a Gaussian spatial profile and for a medium with no linear attenuation ( $a_1=0$ ), the transmitted intensity  $I(L)$  can be shown to be:

$$I(L) = \frac{1}{La_2} [\ln(1 + I_0 La_2)] \quad [21]$$

where  $I_0$  is the incident intensity and  $L$  is the thickness of the sample. The molecular two photon absorption cross section  $\sigma_2$  is related to  $a_2$  by:

$$h\nu a_2 = \sigma_2 N_0 = \sigma_2 N_A d_0 \times 10^{-3} \quad [22]$$

where  $h\nu$  is the incident photon energy,  $N_0$  is the molecular density ( $\text{cm}^{-3}$ ),  $N_A$  is the Avogadro number and  $d_0$  the concentration ( $\text{mol l}^{-1}$ ).

### 2.2.1.4 Computation of multiphoton absorption coefficients at the molecular level

For the calculation of nonlinear coefficients we use the sum over states method which is based on a perturbative expansion of the Stark energy. The optical nonlinearities are introduced as a result of Stark mixing with various excited states.

For one photon transitions the most important quantity for one photon transitions is the transition moment  $M_{0f} = \langle 0|r|f \rangle$ , where  $|0\rangle$  and  $|f\rangle$  are the wave functions of the initial and final states involved in the transition, respectively. For a two photon absorption transition, the expression for the cross section contains terms of the type  $M_{0i}M_{if}$ , where  $i$  stands for the intermediate time-dependent state involved in the transition.

Then the quantity, that is important for two photon transition, is the transition tensor  $S_{0f}$  given by the following equation:

$$|S_{f0}(\lambda, \mu)|^2 = \left[ \sum_i^N \left[ \frac{(\lambda \langle i|r|0 \rangle) (\langle f|r|i \rangle \mu)}{E_i - E_\lambda + i\Gamma} + \frac{(\mu \langle i|r|0 \rangle) (\langle f|r|i \rangle \lambda)}{E_i - E_\mu + i\Gamma} \right] \right]^2 \quad [23]$$

where  $\lambda$  and  $\mu$  are the unit vectors defining the polarizations of the two photons in the laboratory coordinates, 0 and f are the ground electronic state and the final excited state, and  $i$  is one of the N intermediates states. The terms  $\langle i|r|0 \rangle$  and  $\langle f|r|i \rangle$  are the transition moments for the  $0 \rightarrow i$  and  $i \rightarrow f$  transitions.  $E_\lambda$  and  $E_\mu$  are the energies of the two photons respectively and  $E_i$  and  $\Gamma_i$  are the energy and linewidth corresponding to the  $i_{th}$  intermediate state respectively. In terms of the transition tensor, the basic cross section for TPA is given by the expression:

$$\sigma_2 = \frac{(2\pi e)^4}{(ch)^2} [E_\lambda E_\mu g(E_\lambda + E_\mu)] S_{f0}(\lambda, \mu)^2 \quad [24]$$

where  $g$  is the line shape function and is Gaussian.

The design of molecules that have a large TPA cross-section is an important task of stereolithography using two-photon polymerization. First, a femtosecond laser carries much greater peak power. With conventional light sources the strength of the light field is in the range of 1 V/cm and the resulting elongation of dipole is smaller than  $10^{-16}$  m, much smaller than atomic or molecular diameters ( $10^{-10} \sim 10^{-7}$  m). With femtosecond laser irradiation, the field strength is  $10^8$  V/cm, which corresponds to an incident light intensity of  $100 \text{ GW/cm}^2$  and is sufficient to induce direct bond breaking.

Two photon absorption has an extremely small cross-section, it is confined to occur only in a small 3D volume around the close vicinity of the laser focus, less than the cubic wavelength ( $\lambda^3$ ).

Typical values for TPA cross section are  $10^{-48}$  -  $10^{-50}$  cm<sup>4</sup> sec/photons. Hence, a quite high 3D spatial resolution can be achieved in the pinpoint exposure. Secondly, when materials are irradiated with femtosecond laser pulses, the photon energy is deposited much faster than electrons could transfer it to the lattice, or molecule/ atom oscillations through phonon emission, meaning that the excitation is a heat insulation process<sup>72,74,75</sup>.

### 2.2.2 Two photon polymerization

Two-photon polymerization (2PP) was experimentally reported for the first time in 1965 by Pao and Rentzepis<sup>76</sup> as the first example of multiphoton excitation-induced photochemical reactions. They focused 694nm laser from a pulsed Ruby laser into a sample of styrene that was cooled to 77 °K. After developing in methanol, solid precipitate was extracted and confirmed to be polystyrene through IR absorption. In the particular experiment, no photo sensitizer was used and the author tried to increase the two photon absorbance by using monomers with added functional groups, such as para-iso-propylstyrene and chlorine-substituted derivatives of styrene. As a result, much enhanced two-photon polymerization was observed.

Two-photon polymerization has unique advantages:

- First of all, it has intrinsic ability to produce 3D structures. In addition, the long wavelength chosen for TPA has less absorption and less scattering, which gives rise to the deep penetration of light; use of ultrashort pulses can start intense nonlinear processes at relatively low average power, without thermally damaging the samples.
- The two-photon polymerization system doesn't need vacuum condition for operation. The system is easy to operate and maintain.
- No mask or stamp is needed for fabrication too. It directly converts computer-designed patterns into matter structure. The rapid turnaround time for fabrication allows one to quickly iterate and modify design.

#### 2.2.2.1 Fundamentals of Stereolithography using Two Photon Polymerization Method

Photopolymerization is one of the most important types of photochemical reactions that have been used for laser fabrication<sup>77</sup>. This is because the material resins undergo a significant phase transition after laser irradiation, from liquid to solid, and non-polymerized liquid is easily removed by a developing process so that solidified 3D structures stand out<sup>78</sup>. The basic components of the starting liquid material are monomers and oligomers (or prepolymer). Upon light excitation, the monomers or oligomers may be solidified by two means: polymerization and crosslinking<sup>77</sup>.

### 2.2.2.1.a Descriptions of polymerization based on radical initiators

An important feature of polymerization is the chain reaction by which macromolecules are created, while cross-linking is concerned more with the formation of crosslinks with chemical bonds. An important difference of these two kinds of reaction lies in their quantum yield, which is defined as the ratio of number of polymerized monomer units to the number of photons that are needed to cause this polymerization.

In the case of photocrosslinking, addition of each monomer unit requires absorption of a photon, leading to a quantum yield less than 1.

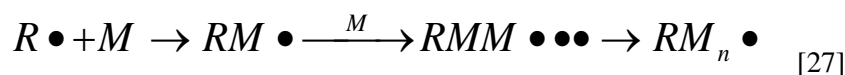
In contrast, photopolymerization is realized via chain reactions as shown in the following equation [26], so the quantum yield can reach several thousands.



Here M is the monomer or oligomer unit, and  $M_n$ , the macromolecule containing n monomer units. The quantum yield of general monomers and oligomers is low. In order to increase the initiating efficiency, one or several low-weight molecules that are more sensitive to light irradiation are added. They form initiating species of radicals or cautions by absorbing photons. Such small molecules are called photoinitiators:



where symbols denote photoinitiator (I), radical ( $R\bullet$ ) and  $I^*$ , an intermediate state of the photoinitiator after absorbing a photon:



The photoproduced radicals react with monomers or oligomers, producing monomer radicals, which combine with new monomers, and so on, so the monomer radicals expand in a chain reaction, until two radicals meet with each other. This chain propagation stops in either of the following channels:

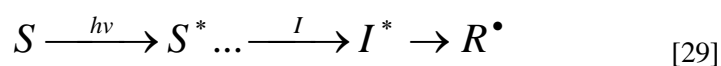


Therefore the polymerization process consists of several steps: (i) photoinitiation, (ii) chain propagation and (iii) termination.

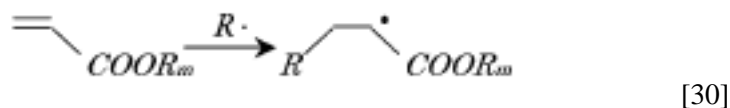
A good photoinitiator should be (i) easily reduced to an initiating species upon light irradiation, and (ii) provide photoproducted radicals or cautions active enough to react with monomers or oligomers.

The nonlinear response of photopolymerization is caused by highly reactive oxygen molecules absorbed by resin. Oxygen molecules inhibit polymerization reaction at the beginning of polymerization, because oxygen molecules scavenge the radicals that generate the polymerization reaction. Accordingly, when the intensity of light is adequately low, polymerization reaction does not propagate, because almost all the photons are consumed by the oxygen molecules.

A photosensitizer is a molecule that absorbs light and then transfers the energy to a photoinitiator. With such a scheme, the photoinitiation process is expressed as:



where S is the photosensitizer. A co-initiator itself doesn't absorb light, but it is involved in the production of radical species. Reactions that are typically used for laser fabrication are: double-bond addition of acrylates (radical-type)



For a radical type initiator, benzoyl is the most widely used chromophore, which must have the initiator, since it exhibits good absorption in the UV region.

After polymerization, the oligomer constitutes the backbone of the polymer network. The physical, chemical and mechanical properties of the solidified resin strictly depend on the nature and structure of the oligomer.

Oligomers generally contain at least two reactive groups, from which both cross-linking and polymerization could occur.

Monomers have a much smaller molecular weight and consist of one or several reactive groups. They polymerize similarly to oligomers and are an important factor in determining the efficiency of polymerization. In addition, monomers are also useful for diluting resins so that the polymer is easier to handle for a particular use.

For 3D micro-nanolithography, a suitable viscosity is of particular importance due to the opposite requirements in different steps of processing: a high viscosity is needed for keeping early produced volumes where they are created, while a low viscosity facilitates removal of unsolidified resin from intervals. For a successful fabrication the following behaviours are preferred: (i) high polymerization efficiency upon light irradiation, (ii) lower shrinkage after polymerization, (iii) fast reaction time and low dark polymerization.

### 2.2.2.1.b Stepwise 2PA –Simultaneous 2PA

Selection rules for single-photon and two-photon excitation (2PE) are different, even parity transitions for 2PA and odd parity transitions for one photon absorption. Electron excitations can occur stepwise or simultaneously as shown in Figures 13a,b.

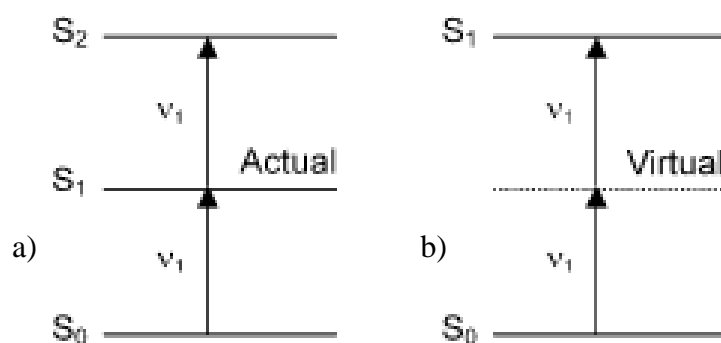


FIGURE 13: Illustration of two-photon absorption schemes. a) stepwise 2PA with an actual intermediate energy level, and b) simultaneous 2PA with a virtual energy level.

The former could be treated as two sequential single-photon absorption processes and relies on the existence of a real intermediate state, from which an excited population is further pumped to a higher energy level by absorbing photons of the same energy as the ground state (excited state absorption). Such a process, although on some occasions also called 2PA or stepwise 2PA.

Simultaneous 2PA is a quantum mechanical three-body process, where an electron absorbs two photons simultaneously to transcend the energy gap in one excitation event<sup>70</sup>. As light passes through a molecule, a virtual state is formed when the first photon is absorbed. It persists for a very short duration (of the order of several femtoseconds as prescribed by Heisenberg's Uncertainty Principle), which contrasts with the long lifetime of the actual intermediate energy level in stepwise absorption. 2PA can result if the second photon arrives before the decay of this virtual state. If the energy of the two photons is identical, the process is referred as degenerate 2PA, otherwise, the process is a non-degenerate one. For femtosecond laser micro-nanofabrication, simultaneous 2PA is more relevant.

However, since the transition probability of two-photon absorption tends to be extremely small, these processes generally require an expensive short-pulsed laser such as a Ti: Sapphire type.

The 2PA can be utilized for inducing photopolymerization. The difference between one-photon and two-photon induced photopolymerization lies in how the energy for activating initiators is provided.

#### 2.2.2.1.c High Efficiency Two-Photon Materials

Molecules of large TPA cross-section<sup>79</sup> are very important for the broad application of two-photon photopolymerization technology. Polar molecules were found to have a large change of dipole moment ( $\Delta\mu > 10D$ ) upon excitation from ground state to excited state<sup>80</sup>. Since both the ground and excited state can participate in the formation of the virtual energy level, the transition probability is proportional to  $(\Delta\mu)^4$ . For example TPA cross-section can be larger than  $\sigma_2 \sim 10^{-50} \text{cm}^4 \text{s photon}^{-1}$ .

One important effort in the molecular design of large  $\sigma_2$  is searching for a molecular structure that potentially has larger  $\Delta\mu$ . It was found that  $\pi$ -conjugated systems such as those with phenylethenyl, fluorenyl<sup>80</sup>, or polyenyl constructs were good candidates.

In these molecules, electron-donating (D) and/or electron-withdrawing (A) moieties were separated by a conjugated  $\pi$ -electron system (A- $\pi$ -A, D- $\pi$ -D, D- $\pi$ -A- $\pi$ -D and A- $\pi$ -D- $\pi$ -A). It is theoretically predicted and experimentally found<sup>5</sup> that  $\sigma_2$  can be enhanced by increasing the conjugation length and the donor and acceptor strengths.

Another concern in two-photon molecule design is wavelength sensitivity<sup>80</sup>. This arises from the fact that the most suitable femtosecond laser is solid wavelength-tunable Ti:Sapphire laser, of which the wavelength ranges from 680 nm ~ 840 nm.

In addition for increasing TPA cross-section of chromophores, there is another route to enhance TPA by increasing the chromophore number density without causing aggregation.

#### 2.2.2.1.d Dynamic Power Range

The polymerized size increases with the increase of the irradiation duration ( $\Delta t$ ) and the square of light intensity, S.L.I., ( $I^2$ ). The dynamic power range is defined by the window between the two-photon polymerization threshold and the laser-induced breakdown threshold<sup>76</sup>. The photopolymerization threshold is determined by the production efficiency of initiating species from excited triplet states, which is characterized by the quantum yield of polymerization.

The reactions that produce radicals should compete with monomer quenching, oxygen quenching and other pathways of deactivation of the excited states like phosphorescence emission. The threshold is also determined by the reactivity of radicals and monomers. When laser irradiation is greater than a particular value, intense damage is induced in materials. This phenomenon is called laser-induced breakdown. The breakdown is dominated by a thermal process when pulse width is long (e.g. >10 ps) for most transparent materials<sup>70,76</sup>.

This was evidenced by observations that the breakdown threshold scales approximately with pulse width by  $\tau^{1/2}$  for  $t > 10$  ps<sup>6</sup>. For shorter pulse widths (<1 ps), it is believed that the breakdown occurs in various materials via plasma generation<sup>81</sup>. Plasma can be produced via an avalanche process whereby free electrons are accelerated by the incident light field, causing an explosive cascade growth in electron density.

The generated plasma can absorb and defocus the remaining incident light field. The breakdown causes the ablation process at sample surface and micro-explosion inside bulk, both accompanied by vaporization and atomization of the sample constituents.

Therefore, measures could be taken to increase the quantum yield of polymerization, and therefore the dynamic power range. A simple and effective method is choosing laser wavelength so that radicals are produced more efficiently. It was experimentally observed<sup>82</sup> that the two-photon exposure threshold at 660 nm is roughly half of that at 700 nm, and approximately five times lower than that at 800 nm, while the breakdown threshold didn't vary significantly. The most efficient method is use of high TPA cross-section initiators.

### **2.2.3 Advanced techniques in two-photon micro-fabrication**

The progress of femtosecond laser technology and exploration of high efficiency photoinitiators and photosensitizers have fuelled the progress of two photon polymerization lithography. Its basic principle and potential applications have been demonstrated. However, to establish this technology as a micro-processing tool, a lot of work on optics, materials and electronic controlling has been done to reduce the writing laser power, evaluate and improve the fabrication accuracy and efficiency, and launch new applications.

#### **2.2.3.1 Laser Diffraction Limit**

Compared with projection lithography (photo, x-ray and electron beam) and soft lithography technologies, two-photon photopolymerization is unique in its 3D processing capability. However, the use of relatively long wavelength worsens the spatial resolution, for which the bottleneck is set by the optical diffraction limit.

This is a limiting factor for the wide application of this technology. In this section, we will introduce how to avoid this problem and achieve SDL accuracy in 3D fabrication.

In two-photon 3D lithography, the Gaussian output of the laser undergoes beam expansion and focusing, and is spatially filtered, producing a relatively flat wave front. Light distribution at the focal plane arises essentially from Fraunhofer diffraction on the aperture of an objective lens, of which the diffraction pattern is shown by the Figure 14. The light intensity due to the constructive and destructive interference in the focal plane was assumed to follow a formula due to Airy:

$$I(x) = \left(2J_1(x)/x\right)^2 I_0 \quad [31]$$

where  $x=2\pi aw/\lambda$ ,  $w$  is the coordinate in the diffraction pattern, and  $I_0=ED/\lambda^2R^2$  is the intensity at the centre of the pattern,  $E$  is the total energy incident upon the aperture and  $D=\pi a^2$  is area of the aperture with an effective radius  $a$ .

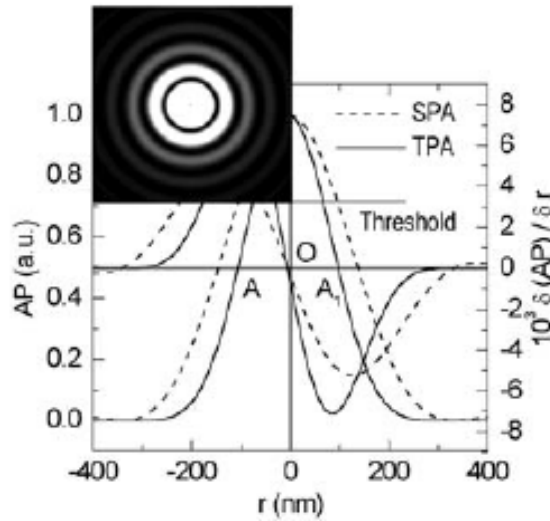


FIGURE 14: Light intensity analysis for understanding the achievement of sub-diffraction-limit spatial resolution. Focal plane light intensity (dashed line) and the square of light intensity (solid line) distribution are associated with single-photon and two-photon excitation, respectively. Their derivative distribution is also shown. The inset is the diffraction pattern at the focal plane

For imaging, the resolving power was limited by Rayleigh's criterion,  $r=k_1\lambda/NA$ , due to the signal overlapping from neighbouring object points, where  $k_1=0.4\sim 0.6$  is a constant depending on the laser line width and projection geometry. The spatial resolution could be improved by utilizing either shorter wavelengths or larger NA focusing, but the diffraction limit cannot be circumvented.

For direct laser writing, a single focused beam is employed, producing an Airy pattern. The issue of light intensity overlapping is eliminated and the light intensity at the focal point was continuously adjustable.

Therefore, even if the focal spot size is fixed for a given optical system (wavelength and objective lens), the diffraction limit can be circumvented, provided that the photochemical processes responsible for the formation of voxels have a threshold response to light excitation. Here the threshold was a level of light intensity (Fig.14), above which the photochemical reactions become irreversible (for example, photopolymerized). In this case, the diffraction limit becomes just a measure of the focal spot size; it does not put any actual restraint on voxel sizes.

### 2.2.3.2 Thresholding Mechanism: Radical Quenching Effects

Thresholding performance depends on the individual mechanism of photochemical reactions. In radical type photopolymerization, oxygen molecules play an important role in the reaction process<sup>83</sup> (Fig.15). Oxygen quenches polymerization via two possible routes:

- The first is triplet state quenching (T-quenching), where the triplet state of the initiator molecules can be directly consumed by reacting with oxygen molecules without generating any radicals.

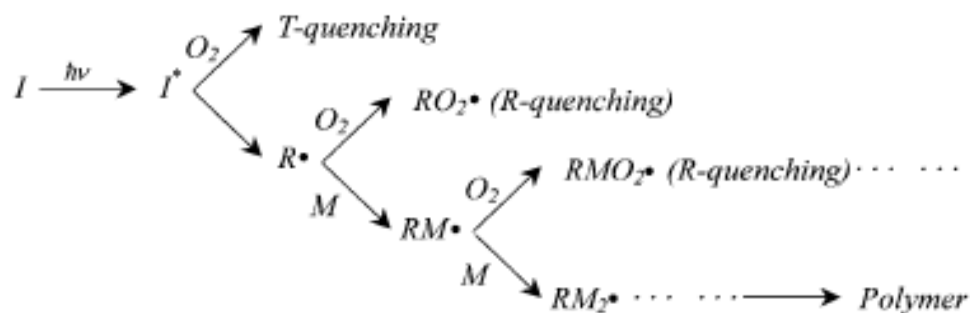


FIGURE 15: Photopolymerization quenching by oxygen molecules under two mechanisms: triplet state quenching (T-quenching) and radical quenching (R-quenching). The latter is the major factor that works in the sub-diffraction-limit fabrication.

- The second effect is radical quenching (R-quenching), where radicals combine with oxygen molecules, producing much less active peroxy radicals. This phenomenon, common in radical type polymerization, is the origin of the reaction induction period and it reduces polymerization efficiency. The two-photon photopolymerization threshold is closely related to the radical quenching effect.

By tailoring the light intensity at the focal volume, it is possible to reach a state where TPA-induced radicals survive and initiate polymerization only at the region where exposure energy is larger than the threshold. The intensity of high-order diffraction features (see the subsidiary maxima in the inset of Fig.14) was low, and therefore easily controlled under the TPA threshold. Any chemical species that tends to prohibit photopolymerization reactions, even in small concentrations, is called quencher. Oxygen is just one of many choices of quencher<sup>84,85</sup>.

### 2.2.3.3 Two-Photon Excitation Related Focal Spots

When IR ultra-short laser pulses are tightly focused in a resin, initiators are decomposed into radicals by simultaneously absorbing two photons. The number of photons absorbed per molecule per unit time by means of TPA is proportional to the TPA cross-section, to  $\sigma_2$  and to SLI. The total number of photons absorbed per unit time is also a function of initiator concentration,  $C$ , and the volume  $V$ . In the absence of saturation and photobleaching, the number of radicals generated per unit time,  $N$ , is given by:

$$N = C\sigma_2\phi I_0^2 \int_V S^2(r, \theta, z) dV \quad [32]$$

where  $I_0$  is the light intensity at the geometrical focal point,  $S(r, \theta, z)$  is a unitless function used to describe the spatial distribution of the incident light, and  $\phi$  is the quantum efficiency of radical yield. The shape of the TPE focal spot is determined by  $S^2(r, \theta, z)$ .

### 2.2.4 Three photon polymerization

The 3PP initiated through the non linear process of three-photon absorption of a photoinitiator, and induces several chemical reactions between starter molecules and monomers in a transparent resin. The probability of three-photon absorption by the photoinitiator is proportional to  $P^3$ , where  $P$  is the laser pulse energy and 3 is the number of photons involved in the process<sup>86</sup>.

Thus, under tight-focusing conditions, three-photon absorption occurs only at the focal point and polymer is only formed within a volume on the order of  $\lambda^3$ , where  $\lambda$  is the laser wavelength<sup>86</sup>. By scanning the focal point in the  $x$ ,  $y$ , and  $z$  directions throughout the sample, the desired pattern can be formed<sup>87</sup>.

### 2.2.4.1 Cross section of Three Photon Absorption

The three photon absorption is a nonlinear process and requires high intensities  $10^{30}$  photon/cm<sup>2</sup>sec. Just as the two photon absorption cross section is proportional to  $\text{Im}(X^{(3)})$  the three photon absorption cross section is proportional to  $\text{Im}(X^{(5)})$ . The analysis of three photon absorption is an extension of three photon absorption case. If we include three photon absorption equation [22] will be modified as:

$$\frac{dI}{dz} = -(a_1 I + a_2 I^2 + a_3 I^3) \quad [33]$$

where  $a_3$  is the three photon absorption coefficient and is related to the imaginary part of  $X^{(5)}$ .

If we assume negligible linear and two photon absorption, and a rectangular spatial and temporal profile the solution to this equation is:

$$I(Z) = \frac{I_0}{\sqrt{1 + 2a_3 z I_0^2}} \quad [34]$$

The three photon absorption cross section  $\sigma_3$  (cm<sup>6</sup>s<sup>2</sup>) is related to  $a_3$  and the number density of the solute molecules  $N_0$  by

$$(h\nu)^2 a_3 = \sigma_3 N_0 \quad [35]$$

The TPA cross section is related also with single photon absorption cross section.

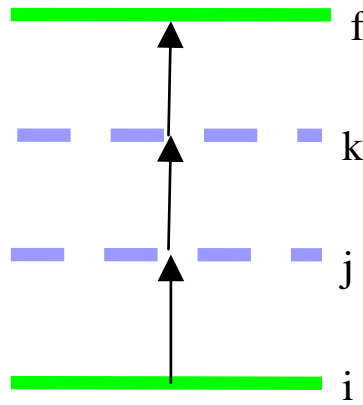


FIGURE 16: Three layer system

$$\sigma_3 = \sigma_{ij} \sigma_{jk} \sigma_{kf} \tau_j \tau_k \quad [36]$$

where  $\sigma_{ij}$  is one photon cross section which is  $10^{-16}$  cm<sup>2</sup> and  $\tau$  can be calculated by Heisenberg principle and is  $10^{-16}$  sec. So the TPA cross section is:

$$\sigma_3 = 10^{-80} \text{ cm}^6 \text{ s}^2 \quad [37]$$

### 2.2.4.2 Applications of 3PP

Three photon polymerization, a micro-nanotechnology still in its infancy and a subject of active research, has potential use in fields such as photonics, optoelectronics, biology, micro-machines and MEMS, and so forth. Among many, here we introduce applications that already have proof of concept.

#### 2.2.4.2.a Fabrication of PhCs

One of the most important applications of 3PP is the fabrication of PhCs. Photonic crystals<sup>89,90</sup> (PhCs) are microstructures with a periodical distribution of refractive indexes. They are the optical analogue of semiconductors, where a band gap is open due to the electron wave modulation by periodic Coulombic potential. In a PhC, the multiple interference among waves scattered from each primitive unit may lead to a frequency region, called a photonic band gap (PBG), where light propagation in all directions is forbidden.

There are at least two advantages to fabricating PhCs using 3PP technology. First of all is the potential to produce PhCs of arbitrarily designed lattices. PhCs of varied lattice types, lattice constant and filling factors are realizable just by scanning different CAD patterns. This simplicity in fabrication permits a systematic study of PhC physics and suits various requirements for a practical system. Secondly, there is the diversity of usable materials and functions.

The progress of molecular material engineering has made it possible to synthesize polymers with performances similar to or better than their inorganic counterparts. By introducing functional groups to unsaturated monomer or oligomer units in a molecular structure, or just by doping the functional polymers into known photopolymerizable materials, optical, electronic, magnetic, and mechanical functions can be imparted to devices.

#### 2.2.4.2.b Functional Micromachines and Microelectromechanical Systems and their Optical Actuating

A number of micro components have been fabricated by 3PP. These structures are good proof of the fabrication capability of 3PP technology. Even more complicated devices can be produced, which should be composed of two types of components classified according to their functions, static parts for support, connection or confinement, and movable parts. Both need precise shaping, positioning and jointing during photofabrication.

For movable components, an essential issue to address prior to fabrication is finding a suitable actuating mechanism. Appropriate electric, optical, thermal, magnetic, and chemical effects need to be found to achieve this end. Electrically controlling micro systems, the requirement of MEMS, is most desirable. However, there is a long way to go before introducing conductive polymer into structures and integrating polymer devices on an IC-contained semiconductor chip or developing polymer ICs. Optical force provides a simple solution, which is the currently most practical mechanism for actuating micro- or nano-devices. The technique of optical manipulation has been employed as a unique means of controlling micro-dynamics of small objects without physical contact since the pioneering works by Ashkin<sup>91,92</sup>.

The laser irradiation pressure (gradient and scattering forces) forms the basis of light actuation of micromechanical devices, which falls into three categories: windmill rotation, rotating by photon angular momentum transfer, and push-pull due to 3D trapping. In the following sections, we will describe how these optical powering approaches have been or will be applied for driving micro-machines.

For example, windmills rotate when facing wind, a phenomenon known since ancient times. It is not surprising that similar rotational phenomena have been frequently observed in laser-trapped particles. The rotational torque arises from the axial irradiation force and from the asymmetrical or rotation-symmetrical shape of the particles. The rotation rate is proportional to the trapping laser's power, and is related to the shape of the objects and the viscous drag from the ambient medium.

In a micro-machine, it is important to design a device structure of helical shape and of proper rotation symmetry so that the structure could be fixed (trapped) at a suitable position and with the desired orientation, for high stability and for minimizing the friction between the rotating parts and its axle (if there is one). The translation momentum from the "photon wind" needs to be efficiently converted to the spinning momentum of the object. A number of micro-components satisfying the above requirements have been produced by various micro-fabrication technologies<sup>93,94</sup>.

#### **2.2.4.2.c Mechanics of Three Photon Polymerized Nanodevices**

Like numerous electronic devices, such as personal computers and cellular phones, that have gained cost advantage from integrating most of their functions onto a single chip, mechanical micro-nanodevices and their integrated systems are expected to spur the next revolution in the manufacturing industry.

It is already a well known principle in the aircraft manufacturing industry that real-size systems that are proportionally scaled up from designed models don't work. This is because the surface area and mass (or volume) of an object do not proportionally increase with dimensions and they follow different laws (square and cubic laws respectively). The same principle applies when the size of devices are scaled down to micro nanometer sizes. For example, if the feature size of a device is reduced from millimetres to nanometers, the surface-to mass ratio increases by  $10^6$  times.

Therefore, in the nano realm, mass and inertia are no longer important, while physical, mechanical and electric characteristics such as stress and tension, thermal transfer, phase transition, fluid phenomena, and achievable field strength abide by rules much different from current experience and would dominate.

The 3PP has been recognized as an important method for producing micromechanical and MEMS devices. It provides a good opportunity to explore nano-device mechanics. Sun et al.<sup>72,95</sup> fabricated a nano-spring using this technology. The laser system for TPA photopolymerization, with a wavelength tuned to 820 nm, was used for the laser trapping. When the laser focus was carefully adjusted, the bead was found to be three-dimensionally trapped and able to be freely manipulated. The spring was pulled by moving the trapped bead, and then it was released by blocking the laser, initiating an oscillation.

The spring was observed to be prolonged from its original length, and restored to its original state after the laser was turned off. Elongations of up to 7  $\mu\text{m}$  over many cycles didn't cause any elasticity failure, as evidenced by the fact that the spring always returned to its original length.

## REFERENCES

1. Martinsky, T. 2004. Protein microarray manufacturing. *PharmaGenomics*. 2: 42-46.
2. Martinsky, T. 2005. Enabling Tools for Protein Microarrays. In: *Protein Microarrays*. pp. 441-461. Schena, M., Ed., Jones and Bartlett Publishers, Inc., Sudbury, MA.
3. A. Schwartz, J.S. Rossier, E. Roulet, N. Mermoud, M.A. Roberts, H.A. Girault, *Langmuir* 14, 5526, (1998).
4. Flaim, C. J., Chien, S., and Bhatia, S. N. 2005. An extracellular matrix microarray for probing cellular differentiation. *Nature Methods*. 2(2):119-125.
5. R. K. Singh, D. H. Lowndes, D. B. Chrisey, E. Fogarassy, and J. Narayan, eds., *Advances in Laser Ablation of Materials* (Materials Research Society, Warrendale, 1998).
6. Kononen, J., Bubendorf, L., Kallioniemi, A., Barlund, M., Schraml, P., Leighton, S., Torhorst, J., Mihatsch, M. J., Sauter, G., and Kallioniemi, O. P. 1998. Tissue microarrays for high-throughput molecular profiling of tumor specimens. *Nature Medicine*. 4(7): 844-847.

7. Nocito, A., Kononen, J., Kallioniemi, O. P., and Sauter, G. 2001. Tissue microarrays (TMAs) for high-throughput molecular pathology research. *International Journal of Cancer*. 94(1): 1–5.
8. Choudhuri, S. 2004. Microarrays in biology and medicine. *Journal of Biochemical and Molecular Toxicology*. 18(4): 171–179.
9. Heller, M. J. 2002. DNA microarray technology: Devices, systems, and applications. *Annual Review of Biomedical Engineering*. 4: 129–153. 257 **Bio-Microarray Fabrication Techniques** Downloaded By: [HEAL-Link Consortium] At: 10:54 18 January 2008.
10. Pirrung, M. C. 2002. How to make a DNA chip. *Angewandte Chemie-International Edition*. 41(8): 1277–1289.
11. Moore, S. K. 2001. Making chips to probe genes. *IEEE Spectrum*. 38(3): 54–60.
12. Morozov, V. N. 2005. Protein microarrays: Principles and limitations. In: *Protein Microarrays*. pp. 71–106. Schena, M., Ed., Jones and Bartlett Publishers, Inc., Sudbury, MA.
13. R.E. Bonner et.al. *Science*, 278, 1481, (1997).
14. Rose, D. 2000. Microfluidic technologies and instrumentation for printing DNA microarrays. In: *Microarray Biochip Technology*. pp. 19-38. Schena, M., Ed., Eaton Publishing, Natick, MA.
15. B.A. Gryzybowski, R. Haag, N. Bowden, G.M. Whitesides, *Acc. Chem. Res.* 70, 4645, (1998).
16. Allain, L. R., Askari, M., Stokes, D. L., and Vo-Dinh, T. 2001. Microarray sampling-platform fabrication using bubble-jet technology for a biochip system. *Fresenius Journal of Analytical Chemistry*. 371(2): 146–150.
17. Ito, S. and Tachibana, M. 2004. Spotting Pin. U. S. Patent 6,835–352 B2.
18. D. Odde, M.J. Renn, *Biotech. Bioeng.* 67, 312, (2000).
19. Y. Tsuboi, M. Goto, A. Itaya, *Chem. Lett.* 521, (1998).
20. Kumar, A., and Whitesides, G. M. 1993. Features of gold having micrometer to centimeter dimensions can be formed through a combination of stamping with an elastomeric stamp and an alkanethiol ink followed by hemical etching. *Applied Physics Letters*. 63(14): 2002–2004.
21. Martin, B. D., Gaber, B. P., Patterson, C. H., and Turner, D. C. 1998. Direct protein microarray fabrication using a hydrogel “stamper,” *Langmuir*. 14: 3971–3975.
22. P.C.Becker, H.L.Fraguito, C.H.Brito Cruz, R.L. Fork, J.E. Cunningham, J.E.Henry, C.V.Shank, *Phys. Rev. Lett.* 61, 1647 (1988).
23. Libioulle, L., Bietsch, A., Schmid, H., Michel, B., and Delamarche, E. 1999. Contact-inking stamps for microcontact printing of alkanethiols on gold. *Langmuir*. 15(2): 300–304.

24. Renault, J. P., Bernard, A., Juncker, D., Michel, B., Bosshard, H. R., and Delamarche, E. 2002. Fabricating microarrays of functional proteins using affinity contact printing. *Angewandte Chemie-International Edition*. 41(13): 2320–2323.
25. Kleinfeld, D., Kahler, K. H., and Hockberger, P. E. 1988. Controlled outgrowth of dissociated neurons on patterned substrates. *Journal of Neuroscience*. 8(11): 4098–4120.
26. Kane, R. S., Takayama, S., Ostuni, E., Ingber, D. E., and Whitesides, G. M. 1999. Patterning proteins and cells using soft lithography. *Biomaterials*. 20(23-24): 2363–2376.
27. Lin, S. C., Tseng, F. G., Huang, H. M., Huang, C. Y., and Chieng, C. C. 2001. Microsized 2D protein arrays immobilized by microstamps and micro-wells for disease diagnosis and drug screening. *Fresenius Journal of Analytical Chemistry*. 371(2): 202–208.
28. Lin, S. C., Tseng, F. G., Huang, H. M., Chen, Y. F., Tsai, Y. C., Ho, C. E., and Chieng, C. C. 2004. Simultaneous immobilization of protein microarrays by a micro stamper with back-filling reservoir. *Sensors and Actuators B-Chemical*. 99(1): 174–185.
29. Renault, J. P., Bernard, A., Bietsch, A., Michel, B., Bosshard, H. R., Delamarche, E., Kreiter, M., Hecht, B., and Wild, U. P. 2003. Fabricating arrays of single protein molecules on glass using microcontact printing. *Journal of Physical Chemistry B*. 107: 703–711.
30. Blawas, A. S., and Reichert, W. M. 1998. Protein patterning. *Biomaterials*. 19(7-9): 595–609.
31. Lom, B., Healy, K. E., and Hockberger, P. E. 1993. A versatile technique for patterning biomolecules onto glass coverslips. *Journal of Neuroscience Methods*. 50(3): 385–397.
32. Mooney, J. F., Hunt, A. J., McIntosh, J. R., Liberko, C. A., Walba, D. M., and Rogers, C. T. 1996. Patterning of functional antibodies and other proteins by photolithography of silane monolayers. *Proceedings of the National Academy of Sciences of the United States of America*. 93(22): 12287–12291.
33. Pirrung, M. C., and Huang, C. Y. 1996. A general method for the spatially defined immobilization of biomolecules on glass surfaces using "caged" biotin. *Bioconjugate Chemistry*. 7(3): 317–321.
34. Hengsakul, M. and Cass, A. E. G. 1996. Protein patterning with a photoactivatable derivative of biotin. *Bioconjugate Chemistry*. 7(2): 249–254.
35. Pritchard, D. J., Morgan, H., and Cooper, J. M. 1995. Patterning and regeneration of surfaces with antibodies. *Analytical Chemistry*. 67(19): 3605–3607.
36. Britland, S., Clark, P., Connolly, P., and Moores, G. 1992. Micropatterned substratum adhesiveness—a model for morphogenetic cues controlling cell behavior. *Experimental Cell Research*. 198(1): 124–129.
37. Healy, K. E., Thomas, C. H., Rezanian, A., Kim, J. E., McKeown, P. J., Lom, B., and Hockberger, P. E. 1996. Kinetics of bone cell organization and mineralization on materials with patterned surface chemistry. *Biomaterials*. 17(2): 195–208.

38. McGall, G. H., Barone, A. D., Diggelmann, M., Fodor, S. P. A., Gentalen, E., and Ngo, N. 1997. The efficiency of light-directed synthesis of DNA arrays on glass substrates. *Journal of the American Chemical Society*. 119(22): 5081–5090.
39. Pease, A. C., Solas, D., Sullivan, E. J., Cronin, M. T., Holmes, C. P., and Fodor, S. P. A. 1994. Light-generated oligonucleotide arrays for rapid DNA-sequence analysis. *Proceedings of the National Academy of Sciences of the United States of America*. 91(11): 5022–5026.
40. Mace Jr., M. L., Montagu, J., Rose, S. D., and McGuinness, G. M. 2000. Novel microarray printing and detection technologies. In: *Microarray Biochip Technology*. pp. 39–64. Schena, M., Ed., Eaton Publishing, Natick, MA.
41. R. Singh, D. Norton, L. Laude, J. Narayan, and J. Cheung, eds., *Advanced Laser Processing of Materials— Fundamentals and Applications* (Materials Research Society, Pittsburgh, 1996).
42. Chrisey, D. B., McGill, R. A., and Pique, A. 2001. Matrix assisted pulsed laser evaporation direct write. U. S. Patent 6,177–151.
43. Ringeisen, B. R., Wu, P. K., Kim, H., Pique, A., Auyeung, R. Y. C., Young, H. D., Chrisey, D. B., and Krizman, D. B. 2002. Picoliter-scale protein microarrays by laser direct write. *Biotechnology Progress*. 18(5): 1126–1129.
44. Schwarz, A., Rossier, J. S., Roulet, E., Mermod, N., Roberts, M. A., and Girault, H. H. 1998. Micropatterning of biomolecules on polymer substrates. *Langmuir*. 14(19): 5526–5531.
45. C.A.Spindt, *J.Appl.Phys* **39**, 1968, 3504.
46. A. W. Johnson, D. J. Ehrlich, and H. R. Schlossberg, eds., *Laser-Controlled Chemical Processing of Surfaces* (North-Holland, New York, 1984).
47. A.A. Evtukh, E.B. Kaganovich, V. G. Litovchenko, Yu.M. Litvin, D.V. Fedin, E.G. Manoilov, S.V. Svechnikov, Semiconductor Physics, *Quantum Electronics & Optoelectronics*, **3(4)**, 474 (2000).
48. D.von der Linde, K.Sokolowski-Tinten, J. Bialkowski, *Appl. Surf. Sci.* **109/110**, 1 (1997).
49. A.C. Tien, S. Backus, H. Kapteyn, M. Mourane, G. Mourou, *Phys. Rev. Lett.* **82**, 3883 (1999)
50. K.L. Saenger, *Processing of Advanced Materials* **3**, 63 (1993)
51. Bauerle, *Laser Processing and Chemistry*, 2nd ed. Springer, Berlin, (1996)
52. M.R. Emmert-Buck et.al. *Science*, 274, 998, (1996)
53. R. Vaidya, L.M. Tender, G. Brandley, M.J. O'Brien, M. Cone, G.P. Lopez, *Biotechnol. Prog.* 14, 371, (1998)
54. M.J. Renn D. Odde, *Trends Biotech.* 17, 383, (1999)
55. R.W. Nelson, R.M. Thomas, P. Williams, *Rapid Commun. Mass. Sp.* 4, 348, (1990)
56. R.S. Phadke, G. Agarwal, *G. Mat. Sci. Eng. C*, 5, 237, (1998)
57. G. Agarwal, R.S. Phadke, *Nanotech.* 10, 336, (1999)

58. B.R. Ringeisen, D.B. Chrisey, A. Pique, H.D. Young, R.Modi, M. Bucaro, J. Jones-Meehan, B.J. Spargo, *Biomaterials*, 23, 161-166, (2002)
59. P.K. Wu, B.R. Ringeisen, J. Callahan, M. Brooks, D.M. Budd, A. Pique, B.J. Spargo, R.A. McGill, D.B. Chrisey, *Thin Solid Films*, 398-399, 607-614, (2001)
60. I. Zergioti, A. Karaiskou, D. Papazoglou, E. Kapsetaki, C. Fotakis, D. Kafetzopoulos, "Lasers Print Biomaterials", submitted *Nature Biotechnology*, June (2002)
61. S. I. Anisimov, Y. A. Imas, G.S. Romanov, Yu v. Khodyko, *Action of High-Power Radiation of metals* (Consult. Bureau, Springfield, 1971).
62. J. Bohandy, B.F. Kim, F.J. Adrian, A. N. Jette, *J. Appl. Phys.* 63, 1158-1162, (1988)**103**. D.G. Papazoglou, A. Karaiskou, I. Zergioti and C.Fotakis, *Shadowgraphic imaging of the sub-ps laser-induced forward transfer process*, *Applied Physics Letters*, 81, 9, (2002)
63. I.Zergioti, D.G.Papazoglou, A. Karaiskou, C. Fotakis, E.Gamaly, A Rode, *A comparative schlieren imaging study between ns and sub-ps laser forward transfer of Cr*, *Applied Surface Science*, 208-209, 177-180, (2003)
64. I.Zergioti, D.G.Papazoglou, A. Karaiskou, N.A. Vainos, C. Fotakis, *Laser microprinting of InO<sub>x</sub> active optical structures and time resolved imaging of the transfer process*, *Applied Surface Science*, 197-198, 868-872, (2002)
65. A.Karaiskou, I.Zergioti, C. Fotakis, M. Kapsetaki and D. Kafetzopoulos, *Microfabrication of biomaterials by the sub-pw laser-induced forward transfer process*, *Applied Surface Science*, 208-209, 245-249, (2003)
66. P. Serra, J.M. Fernandez-Pradas, F.X.Berthet, M.Colina, J.Elvira, J.L.Morenza, *Laser direct writing of biomolecules microarrays*, *Appl. Phys.A*, A 79, 949-952,(2004)
67. Parthenopoulos DA, Rentzepis PM (1989) *Science* 245:843
68. Kawata S., Sun HB, Tanaka T., Takada K. (2001) *Nature* 412:697
69. Farsari M., Filippidis G., Fotakis C., *Opt. Lett.* (2005) 30:3180
70. Boyd RW (1992) *Nonlinear optics*. Academic, San Diego
71. Denk W., Strickler JH, Webb WW (1990) *Science* 248:73
72. Bhawalkar JD, He GS, Prasad PN (1996) *Rep Prog Phys* 59:1041
73. Stuart BC, Feit MD, Herman S, Rubenchik AM, Shore BW, Perry MD (1996) *Phys Rev B* 53:1749
74. Saeta P, Wang JK, Siegal Y, Bloembergen N, Mazur E (1991) *Phys Rev Lett* 67:1023
75. Glezer EN, Milosavljevic M, Huang L, Finlay RJ, Her TH, Callan JP, Mazur E (1996) *Opt Lett* 21:2023
76. Pao YH and Rentzepis PM (1965) *Appl Phys Lett* 6:93
77. Glezer EN, Mazur E (1997) *Appl Phys Lett* 71:882
78. Odian G (1991) *Principles of polymerization*, 3rd edn. Wiley, New York
79. Maruo S, Ikuta K (2002) *Sensor Actuat A-Phys* 100:70

80. Hopfield JJ, Worlock JM, Park KJ (1963) *Phys Rev Lett* 11:414
81. Kaiser W, Garrett CGB (1961) *Phys Rev Lett* 7:229
82. Maruo S, Ikuta K (2000) *Appl Phys Lett* 76:2656
83. Flory PJ (1952) *Principles of polymer chemistry*. Cornell University Press, New York
84. Li CD, Luo L, Wang SF, Huang WT, Gong QH, Yang YY, Feng SJ (2001) *Chem PhysLett* 340:444
85. Belfield KD, Schafer KJ, Mourad WJ (2000) *J Org Chem* 65:4475
86. J. D. Pitts, P. J. Campagnola, G. A. Epling, S. L. Goodman, *Macromolecules* 2000, 33, 1514.
87. B. H. Cumpston, S. P. Ananthavel, S. Barlow, D. L. Dyer, J. E. Ehrlich, L. L. Erskine, A. A. Heikal, S. M. Kuebler, I. Y. S. Lee, D. McCord- Maughont, J. Qin, H. Rockel, M. Rumi, X.-L.Wu, S. R. Marder, J. W. Perry, *Nature* 1999, 398, 51
88. *Advanced Materials* 14 271
89. Brodeur A, Chin SL (1999) *J Opt Soc Am B* 16:637
90. Maruo S., Nakamura O., Kawata S. (1997) *Opt Lett* 22:132
91. vonderLinde D, Schuler H (1996) *J Opt Soc Am B* 13:216
92. Witzgall G, Vrijen R, Yablonovitch E, Doan V, Schwartz BJ (1998) *Opt Lett* 23:1745
93. Higurashi E, Sawada R, Ito T (1998) *Appl Phys Lett* 72:2951
94. Galajda P, Ormos P (2001) *Appl Phys Lett* 78:249
95. Sun HB, Takada K, Kawata S (2001) *Appl Phys Lett* 79:3173



CHAPTER 3  
MATERIALS



In this chapter the materials that were used in this study are being described. This chapter is separated in two parts, too. In the first part we focus in presentation of the materials that were used during the 2D deposition by using the Laser Induced Forward Transfer-LIFT method. In the second part are described the materials that were used during the 3D deposition by using the Multi-Photon-polymerization method.

## A. Materials that were used for the 2D deposition by L.I.F.T. Method

### 3.1 Self-Assembled Peptide Fibrils

#### 3.1.1. Self-Assembly in Biology

If we make a search in history books about the relationship between human civilizations and materials through the years, we will see that each era is characterized by the material that was used mostly or discovered at that time. This made us to name those eras and characterize them as Stone Age, Bronze Age, Iron Age, Concrete/Steel Age, Polymer Age and Silicon Age. In the Table 1 below, we can see an estimation of the duration of each Age. The dates show that humanity started working with modern materials only since the 20th century. These modern materials have transformed the whole world in many different domains that have to do for example with medicine, lifestyle, transportation and communication, etc.

- Age -	Duration (Years)
Stone	~Past – 3500 BC
Bronze	~3500 – 1600 BC
Iron	~1600 BC – 1900 AC
Concrete/Steel	1900 – 1960 AC
Polymer	1940 – today
Silicon	1960 – today

*Table 1: Duration of Materials Ages*

As the materials world is improving and new technologies are applied to materials, we start having the ability to design our own materials. The word ‘Design’ means our own desired type of material with shape, size and all the properties that will satisfy our need. We can design soft or hard materials; nano-scale or macro-scale materials and we can also insert materials to function into different environments like the human body.

Collecting all the achievements that show us what hides behind the properties of each material in nature through the years, enables us to reach the goal of designing and predicting the properties of a new material. Leonardo Da Vinci stated about materials: ‘when nature finishes to produce its own species, man begins using natural things in harmony with this very nature to create infinity of species’. The name that will characterize the new Age of the 21th century is ‘Designed Materials’ and it covers a very wide range of materials such as metals, polymeric, magnetic, ceramic, semi-conducting and biological materials<sup>1</sup>.

### 3.1.2 Fibrous Proteins in Nature

An important inspiration from Nature that has provided many applications in our daily life is drawn from fibrous proteins. We can find those proteins in our body’s skin, tendons, and bones and also in the silks of insects. Inside cells there are mainly three types of fibrous proteins such as microtubules, actin filaments and intermediate filaments (Figure 1A, B, and C respectively). We see from Figure 1 that those proteins are composed of a single subunit which is repeated thousands of times in order to give a very stable structure. This type of structure is called ‘assembly’ of monomers and attributes its stability to electrostatic interactions, hydrogen bonds, aromatic stacking interactions and hydrophobic interactions. Actin filaments are 8nm width and consist of a tight helix. The monomer is globular actin (G actin) and the stability is attributed to polar interactions. Actin filaments are used in muscle cells and in cell movements.

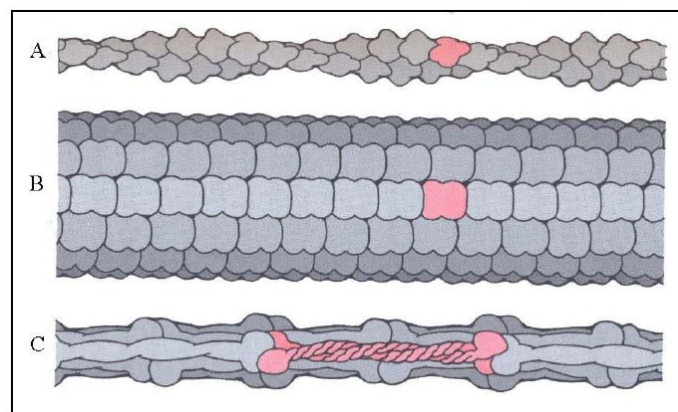


FIGURE 1: A. Actin filament, B. Microtubule, C. Intermediate filament

Microtubules are 25nm wide and have a cylindrical structure. The monomer is tubulin which assembles into 13 protofilaments that are aligned parallel to form the microtubule. Microtubules can be used as carriers for proteins, such as kinesin and dynein, or cell components. Intermediate filament monomers are composed of an alpha helical rod domain which connects the amino (head) and carboxyl (tail) terminals. The rods coil around another filament in a rope-like fashion to form a dimer. The size of the intermediate filaments is between 8-10 nm. There are many types of intermediate filaments and their function is to reinforce cells and to organize cells into tissues. Other fibrous proteins that are located extracellularly are elastin, resilin, keratin and collagen.

Those proteins play a very important role in the substructure of skin, bones and tissues in mammals, and insects. Elastin helps in the function of arteries and also exists in large quantities in the blood vessels such as the aorta. Its primary sequence is rich in valine, glycine, alanine and proline amino acids. The real internal structure is modeled as a beta-spiral and is reinforced with cross-links which are attributed to covalent bonds between lysine residues (Figure 2)<sup>2</sup>. Resilins are major components in the structures of insect tendons. Their primary sequence contains elastin-like repeats, reinforced with cross links, and therefore have similar mechanical properties with elastin. Keratins exist in hair, horns and nails of mammals, fish scales, and exoskeleton of the arthropods. Keratins contain many hydrophobic and hydrophilic residues that are arranged in a way to give an alpha-helical coiled-coil structure. They also contain cysteines which provide a network of disulfide bridges across the helix. This gives the unique characteristics of our hair and enables us to modify their structure with heat and reducing/oxidizing agents. Collagen is considered as the most important fibrous protein in mammals; it plays a vital role in the skin, teeth, bones and tissues, has very large tensile strength and its building block called “tropocollagen” is a long, triple stranded helical structure. Each collagen fibril contains many tropocollagen subunits which selfassemble and cross-link with covalent bonds (Figure 3). Collagen is used as a compound for many applications such as dermal augmentation, drug delivery, wound healing, tissue engineering and cell attachment<sup>3</sup>. Finally another important family of fibrous proteins that exist in nature is silks; silks can be synthesized by spiders and insects. Silkworm (*Bombyx mori*) cocoons are composed of two major proteins, fibroin and sericine<sup>4</sup>. Fibroin contains glycine 44.5%, alanine 29.3% and serine 12.1% and adopts a  $\beta$ -sheet configuration with beta-strands been parallel to the axis of the fibril (Figure 4).

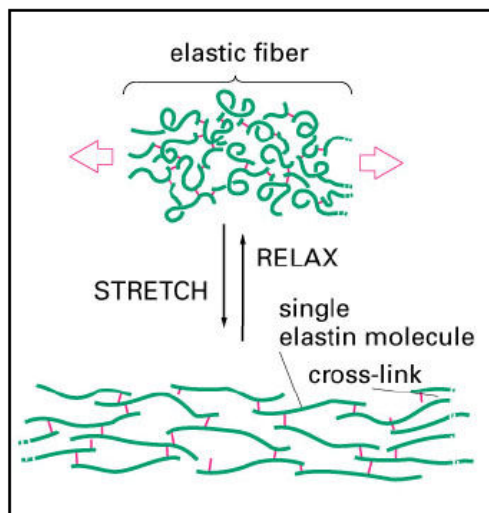


FIGURE 2: Elastin structure

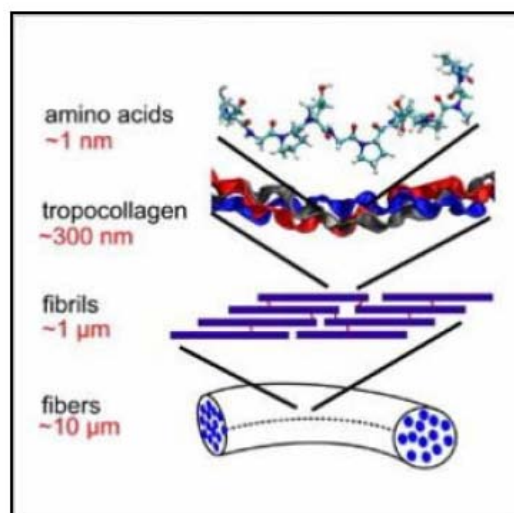


FIGURE 3: Collagen structure

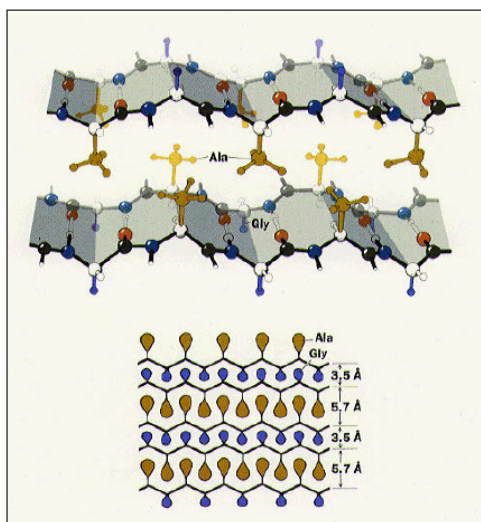


FIGURE 4: Silk fibroin structure

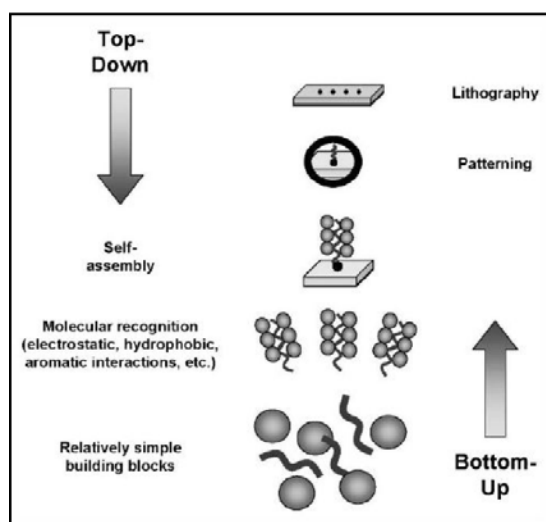


FIGURE 5: Top-down and Bottom-up process

Inspired from Nature and after the enormous developments in the synthesis of polymeric materials, scientists have created synthetic fibrils that have changed our daily life to a great extent. Protein fibrils offer many advantages compared to the synthetic ones because they assemble under mild conditions and we can use many variations of building units in order to improve their properties. However for large scale technological applications their synthesis is still limited, but this will hopefully be overcome in the near future. Before we proceed to a further explanation of self-assembled biomaterials, it is useful to compare the two ways that mankind on one hand, and Nature on the other hand, design and build new materials. There are two different approaches: the top-down and the bottom-up. The top-down approach is used to fabricate materials from macro to nano-scale<sup>3</sup> (Figure 5).

In Table 2 we can see the diameter of each fibrous assembly. Some of those building blocks can be arranged into fibrils that reach micrometers in length. Those fibrils in combination with other molecules can help for motility, scaffolding, stabilization and protection purposes. In order to study those fibrils and use them for biological applications we need to assemble them under our own desired conditions *in vitro*. During the last 15 years this ‘*in vitro*’ approach has made a tremendous progress and improved our understanding of the mechanisms that underlie the self-assembly of these proteins.

Fibrous assembly	Diameter
Collagen	~1.4 nm
Keratins	10 nm
Microtubules	25 nm
Actin Filaments	8 nm
Intermediate Filaments	10 nm
Amyloid Fibrils	~10 nm

*Table 2: Diameter of Fibrous Assemblies*

### 3.1.3 Amyloid fibrous assemblies

Amyloid fibrils are fibrillar aggregates that have specific morphological and structural properties. They are widely known for their pathological role in living organisms since they are associated with a large group of neurodegenerative diseases, (Table 3). However there are examples in Nature which show that amyloids might play a functional role in living systems such as in *Escherichia coli* and *Streptomyces coelicolor*<sup>4</sup>. When we use the term amyloid, we describe a proteinaceous assembly consisting of unbranched long fibrils. There is not a specific protein associated with amyloid assemblies since many proteins or peptides can form amyloid fibrils. More than 30 proteins that cause amyloid diseases and many amyloid forming peptides from various proteins have been identified so far. In Table 3 we list a number of amyloid forming proteins that are connected with some of the most important diseases of our times. Amyloid deposits can occur in several parts of the body as kidney, heart, spleen and mostly the brain.<sup>4</sup>

Alzheimer’s disease is one of the most common types of dementia. Dementia is a group of symptoms that cause damage to brain cells. In 1901 an unusual patient was examined by the German Physician Alois Alzheimer; the patient showed symptoms of confusion, failing memory and expression of thoughts. After some years the patient became bedridden and mute and Alzheimer decided to perform an autopsy. The patient’s brain had a smaller size than usual and there were some microscopic deposits on it. This strange disorder soon became known as ‘Alzheimer’s disease’ and the deposits renamed as ‘plaques’ and ‘tangles’.

According to the *Alzheimer's disease Facts and Figures 2007* from the *Alzheimer's Association website* (<http://www.alz.org>) 5.1 million Americans suffer from Alzheimer's disease; 4.9 million people are age 65 or older.

Polypeptide	Disease state
Amyloid $\beta$ -protein ( $A\beta$ )	Brain (Alzheimer's disease)
$\alpha$ -Synuclein	Brain (Parkinson's disease)
Prion Protein (PrP)	Brain (Creutzfeldt-Jakob disease)
Fibrinogen $\alpha$ -chain	Kidney
Atrial natriuretic peptide	Heart

Table 3: Proteins associated with neurodegenerative diseases

The nerve cells have many long branching extensions which are connected to points called synapses; the information flows within chemical pulses from one neuron to the receiving cell through these synapses. In Alzheimer's disease the amyloid plaques formed cause degeneration of those synapses, eventually leading to cell death and dementia<sup>5</sup> (Figure 6). All disease-associated insoluble fibrils and plaques have the same overall morphological characteristics and vary with the type of the building block that is responsible for the amyloid structure.

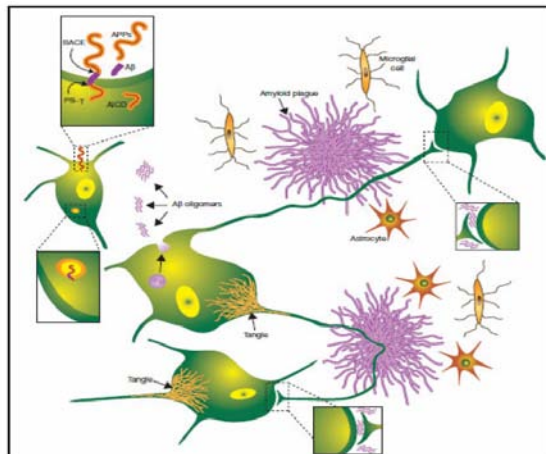


FIGURE 6: Pathogenesis of Alzheimer's disease. After the oligomerization of the A peptides, amyloid plaques form and diffuse into the synapses of the nerve cells, blocking the transfer of the signal between them.

### 3.1.3.1 Characteristics of Amyloid Assemblies

Amyloid assemblies can also be formed by proteins and peptides that are not associated with disease as a result of misfolding and/or misassembly events<sup>6</sup> (Figure 7). The type of aggregation or transition between each state shown in Figure 7 is controlled in several steps by enzymes, chaperones, the environment and many other factors. The amyloid fibril is one form of aggregate which is organized in a specific way and shows unique morphological and structural characteristics.

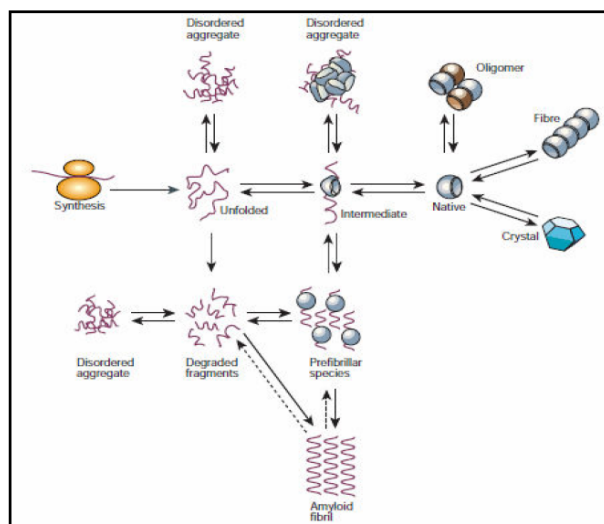


FIGURE 7: Generalized protein folding pathway. Amyloid fibrils can be formed at various stages before the unfolded protein reaches its native structure

Morphologically, amyloid fibrils have a width of about ~10nm and length ranging from 1 to 10  $\mu\text{m}$  (Figure 8)<sup>7</sup>. They are visible with Transmission Electron Microscopy and Scanning Electron Microscopy. The internal structure of the fibril is composed of several  $\beta$ -strands perpendicular to the axis of the fibril<sup>12</sup> (Figure 9). This is the cross  $\beta$ -sheet backbone of the fibril and has a unique X-ray diffraction pattern (Figure 10). Amyloid fibrils bind the dye Congo red and show gold-green birefringence when viewed under crossed polars<sup>8,9</sup> (Figure 11). In order to study amyloid fibril formation we must be able to synthesize those proteins or peptides in vitro and study the early stages of their assembly as well as their behavior after the formation of the fibrils.

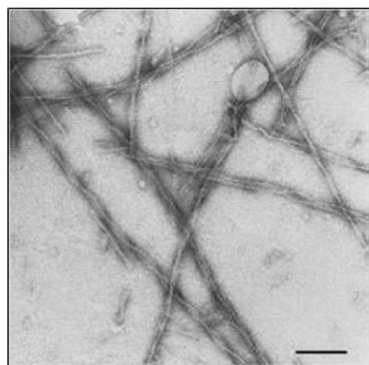


Figure 8: Morphology of amyloid fibrils

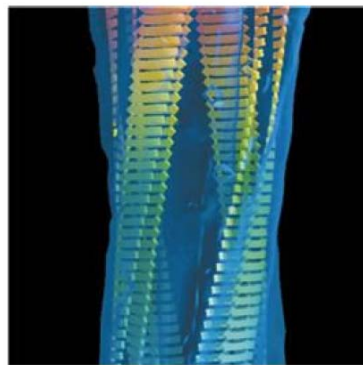


Figure 9: Cross  $\beta$ -sheet structure

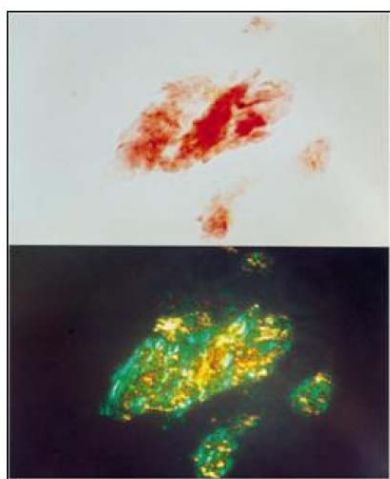


Figure 10: X-ray Diffraction pattern of amyloid fibrils

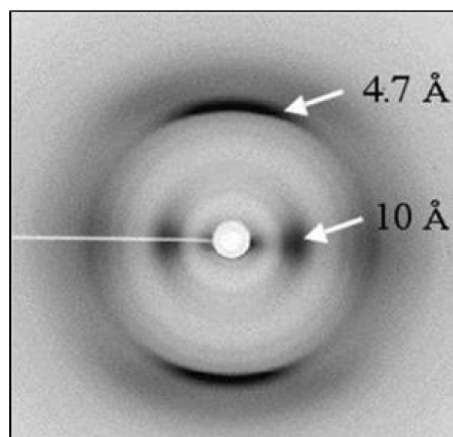


Figure 11: Birefringence effect on amyloid deposits

In order to achieve these goals scientists have used a large number of tools from different fields. Scientists use solid state NMR, Transmission & Scanning Electron Microscopy (TEM, SEM), Atomic Force Microscopy (AFM), Light Scattering, Molecular Dynamics simulations, X-Ray Fiber Diffraction, Fourier Transform Infrared Spectroscopy (FTIR) or Raman Spectroscopy and staining with dyes such as Congo-red or Thioflavin T<sup>8-11</sup>. It requires a lot of effort to interpret the information given by each technique and is very difficult to do it individually. As a result many groups around the globe gather together to investigate various types of amyloid assemblies for medical and nano-technological applications. Combining the understanding of the self-assembly mechanisms with creative thinking and novel technologies opens a new era for the use of these self assembled structures for applications in the nano-scale, field that is called bionanotechnology.

### 3.1.3.2 Applications of Self-Assembly

Bionanotechnology is an interdisciplinary field that combines many scientific areas. Scientists try to synthesize or modify structures and molecules up to several nanometers; this can be achieved by the bottom up approach that we described above. By combining chemistry, biology and physics and studying the way that proteins or peptides self-assemble, scientists draw inspiration for new applications. The self-assembly process and the specific design of the building block play a key role to the formation of the supramolecular structures. DNA Nanotechnology has opened the way for the design of new self-assembling materials. Nadrian Seeman's group at NYU did pioneering work in the field of DNA self-assembly. DNA is known as the unique carrier of biological information in each living species.

However DNA with the correct alterations in the sequence of the nucleic acids can be used as a self assembly building block in order to create branches<sup>11</sup>, two dimensional DNA arrays<sup>12</sup> and nanowires.<sup>13</sup> The specific recognition information embedded in the fibrous DNA molecule was exploited for nanowire fabrication. As starting building blocks 12-base oligonucleotides which are modified with thiol chemistry for specific attachment to gold electrodes were used. These anchoring points were subsequently connected with a 16 $\mu$ m single stranded-DNA molecule which had complementary ends to the 12-base oligonucleotides in each side.

In order to understand the self-assembly mechanisms of the amyloid- $\beta$  peptide A $\beta$  (1-42) involved in Alzheimer's disease, Ehud Gazit's group from the University of Tel-Aviv started working with peptides derived from its amino acid sequence (Figure 12).



FIGURE 12: Amyloid- $\beta$  peptide A $\beta$  (1-42) amino acid sequence

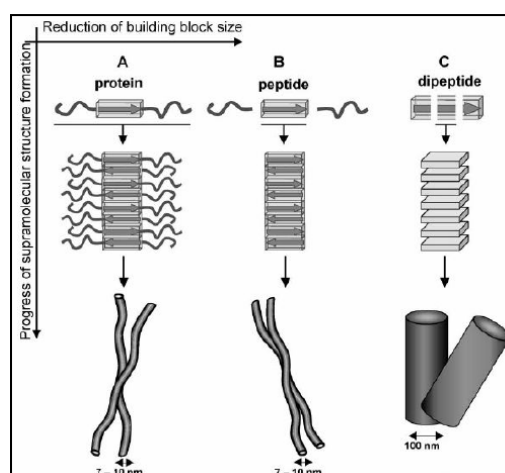


FIGURE 13: Self-assembly from proteins to peptides

The discovery that a building block composed only from 2 identical amino acids (diphenylalanine) can form hollow nanotubes prompted them to use these nanotubes as templates for nanowire fabrication. They incorporated ionic silver into the nanotubes, they subsequently reduced to metallic silver and by ‘removing’ the biological part with proteinase K they ended up with a silver nanowire<sup>14</sup>(Figure 14).

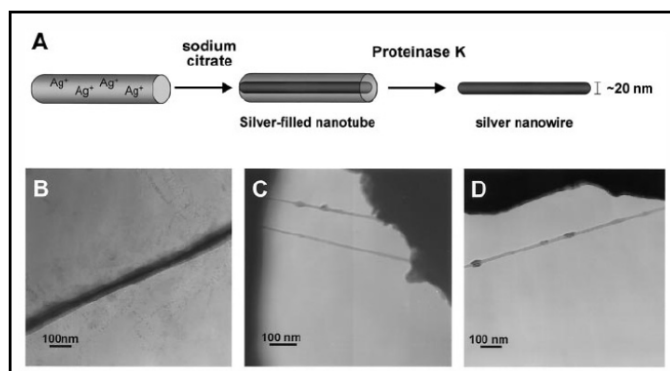


FIGURE 14: Peptide nanotubes as templates for metallic nanowire fabrication

Derek Woolfson’s group has synthesized peptides that form amyloid fibrils, straight or branched, with  $\beta$ -helical infrastructure<sup>15,16</sup> (Figure 15).

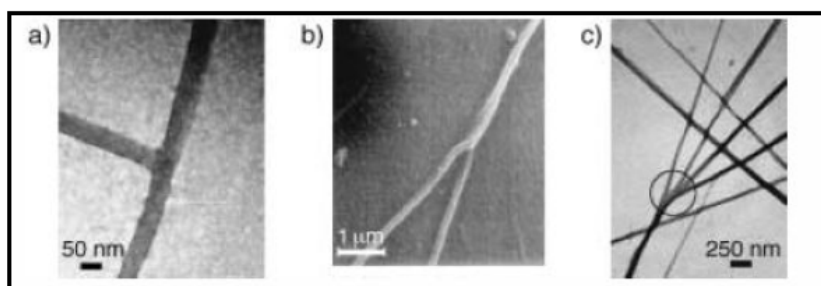


FIGURE 15: Branches on amyloid fibrils

Shuguang Zhang’s group at MIT has designed many types of peptides that self-assemble into various morphologies. One type of peptides consists of alternating hydrophobic and hydrophilic residues that can form amyloid fibrous structures and macroscopic gels (Figure 16a). Another type of peptides can self-assemble more preferably on surfaces, feature useful for cell culture and tissue engineering (Figure 16c). Finally peptides composed of hydrophobic residues segregated on one end of the sequence and hydrophilic on the other self assemble into nanotubes and nanovesicles<sup>17,18</sup> (Figure 16b).

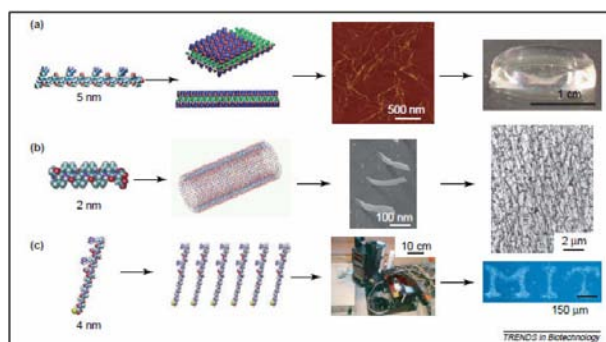


FIGURE 16: Different peptide assemblies from amphiphilic molecules

Another pioneering work of using amyloid fibrils as templates was done by Thomas Scheibel and Susan Lindquist; they studied a fragment from the yeast *Saccharomyces cerevisiae* Sup35 protein. This protein forms amyloid fibrils which have very high chemical stability and were suggested as a good candidate for applications. Engineering a cysteine residue not present in the original protein enabled them to use the fibrils for controlled deposition of gold and silver. The thiol group of the cysteine is accessible after fibril formation and served as a nucleation site for the deposition of the metal on the fibrils. They successfully fabricated conducting wires at the scale of 100 nm and proposed this system for nano-circuit construction<sup>19</sup> (Figure 17).

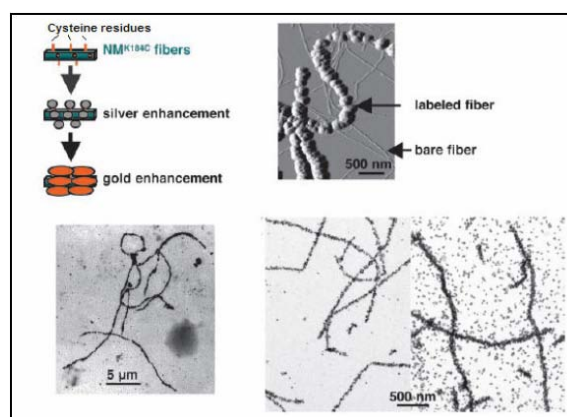


FIGURE 17: Gold/silver nanowires using amyloid fibrils as a template. Orange 'spikes' on the surface of the fibrils symbolize accessible cysteine residues

## 3.2 ALGINATE

### 3.2.1 Introduction

Most of the large brown seaweeds are potential sources of alginate. The properties of the alginate varies from one species to another, so the choice of which seaweeds to harvest is based on both the availability of particular species and the properties of the alginate that they contain. The main commercial sources are species of *Ascophyllum*, *Durvillaea*, *Ecklonia*, *Laminaria*, *Lessonia*, *Macrocystis*, *Sargassum* and *Turbinaria*. Of these the most important are *Laminaria*, *Macrocystis* and *Ascophyllum*. Alginic acid is a linear polymer based on two monomeric units,  $\beta$ -D-mannuronic acid and  $\alpha$ -L-guluronic acid. The classical Haworth formulas for these monomers are shown in Figure 18.

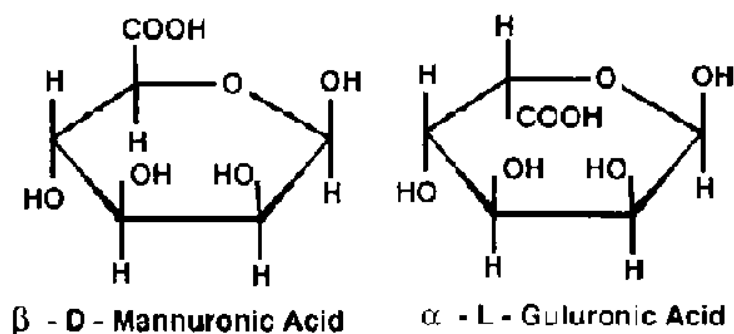


FIGURE 18: Classical formulas of the two monomeric units of alginic acid

The basic structure of each monomer is the tetrahydropyran ring and this has two possible chair forms, C1 and 1C,  $\beta$ -D-mannuronic acid assumes the C1 form; in the other form, 1C, there would be steric interaction between the axial -COOH on C-5 and the axial -OH on C-3; the C1 form has these groups in the equatorial positions and so is more stable. For similar reasons,  $\alpha$ -L-guluronic acid assumes the 1C form rather than the C1 form<sup>20,21</sup>. The alginate polymer is formed by joining these monomers at the C-1 and C-4 positions. An ether-oxygen bridge joins the carbon at the 1-position in one molecule to the 4-position of another molecule. It has been shown that the polymer chain is made up of three kinds of regions or blocks. The G blocks contain only units derived from L-guluronic acid (Figure 19), the M blocks are based entirely on D-mannuronic acid (Figure 20) and the MG blocks consist of alternating units from D-mannuronic acid and L-guluronic acid<sup>22-24</sup>. Note the differing shapes of the M blocks and G blocks. Because an M block is formed from equatorial groups at C-1 and C-4, it is a relatively straight polymer, like a flat ribbon. However the G block is formed from axial groups at both C-1 and C-4 so the resulting chain is buckled; the importance of this buckled shape will be apparent later when the formation of gels from alginate solutions is

discussed. So an alginate molecule can be regarded as a block copolymer containing M, G, and MG blocks, the proportion of these blocks varying with the seaweed source. However Larsen (1981) warns that this is an idealized structure which is at best an approximation of the actual situation. It has been shown that the physical properties of alginates depend on the relative proportion of the three types of blocks<sup>24-27</sup>. For example formation of gels, by addition of calcium ions, involves the G blocks so the higher the proportion of these, the greater the gel strength; solubility of alginate in acid depends on the proportion of MG blocks present. The industrial utilization of any particular alginate will depend on its properties and therefore on its uronic acid composition so it has become important to have some measure of the relative proportions of the uronic acids. Various methods have been developed to measure the ratio of mannuronic acid to guluronic acid (the M/G ratio) in a sample of alginic acid<sup>41</sup>. Even more useful, but more difficult to obtain, is a measure of the M, G and MG blocks in a sample and methods have been developed to achieve this<sup>25-28</sup>.

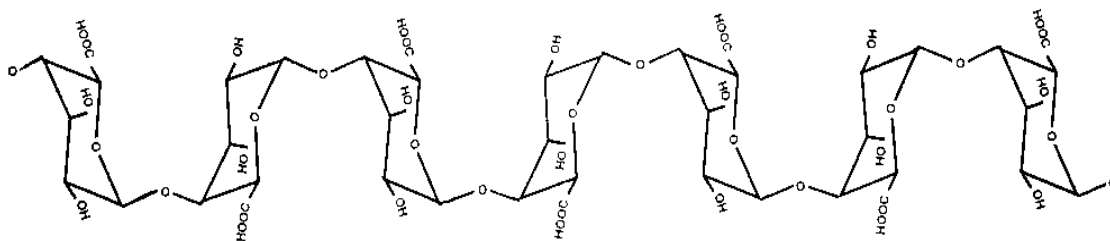


FIGURE 19: G-Block

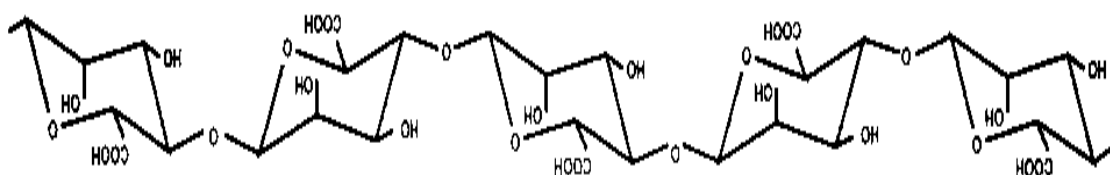


FIGURE 20: M-Block

The alginate of greatest industrial importance is the sodium salt. Uses are also found for the potassium, ammonium and calcium salts, as well as alginic acid itself. The only synthetic derivative of alginic acid to find wide use, and acceptance as a food additive, is propylene glycol alginate. This is formed by reacting propylene oxide with moist alginic acid<sup>29-33</sup>. Esterification occurs at the carboxylic acid groups on the alginate chain, mainly with the primary hydroxyl group of propylene glycol. Depending on reaction conditions, such as reaction temperature and ratios of propylene oxide to alginic acid, varying degrees of esterification can be achieved. A product with about 60-70% esterification is satisfactory for most purposes but up to about 90% esterification can be achieved and this type of product (80-90%) is useful in very acidic, short term applications.

### 3.2.2 Extraction Processes

#### 3.2.2.1 Introduction

Alginic acid was first discovered by Stanford (1881). An excellent history of the evolution of the alginate industry has been written by Booth (1975). He traces a path from Stanford's successful exploitation of crude extracts to the failure by F.C. Thornley, in Orkney about 1923, to establish a briquette business based on using alginate as a binder for anthracite dust. Thornley moved to San Diego and by 1927 his company was producing alginate for use in sealing cans. After some difficulties the company changed its name to Kelp Products Corp. and in 1929 it was reorganized as Kelco Company. Production in the United Kingdom was established in the period 1934-1939 and in Norway after World War II. It is estimated that there are 17 factories in 9 different countries (ITC, 1981), excluding the People's Republic of China. The two largest producers, Kelco Company in USA and Alginate Industries Ltd in UK, have been acquired by Merck and Co. Inc., USA; these combined companies produce about 70% of the world's alginate. The next largest producer is Protan A/S of Norway, followed by companies in Japan and France (ITC, 1981). Production in China is increasing and is now 7 000-8 000 tonnes per annum.

Some of the early patents still provide useful basic information about alginate extraction<sup>34</sup> as does work published by the former Institutes of Seaweed Research in Scotland and Norway<sup>34,35</sup> and more recently by Braud et al.<sup>38</sup>. Processes used in Japan have been described by Okazaki et al.<sup>39</sup>. The minimal requirements for the profitable operation of an alginate extraction plant have been estimated by Moss and Doty<sup>40</sup>. They discuss the minimal seaweed input, colloid output and capital investment needed; they also list estimates of production costs. This analysis is made for agar and carrageenan as well as alginate.

#### 3.2.2.2 Processes

The chemistry of the processes used to make sodium alginate from brown seaweeds is relatively simple. The difficulties of the processes arise from the physical separations which are required, such as the need to filter slimy residues from viscous solutions or to separate gelatinous precipitates which hold large amounts of liquid within their structure and which resist both filtration and centrifugation. Processes for the manufacture of sodium alginate from brown seaweeds fall into two categories. Picture 34 is a diagram of the processes, simplified to show their essential difference. In one, the principal intermediates are calcium alginate and alginic acid. In the other, no calcium alginate is formed, only alginic acid.

The advantage of the first process is that calcium alginate can be precipitated in a fibrous form which can be readily separated; it can then be converted into alginic acid which is still fibrous and can also be readily separated. A further advantage of this process is that some calcium alginate can be allowed to remain in the final sodium alginate produced. This gives the manufacturer another method of controlling the viscosity of the final product, as discussed later in the "Properties" section. The second process does save one step, the formation of calcium alginate, but it also has some disadvantages. When alginic acid is precipitated in this process, it forms a gelatinous precipitate which is very difficult to separate and the overall losses of alginic acid are generally greater than in the former process. The removal of liquid ("dewatering") from within the gel structure of the separated alginic acid also presents difficulties in this second process. The water content in the dewatered alginic acid is often high, so that alcohol must be used as a solvent for the conversion to sodium alginate. This usually makes the process more expensive unless the alcohol recovery rate is very good, and this is not easy to achieve.

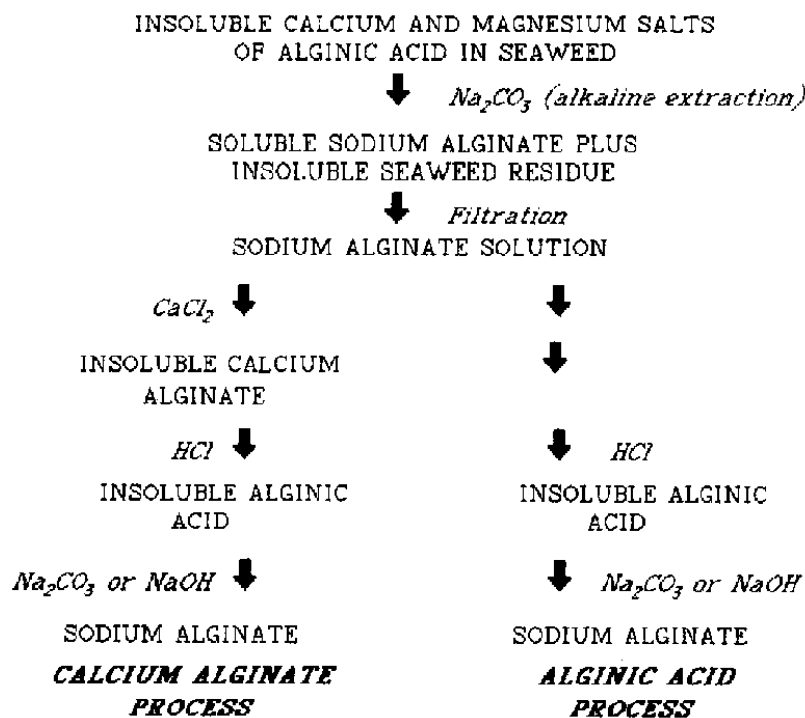
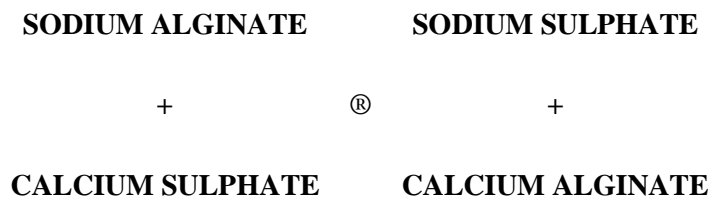


FIGURE 21: Production of sodium alginate

On mixing the powder with water a sol is formed, a chemical reaction takes place and a gel is formed. The powder contains:

1. Alginate salt (e.g. sodium alginate)
2. Calcium salt (e.g. calcium acetate)
3. Trisodium phosphate

The setting reaction is as follows: On mixing the powder with the water



The above reaction occurs too quickly often during mixing or loading of the impression tray. It can be slowed down by adding trisodium phosphate to the powder. This reacts with the calcium sulphate to produce calcium phosphate, preventing the calcium sulphate reacting with the sodium alginate to form a gel. This second reaction occurs in preference to the first reaction until the trisodium phosphate is used up, then the alginate will set as a gel. There is a well-defined working time during which there is no viscosity change.

### 3.2.2.3 Properties

- Good surface detail
- Reaction is faster at higher temperatures
- Elastic enough to be drawn over the undercuts, but tears over the deep undercuts
- Not dimensionally stable on storing due to evaporation
- Non toxic and non irritant, good for bioapplications
- Setting time can depend on technique
- Alginate powder is unstable on storage in presence of moisture or in warm temperatures

### 3.2.2.4 Advantages

1. Non toxic and non irritant
2. Good surface detail
3. Ease of use and mix
4. Cheap and good shelf life
5. Setting time can be controlled with temperature of water used

### 3.2.2.5 Disadvantages

1. Poor dimensional stability
2. In compatibility with some dental stones
3. Setting time very dependent on operator handling
4. Messy to work with

### 3.2.3 USES

Most alginate used in foods is in the form of sodium alginate. In order to form a gel, sodium alginate needs to come into contact with divalent ions such as calcium ( $\text{Ca}^{2+}$ ). As soon as sodium alginate (Picture 36) is added to a solution of calcium chloride, a gel forms as the sodium ions ( $\text{Na}^+$ ) are exchanged with calcium ions ( $\text{Ca}^{2+}$ ) and the polymers become crosslinked (Picture 37). The calcium ions are able to crosslink the alginate polymers because they can form two bonds, as opposed to monovalent ions such as sodium, which can only form one bond.

The longer the alginate is in contact with the calcium chloride solution, the more rigid the gel will become, as more crosslinks are formed. Also, depending on the concentration of calcium ions, the gels are either thermoreversible (low concentrations) or not (high concentrations). Reviews which are more specific to a particular use are listed in the following subsections.

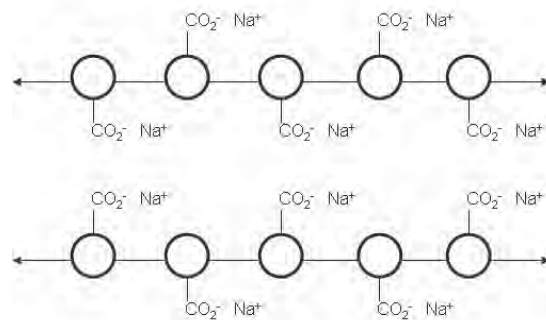


FIGURE 22: Alginate polymer in NaCl solution (no crosslinking)

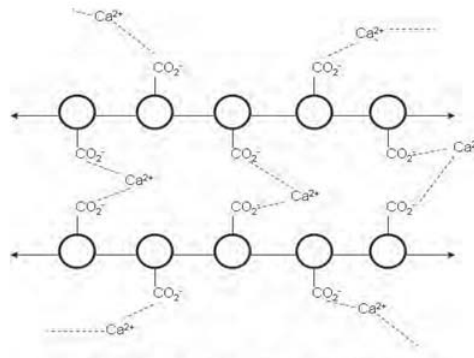


FIGURE 23: Alginate polymer in  $\text{CaCl}_2$  solution (crosslinking)

### 3.3 Cells

#### 3.3.1 Fibroblasts cells

A fibroblast is a type of cell that synthesizes the extracellular matrix and collagen, the structural framework (stroma) for animal tissues, and play a critical role in wound healing. They are the most common cells of connective tissue in animals. Fibroblasts and fibrocytes are two states of the same cells, the former being the activated state, the latter the less active state, concerned with maintenance. Currently, there is a tendency to call both forms fibroblasts. The suffix "blast" is used in cellular biology to denote a stem cell or a cell in an activated state of metabolism. The main function of fibroblasts is to maintain the structural integrity of connective tissues by continuously secreting precursors of the extracellular matrix. Fibroblasts secrete the precursors of all the components of the extracellular matrix, primarily the ground substance and a variety of fibres. The composition of the extracellular matrix determines the physical properties of connective tissues.



FIGURE 24: NIH/3T3 Fibroblasts in cell culture

Fibroblasts are morphologically heterogeneous with diverse appearances depending on their location and activity (Figure 24). Though morphologically inconspicuous, ectopically transplanted fibroblasts can often retain positional memory of the location and tissue context where they had previously resided, at least over a few generations. Unlike the epithelial cells lining the body structures, fibroblasts do not form flat monolayers and are not restricted by a polarizing attachment to a basal lamina on one side, although they may contribute to basal lamina components in some situations (eg subepithelial myofibroblasts in intestine may secrete the  $\alpha$ -2 chain carrying component of the laminin which is absent only in regions of follicle associated epithelia which lack the myofibroblast lining). Fibroblasts can also migrate slowly over substratum as individual cells, again in contrast to epithelial cells. While epithelial cells form the lining of body structures, it is fibroblasts and related connective tissues which sculpt the "bulk" of an organism. Like other cells of connective tissue, fibroblasts are derived from primitive mesenchyme. Thus they express the intermediate filament protein vimentin, a feature used as a marker to distinguish their mesodermal origin. However, this test is not specific as epithelial cells cultured in vitro on adherent substratum may also express vimentin after some time. In certain situations epithelial cells can give rise to fibroblasts, a process called epithelial-mesenchymal transition (EMT). Conversely, fibroblasts in some situations may give rise to epithelia by undergoing a mesenchymal to epithelial transition (MET) and organizing into a condensed, polarized, laterally connected true epithelial sheet. This process is seen in many developmental situations (eg. nephron and notocord development). Fibroblasts have a branched cytoplasm surrounding an elliptical, speckled nucleus having one or two nucleoli. Active fibroblasts can be recognized by their abundant rough endoplasmic reticulum. Inactive fibroblasts, which are also called fibrocytes, are smaller and spindle shaped. They have a reduced rough endoplasmic reticulum. Although disjointed and scattered when they have to cover a large space, fibroblasts when crowded often locally align in parallel clusters. Also fibroblasts make collagens, glycosaminoglycans, reticular and elastic fibers, and glycoproteins found in the extracellular matrix. Growing individuals' fibroblasts are dividing and synthesizing ground substance. Tissue damage stimulates fibrocytes and induces the mitosis of fibroblasts. Mouse embryonic fibroblasts (MEFs) are often used as "feeder cells" in human embryonic stem cell research. However, many researchers are gradually phasing out MEF's in favor of culture media with precisely defined ingredients of exclusively human derivation. Further, the difficulty of exclusively using human derivation for media supplements is most often solved by the use of "defined media" where the supplements are synthetic and achieve the primary goal of eliminating the chance of contamination from derivative sources. In this study we used fibroblasts rattail and fibroblasts 3T3 NIH.

### 3.3.2 Granulosa cells

A granulosa cell is a somatic cell found closely associated with the developing female gamete (called an oocyte or egg) in the ovary of mammals. In the primary ovarian follicle and later in follicle development (folliculogenesis) they advance to form a multilayered cumulus oophorus surrounding the oocyte in the preovulatory or Graafian follicle. The major functions of granulosa cells include the production of steroids, as well as a myriad of growth factors thought to interact with the oocyte during its development. Also FSH stimulates granulosa cells to convert androgens (coming from the thecal cells) to estradiol by aromatase. However, after ovulation the granulosa cells produce progesterone that may maintain a potential pregnancy and produce a thick cervical mucus which inhibits sperm entry into the uterus. In the development of the urinary and reproductive organs, the oogonia become invaginated in the gonadal ridge. In the 1970's, evidence emerged that the first cells to make contact with the oogonia were of mesonephric origin. It was suggested that mesonephric cells already closely associated with the oogonia proliferated throughout development to form the granulosa cell layer. Recently this hypothesis has been challenged with some thorough histology. Sawyer et al. hypothesised that in sheep most of the granulosa cells develop from cells of the mesothelium (i.e., epithelial cells from the presumptive surface epithelium of the ovary). The embryological origin of granulosa cells remains controversial as it is seen in the following



*FIGURE 25: Oocyte granulosa cells*

### 3.3.3 Gelatin

Gelatin (also gelatine, from French *gélatine*) is a translucent, colourless, brittle, nearly tasteless solid substance, extracted from the collagen inside animals' connective tissue. It has been commonly used as an emulsifier in food, pharmaceutical, photography, and cosmetic manufacturing. Substances containing gelatin or functioning in a similar way are called *gelatinous*. Gelatin is an irreversibly hydrolyzed form of collagen. Gelatin is classified as a foodstuff and has E number 441. Gelatin is a protein produced by partial hydrolysis of collagen extracted from the bones, connective tissues, organs, and some intestines of animals such as the domesticated cattle, and horses. The natural molecular bonds between individual collagen strands are broken down into a form that rearranges more easily. Gelatin melts when heated and solidifies when cooled again. Together with water, it forms a semi-solid colloidal gel. Gelatin forms a solution of high viscosity in water, which sets to a gel on cooling, and its chemical composition is, in many respects, closely similar to that of its parent collagen<sup>40</sup>. Gelatin solutions show viscoelastic flow and streaming birefringence. If gelatin is put into contact with cold water, some of the material dissolves. The solubility of the gelatin is determined by the method of manufacture. Typically, gelatin can be dispersed in a relatively concentrated acid. Such dispersions are stable for 10-15 days with little or no chemical changes and are suitable for coating purposes or for extrusion into a precipitating bath. Gelatin is also soluble in most polar solvents. Gelatin gels exist over only a small temperature range, the upper limit being the melting point of the gel, which depends on gelatin grade and concentration and the lower limit, the ice point at which ice crystallizes. The mechanical properties are very sensitive to temperature variations, previous thermal history of the gel, and time. The viscosity of the gelatin/water mixture increases with concentration and when kept cool ( $\approx 40^\circ\text{F}$ ).

## B. Materials that were used for the 3D deposition by Multi-Photon Polymerization Method

### 3.4 Ormocer polymer

#### 3.4.1 Introduction

ORMOCER stands for ORganically MODified CERamic and it is a family of organic-inorganic hybrid polymers created by the Fraunhofer Gesellschaft (Fraunhofer-Institut für Silicatforschung, Würzburg, Germany)<sup>41</sup>. Because of their physical and chemical properties which result from their hybrid nature inorganic-organic polymers have been developed and tested for evaluation in optical and electrical interconnection technology over the last decade<sup>42</sup>. The specific ORMOCER used in this work is a hybrid developed for optical applications so that shows high transparency in the visible and near infrared ranges. It consists of an inorganic Si-O-Si backbone and the polymerizable functionality is introduced into the system by organic side chains R, e.g., (meth-) acryl groups (Fig.25). The optical and mechanical properties, that is, absorption and refractive index, are controlled by the other side chains such as methoxy (Me) and phenyl (Ph) groups.

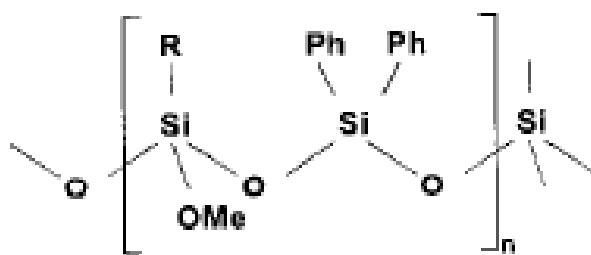


*FIGURE 25: Chemical structure of ORMOCER polymers. Methoxy (Me) and phenyl (Ph) groups are linked to the inorganic Si-O backbone.*

The light sensitivity of the ORMOCER-type hybrid polymers in combination with appropriate photoinitiators permits the photolithographic fabrication of optical microstructures. In the specific ORMOCER used in this thesis, initiation of the free-radical photopolymerization process is due to a photoinitiator Irgacure 369 (fig.26), which absorbs strongly in the UV wavelength range around 350 nm (fig.27).

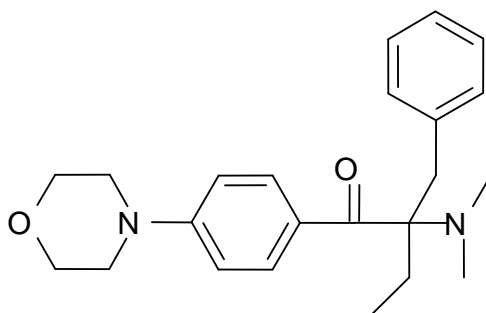


FIGURE 26: Chemical structure of Irgacure 369

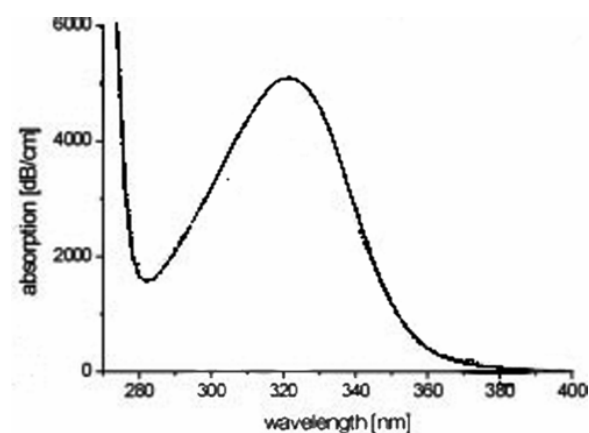
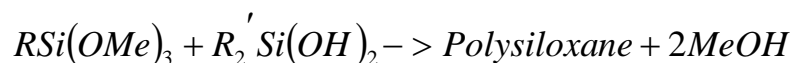


FIGURE 27: Absorption spectrum of ORMOCER

### 3.4.2 Production of ORMOCER

The ORMOCER used in the worked is obtained prepared from Microresist (Germany). The preparation of the material is, however, straightforward and described below.

In order to either achieve a suitable inorganic–organic hybrid polymer, an inorganic backbone is established via poly condensation (alkoxylation) of diphenylsilanediol (P2) and 3-methacryloxypropyltrimethoxysilane (MEMO) referred to as ORMOCER I. Fig.4 shows the reaction scheme for the resin of ORMOCER\_I which is used as the core material for optical waveguide applications, where P2 and MEMO react using a suitable catalyst at an elevated temperature.



where R is the methacrylic group and R<sub>2</sub>' is the diphenyl.

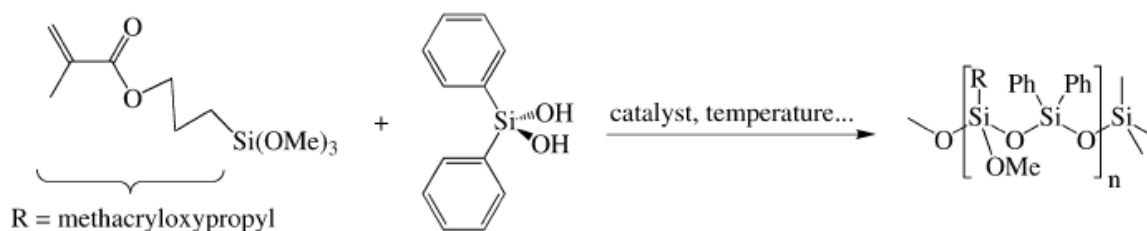
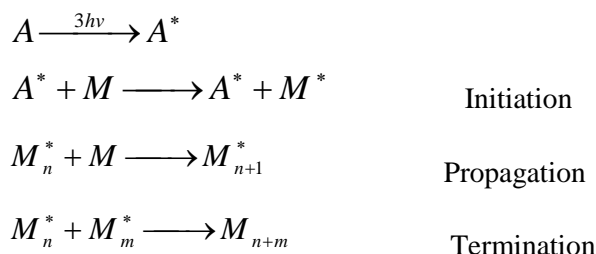


FIGURE 28: Reaction Scheme of silane precursors of polysiloxane network used as polymer core material. ORMOCER I results after UV polymerization of the organic group R.

After this reaction, volatile products such as methanol (MeOH) are evaporated resulting in a viscous, storage-stable ORMOCER resins<sup>43</sup>.

### 3.4.3 Polymerization of ORMOCER

The infra-red laser passes through the out of focus photosensitive resin with no absorption. Nonlinear absorption of laser pulses breaks chemical bonds on starter photoinitiator molecules within a small focal volume. The monomers react with radicalized starter molecules to create radicalized polymolecules. Reactions are terminated when radicalized polymolecules react with one another. The main reaction series in three photon-induced polymerization is shown below:



where A is photoinitiator, M is monomer and  $M^*$  is growing radical.

The self-organizing character of photosensitive polymers like ORMOCER arises from the change of the material density during the polymerization process. This density change corresponds to a change in the refractive index. This index change is permanent and saturable. As long as oxygen is kept away, the nonlinear response is available directly after the illumination is started, when the first photons are absorbed by the photoinitiator. If the inhibition by oxygen is not avoided, a certain threshold energy  $E_{\text{thres}}$  has to be passed to get over the inhibition of the polymerization due to the interception of free radicals. Once the polymerization reaction is initiated, the refractive index grows fast at first.

This is because all radicals find directly suitable reaction partners after short diffusion lengths in their closest neighbourhood. The index change passes then over into saturation with a slowly rising index, owing to the more and more limited mobility of monomer radicals in the partly cross-linked polymer matrix. In addition, the radicals have to diffuse longer to find available reaction partners. So the reaction velocity slows down, and the polymerization terminates. Besides the basic material properties, the nonlinear response depends strongly on a set of process parameters, such as the exposure intensity and the photoinitiator concentration and type.

### **3.4.4 General Properties of ORMOCER (Porosity and density)**

Classic ORMOCER is a dense material and its density lies between  $1.1 \text{ g/cm}^3$  and  $1.6 \text{ g/cm}^3$  which is slightly above the range for organic polymers, but well below the density of oxide materials ( $2.2 \text{ g/cm}^3$ ).

#### **3.4.4.1 Mechanical and Thermal Properties**

The inorganic structures of ORMOCERs are responsible for their high stiffness and hardness compared with organic polymers. Due to their transparency and easy of processing as lacquers ORMOCERs find widespread applications as coatings which exhibit high mechanical strength, hardness and abrasion resistance. ORMOCER materials demonstrate mechanical properties that may vary from those of polymers to those of ceramics. For example, Young's modulus values for ORMOCER materials may be adjusted between 1Mpa and 4000Mpa and thermal expansion coefficients from 183 to  $67 \times 10^{-6} \text{ K}^{-1}$  through the use of various precursors.

#### **3.4.4.2 Optical and Electrical Properties**

The high optical transparency of ORMOCERs is mainly due to their amorphous nature and their lack of structures absorbing light in the visible region. ORMOCERs in their non-modified form are highly electrically insulating materials comparable to inorganic glasses and non-polar organic polymers. In addition, ORMOCERs adhere very well on most substrates such as (metallized) Si wafers, inorganic glasses and polymers. ORMOCER materials demonstrate optical transparency in the 1600nm range, refractive indices in the 1.47-1.56 range, and low optical losses in the near infrared range. These materials remain stable to  $350^\circ\text{C}$  in an oxygen atmosphere and exhibit duroplastic behaviour on heating. ORMOCERs are highly insulating materials with bulk resistivities in the range of  $10^{13}$ - $10^{16} \Omega \text{ cm}$ . Therefore they show good passivation properties for electronic applications, due to their

good adhesion to most of the interconnection materials and good barrier properties<sup>44</sup>. Their low dielectric constant makes them good candidates for interlayer dielectrics in electrical interconnection technology.

### 3.4.5 Applications of ORMOCER

#### 3.4.5.1 Fabrication of 3D microstructures

Three photon polymerization (3PP) of photosensitive materials allows one to fabricate complicated three-dimensional (3D) microstructures. When they are tightly focused into the volume of a liquid resin (which is transparent in the infrared), femtosecond laser pulses can initiate 3PP and produce structures with submicrometer resolution. The desired microstructures are created by shifting the laser focus along three dimensions using a piezo stage. The non irradiated resin is removed using a developer solution after processing.

#### 3.4.5.2 Fabrication of photonic crystals

Liquid resins, like ORMOCER, are used to fabricate photonic crystals because they exhibit high transparency in the visible and near infrared ranges by means of 3PP. The rods have a thickness of 300nm and the woodpile structure possesses a photonic band gap in the near infrared spectral range. The central frequency of the bandgap can be tuned by varying the period of the crystal<sup>45,46</sup>.

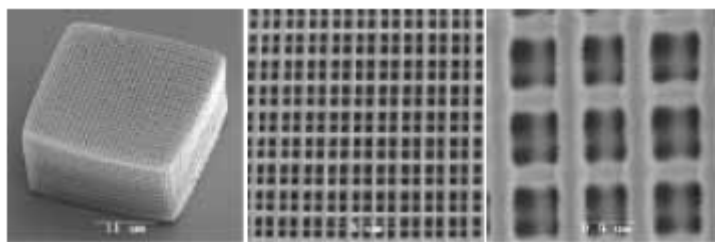


FIGURE 29: SEM images of woodpile structures fabricated by 2PP in ORMOCERs

#### 3.4.5.3 Medical applications

The precision of 3PP along with the unique properties of Ormocer allow the development of microneedle arrays for drug delivery. Micron-scale needles can increase skin permeability and improve the transdermal delivery of macromolecules. Arrays of these needles could provide painless injections to people suffering from diabetes, blood clotting or other disorders<sup>57</sup>. Finally 3D structures of Ormocer are fabricated by 3PP in order to be used as scaffolds for tissue engineering.

## REFERENCES

1. Zhang SG. et al *Biotechnology Advances* (2002) 20 (5-6): 321-339
2. Daamen WF. et al *Biomaterials* (2007) 28 (30): 4378-4398
3. Gazit E. et al *Chemical Society Reviews* (2007) 36 (8): 1263-1269
4. Chiti F., Dobson CM. *Annual Review of Biochemistry* (2006) 75: 333-366
5. Sipe JD, Cohen AS. *Journal of Structural Biology* (2000) 130 (2-3): 88-98
6. Selkoe DJ. et al *Nature Cell Biology* (2004) 6 (11): 1054-1061
7. Dobson CM. et al *Nature* (2003) 426 (6968): 884-890
8. Dobson CM. et al *Trends in Biochemical Sciences* (1999) 24 (9): 329-332
9. Serpell LC. et al *Biochimica et Biophysica Acta-Molecular Basics of Disease* (2000) 1502 (1): 16-30
10. Luckey M., Hernandez JF., Arlaud G., Forsyth VT., Ruigrok RWH, Mitraki A. (2000) *FEBS Letters* 468 (1): 23-27
11. Nilsson MR (2004) *Methods* 34 (1): 151-160
12. Stromer T., Serpell LC (2005) *Microscopy Research and Technique* 67 (3-4): 210-217
13. Seeman NC (2003) *Nature* 421 (6921): 427-431
14. Gilead S., Gazit E. (2005) *Supramolecular Chemistry* 17 (1-2): 87-92
15. Ryadnov MG, Woolfson DN (2003) *Nature Materials* 2 (5): 329-332
16. Ryadnov MG, Woolfson DN (2007) *Journal of the American Chemical Society* 129 (45): 14074-14081
17. MacPhee CE, Woolfson DN (2004) *Current Opinion in Solid State & Materials Science* 8 (2): 141-149
18. Zhang SG. (2002) *Biotechnology Advances* 20 (5-6): 321-339
19. Zhang SG. (2003) *Nature Biotechnology* 21 (10): 1171-1178
20. Penman, A. and G.R. Sanderson, (1972), A method for the determination of uronic acid sequence in alginates. *Carbohydr.Res.*, 25:280
21. Atkins, E.D.T., et al., (1973), a. Structural components of alginic acid. 2. Crystalline structure of poly- $\alpha$ -L-guluronic acid. Results of x-ray diffraction and polarized infrared studies. *Biopolymers*, 12:1879-87
22. Haug, A., B. Larsen and O. Smidsrod, (1966), A study of the constitution of alginic acid by partial acid hydrolysis. *Acta Chem.Scand.*, 20:183-90
23. Haug, A., B. Larsen and O. Smidsrod, (1974), Uronic acid sequence in alginate from different sources. *Carbohydr.Res.*, 32:217-25
24. Grasdalen, H., B. Larsen and O. Smidsrod, (1981),  $^{13}\text{C}$ -NMR studies of monomeric composition and sequence in alginate. *Carbohydr.Res.*, 89:179-91

25. Haug, A., et al., (1967), Correlation between chemical structure and physical properties. Acta Chem.Scand., 21:768-78
26. Smidsrod, O. and A. Haug, (1972), Dependence upon the gel-sol state of the ion-exchange properties of alginates. Acta Chem. Scand., 26:2063-74
27. Smidsrod, O., A. Haug and S.G. Whittington, (1972), The molecular basis for some physical properties of polyuronides. Acta Chem.Scand., 26:2563-4
28. Morris, E.R., D.A. Rees and D. Thom, (1980), Characteristics of alginate composition and block-structure by circular dichroism. Carbohydr.Res., 81:305-14
29. Steiner, A.B., (1947), Manufacture of glycol alginates. U.S. Patent 2,426,215
30. Steiner, A.B. and W.H. McNeely, (1950), High-stability glycol alginates and their manufacture. U.S. Patent 2,494,911.
31. Kelco, (1952), Alkylene glycol esters of alginic acid. British Patent 676,618
32. Pettitt, D.J. and V.H. Noto, (1973), Process for the preparation of propylene glycol alginate from partially neutralized alginic acid. U.S. Patent 3,772,266
33. Noto, V.H. and D.J. Pettitt, (1980), Production of propylene glycol alginic acid esters. British Patent 1,563,019
34. Thornley, F.C. and M.J. Walsh, (1931), Process of preparing alginic acid and compounds thereof. U.S. Patent 1,814,981
35. Black, W.A.P. and F.N. Woodward, (1954), Alginates from common British brown marine algae. In Natural plant hydrocolloids. Adv.Chem.Ser.Am.Chem.Soc., 11:83-91
36. Haug, A., (1964), Composition and properties of alginates. Rep.Norw. Inst.Seaweed Res., (30):123 p
37. Braud, J.-P., R. Debroise and R. Pérez, (1977), Nouvelles perspectives dans l'exploitation des laminaires (New prospects for utilization of marine algae of the genus Laminaria). Rev.Trav.Inst.Pêches Marit.,Nantes, 41:203-11 (in French)
38. Okazaki, A., (1971), Seaweeds and their uses in Japan. Tokyo, Tokai University Press, 165 p.
39. Moss, J.R. and M.S. Doty, (1987), Establishing a seaweed industry in Hawaii: an initial assessment. Honolulu, Hawaii State Department of Land and Natural Resources. 73 p.
40. Ward, A.G.; Courts, A. (1977). *The Science and Technology of Gelatin*. New York: Academic Press.
41. R.J. Narayan, C.M. Jin, T. Partz, A. Doraiswamy Modi, D.B. Chrisey, Y.Y. Su, S.J. Lin, A. Ovsianikov, B. Chichkov, Adv.Mater.Processes (2005),163,39
42. Popall, M. Dabek, A. Robertsson, M. E. Valizadeh, S. Hagel, O. J. Buestrich, R. Nagel, R. Cergel, C. Lambert, D. Schaub, M. Mol Cryst LiqCryst (2000), 354, 123–142

43. R. Houbertz, G. Domanna, C. Cronauera, A. Schmitt, H. Martin, J.-U. Park *Thin Solid Films* 442 (2003) 194–200
44. *Current Opinion in Solid State and Materials Science* 4 (1999) 571–580
45. J. Serbin, A. Ovsianikov, and B. Chichkov, *Optics Express* 12 (2004) 5221-5228
46. J. Serbin, A. Egbert, A. Ostendorf, B. N. Chichkov, R. Houbertz, G. Domann, J. Schulz, C. Cronauer, L. Fröhlich, and M. Popall, *Optics Letters* 28 (2003)301-303
47. “Laser processing of advanced biomaterials” *Adva.Mat.Proc* 39 (2005)
48. S. Kawata, H.-B. Sun, T. Tanaka, and K. Takada, *Nature* 412, 697 (2001)
49. S. Maruo and S. Kawata, *IEEE J. Microelectromech. Syst.* 7, 411 (1998)
50. H.-B. Sun, K. Takada, and S. Kawata, *Appl. Phys. Lett.* 79, 3173 (2001)
51. H.-B. Sun, T. Kawakami, Y. Xu, J.-Y. Ye, S. Matuso, H. Misawa, M. Miwa and R. Kaneko, *Opt. Lett.* 25,1110 (2000)
52. H.-B. Sun, T. Tanaka, K. Takada, and S. Kawata, *Appl.Phys. Lett.* 79, 1411 (2001)
53. Two-photon polymerization of an Eosin Y-sensitized acrylate composite *Journal of Photochemistry and Photobiology A: Chemistry* xxx (2005)
54. A. Espanet, C. Ecoffet, D.J. Loughnot, PEW: photopolymerization by 228 evanescent waves. II. Revealing dramatic inhibiting effects of oxygen at 229 submicrometer scale, *J. Polym. Sci.: Part A: Polym. Chem.* 37 (1999) 230 2075–2085.
55. <http://www.ce-mag.com/archive/01/Spring/Rosner.html>
56. Covalent DNA immobilization on polymer-shielded silver-coated quartz crystal microbalance using photobiotin-based UV irradiation *BIOCHEM BIOPH RES CO* 290 (3): 962-966 JAN 25 (2002)
57. Molecular patterning on carbon based surfaces through photobiotin activation† *Analyst* 126, 195



CHAPTER 4  
EXPERIMENTAL



In this chapter follows in details the description of experimental techniques that were used in the frames of experiments. Concretely in this chapter are been described:

1. The experimental set-up that was used, during the application of L.I.F.T. method.
2. The experimental set-up that was used, during the application of the Multi-Photon Polymerization method.
3. The experimental techniques that were used for the characterization of the patterns, structures and their morphology.

## 4.1. Experimental Set-ups

### 4.1.1. L.I.F.T. Set-up

The experimental set-ups that were used for the 2D deposition of peptides solution, alginate gel, and cells, by using the L.I.F.T. method, are being presented in pictures 1, 2 that follow. The laser sources that were used: fs laser that was drawn from a laser organic pigment77 (248nm, 13mJ energy of pulse, duration of pulse 500 fs, 1-10 pps repetition rate, size of beam 30-10 mm) and a ns laser (KrF 248nm laser, 1Hz, 15ns duration of pulse). The laser beam was focused in the material-objective after the use of mirrors, diffractive and reflective lenses. The energy of laser pulse can be regulated with the help of an optical set-up of reduction of energy so that are achieved densities of energy bigger than the energy threshold of transfer but lower than the energy that we know as energy of destruction or evaporation of the materials that we want to transfer.

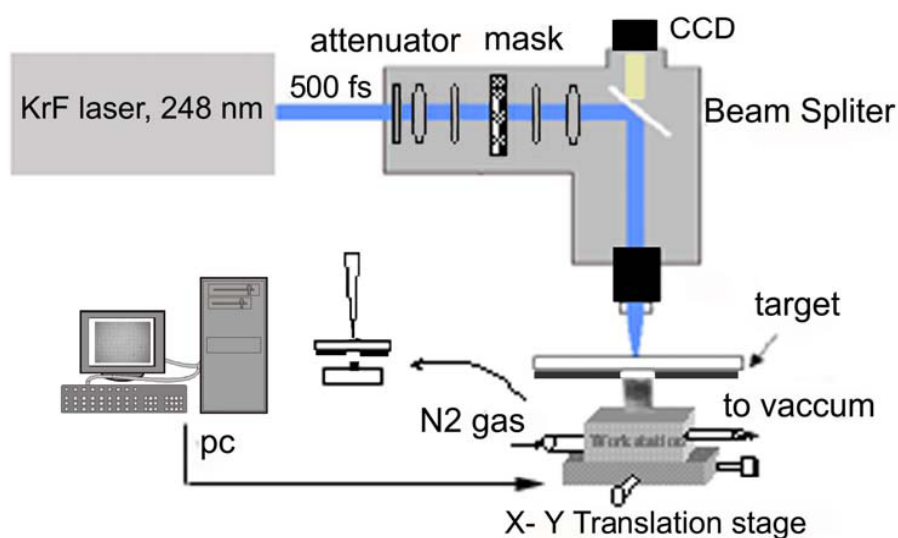


FIGURE 1: fs laser set-up ( KrF 248nm,13mJ, 500fs )

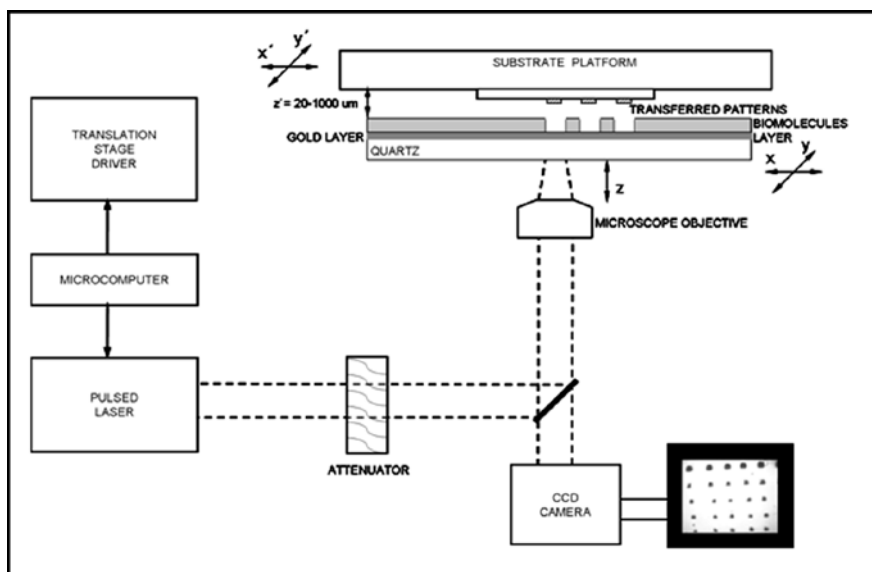


FIGURE 2: ns laser set-up ( KrF 248nm laser, 1Hz, 15ns ).

#### 4.1.1.1 Chamber of Depositions (while using the fs set-up)

The form and the dimensions of laser beam above in the material-objective can be regulated via a variable diaphragm in various forms, as rectangle, triangular or circular etc, so each time certain department of material-objective is exposed, for the aim of one determined and precise quantity of the material to be transferred above in the substrate. An optical system, that has aim the achievement of territorial discreet faculty between 1 and 250 mms, is used for the projection of diaphragm with big diminution above in the material-objective. The beginning of micromechanics with laser is supported in the faculty of the system to focus the laser beam in small regions in the working surface. The size of the region of focus, the smaller possible distance of segregation of two points, the depth of field, and the relative intensity of laser beam are the parameters that we should pay attention at in the case of use of microscopes for the various treatments with laser. Theoretically the smaller possible distance

of discrimination of two points is given by the Rayleigh criterion<sup>1</sup>:  $d = \frac{0.61\lambda}{NA}$  (4.1). Where

$d$  is the distance of distinguished points,  $\lambda$  is the wavelength of radiation, and  $NA$  the numerical opening of the objective lens. For Gaussian distribution of laser beam, the minimal size of focus that is achieved, as it is also presented in equation 3.2 that follows, it is given by

the relation:  $w_0 = \frac{\lambda}{\pi \cdot NA}$  (4.2). According to the equation 4.1, a way to increase the

discreet faculty of system is or to decrease the wavelength or to increase the numerical opening of the objective lens.

According to the laws of diffraction the focused beam does not maintain its homogeneity at its distribution in the free space, but on the contrary deviates and converges.

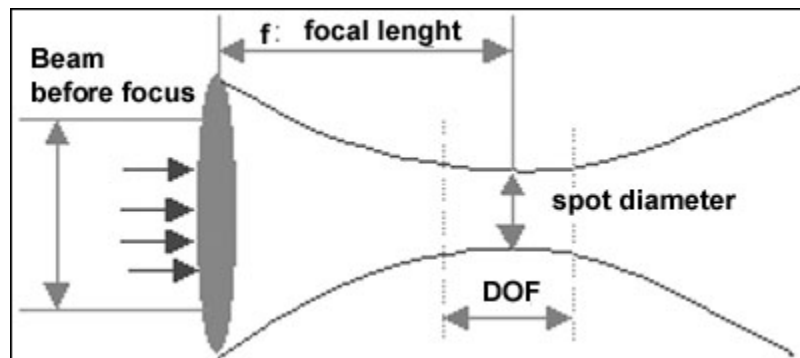


FIGURE 3: Distribution of beam

If the beam has beam  $w$ , the rate of divergence of beam in the distance between sample and point of focus is given by following equation 3.3 and it is characterized as the depth of field:  $DOF = \pm \frac{\pi w_0^2}{\lambda}$  (4.3). The objective lens that was used in the experiments of deposition had numerical opening  $NA = 0.4$  with the result the discrete faculty of the optical system (for  $\lambda = 248$  nm) is  $d = 378$  nm. The substrate should be placed at the same time also in small distance from the target. The usual distance between the down surface of target and the surface of substrate varies between 1mm and 250 mms with the mathematical precision of 1mm. The laser beam, the target material and the substrate can be placed the one concerning the other and can be checked and be shifted the one as for the other via steps engines and their drivers, which are checked by computer. This technology is widely acquaintance in the field of micromechanics with laser.

More specifically, the beam laser is focused at the target and radiates its material with energy that can remove and transfer the certain part of its material of the target o the substrate's surface. The repetition of the transfer process in different places of the target and the substrate, e.g. step-to-step, repeated under the control of computer and the driver of steps engines, it has as a result the creation of forms as the constellation of simple separated elements which they shape patterns, and the repetition of neighbouring elements which they shape coverings. Moreover, abundance of objectives from different materials they can be used for the creation of big number of distinguished depositions.

At the duration of transfer process the region of radiation can be descript with the help of a depiction system that includes a CCD camera and an optical microscope. The natural contact of the target with the substrate is achieved by using a special chamber for the creation of vacuum of order of  $10^{-1}$  Torr (picture 4).

The distance between the target and the substrate is regulated, can be some  $\mu\text{m}$ s by placing the substrate in the mobile department of the chamber during vacuum conditions or in air. Phenomena of contribution of white light are observed in conditions of good contact between the two sublayers (target-substrate).

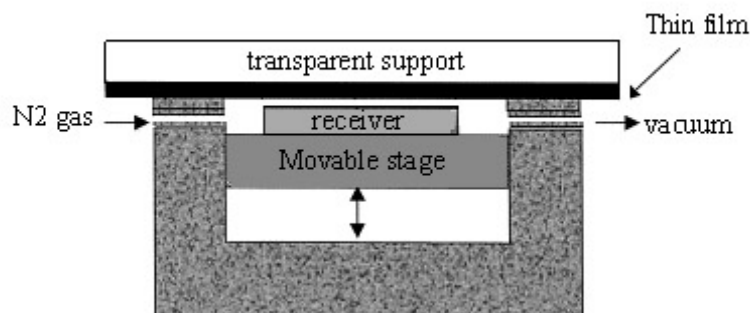


FIGURE 4: Chamber of deposition

#### 4.1.2 Multi-Photon Polymerization set-up

The set-up for the fabrication of three-dimensional microstructures by three-photon micro stereolithography is shown in Fig. 5. The laser sources that were used are: a) an Amplitude Systems t-pulse laser femtosecond oscillator operating at 1028 nm. This source is a compact diode-pumped femtosecond laser oscillator with an average laser power of 1W delivering a series of high energy, short duration pulses of less than 200fs and a repetition rate of 50MHz, b) Depending on whether it is two-or three photon polymerization, the laser can be a Ti:Sapphire femtosecond oscillator operating at 800 nm or an Ytterbium femtosecond oscillator operating at 1030 nm; there are also examples in literature where an Optical Parametric Oscillator (OPO) is used with a Ti:Sapphire laser, to reduce the laser wavelength to visible wavelengths [i,ii]. The laser will typically have a pulse length of less than 200 fs and a repetition rate of 50-80 MHz. The energy required for the polymerization process will depend on the material, the photoinitiator and the focusing, but is usually in the order of a few nanojoules per pulse.

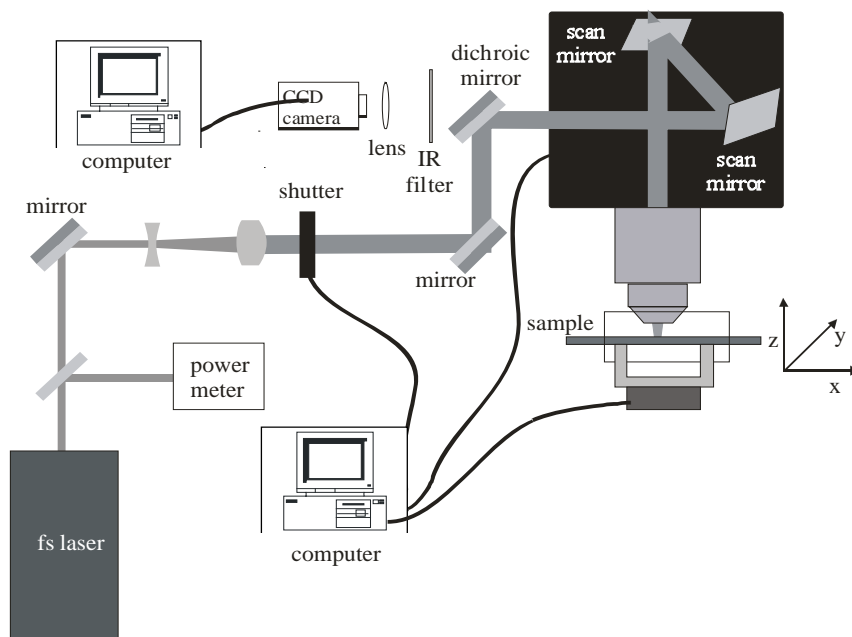


FIGURE 5: Experimental set-up

By moving the laser focus in a three-dimensional manner through the liquid, three-dimensional structures can be fabricated<sup>1</sup>. The photopolymerized structure is usually generated in a layer by layer format. Each layer either using an x-y galvanometric mirror scanner or x-y piezoelectric stages. The main difference between the two cases is that in the former case, the structure remains immobile and the structure is generated by the laser beam moving, while in the latter case the x-y stages move the structure and the laser beam remains immobile. Movement on the z-axis can be achieved using a piezoelectric or a high resolution linear stage. So the photopolymerized structure can be generated using an x-y-z galvanometric mirror digital scanner (Scanlabs Hurryscan II), controlled by SAMLight (SCAPS) software. SAMlight software allowed the drawing of various structures built layer by layer. To achieve the tight focusing conditions required for multi-photon polymerization to occur, a microscope objective needs to be used; when the numerical aperture (N.A.) of the objective is higher than 1, immersion oil is used for index matching. Galvo scanners have to be adapted to accommodate microscope objectives, as usually they are designed to take lenses with long focal lengths. The beam waist of the focused laser beam is given by  $r = 0.61\lambda/\text{N.A.}$

Beam control can be achieved by either using a fast mechanical shutter or an acousto-optic modulator, while beam intensity control can be achieved using neutral density filters, a variable attenuator or a combination of a polarizer and a waveplate. For the online monitoring of the photopolymerization process, a CCD camera can be mounted behind a dichroic mirror, as shown in Fig.5 above. This is possible as the refractive index of most photopolymers changes during polymerization, so that the illuminated structures become visible during the building process.

After the completion of the photopolymerization process and in order to remove the unphotopolymerized resin, the samples need to be developed like in any lithographic process. The developer used and the time for development will depend on the material.

## 4.2 Techniques of Characterizations

### 4.2.1 Electron Microscopy

In order to study the size of single fibrils in detail Transmission Electron Microscopy (TEM) was used and for the three dimensional morphology the Scanning Electron Microscopy (SEM) was combined. Transmission Electron Microscopy consists of an electron source, an electron beam, the specimen area and the viewing screen. The electromagnetic lenses are used to guide the electron beam in order to be coherent and give us the best resolution that we can have. Also the electron source plays a very important role for the quality of image that we obtain.

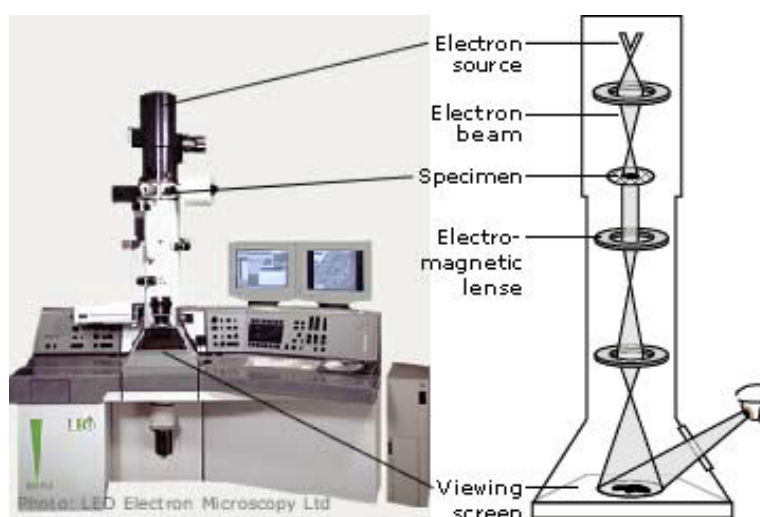


FIGURE 6: Typical TEM instrument

The electrons are generated through thermionic emission from a filament, usually tungsten; they are subsequently accelerated by using high voltage, usually 80kV. This beam is controlled by electromagnetic lenses and focuses on the sample. Our sample is usually on a grid which is made from copper or nickel and is covered with a very thin film of a membrane which allows the sample not to fall (Figure 8). The grid has 300 areas of observation of approximately 60x60  $\mu\text{m}$  area. In order to observe biological samples specific staining techniques are required to improve the contrast of the samples, since biological samples are transparent. This method is called negative staining; a heavy metal solution such as uranylacetate is embedded on the grid with the sample, in order to be deposited around the molecule or structure and provide contrast for better visualization (Figure 7).

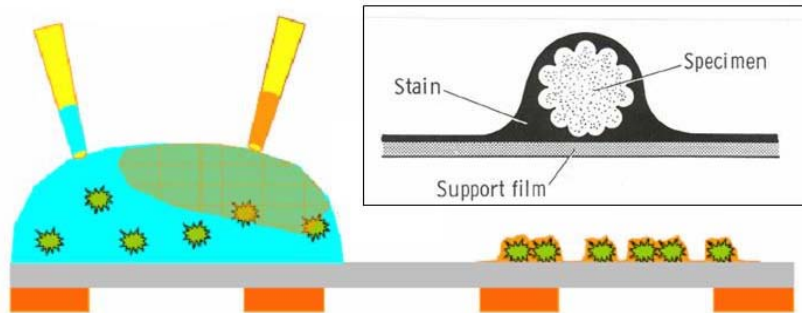


FIGURE 7: Negative staining method in TEM analysis

After the beam passes through the sample is collected again with electromagnetic lenses and it is guided to a fluorescent screen. Modern technologies have introduced high quality cameras for real time observation on computers and high quality pictures.

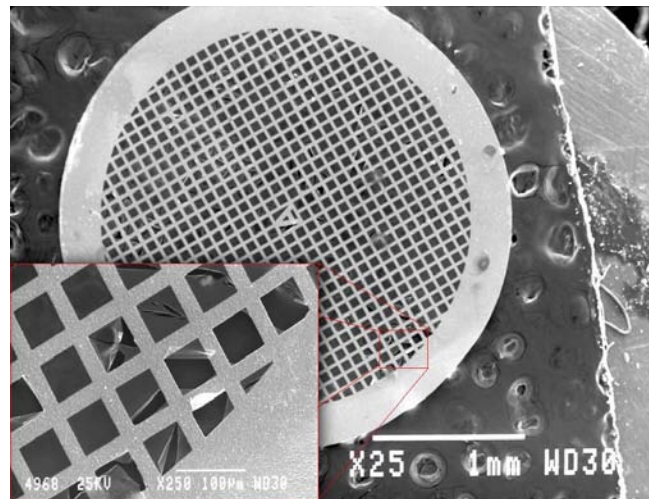


FIGURE 8: Electron microscopy grid for sample support with membrane

This type of microscopy is used a lot in Materials Science for many diverse groups such as polymers, inorganic chemists and biomaterials. The most important part of this experimental technique is the sample preparation. The sample should be at most  $1\mu\text{m}$  thick and transparent as well. It must be stable on the surface of the grid and relevant to the resolving power of the instrument. Nowadays Electron Microscopes can achieve resolution up to  $0.1\text{ nm}$  at magnifications of 50 million times.

Scanning Electron Microscopy gives information about the surface and morphology of the sample. The instrument has approximately the same concept as TEM; it consists of an electron gun, electromagnetic lenses and detectors that collect the information from the interaction between the sample and the high energy beam of electrons (Figure 9). The difference here is the way that information is analyzed from the detector of the instrument. After the electrons are produced in a thermionic way, they are accelerated with various types

of energies up to 100kV and focused by electromagnetic lenses and coils in order to have a very small focal spot. This primary electron beam interacts with the specimen and the scattered electrons, secondary or backscattered, are further detected and analyzed. Same as above, the sample preparation is very crucial and requires different approach for various types of materials. As a rule the material should be conductive otherwise we have charging effect<sup>2</sup>.

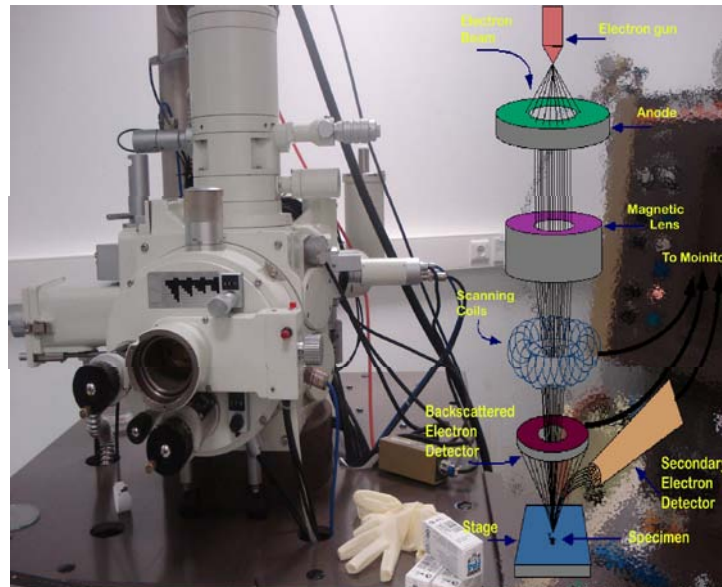


FIGURE 9: Typical SEM instrument

The metal samples require only trimming or sectioning to the appropriate size. Nonconductive samples require coating of a very thin layer of metal using an instrument named as sputter coater. This instrument has a target of a metal, which can be gold, gold/palladium, platinum, tungsten or graphite, and using plasma sputtering we deposit the desired layer of the metal. Apart from the conductivity this process increases the contrast and reveals the details of our sample. The resolution of this technique can be around 1 nm although each time it depends on the conditions and the interaction between the sample and the electron beam.

## REFERENCES

1. E. Hecht, "Optics", Addison Wesley Longman, third edition, (1998)
2. Shaffner TJ and Vanveld RD (1971), Charging effects in scanning electron microscope, JOURNAL OF PHYSICS E: SCIENTIFIC INSTRUMENTS 4: 633-637

[<sup>i</sup>] M. Straub, L. H. Nguyen, A. Fazlic, and M. Gu, Optical Materials **27**, 359–364 (2004).

[<sup>ii</sup>] W. Haske, V. W. Chen, J. M. Hales, W. Dong, S. Barlow, S. R. Marder, and J. W. Perry, Opt. Express **15**, 3426-3436 (2007).

CHAPTER 5  
RESULTS



This chapter is separated in two parts. In the first part the results after the 2D deposition by using the L.I.F.T. method are been presented. Firstly for the optimization of the process, these parameters have been studied: distance between target-substrate, pulse duration, laser energy and target's film thickness. Then the optimized conditions were applied in order to fabricate 2D patterns of peptides, 2D patterns of cells and 3D deposition of alginate gel in order to built 3D structures that can be used for tissue engineering. Finally in the second part the 3D structures of ormoer that were produced by three photon polymerization are been presented. We also present the direct three dimensional patterning of self-assembled peptide fibrils, which were deposited on the 3D structures of ormoer by using a combination of biotin-avidin chemistry. The technique is based on the selective attachment of photo sensitive biotin (photobiotin) on these 3D structures of Ormoer and exploits thiol chemistry and self-assembly of peptide fibrils.

## **A. Results after the 2D deposition by using L.I.F.T. method**

### **5.1 Optimization of the process**

In order to generate and optimize biomolecular microarrays and patterns, microarray quality must be examined. Due to this, the following parameters were studied:

- Distance between target-substrate
- Laser pulse duration
- Laser energy
- Film thickness of the target

The aqueous glycerol and PBS solution (40/60 in volume) was spread on quartz glass coated with 10 nm gold thin layer (BALTEC SCD 050 Sputter Coater) film and used as a target. The liquid film thickness, estimated through the measurement of the film weight, and found approximately 3 nm. Glass slides were used as receiving substrates and a femtosecond (KrF 248nm, 13mJ, 500fs) and a nanosecond (KrF 248nm laser, 1Hz, 15ns) laser based systems were used for the transfer.

### 5.1.1 Distance between target-substrate

In this part the fs and the ns laser based systems were used, in order to examine the dependence of the distance between the target and the substrate surfaces with the receiving droplet's spot size by using these two different laser pulse durations. By the measurements we made the following graph (Fig. 1). The conclusion from the Fig. 1 is that by using different distances between target-substrate surfaces, the spot size of the receiving droplet is not changing very much. But we must notice that there is a big difference for the droplet's spot size when we are using fs pulses than using ns pulses.

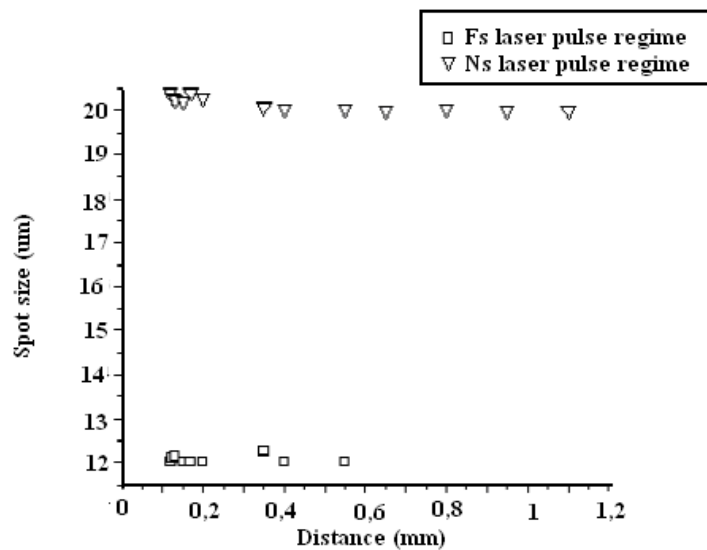
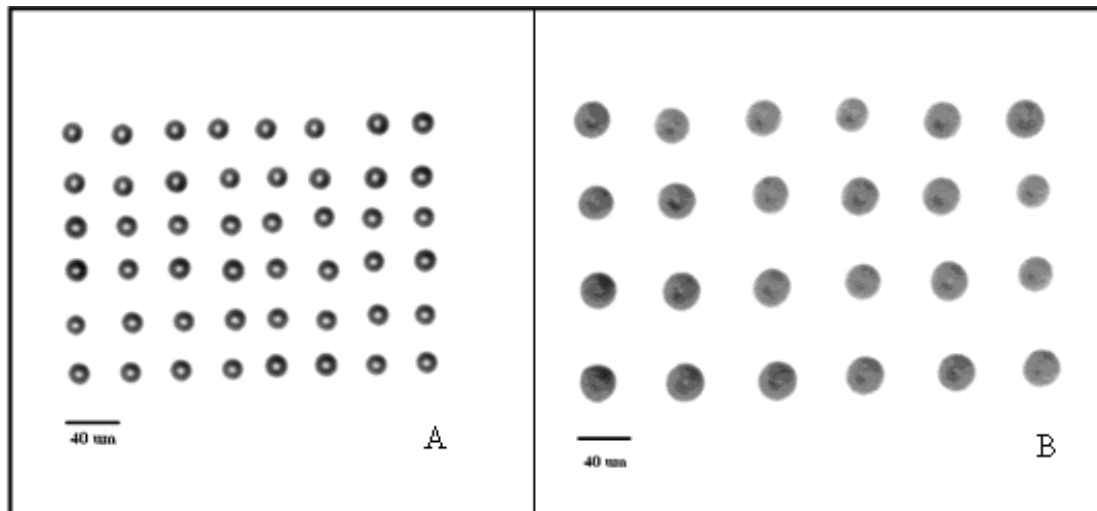


FIGURE 1: Dependence of the spot size of the droplet and the target-substrate distance

### 5.1.2 Laser pulse duration

In order to study this dependence between the receiving droplet's spot size and the laser pulse duration that we notice from the above fig.1, we kept constant the distance between the target and the substrate at 450mm and the thickness of the glycerol/ PBS target was again approximately 3µm. The results presented in the fig. 2 below, that was taken by using an optical microscope.



*FIGURE 2: (A) Optical microscope image of glycerol and PBS pattern on glass substrate obtained by using a fs laser based system, (B) Optical microscope images of glycerol and PBS pattern on glass substrate obtained by a ns laser based system*

The obvious inference from the two pictures of the above fig. 2 is that the receiving droplet's spot size is bigger when a ns laser based system is used, than when a fs laser based system is used. This experimental result is in agreement with the theory about the thermal effects which are produced at the target's surface when the laser pulse radiates it, as it was described at chapter 1, at the description of the interaction of the laser radiation with the material.

### **5.1.3 Distance between target-substrate**

After the previous study about the dependence between the spot size and the target-substrate distance, in this second part of the optimization of the process, follows the study between the receiving droplet's spot size and the laser energy by using again the ns and the fs L.I.F.T systems. The distance between the target and the substrate was kept constant at 450mm and the thickness of the glycerol/ PBS target was approximately 3 $\mu$ m.

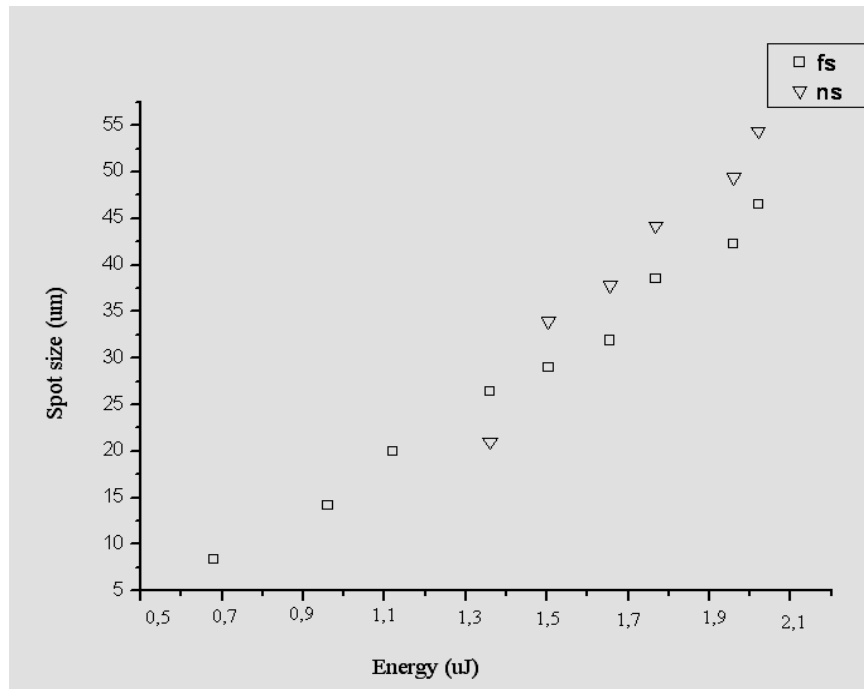


FIGURE 3: Spot size dependence on the laser energy for femtosecond and nanosecond lasers

As it is presented above in Fig.3, by using both laser systems, the dependence between the receiving droplet's spot size and the laser energy is that by using higher energies the droplet's spot size is getting bigger, that conclusion is again in agreement with the theory about the thermal effects, cause by using higher energies, more material will be radiated, so more material will be transferred at the substrate, so as a result the receiving droplet's spot size will get bigger.

#### 5.1.4 Film Thickness

The last parameter that was studied is the film thickness of the target. Both laser based systems were used as in the previous studies, and in this part we examine the energy threshold dependence on the thickness of the target's film. Finally it was studied the receiving droplet's spot size dependence on the thickness of the film too. The results are presented at the figure 4 that follows.

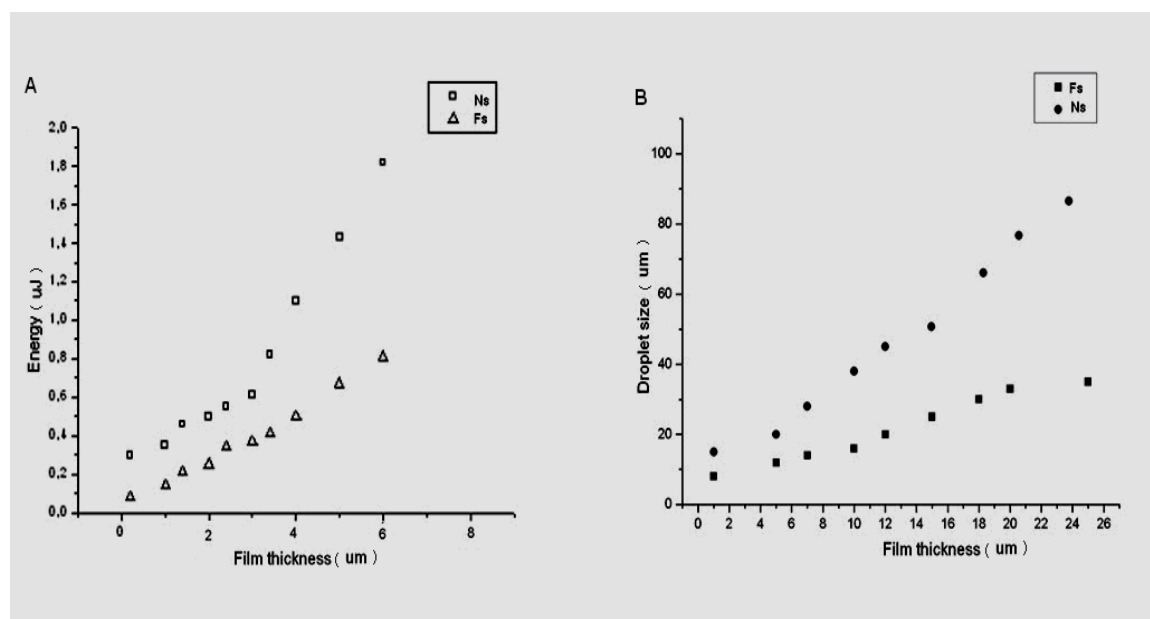


FIGURE 4: (A) Threshold energy dependence on the thickness of the film; (B) Droplet size dependence on the thickness of the film

The dependence between the laser energy and the film thickness (Fig. 4.a) is that by using thicker target's films we need to use higher energies in to transfer the material and the droplet's spot size is getting bigger since the target's film is getting thicker (Fig 4.b), that is a logical result, since we will have more material to transfer when we will use thicker target's film, so bigger droplet's spot size.

## 5.2 Apply the optimized conditions to transfer peptides, alginate gel, cells

### 5.2.1 Two dimensional (2D) Deposition of self-assembled peptides fibrils

In this part, is presented a nanosecond Laser-Induced Forward Transfer, for the generation of high density peptide arrays and patterns on modified glass surfaces. It is shown that peptide-based microarrays can be fabricated on solid surfaces and specifically recognized by appropriate fluorescent tags, with the transfer not affecting the ability of the peptides to form fibrils. These results are poised to the construction of larger peptide patterns as scaffolds for the incorporation and display of ligands critical for cell attachment and growth, or for the templating of inorganic materials. The peptides used in this study were self-assembled octapeptides derived from sequences of a natural fibrous protein, the adenovirus fiber, as described previously in chapter 3<sup>1</sup>.

The aqueous peptide solution (1 mg/ml) was spread on quartz coated with 10 nm gold thin layer (BALTEC SCD 050 Sputter Coater) film and used as a target. The liquid film thickness, estimated through the measurement of the film weight, was approximately ~10nm. Gold-coated glass slides prepared as above mentioned were used as receiving substrates.

The gold-coated quartz targets and the receiving surfaces were sterilized with UV lamp irradiation before use. The peptide concentration was kept constant for all experiments (1 mg/ml). The fibrils that the peptides are forming are shown at the Figures 5, 6 below, that were taken by using SEM and TEM microscopes that were described in appendix.

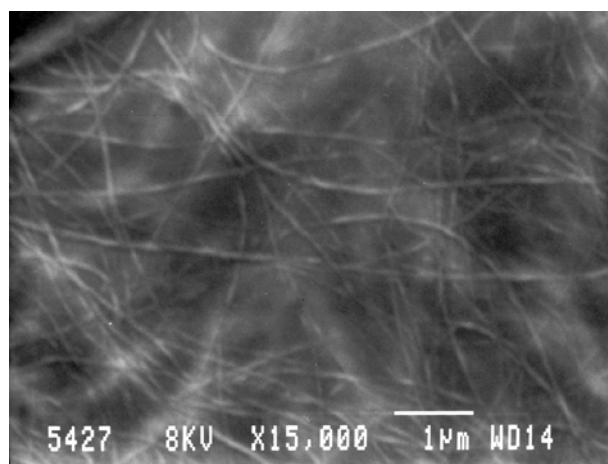


*FIGURE 5: SEM image of self-assembled octapeptides fibrils*

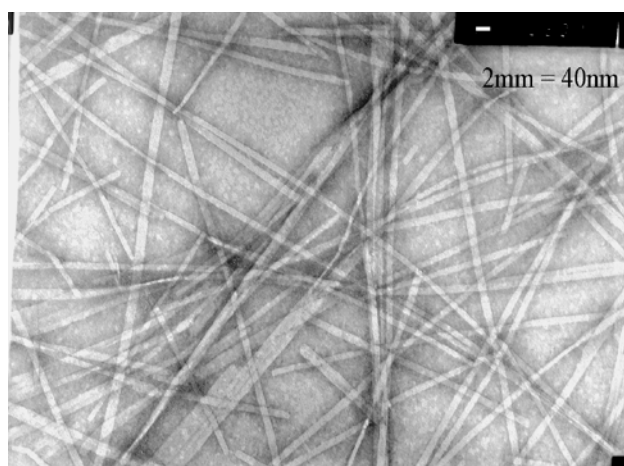


*FIGURE 6: TEM image of self-assembled octapeptides fibrils*

The laser source was a KrF excimer Lambda EMG150 ET Laser System with 15 ns pulse and a repetition rate of 1 Hz. The experimental set-up employed has been described previously in chapter 4<sup>2</sup>; in short, the pulsed UV KrF laser beam was focused through the quartz glass and onto the gold-coated quartz surface, and used to transfer microdroplets from the liquid target to the gold receiving surface. The process was performed in air and at room temperature.

The laser energy was varied from 10 to 40 mJ per pulse. The distance between the receiving surface and the target was kept constant at 500 mm. A xyz translation stage was used to allow the precise translation of the donor–receptor system in respect to the laser beam. A single laser pulse was used to transfer one droplet of solution from the target to the substrate, and the transferred arrays were visualized using optical and scanning electron microscopy.

### 5.2.1.1 T-Thioflavin and Congo Red staining

Two well-established diagnostic tests that use Thioflavin T and Congo Red solutions were used for the visualization of the amyloid fibrils transferred in the microarrays. Congo Red binds to fibrils and gives gold/green birefringence under crossed polarization, while Thioflavin T, when bound to fibrils, gives blue colour in fluorescence microscopy (emission wavelength at 485 nm after excitation at 440 nm)<sup>3</sup>. To avoid the formation of Congo Red crystallites, a mixture of water and ethanol (9:1) was used as solvent. The peptides were obtained from Eurogentec; all the other reagents were obtained from Sigma–Aldrich. The transferred patterns were analyzed using a Leica optical microscope (5\* to 100\*). After incubation with the fluorescence labeling solution, the samples were rinsed with distilled water and their fluorescence was detected using a Zeiss fluorescence microscope equipped with a Laser Scanning System Radiance 2100 (400–700 nm) and a Carl Zeiss Axio Camera HR.

### 5.2.1.2 Peptide patterns

During LIFT, a single laser pulse is used to transfer a small quantity of the liquid film target to the receiving substrate. The transferred material has the form of a droplet and its size is related to the focused laser beam diameter and the film thickness, as it was shown before at the parameter study. The mechanism of the peptide transfer with respect to the laser–target interaction can be described as following: Firstly, the incident laser energy interacts with the absorption gold layer on the target. At low intensities, the process relates to a simple excitation of the metal layer, with low thermal effects and only minor perturbation of the target<sup>4,5</sup>. For sufficient laser energies, the absorption layer acts as an energy conversion material; the energy absorbed is transformed into heat and the liquid that is in contact with the metallic layer is “forwarded” towards the substrate.

Small quantities related to the laser beam dimension from the viscous solution are transferred to the receiving glass substrate as droplets. The transfer is possible for distances longer than 1 mm<sup>2</sup>. The size and the shape of the transferred patterns depend on the laser pulse energy; for low, close to the threshold energy, the transfer is uniform with no splashes.

This can be explained by the transferred material travelling velocity; as the speed of expelled material is low, the impact with the substrate is not strong and the transfer is uniform<sup>6</sup>. The threshold energy for the 10 mm thick films used in this work was found to be 2.5 mJ. The droplet size was varied between 20 and 150 mm. The larger spots were obtained in order to allow a better observation of the peptide fibril formation during drying. As shown in Fig. 7, well-defined patterns of peptides on gold-coated glass were obtained. Figs. 8 and 9 compare ordinary spotting with laser transfer and show that peptide functionality was not affected by the laser transfer process. The control experiments were done by ordinary spotting of the peptide solution on the gold surface and dried (Fig. 5A for Congo Red and Fig. 6A for Thioflavin staining).

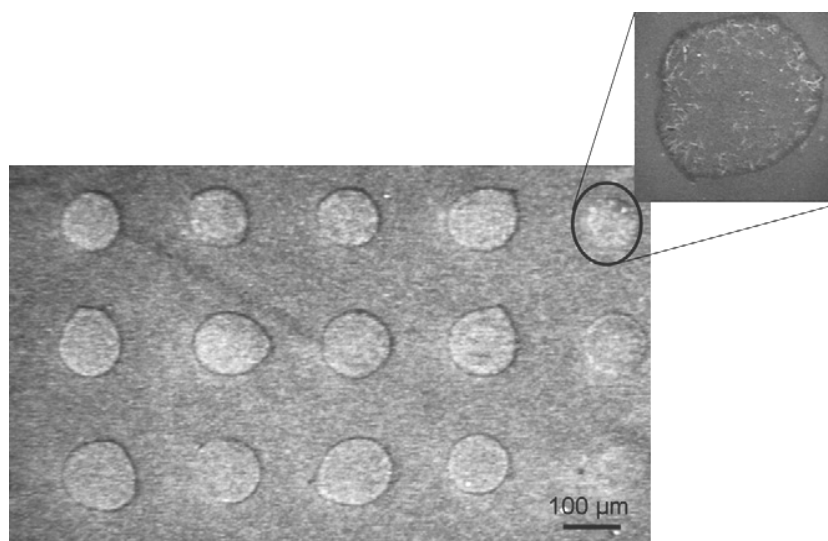


*FIGURE 7: Scanning electron microscopy image of printed peptide micro-array using LIFT.*

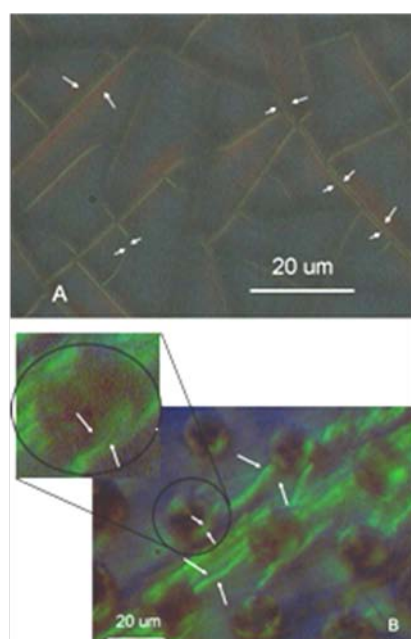


*FIGURE 8: Inverted microscope image of the control (A), where large fibrils can be seen by staining with Congo Red; inverted microscope image of the LIFT fabricated array of peptides (B), the peptides are absorbed nonspecifically on the surface and form fibrils not only in the spot area; this can be explained by the effect of not blocking the array with Bovine Serum Albumin after transfer. The presence of birefringence is a proof of the presence of the self-assembled peptides.*

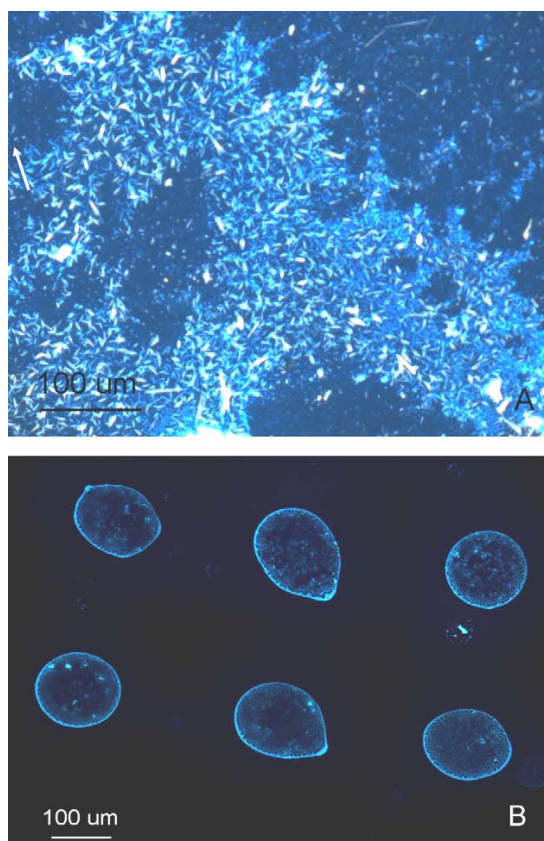


*FIGURE 9: Fluorescence microscopy image of the control (A) and of six Thioflavin stained peptides droplets on gold surface (B). The presence of fibrils inside the spot can be seen through the blue colour given by Thioflavin. (For interpretation of the references to colour in this figure legend, the reader is referred to the web version of the article.)*

As shown by the fluorescence Thioflavin (Fig. 9B) and Congo Red (Fig. 11B) staining assay, the formation of the peptide fibrils occurs for both kinds of spots, which proves that the transfer by laser did not affect the fibril integrity and/or formation process. A generally accepted model for amyloid fibril formation *in vitro*<sup>7</sup> is the following: First, monomers self-associate into protofibrils via a nucleation and/or seeding process depending on the solution concentration. For the range of concentrations that we have used (1 mg/ml) the peptide self-assembles to form nuclei, which initiate further the aggregation of the protofibrils. The second step involves the interaction of the protofibrils with each other to form fibrils. The fibril elongation occurs by irreversible binding of the monomers to the fibril ends. pH, temperature and humidity are also important conditions for the process of fibril rearranging. These structures are composed of beta-sheets, which are held together mainly by hydrogen bonding.

In this study, when the samples were prepared in a pH 6 aqueous solution and let to dry in air, the adsorbed peptides took the form of flat and elongated aggregates up to 10 mm long and 2 mm thick. When the samples were kept in humidity chamber and the drying process was slower, the formed tapes were smaller (Fig. 10A and B).

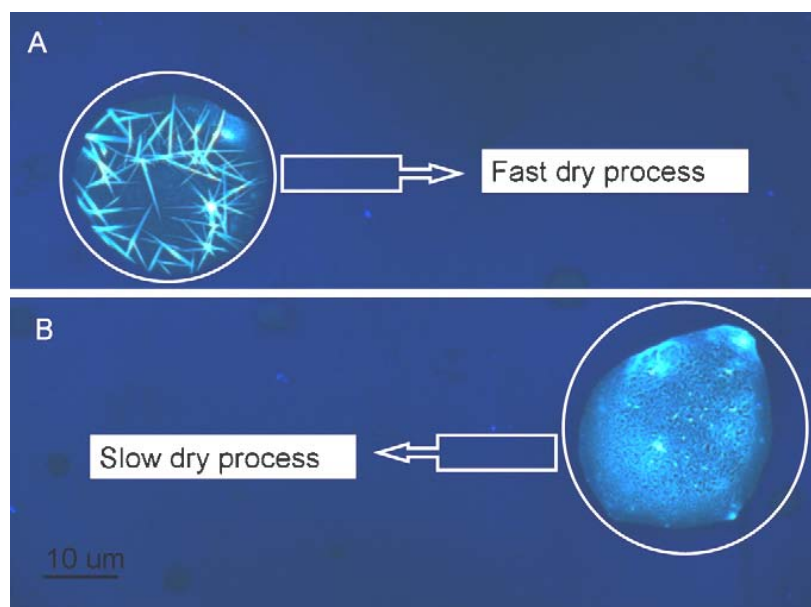


**FIGURE 10:** Fluorescence microscopy image of Thioflavin-stained peptide droplets on gold surface (A) when the samples is left to be dried in air at room temperature after deposition. The presence of flat and elongated aggregates as 10–20 mm long and 2 mm thick tapes can be noticed through the blue colour given by Thioflavin. Fluorescence Microscopy image of the adsorbed peptides for a slow drying process (B). The presence of flat and elongated aggregates (5–10 mm long, 0.7–1 mm thick) can be observed inside the spot.

### 5.2.1.3 Conclusions

In this work we have demonstrated that LIFT can be used for the fabrication of peptide microarrays, and the transfer process does not influence the peptide fibril self assembly process and/ or fibril stability at the solid/solution interface. Peptides as self-assembling materials have enormous potential in a variety of applications, from tissue engineering to molecular electronics<sup>8-12</sup>. By combining the directional deposition of the peptides on specific positions and different surfaces by LIFT, and by their sequence manipulation, it is possible to enable the specific fabrication of a huge number of different structures that can be developed for many important applications, including tissue repair, patterning, miniaturized solar cells, and optical and electronic devices<sup>13</sup>.

We also study the influence of different pH concentration of the solution that was used for the film at target surface (figure 11).

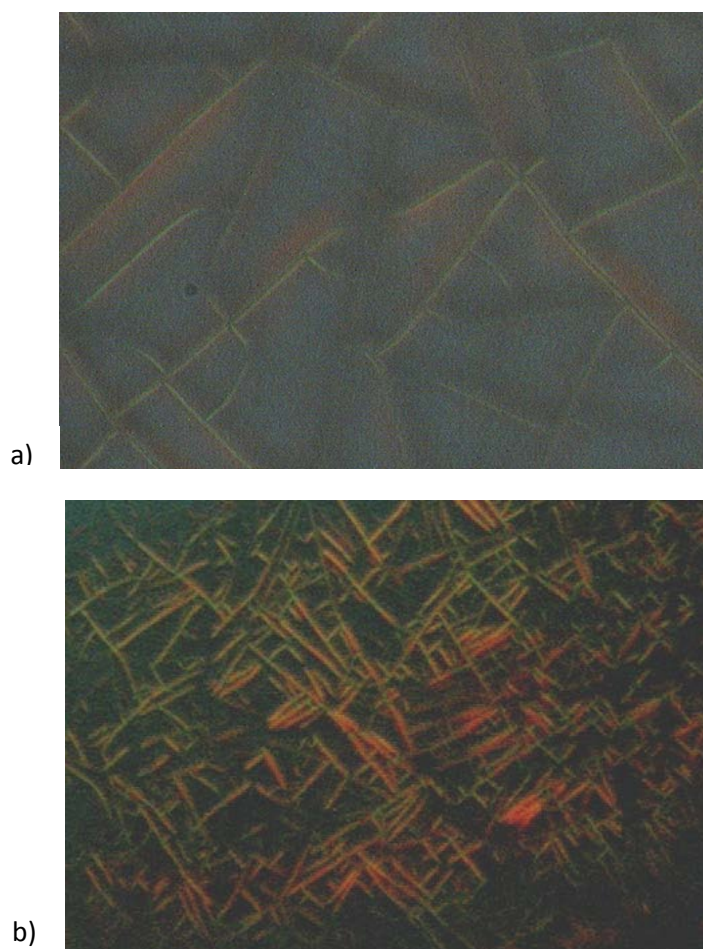


*FIGURE 11: Congo Red staining image of self-assembled octapeptides fibrils (a) in water and (b) in solution pH4*

### **5.2.2 Fabrication of amyloid peptide micro-arrays using laser-induced forward transfer and avidin-biotin mediated assembly**

The methodology presented in this part of this thesis, is based on the direct printing of photosensitive biotin (photobiotin) on ormocer substrate using L.I.F.T. technique, and exploits thiol chemistry of cysteine-containing, self-assembled peptide fibrils. Ormocer, as it has been explained in chapter 3, is an organically modified ceramic, on which photobiotin can be irreversibly attached when exposed to UV light from a laser or a lamp. However the technique is not limited to ormocer; photobiotin can be photolytically attached on a variety of organic and inorganic materials such as silicon, glass and PDMS; this gives this methodology

a large flexibility and applicability. Once biotin has been immobilized on ormoer, then it is first incubated with avidin and subsequently with an iodoacetamide-functionalized biotin, N-(biotinoyl)-N'-(iodoacetyl) ethylenediamine. Finally the samples are immersed in an aqueous solution of peptides that have been functionalized with a cysteine aminoacid. The assembly of the peptide fibrils on the photobiotin spots is initiated through the controlled evaporation of the water. However, in order for this to occur there is a seed, or “anchoring point”, required. This is provided by the bonding between the iodoacetamide group in the biotin derivative and the thiol group in the cysteine. By combining peptide self-assembling characteristics and chemistry with LIFT, new designs in the assembly of more complex topologies using fibers as building blocks, and the decoration of the assembled materials with functional moieties can be produced.

The material used as a substrate is plain glass coated with the organic-inorganic hybrid ormoer (Micro Resist Technology). Ormoer contains a highly crosslinkable organic network as well as inorganic components leading to high optical quality and mechanical as well as thermal stability. The substrates used for experiments were sterilized before use for at least 1h in UV. Photobiotin (100 µg/ml, Sigma Aldrich) solution, Avidin (100 µg/ml, Sigma Aldrich) solution and N-(biotinoyl)-N'-(iodoacetyl) ethylenediamine (100 µg/ml, Molecular Probes) solution were used for the functionalization of Ormoer. In this work we used an octapeptide with the following sequence: NCGAITIG (Arginine-Cysteine-Glycine- Alanine Isoleucine-Threonine-Isoleucine-Glycine). This peptide is a cysteine variant of the peptide NSGAITIG that self-assembles into amyloid-type fibrils in solution. The peptide was purchased from Eurogentec (Belgium) and had a degree of purity higher than 95%. Peptide solutions in double distilled (dd) water at a concentration of 2 mg/ml and aged for 12 days were used for the experiments.

The L.I.F.T. experimental set-up has been described before in chapter 4. Single pulses from KrF laser (248 nm, excimer Lambda EMG150 ET Laser System 15 ns, 1 Hz repetition rate) were used to carry out the LIFT experiments. The centre of the beam size laser output illuminated a slit mask in order to obtain an approximately uniform profile and the aperture was imaged onto the underside of the target interface using a 25x microscope objective (N.A = 0.4). The average incident fluence was  $10 \text{ J} \cdot \text{cm}^{-2}$ . During the deposition process the target area was viewed through a CCD camera. The photobiotin was dissolved in de-ionized water and the solutions were spread on a 10 nm thick gold film covered quartz plates previously sterilized for 1h in UV. For the preparation of films with 3 µm thickness, 10 µl solutions were used. The transferred material was collected on a substrate placed at 100 µm to and parallel to the donor target surface, xyz translation stages allowed precise control of the translation of the donor-receptor system in respect to the laser beam. All L .I.F.T. experiments were performed in air and at room temperature.

### **5.2.2.1 Characterization of the patterns by using transmission electron microscopy (TEM)**

The peptide solutions were diluted to a final concentration of 0.6 mg/ml in dd water and 8  $\mu$ l were placed on a 300 mesh formvar-coated copper grid. After 2 minutes excess fluid was removed with a filter paper and the samples were negatively stained with 8  $\mu$ l of 1% uranyl acetate for 2 minutes. They were subsequently observed with a JEOL JEM-100C microscope operating at 80kV.

### **5.2.2.2 Characterization of the pattern by using scanning electron microscopy (SEM)**

Samples were covered with 10 nm gold using the sputtering technique and were observed with a JSM-840 SEM microscope operating at 5 kV.

### **5.2.2.3 Characterization of the pattern by using thioflavin T solution and fluorescent microscope**

Thioflavin T (5  $\mu$ M dye solution, Sigma) freshly prepared solutions were used for visualization of the amyloid fibrils with fluorescence. After incubation with Thioflavin T the samples were rinsed with double-distilled water. Fluorescence was detected using a Zeiss fluorescence microscope equipped with a Laser Scanning System Radiance 2100 (400-700 nm) and with a Carl Zeiss Axio Camera HR.

### **5.2.2.4 Peptide assembly**

The process of functionalization of ormocer for peptide fibril growth is illustrated in Fig. 1. Firstly an array of photobiotin spots was deposited on the ormocer surface using LIFT. When this array was exposed to UV light (Fig. 12a), it was immobilized irreversibly on the ormocer surface. Photobiotin has a wide area of applications in patterning proteins, ligands, and other species onto solid substrates or for nonspecific labeling of proteins, DNA and RNA probes or other molecules due to its composition: biotinyl group, a linker group and the photoactivatable part: the nitrophenyl azide group. When the epoxy rings on Ormocer are opened, photobiotin can bind to the ionized oxygen and carbon atoms when exposed to UV light and also the aryl azide groups of biotin are converted to an aryl nitrene, which is extremely reactive. The samples were washed thoroughly and they are subsequently functionalized further with avidin (Fig. 12b). Biotin has an extremely high affinity for avidin; their interaction occurs rapidly and is the strongest non-covalent interaction known in nature. These characteristics are the main factors for the functionalization of the Ormocer structures and further binding of N-(biotinoyl)-N'-(iodoacetyl) ethylenediamine (Fig. 12c).

The photobiotin - avidin functionalized Ormocer substrates were subsequently incubated with N-(biotinoyl)-N'-(iodoacetyl) ethylenediamine for 40 minutes in the dark at room temperature and were washed three times with dd water. The final step was the attachment of the peptide fibrils on the functionalized surfaces (Fig. 12d); this was achieved through the thiol group of the peptide, which reacted with the biotin-conjugated iodoacetamide group. The peptide solutions were incubated on the Ormocer substrates for 40 minutes at room temperature. A thin layer of peptides formed on the structures; this layer acted as an “anchoring point”, which triggered the further assembly of the peptide nanostructured fibrils. The samples were subsequently washed a first time by leaving dd water on the sample for 3-5 minutes, and then followed by two more washes.

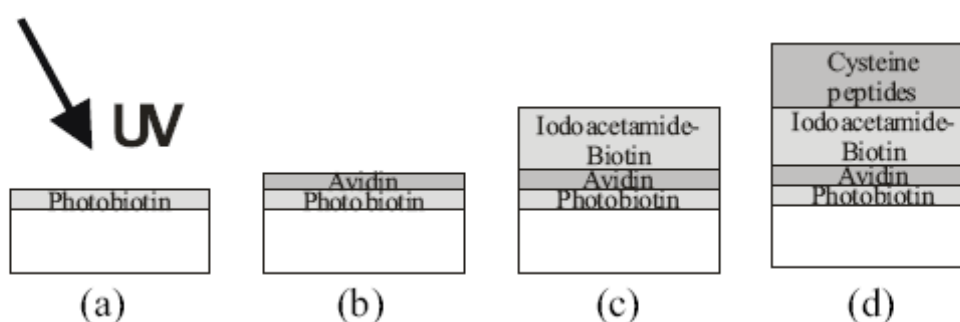
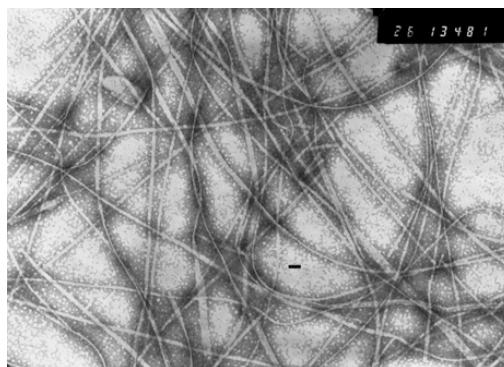


FIGURE 12: Functionalization of Ormocer for peptide fibril deposition. A thin layer of photobiotin is deposited on the Ormocer surface and exposed to UV light (a) before being further functionalized, further with avidin (b) and iodoacetamide-functionalized biotin (c). The final step is the attachment of the cysteine-containing peptide through the SH iodoacetamide reaction (d).

The ability of the cysteine containing peptide to form amyloid-type fibrils in solution was confirmed using all the structural criteria that apply to amyloid fibril structural characterization. A TEM image of the solution used for attachment to the functionalized structures is shown in Fig. 13.

Figure 14 shows the Scanning Electron Microscope (SEM) images of some of the spots obtained using LIFT. As mentioned earlier, arrays of photobiotin were first printed on Ormocer and they were subsequently functionalized with the appropriate biomolecules. Then they were immersed in a peptide solution; as the solution dried, the arrays of fibrils formed. These arrays form everywhere but when the sample was washed, they only remained immobilized on the functionalized locations. In Fig. 14a, an array of peptide fibril spots is shown. The fibrils have assembled only on the locations where photobiotin was immobilized with LIFT. In Fig. 14b, the magnified detail of one of the spots is shown. The first layer of immobilized peptides is clearly visible; then the fibrils further grow on it.



*FIGURE 13: TEM image of amyloid-type fibrils formed by the cysteine containing peptide in solution (CNGAITIG, bar 190 nm).*

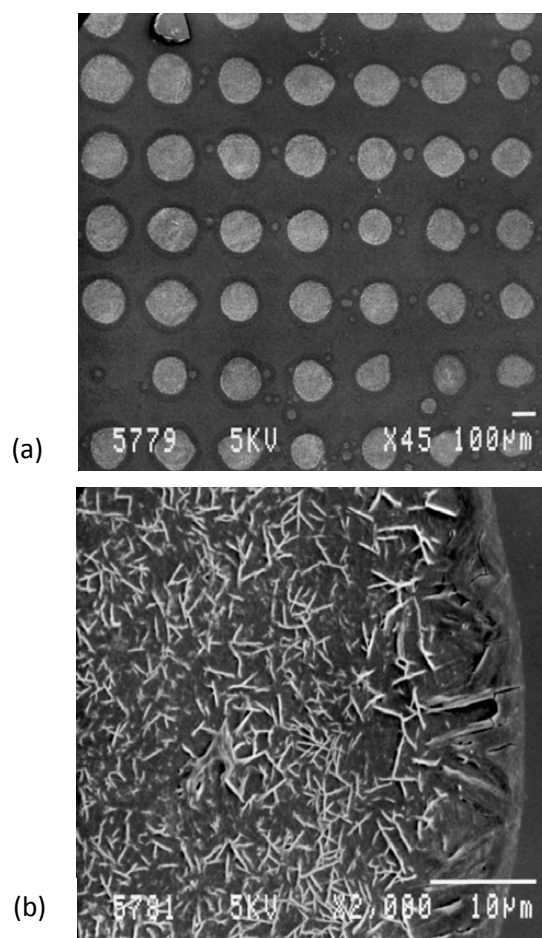


*FIGURE 14: SEM images of a peptide micro-array (a) and detail of a spot (b).*

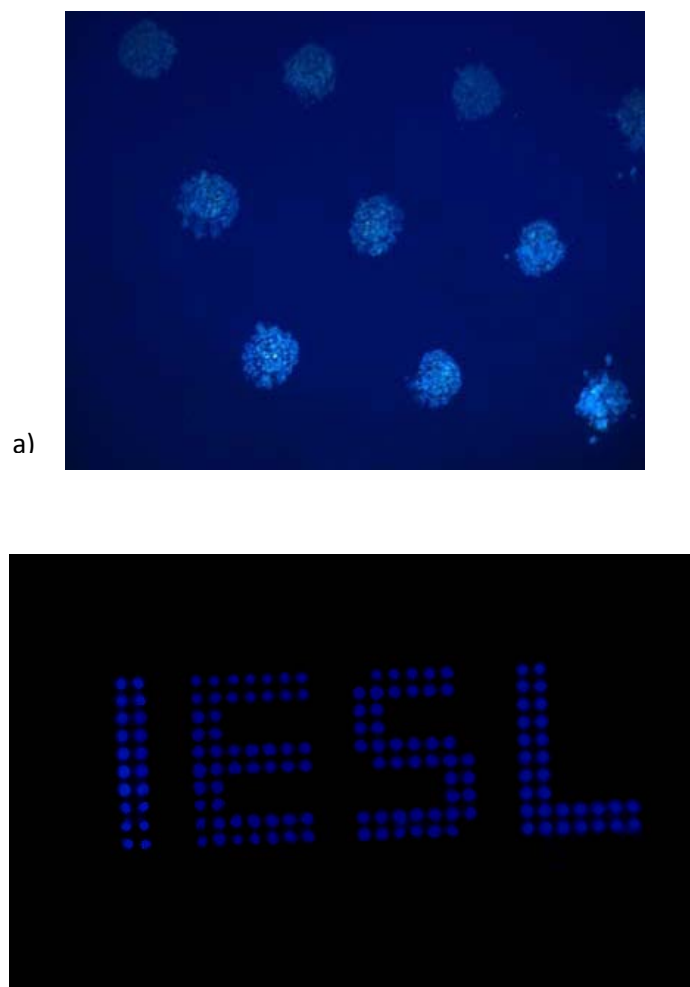


*FIGURE 15: Fluorescence images of (a) peptide micro-array and (b) peptide pattern written I.E.S.L.*

To conclude, we have demonstrated a new method for the controlled self-assembly of peptide micro-arrays. The method is based on biotin-avidin and thiol chemistry and ormoer is used as a substrate. However, as photobiotin can be easily attached to a variety of materials, this technique is suitable for a variety of applications, from molecular electronics to biosensors and tissue engineering.

### **5.2.3 Three dimensional (3D) Deposition of Alginate gel**

#### **5.2.3.1 Materials**

Solutions of sodium alginate's different concentrations were dissolved in water and glycerol was added to the solution in order an alginate gel to be formed (figure 16). This gel like solution (1 mg/ml) was spread on quartz coated with 20 nm gold thin layer (BALTEC SCD 050 Sputter Coater) film and used as a target.

The liquid film thickness, estimated through the measurement of the film weight, was approximately ~10mm. Glass slides were used as receiving substrates.

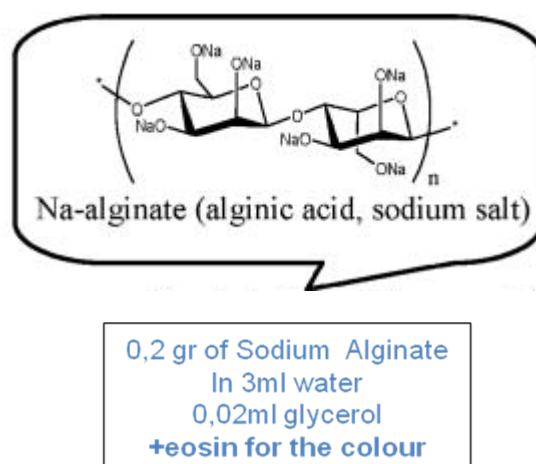


FIGURE 16: Preparation of Sodium Alginate gel

As it was described at the previous chapter 3, when the sodium alginate solution reacts with a calcium chloride or calcium acetate solution, the calcium alginate gel produced which during the drying process it becomes solid, due the chemical formula which is shown at the figure 17 below:

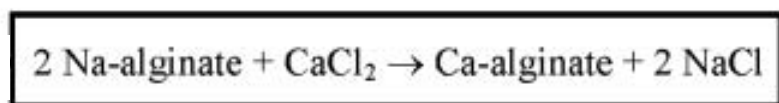


FIGURE 17: Chemical reaction of sodium alginate gel like solution and aqueous calcium chloride solution

For the purpose of making calcium alginate gel structures, we prepared solutions of calcium chloride or calcium acetate (figure 18) in order to transfer them on the substrate's surface where it has already been transferred the sodium alginate gel.



FIGURE 18: Calcium chloride or calcium acetate solutions

As it is shown at the fig. 18 above, Xanthan is added at the solutions. Xanthan is a polysaccharide which has the capability of producing a large increase in the viscosity of a liquid, for this reason is used in this study in order to make our solutions more gel like.

### 5.2.3.2 Construction of 3D structures of calcium alginate gel

The mechanism of the alginate transfer with respect to the laser–target interaction can be described as following: Firstly, the laser energy interacts with the absorption gold layer on the target. Small quantities related to the laser beam dimension from the viscous solution are transferred to the receiving glass substrate as droplets. The transfer is possible for distances longer than 1 mm, the same distances that were used as before at the peptides transfer. The size and the shape of the transferred patterns depend on the laser pulse energy; for low, close to the threshold energy, the transfer is uniform with no splashes. This can be explained by the transferred material travelling velocity; as the speed of expelled material is low, the impact with the substrate is not strong and the transfer is uniform. The threshold energy for the 10 mm thick films used in this work was found to be approximately 3mJ. The droplet size was varied between 200 $\mu$ m and 270 $\mu$ m. As it has been described before, after the first transfer of sodium alginate, a layer of calcium chloride or calcium acetate was transferred on it, then again a layer of sodium alginate gel was transferred on the receiving two layers, and a layer of calcium chloride or calcium acetate was transferred on it, etc. The time that needs the solution of calcium chloride or calcium acetate to dry out on the sodium alginate layer is measured, and it was found around ~7 minutes. The process was performed in air and at room temperature. The laser energy was varied from 100 to 180 mJ per pulse. The distance between the receiving surface and the target was kept constant at 500 mm. A xyz translation stage was used to allow the precise translation of the target–substrate system in respect to the laser beam. The laser that was used in this part was a model Diva laser from Thales Laser with wavelength:  $\lambda=1064$  nm, pulse duration  $\tau=8.5$  ns,  $f_{\text{rep}}=20$  Hz,  $E_{\text{max}}=20$  mJ.

#### 5.2.3.2.1 Samples presentation

We started with the simplest 3D structures, a square, the sketch of that is shown at the figure 19 above with the presentation of the dimensions of these structures, and these structures were prepared in order to measure the height of its gel layer and to see the chemical process for calcium alginate gel production. The dimension's of this structure were 12,5mm\*12,5mm.

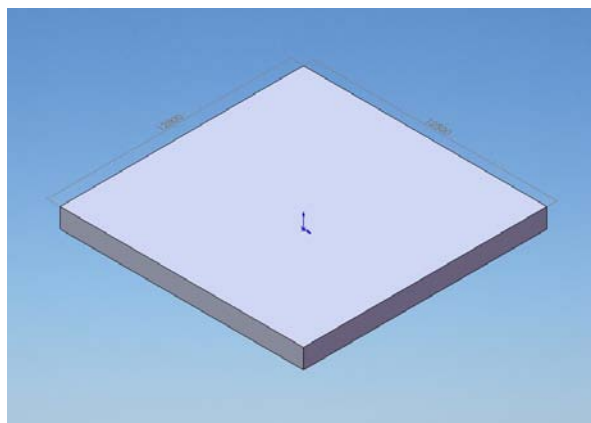


FIGURE 19: Sample's 3D sketch image

#### 5.2.3.2.1.a 3D square structures of calcium alginate gel

These 3D structures were made by transferring lines of alginate gel or calcium acetate gel one beside the other. The first structure is made of one layer of sodium alginate in order to measure the height of the one layer. The second structure was made of one layer of sodium alginate gel and one layer of calcium acetate gel, in order to measure the height of the one layer of calcium alginate gel layer.

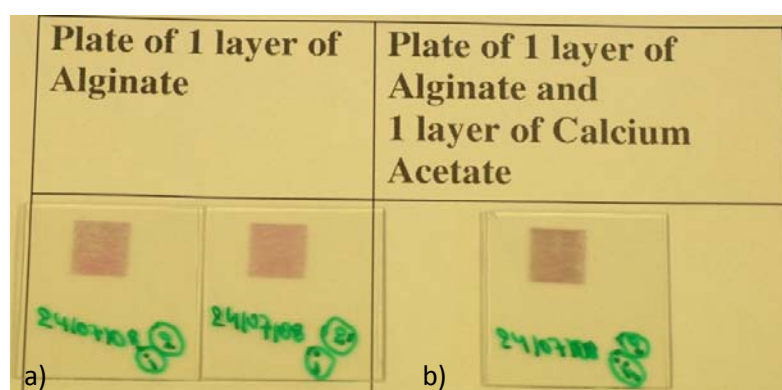


FIGURE 20: Sample's picture of a) 3D structure of one layer of sodium alginate gel, b) 3D structure of one layer of sodium alginate gel and one layer of calcium acetate

The height of the one layer of calcium alginate gel layer 3D structure was around  $3\mu\text{m}$  (Fig.21-Fig.22) and it was measured by using a confocal imaging profiler microscope.

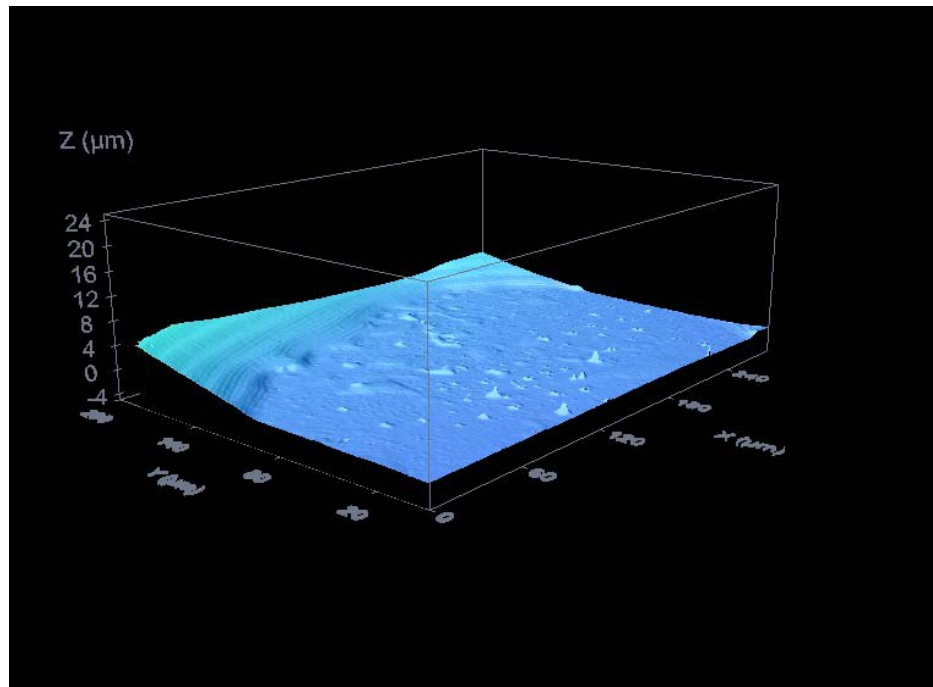


FIGURE 21: Height 3  $\mu\text{m}$  of one layer calcium alginate 3D structure

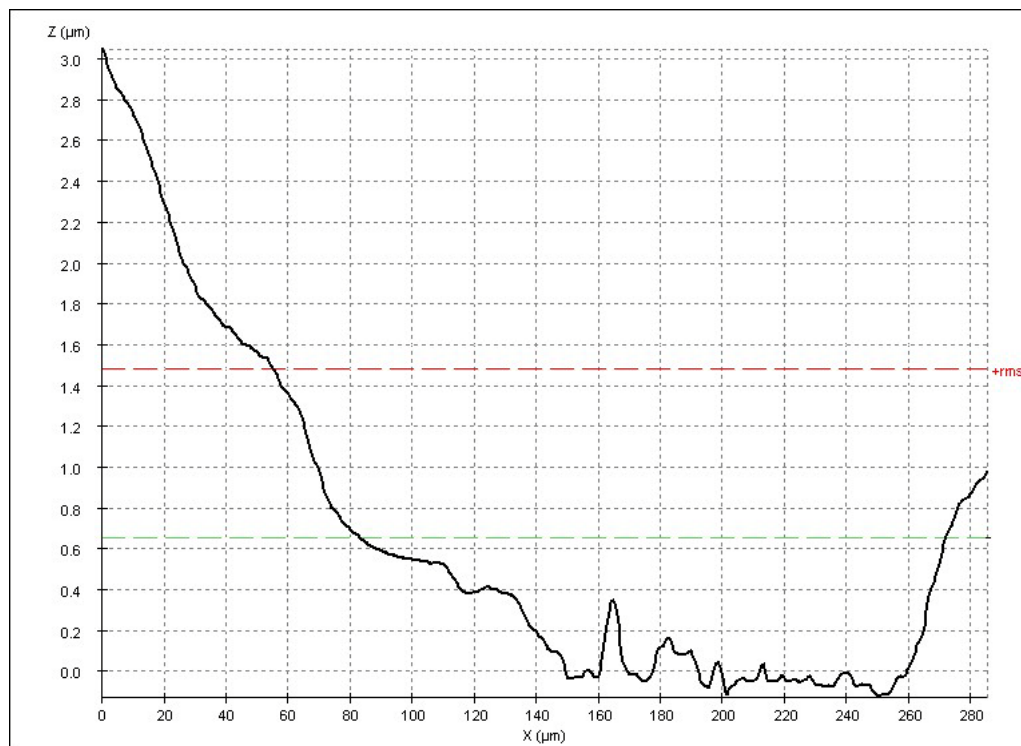
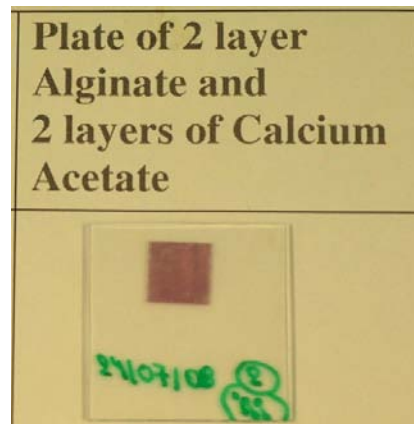


FIGURE 22: Graph of 3  $\mu\text{m}$  height of one layer calcium alginate 3D structure

Continuing on development of calcium alginate gel 3D structures with more layers, structures of two layers of sodium alginate gel and two layers of calcium acetate gel were prepared (Fig.23).



*FIGURE 23: Sample's picture of 3D structure of two layers of sodium alginate gel and two layers of calcium acetate*

The height of this 3D structure of two layers of sodium alginate gel and two layers of calcium acetate was around 9-13  $\mu\text{m}$  (Fig.24-Fig.25) and it was measured by using a confocal imaging profiler microscope again.

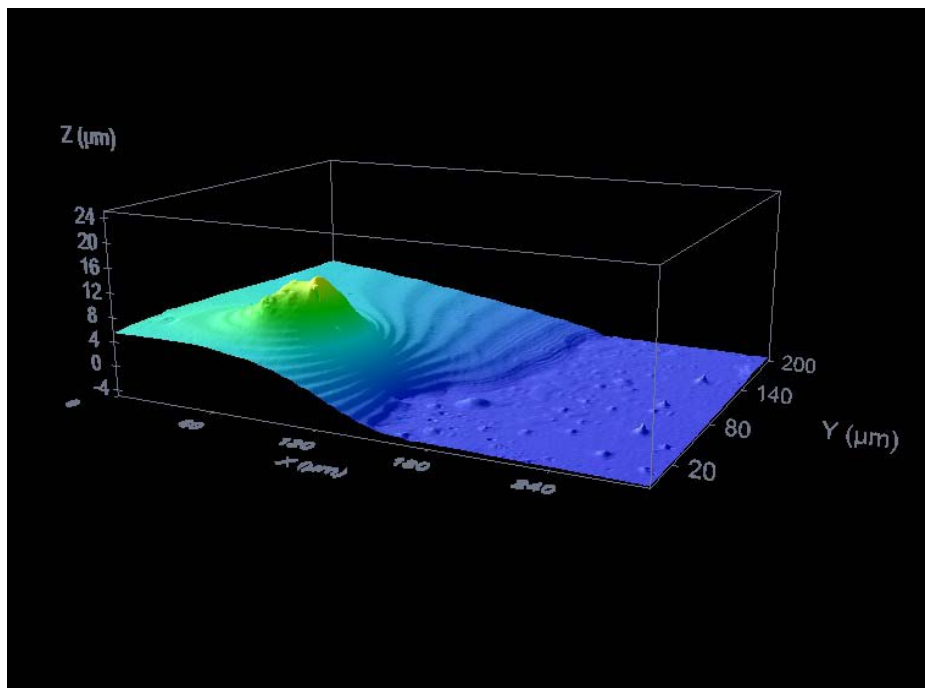


*FIGURE 24: Height 9-13  $\mu\text{m}$*

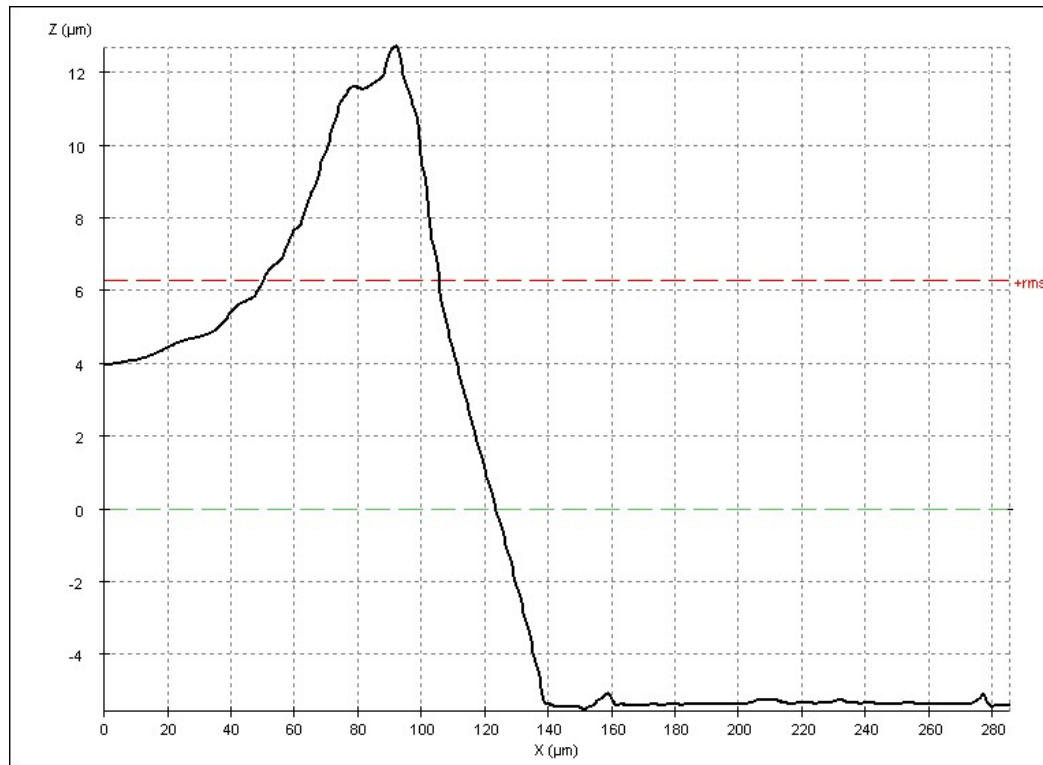


*FIGURE 25: Graph of 9-13  $\mu\text{m}$  height*

The height of the structure is approximately about 9-13  $\mu\text{m}$  and the layers of this structure are double than the ones from the previous results and we can conclude that the height of the structure now is double from the previous height, as it was expected!

#### **5.2.3.2.1.b 3D structures-Matrixes of calcium alginate gel**

The second component of calcium alginate gel built by L.I.F.T. technique is a 3D structure-matrix consisted of  $5 \times 5$  square cells array. The sketch of this 3D structure-matrix that was made is shown at the following figure 26. Each square cell had the dimensions  $2500\mu\text{m} \times 2500\mu\text{m}$  and the whole structure was  $12500\mu\text{m} \times 12500\mu\text{m}$ .

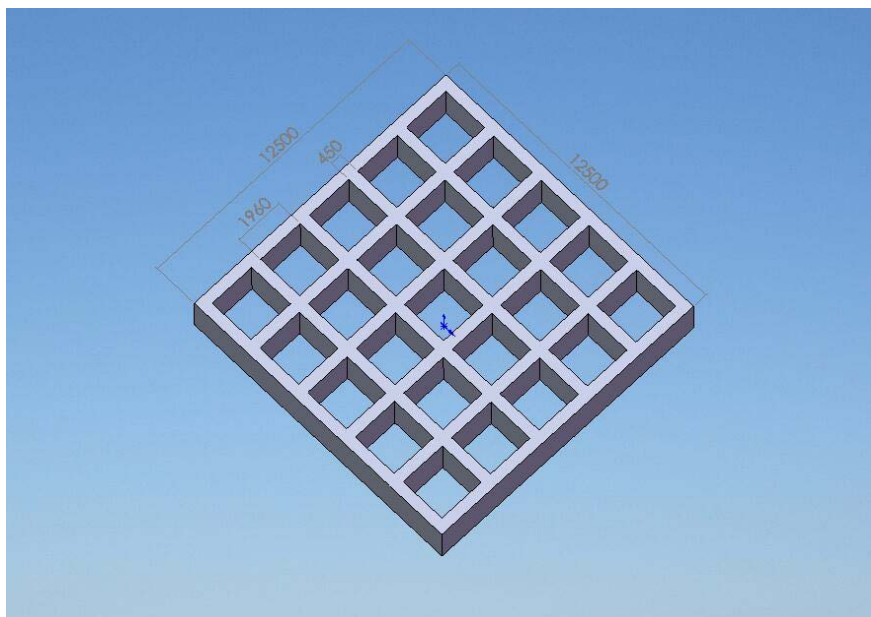


*FIGURE 26: 3D sketch of calcium alginate gel matrix*

At figure 27 below, are presented two photos, during the alginate gel's transfer, that were taken by using an optical microscope. At the first picture fig 27.a, it is shown the target film, with the material that it was removed while the laser radiation, and at the fig 27.b, it is shown the transferred material at the glass substrate.

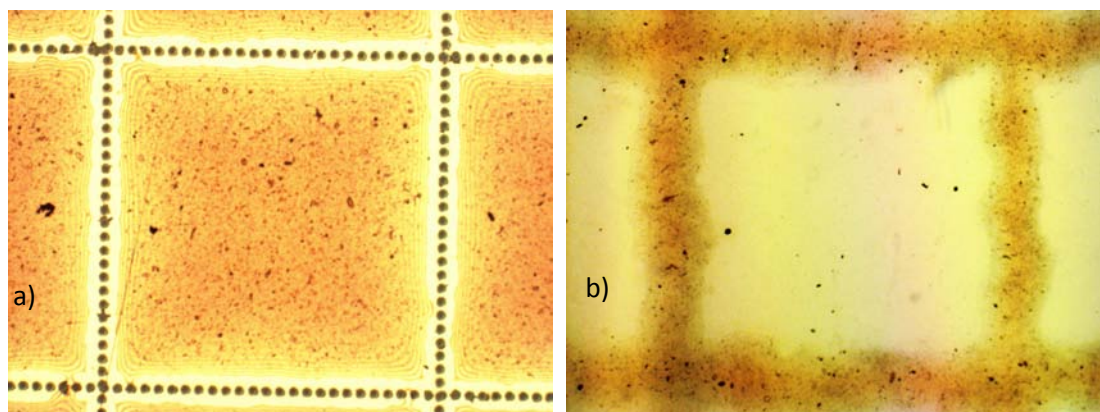


*FIGURE 27: a) target's film with the removing material, b) the receiving pattern at the glass substrate*

At the following figure 28, are presented the samples that were prepared during this study. The 3D structures-matrixes are obvious and it is clear that the intensity of the colour of these 3D structures-matrixes is getting a bit darken while we add more layers at each structure.

	1.Alginate 2.Gel	1.Gel 2.Alginate 3.Gel	1.Gel 2.Alginate 3.Gel 4.Alginate 5.Gel 6.Alginate 7.Gel	1. Gel 2.Alginate 3.Gel 4.Alginate 5.Gel 6.Alginate 7.Gel 8.Alginate 9.Gel 10.Alginate 11.Gel	1.Gel 2.Alginate 3.Gel 4.Alginate 5.Gel 6.Alginate 7.Gel 8.Alginate 9.Gel 10.Alginate 11.Gel 12.Alginate 13.Gel 14.Alginate 15.Gel 16.Alginate 17.Gel 18.Alginate 19.Gel 20.Alginate 21.Gel
Calcium Acetate					
Calcium Chloride					

FIGURE 28: All the samples with the calcium alginate gel's 3D structures-matrixes

5.2.3.2.1.b.1 3D matrix of one layer of calcium alginate gel

The first 3D matrix of calcium alginate gel, was prepared by transferring first a layer of sodium alginate and then a layer of calcium acetate. While the layer of calcium acetate is getting dried, it reacts with the sodium alginate gel layer and a 3D structure–matrix of one layer of calcium alginate gel is created (fig.29).

	1.Alginate 2.Gel
Calcium Acetate	

FIGURE 29: Sample's picture of one layer structure of calcium alginate gel made by calcium acetate's reaction with sodium alginate gel

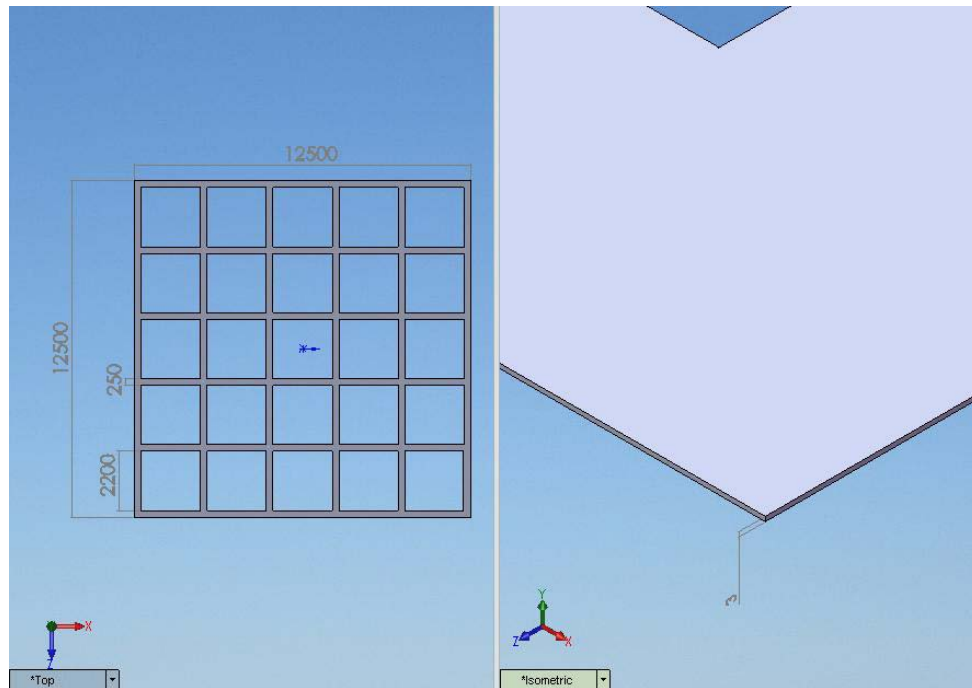


FIGURE 30: Sample's 3D sketch

For the characterization of the calcium alginate 3D structure-matrix, a confocal imaging profiler microscope was used again, in order to measure the height of the structure. For this one layer structure the height was measure around  $3\mu\text{m}$  and the width of the matrix's line was  $300\mu\text{m}$  (figures 31, 32).

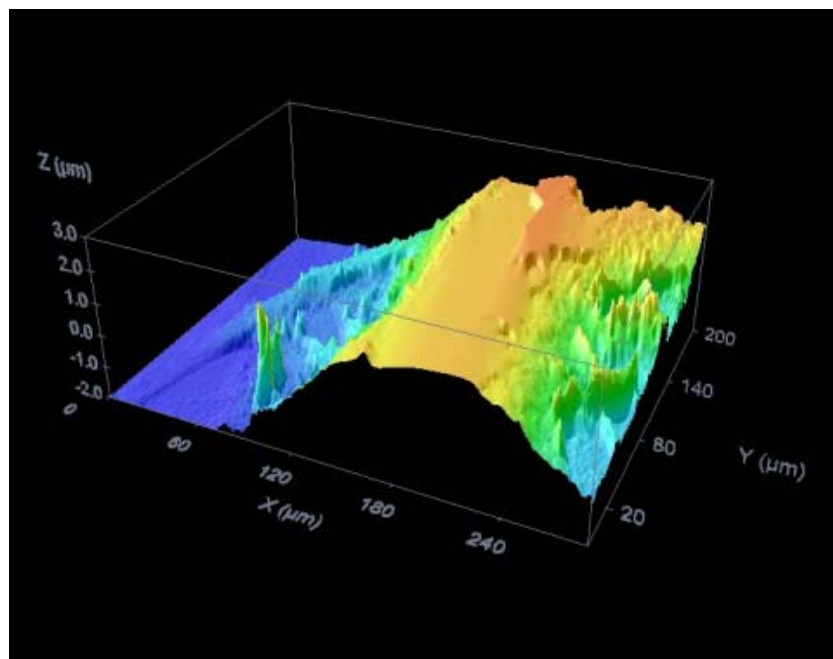


FIGURE 31: Height  $3\mu\text{m}$

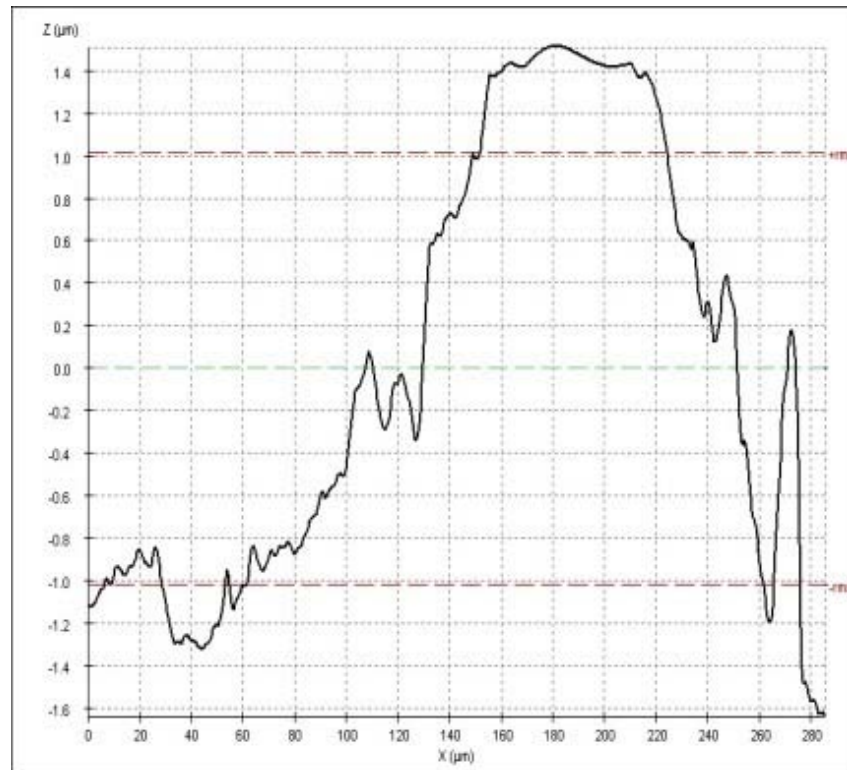


FIGURE 32: Weight 300µm

Calcium chloride solution can also react with the sodium alginate gel, in order to create calcium alginate gel, so in the following study, calcium chloride solution was transferred on sodium alginate gel (fig.33).

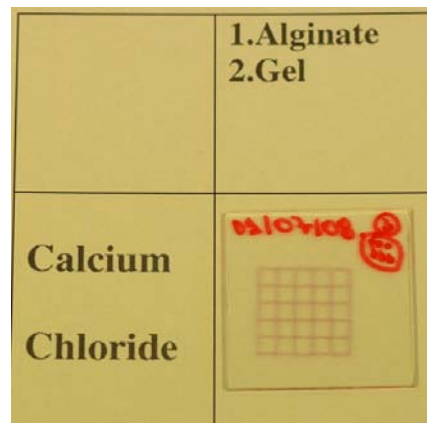


FIGURE 33: Sample's picture of one layer structure of calcium alginate gel made by calcium chloride's reaction with sodium alginate gel

As previously a confocal imaging profiler microscope was used to characterize the one layer calcium alginate gel 3D structure-matrix. The height was 3µm and the width of the matrix's line was 300µm (figures 34, 35).

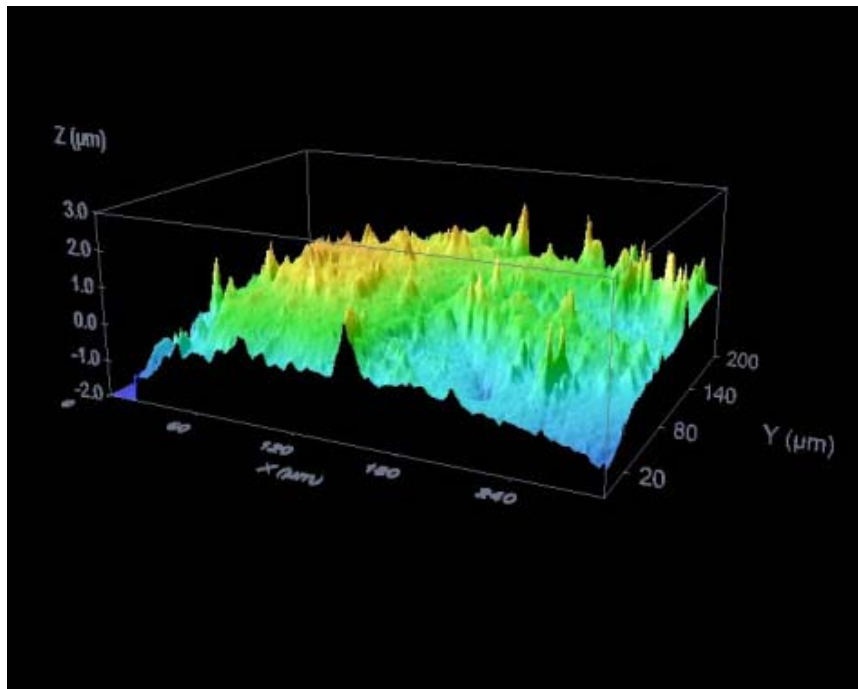


FIGURE 34: Height  $3\mu\text{m}$

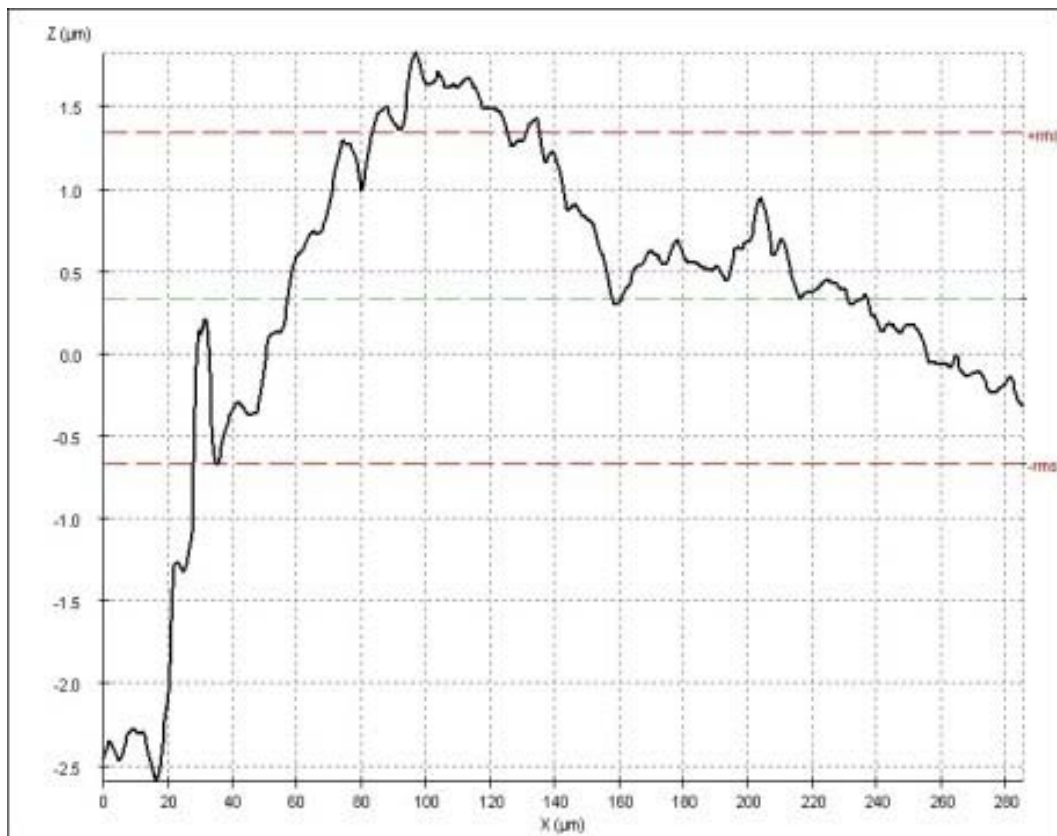
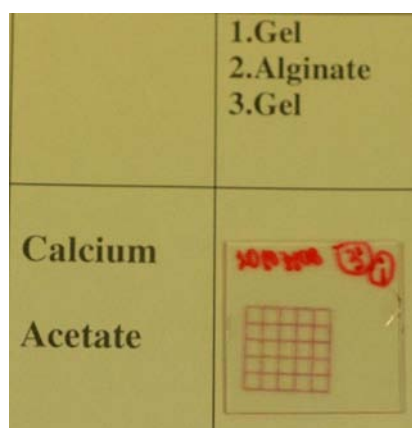


FIGURE 35: Width  $300\mu\text{m}$

As a result for the characteristics of these one layer calcium alginate gel's 3D structures, we can notice that the surface of the calcium alginate structure is more ruff when it is used the calcium chloride solution than the previous result with calcium acetate solution.

#### 5.2.3.2.1.b.2 3D matrix of one layer of alginate gel and two layers of calcium acetate or calcium chloride

We continued the deposition of alginate gel, by adding just one more layer of calcium acetate solution or calcium chloride solution as a base before the second sodium alginate gel layer, in order to measure the dimensions of this layer, and to see if the structure is getting more solid. The first 3D matrix of one layer of sodium alginate gel and two layers of calcium acetate gel picture is presented at Fig. 36 below.



*FIGURE 36: Sample's picture of a 3D structure of one layer of sodium alginate gel and two layers of calcium acetate gel*

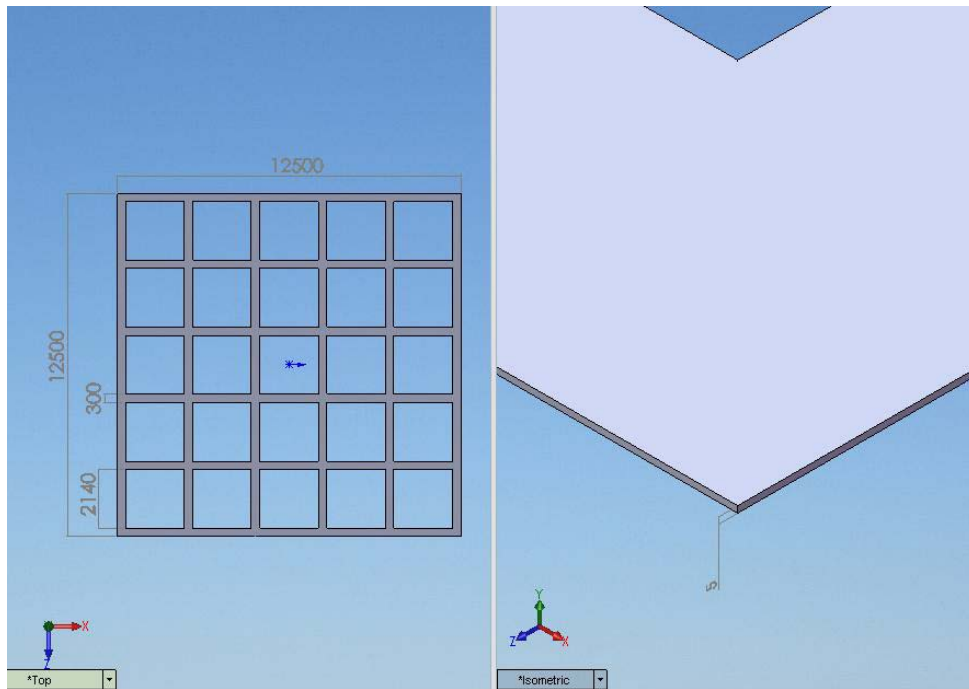


*FIGURE 37: Sample's 3D sketch*

As a result for the characterization of this 3D structure of calcium alginate gel with one layer of sodium alginate gel and two layers of calcium acetate gel: the height of the structure is 4~5 $\mu\text{m}$  and the matrix's line width is around 300 $\mu\text{m}$  again (Fig. 38-Fig. 39) and we can conclude that its layer's height is approximately around 1~2 $\mu\text{m}$ .

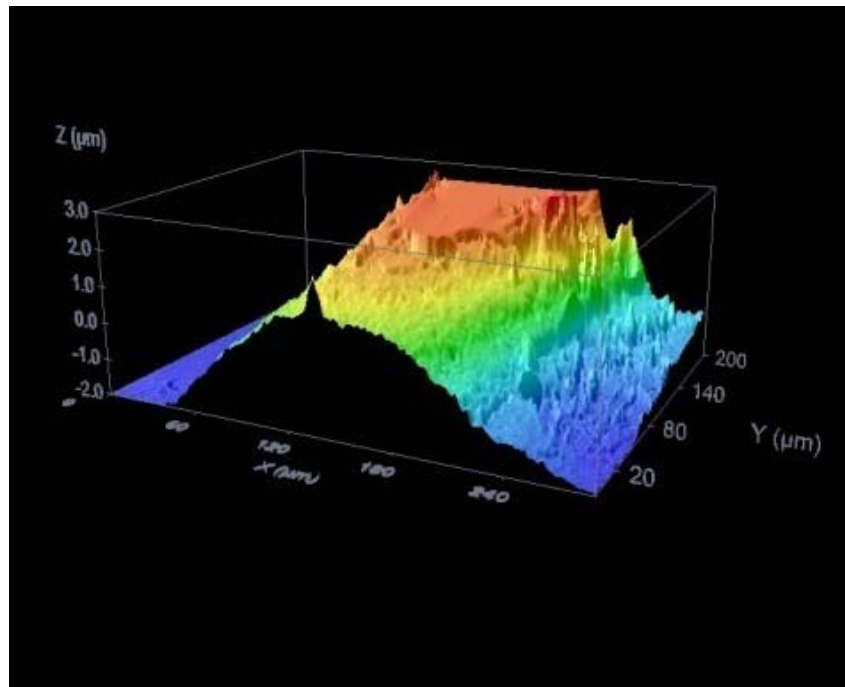


FIGURE 38: Height 4~5  $\mu\text{m}$

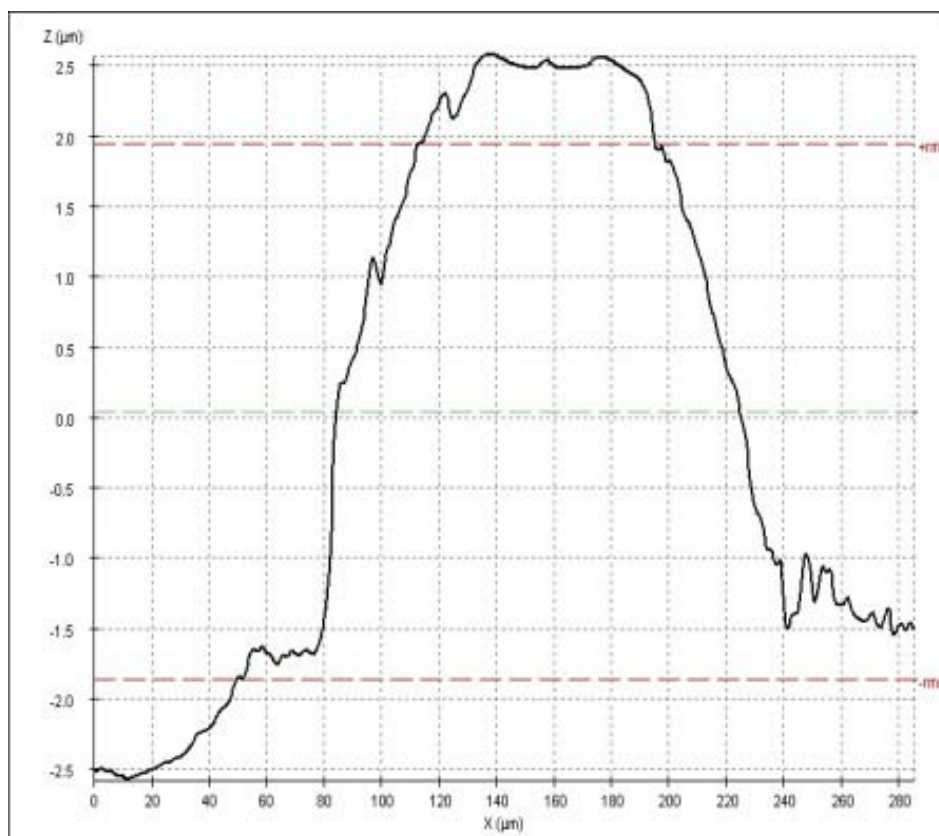
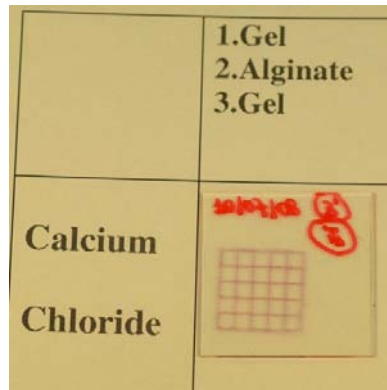


FIGURE 39: Width 300 $\mu\text{m}$

Similarly follows the deposition of sodium alginate gel, by adding just one more layer of calcium chloride in the place of calcium acetate that was used before, in order to exist a base before the second sodium alginate gel layer (figure 40).



*FIGURE 40: Sample's picture of a 3D structure of one layer of sodium alginate gel and two layers of calcium chloride gel*

The result was a 3D structure with 4 - 5 $\mu$ m height and 300 $\mu$ m matrix's line width (Fig. 41-Fig. 42) and the surface is more ruff than the previous result with calcium acetate again.

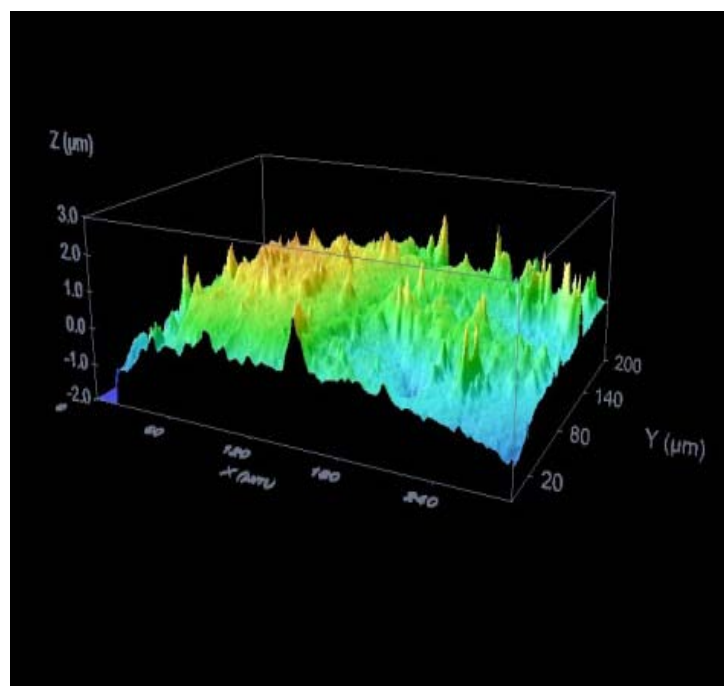


*FIGURE 41: Height 4~5  $\mu$ m*

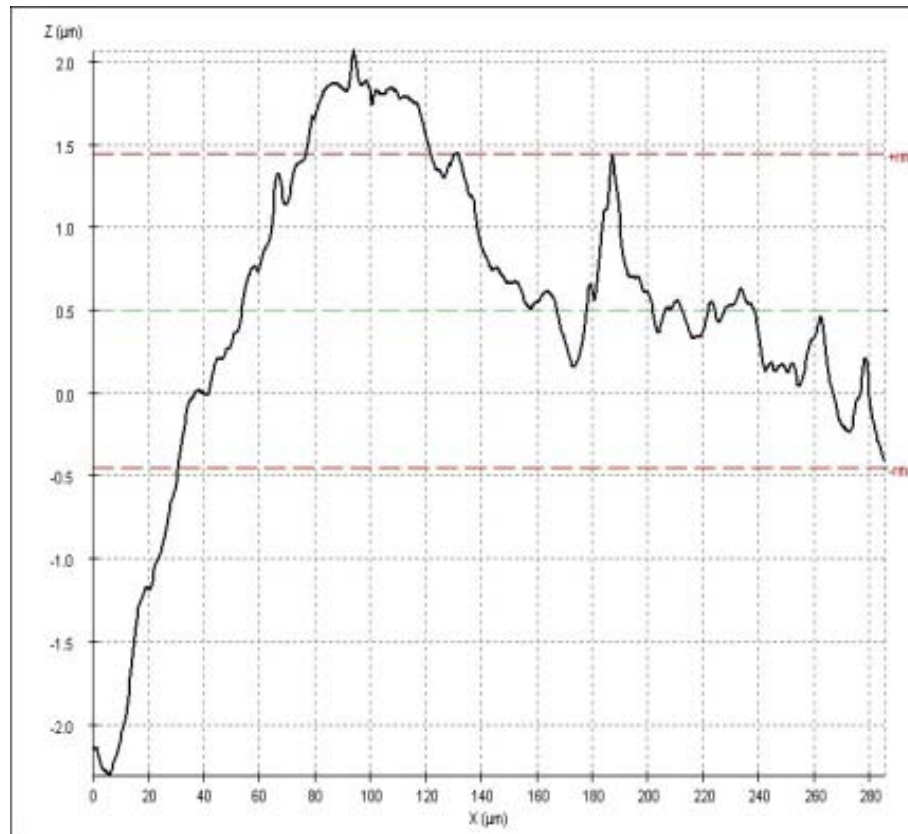


FIGURE 42: Width 300µm

### 5.2.3.2.1.b.3 3D matrix of four layers of alginate gel and three layers of calcium acetate or calcium chloride

In this part 3D structures of calcium alginate gel were prepared, with double layers than the previous try. These 3D matrixes are made of three layers of sodium alginate gel and three layers of calcium acetate gel or calcium chloride gel, and a base of one layer of calcium acetate gel or calcium chloride gel (Fig. 43).

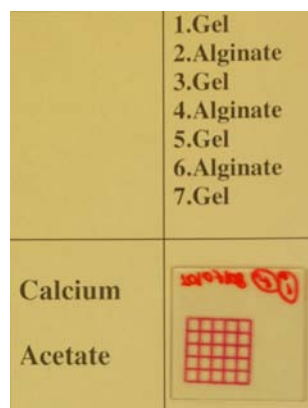


FIGURE 43: Sample's picture of a 3D structure of three layers of sodium alginate gel and four layers of calcium acetate gel

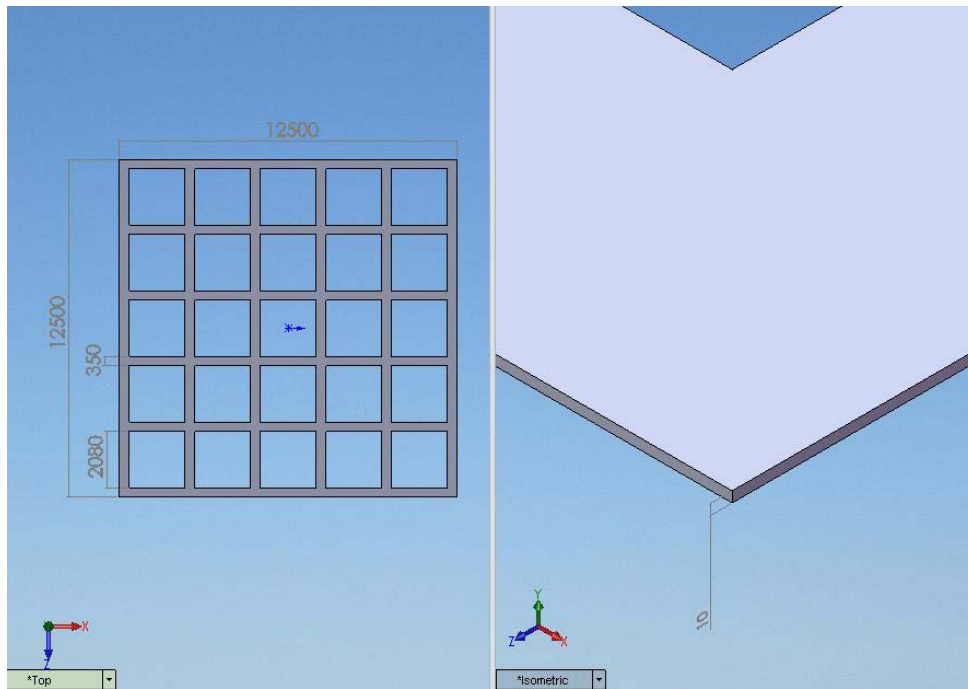


FIGURE 44: Sample's 3D sketch

As previously a confocal imaging profiler microscope was used to characterize the one layer calcium alginate gel 3D structure-matrix. The height was 8~10 $\mu\text{m}$  and the width of the matrix's line was 350 $\mu\text{m}$  (figures 45, 46).

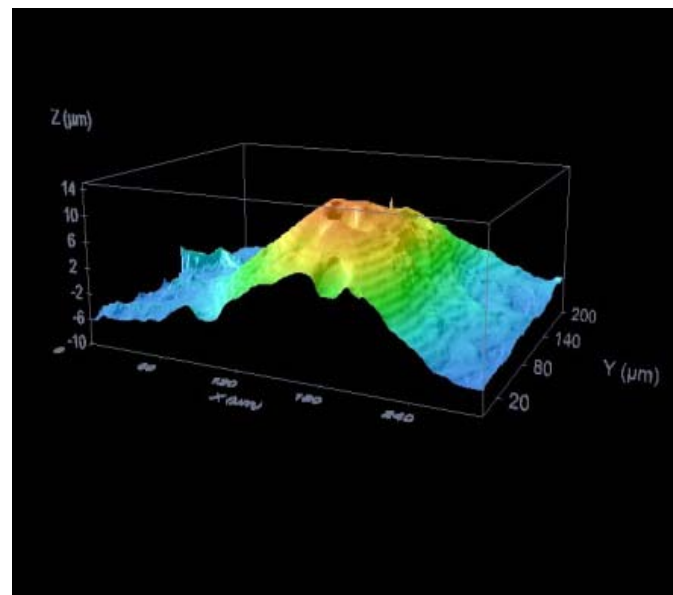


FIGURE 45: Height 8~10  $\mu\text{m}$

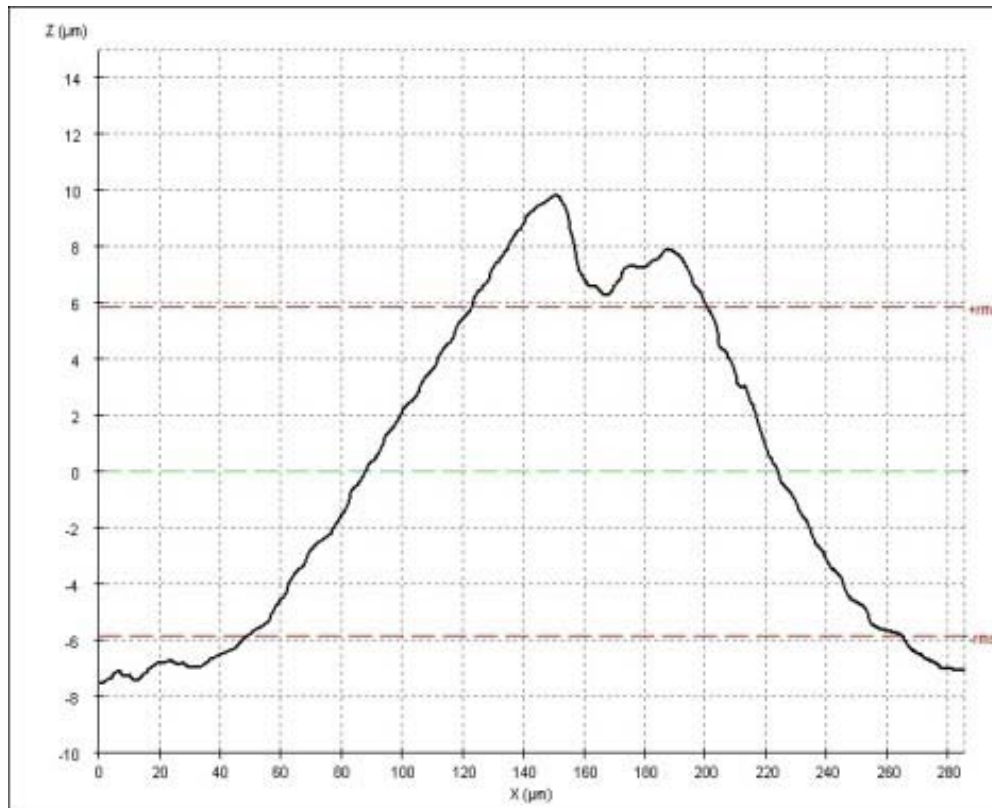


FIGURE 46: Width 350µm

After the study about the characteristics of these 3D structures: the height of the structure was about 8 – 10 µm, as it was expected the double from the previous results! And the width of the matrix's line was now 350 µm. Then the development of 3d structures of calcium alginate gel, with three layers of sodium alginate gel and three layers of calcium chloride gel and one layer of calcium chloride gel as well, for a base, were developed (Fig.47).

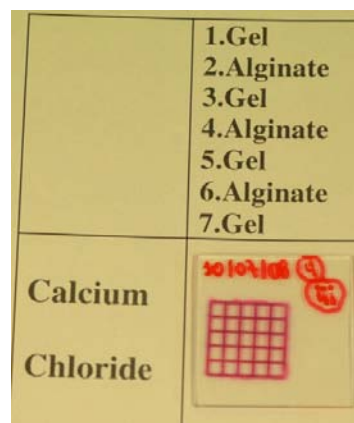


FIGURE 47: Sample's picture of a 3D structure of three layers of sodium alginate gel and four layers of calcium chloride gel

The height of the structure is about 8 – 10  $\mu\text{m}$ , as it was expected the double than the previous results! And the width of the matrix's line is now 350  $\mu\text{m}$  again!

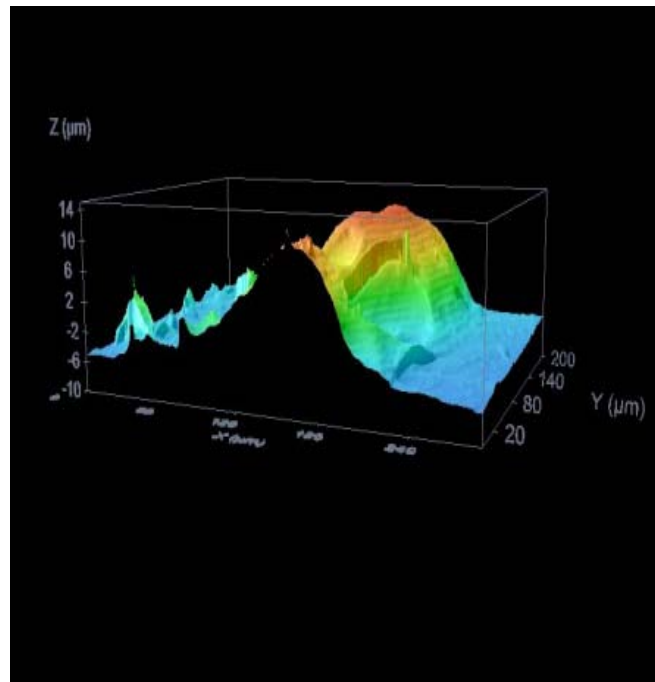


FIGURE 48: Height 8~10  $\mu\text{m}$

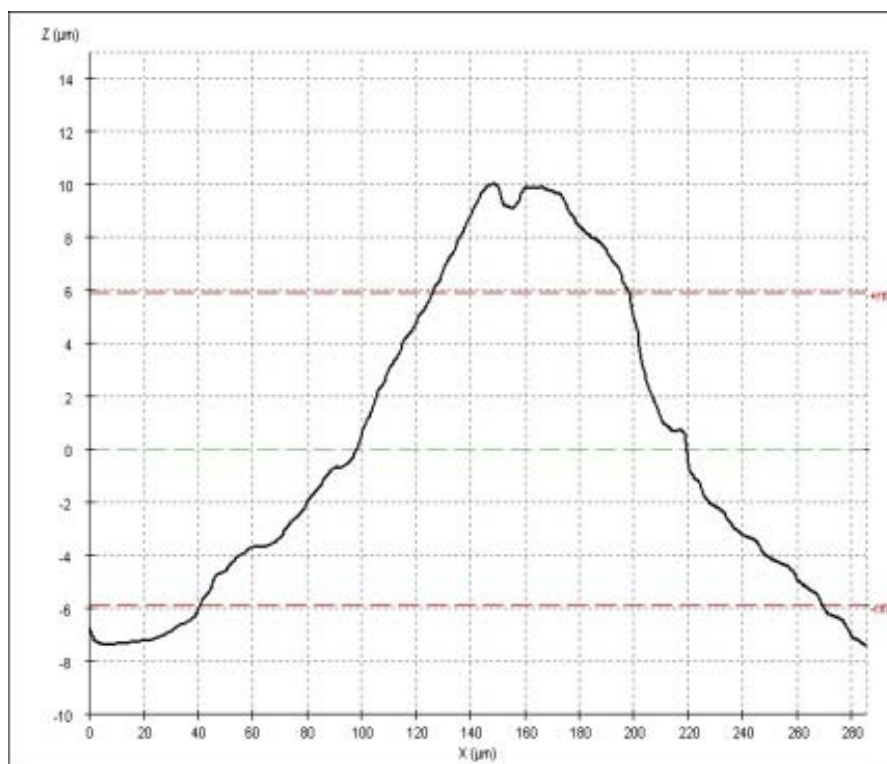


FIGURE 49: Width 350 $\mu\text{m}$

### 5.2.3.2.1.b.4 3D matrix of four layers of alginate gel and three layers of calcium acetate or calcium chloride

Then 3d structures were developed with two more layers of sodium alginate gel and two more layers of calcium acetate gel or calcium chloride gel. These 3d structures-matrixes that are presented here are made of 5 layers of sodium alginate gel and 5 layers of calcium acetate gel or calcium chloride gel, and the base of one layer of calcium acetate gel (Fig.50) or calcium chloride gel too.

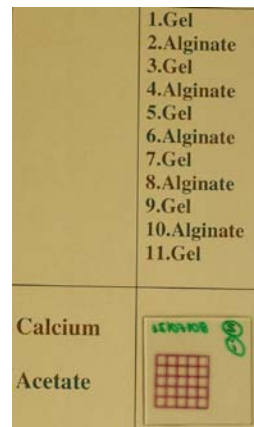


FIGURE 50: Sample's picture of a 3D structure of five layers of sodium alginate gel and five layers of calcium acetate gel

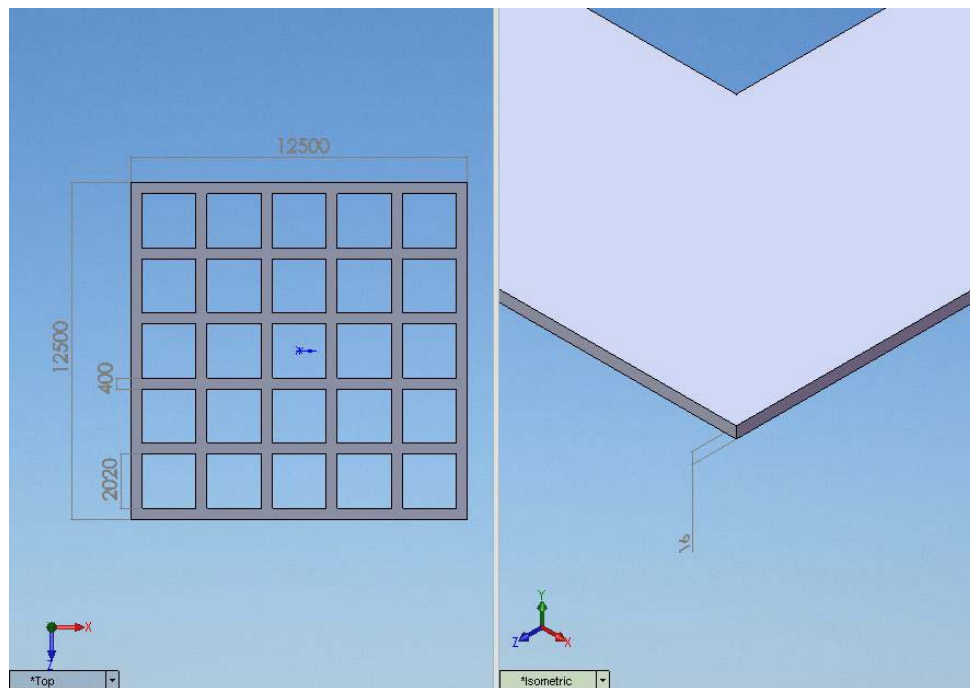


FIGURE 51: Sample's 3D sketch

For the characterization of these 3D structures-matrixes a confocal imaging profiler microscope was used as previously in this study and the height of the structure was about 12 – 16  $\mu\text{m}$  and the width of the matrix's line was 550  $\mu\text{m}$  (Fig.52-Fig.53).

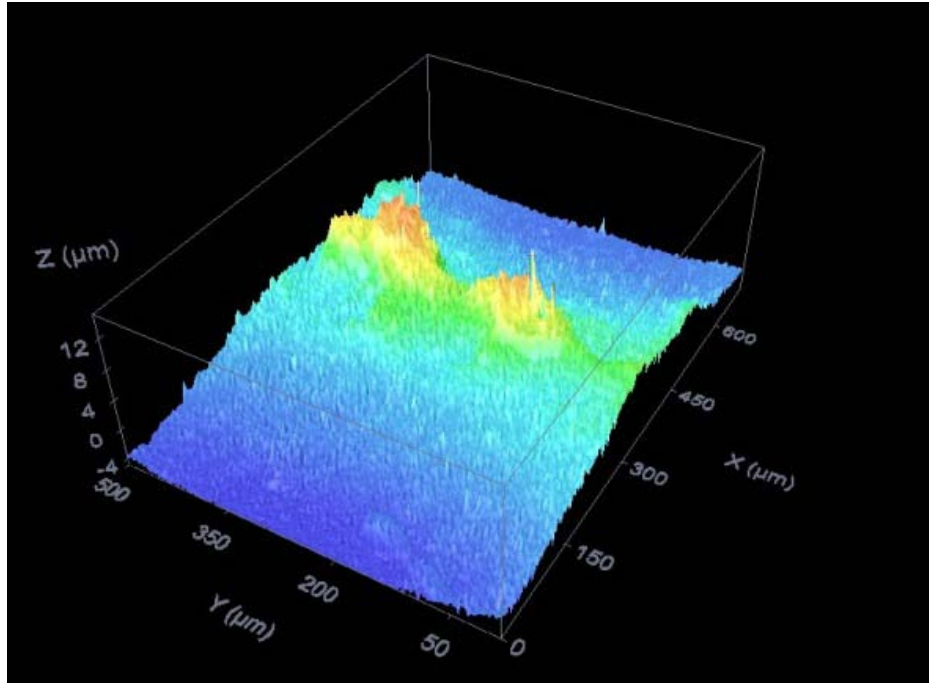


FIGURE 52: Height 12~16  $\mu\text{m}$

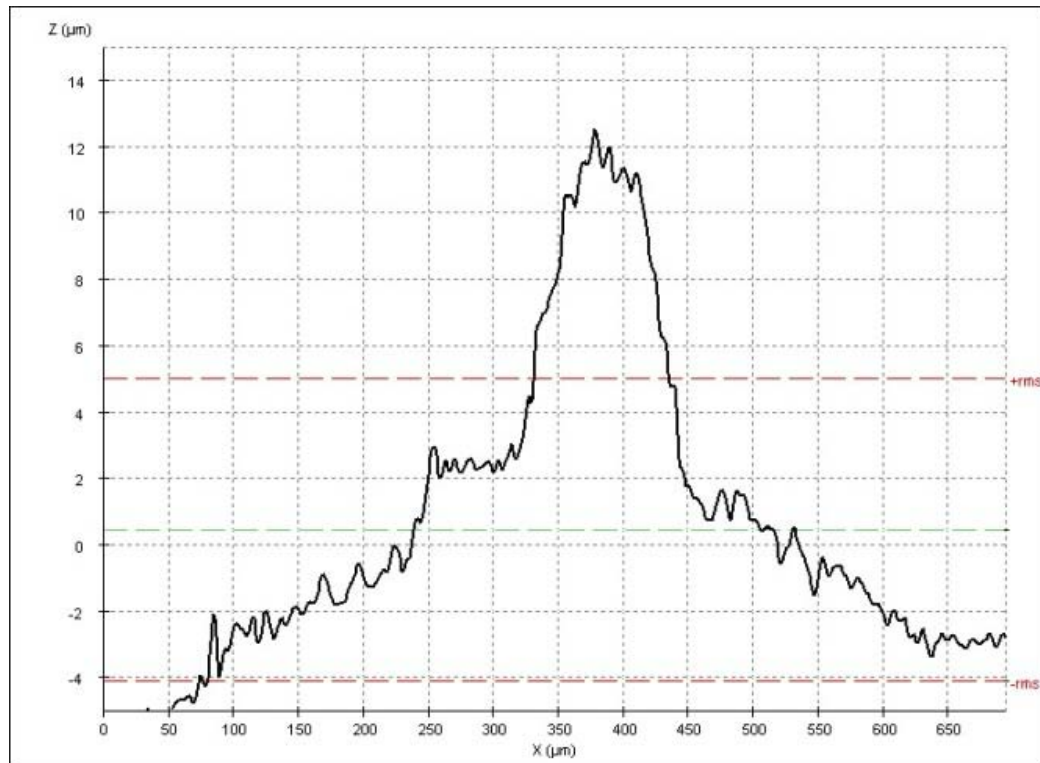


FIGURE 53: Width 550µm

Then we continue working in the same way, but with the deposition of calcium chloride gel. The 3D structures-matrixes that are presenting below are made of 5 layers of sodium alginate gel and 5 layers of calcium chloride gel (Fig.54).

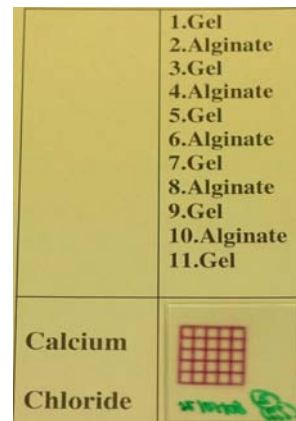


FIGURE 54: Sample's picture of a 3D structure of five layers of sodium alginate gel and five layers of calcium chloride gel

The height of the structures is about 12 – 16 µm and the width of the line is about 400–550 µm again (Fig.55-Fig.56).

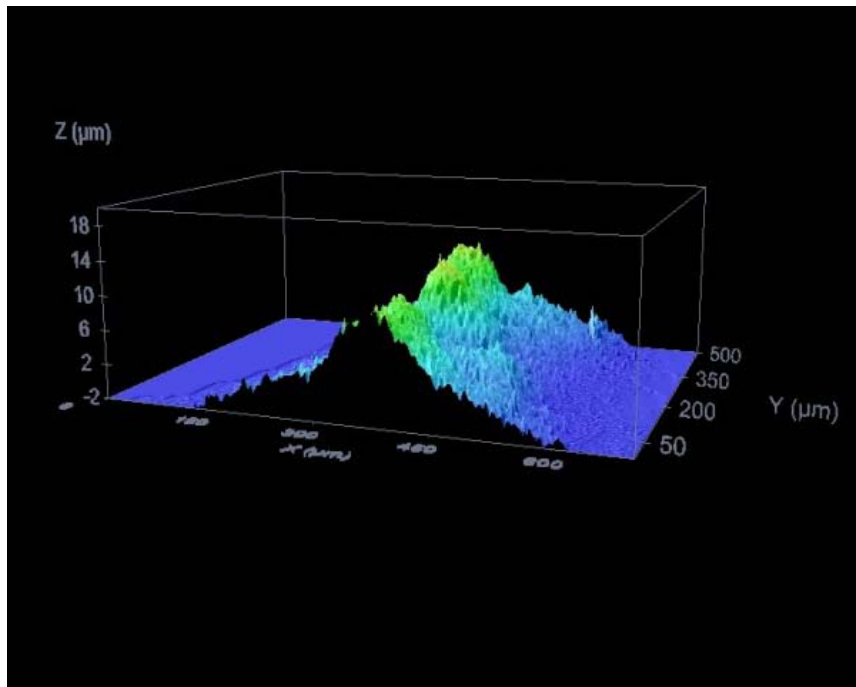


FIGURE 55: Height 12~16  $\mu\text{m}$

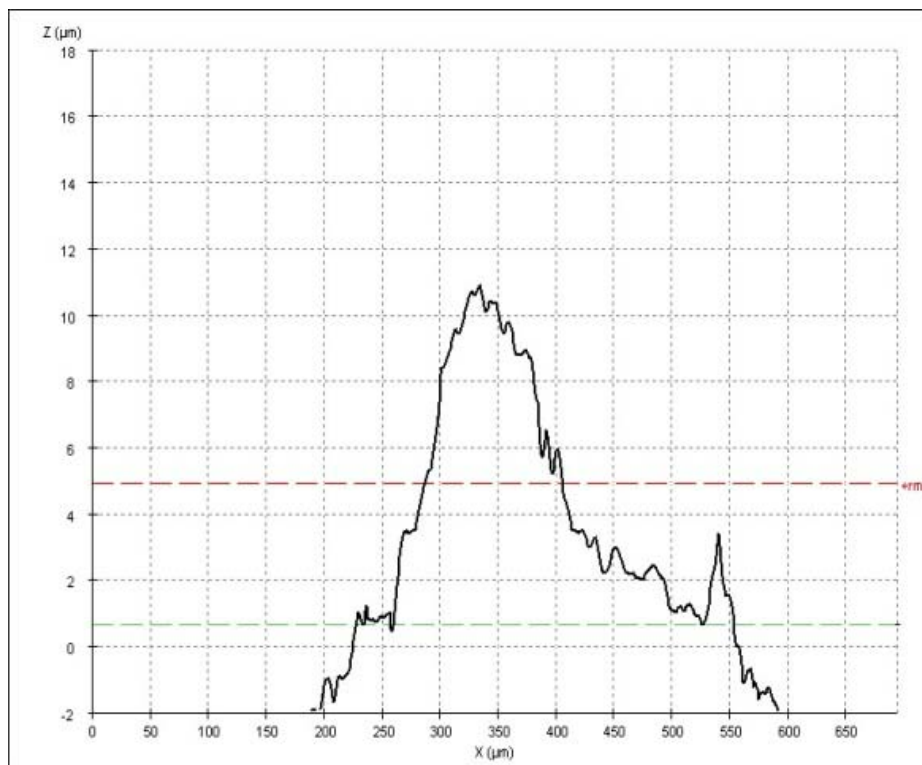


FIGURE 56: Width 400-550  $\mu\text{m}$

### 5.2.3.2.1.b.5 3D matrix of four layers of alginate gel and three layers of calcium acetate or calcium chloride

We continue making 3D structures with double layers than the previous try. These structures that are presented here are made of 10 layers of sodium alginate gel and 10 layers of calcium acetate gel, and the base of one layer of calcium acetate gel (Fig.57).

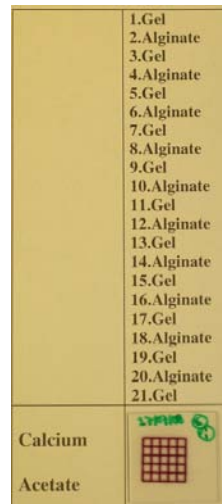


FIGURE 57: Sample's picture of a 3D structure of ten layers of sodium alginate gel and ten layers of calcium acetate gel

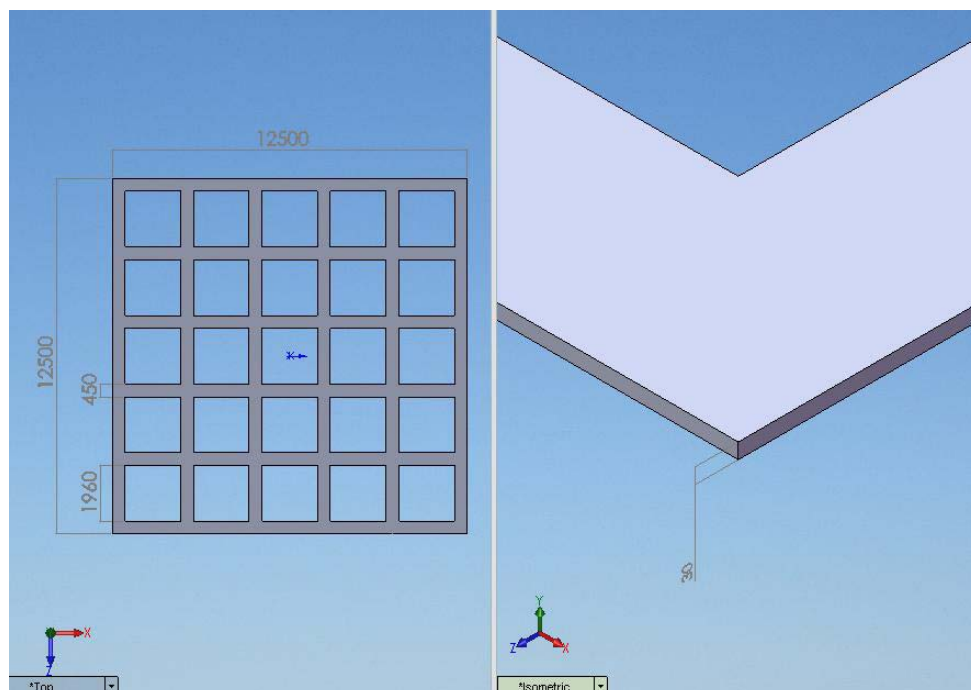


FIGURE 58: Sample's 3D sketch

The height of the structure is about 20 – 30  $\mu\text{m}$  and the width of the line is now 550  $\mu\text{m}$ . These structures that are presented here are made of 10 layers of sodium alginate gel and 10 layers of calcium acetate gel and the base of one layer of calcium acetate gel too. The layers of this structure are double than the ones from the previous results and the height of the structure is about 20–30 $\mu\text{m}$  (Fig.59-Fig.60), as it is expected the double from the previous results!

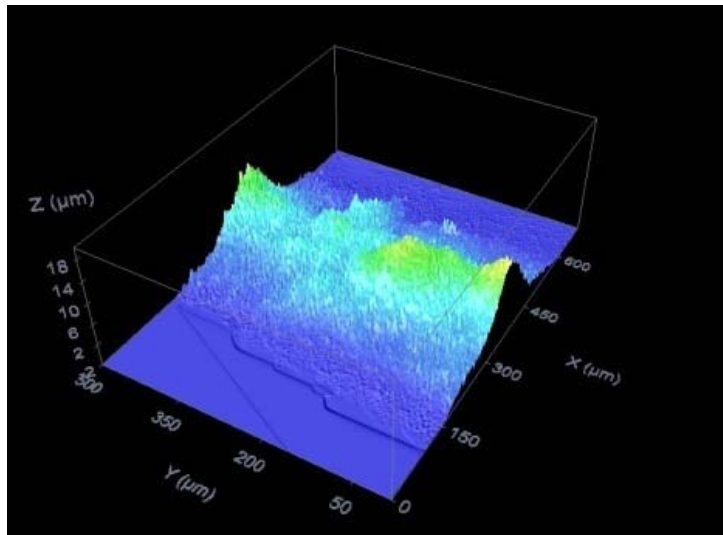


FIGURE 59: Height 20  $\mu\text{m}$

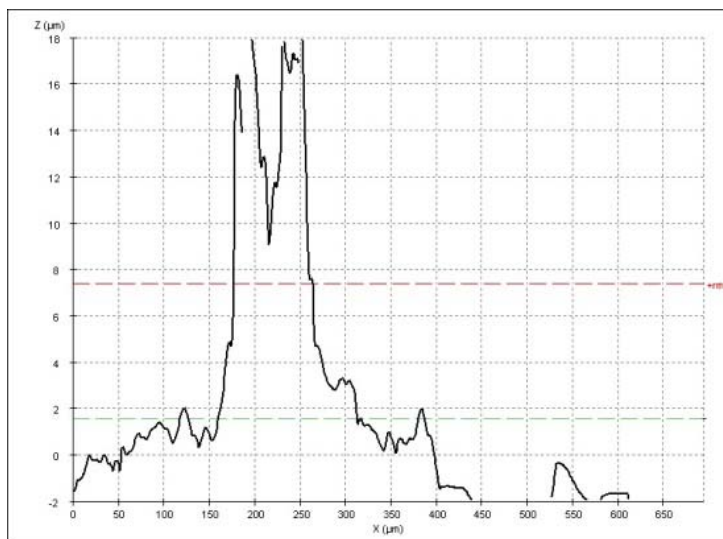
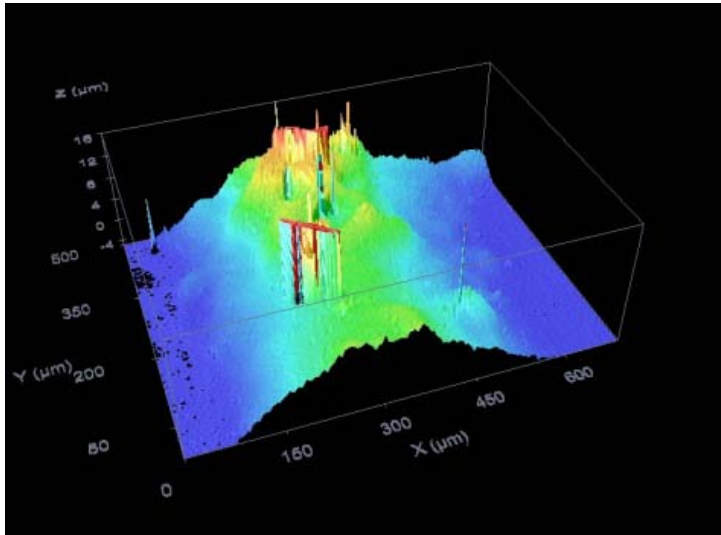
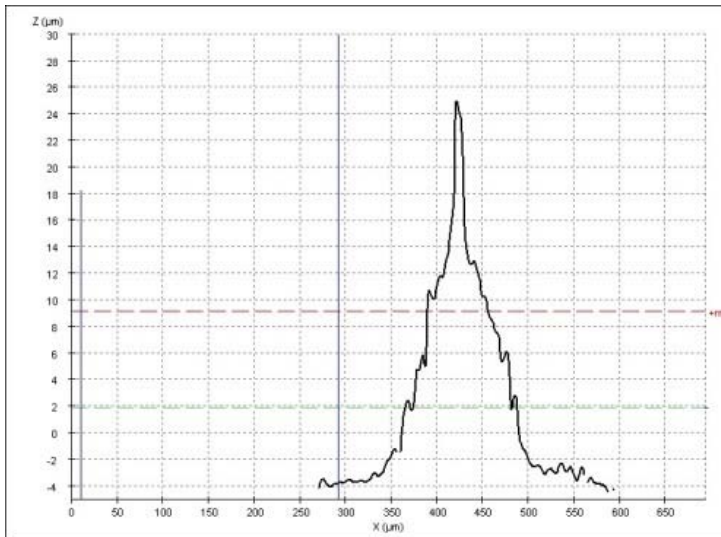
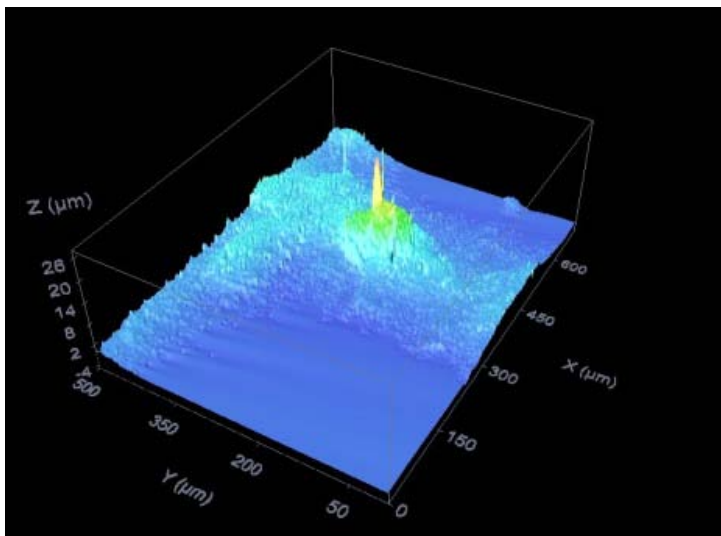


FIGURE 60: Width 450  $\mu\text{m}$

FIGURE 61: Height  $24 \mu\text{m}$ FIGURE 62: Width  $450 \mu\text{m}$ FIGURE 63: Height  $30 \mu\text{m}$

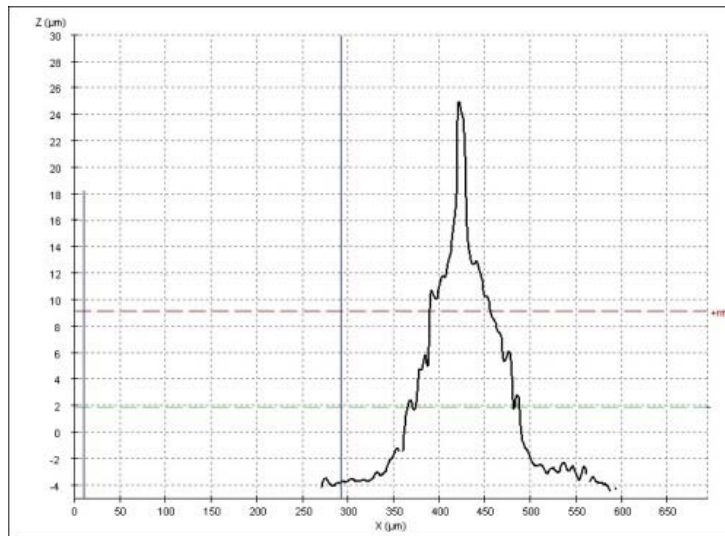


FIGURE 64: Width 450µm

### 5.2.3.2.1.b.6 Calcium alginate gel matrix in smaller dimensions

We develop the 3D matrix of calcium alginate gel in smaller dimensions. This matrix was made of three layers of sodium alginate gel and three layers of calcium acetate gel. There was one layer more of calcium acetate as base too (Fig.65-Fig.66).

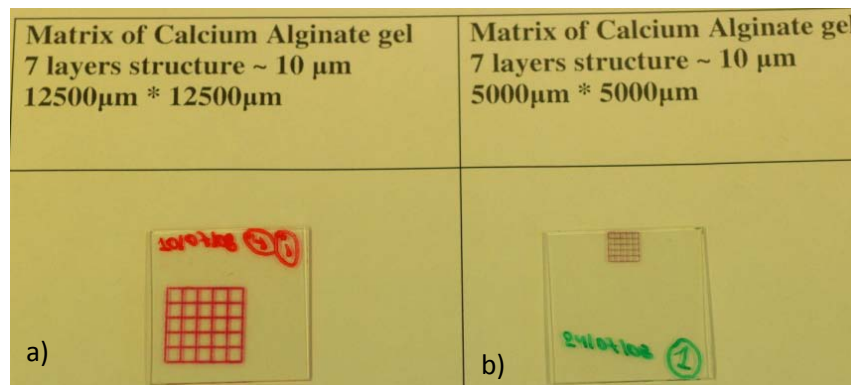
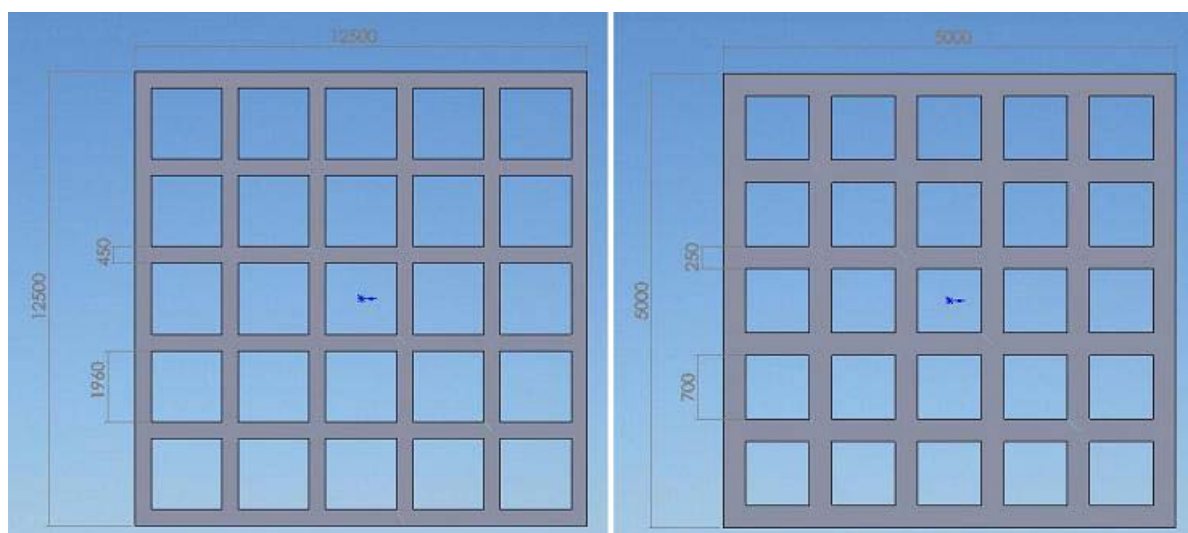
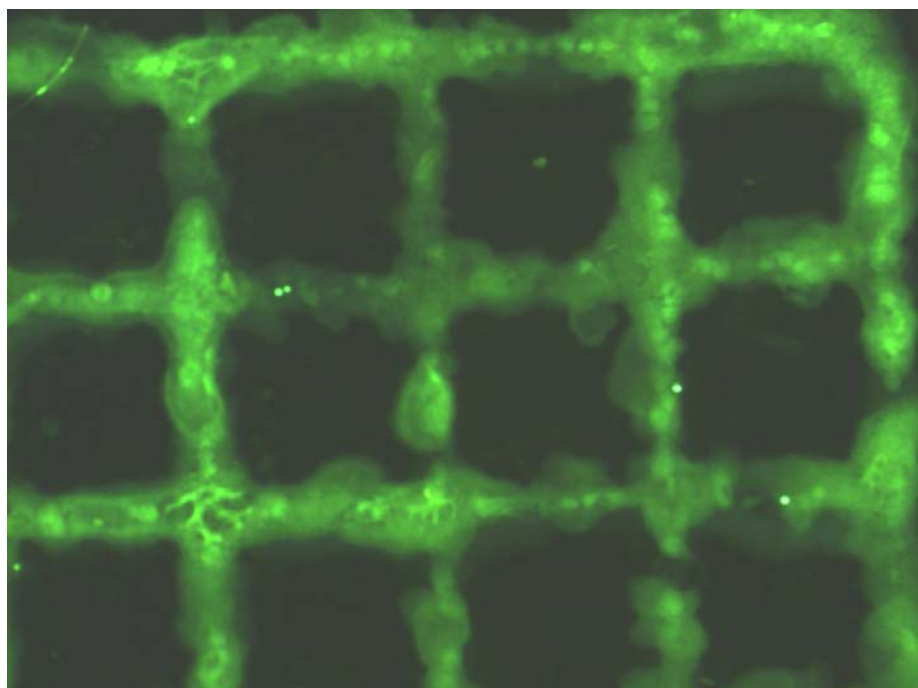


FIGURE 65: Sample's picture of 3D structure of three layers of sodium alginate gel and three layers of calcium acetate: a) in 12,5mm\*12,5mm scale, b) in 5mm\*5mm scale



*FIGURE 66: Samples 3D sketch image*

The height of the structure is approximately about 10  $\mu\text{m}$ , at both 3D structures in each scale! We want to use this smaller matrix of calcium alginate gel of the dimensions of 5mm \* 5mm as a scaffold for cells. Each square of this 3D calcium alginate gel matrix is 1mm\*1mm (Fig.67-Fig.68).



*FIGURE 67: Fluorescent image of calcium alginate gel 3D matrix (5mm\*5mm)*

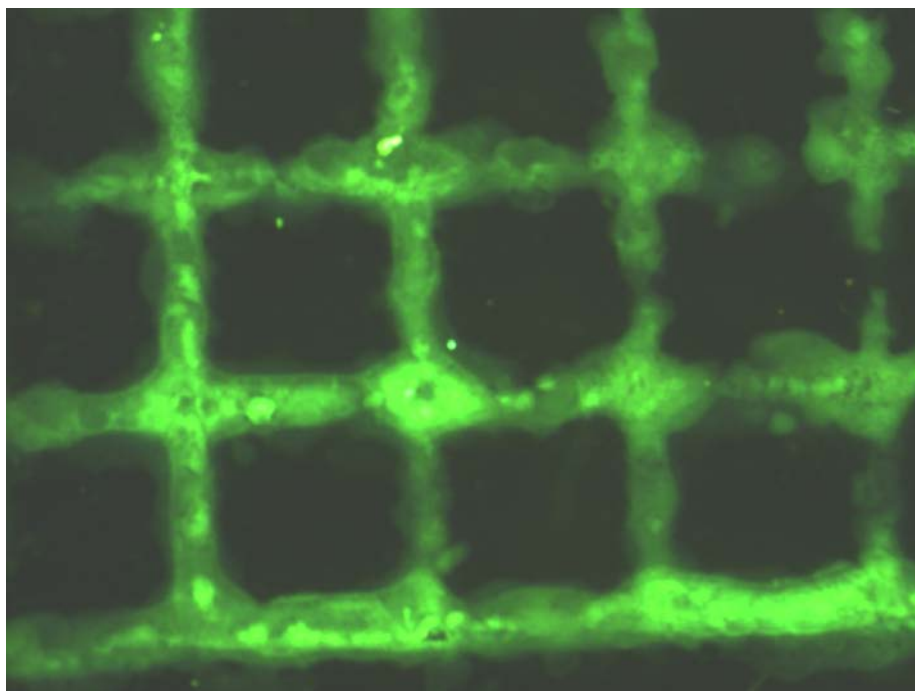


*FIGURE 68: Each square of calcium alginate gel matrix is 1mm\*1mm*

#### **5.2.4 2D Deposition of Cells**

In this subchapter we describe the patterns we created by the cells transfer with the L.I.F.T. technique. The process was performed in air and at room temperature. The laser energy was varied from 80 to 98 mJ per pulse and we examine the energy threshold of the transfer dependence on the viability of cells. After the transfer we put on the sample a droplet with fluorescent substances which will colour the cells: *green* colour for the cells that are alive, *red* colour for the dead cells. These substances were: Calcein (green) and ethidium homodimer-1 (red). The distance between the target and the substrate was kept constant at 500 mm.

##### **5.2.4.1 2D Deposition of Fibroblast Cells**

The aqueous cells solution (1 mg/ml) in the medium DMEM, was spread on quartz coated with 30 nm gold thin layer film and used as a target. The liquid film thickness, estimated through the measurement of the film weight, was approximately ~10mm. Glass slides prepared as above mentioned were used as receiving substrates. The patterns were created by transferring lines of spots of cells and each line of cells was created by using different energy of the transfer.

#### 5.2.4.1.1 2D Deposition of Fibroblasts Rattail Cells

The first line has the smallest energy of the transfer  $\sim 80\text{mJ}$ , and the last line has the biggest energy of the transfer  $\sim 98\text{mJ}$  respectively. The energy change between each line is  $3\text{mJ}$ . The pattern of fibroblasts array is presented in the following Fig.69. In order to study the cells viability we used a fluorescent microscope where we took pictures of the pattern (Fig.70). The different colours that we can see at these pictures from the fluorescent microscope are as a result of the pattern with alive and dead cells.

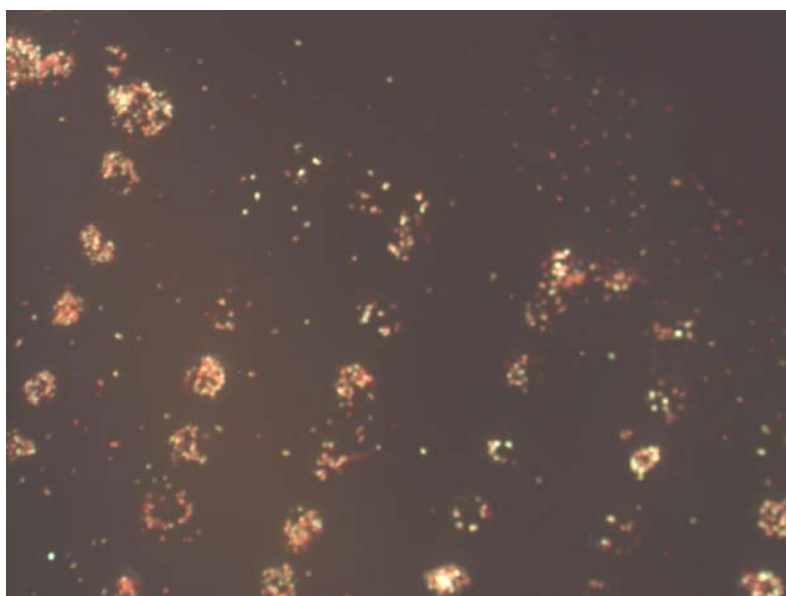


*FIGURE 69: Pattern of spots of fibroblast rattail cells with different energies*

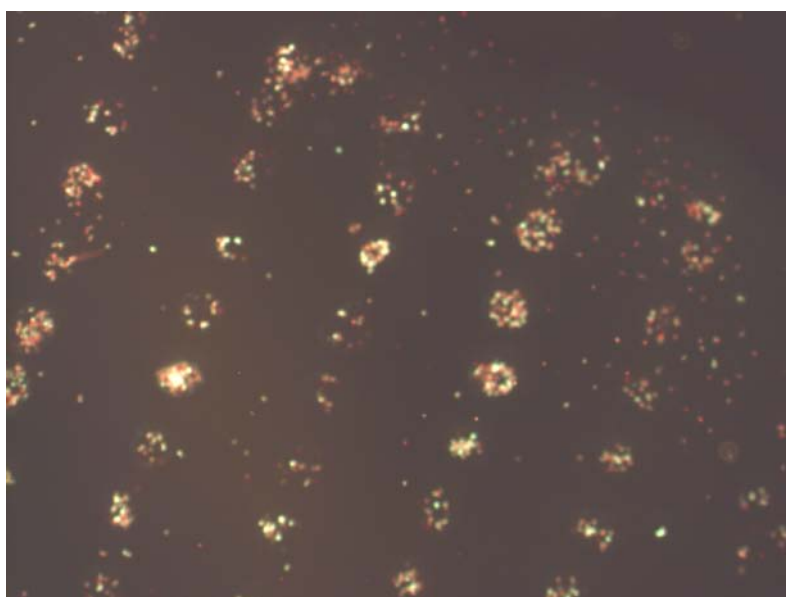


*FIGURE 70: Pattern with alive and dead cells, after the transfer*

In order to find the energy threshold, the lowest energy where the cells will be alive after the transfer, we made pattern of cells by increasing and decreasing the energy of the transfer. By increasing the energy of the transfer  $\sim 90\text{mJ}$ , we took as a result a pattern with dead cells (figure 71), and when we increased a lot the energy  $\sim 98\text{mJ}$  we saw that the material of transfer (fibroblasts rattail cells) was breaking up, and we didn't receive clear spots of the transferred material at the substrate (Fig. 72). The energy threshold where the cells were alive after the transfer was found at  $\sim 85\text{mJ}$  (Fig.73).

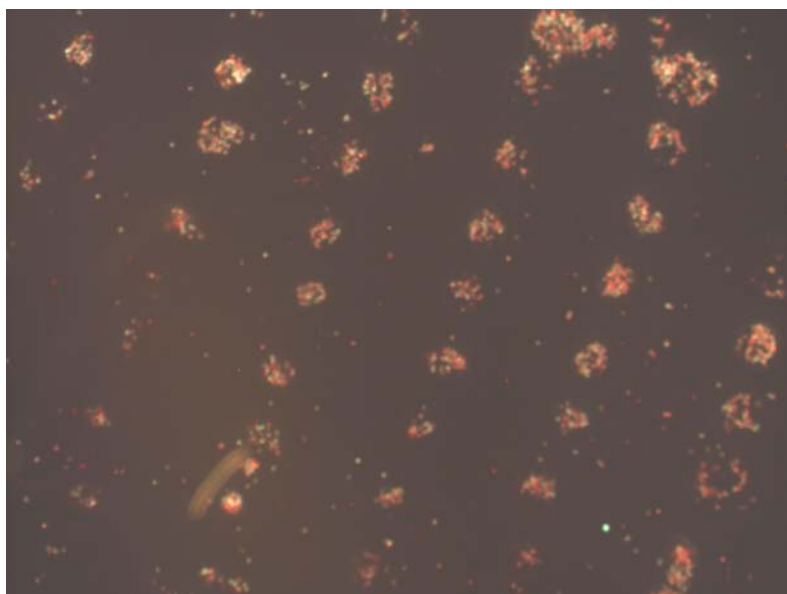


*FIGURE 71: Pattern with dead cells after the transfer*

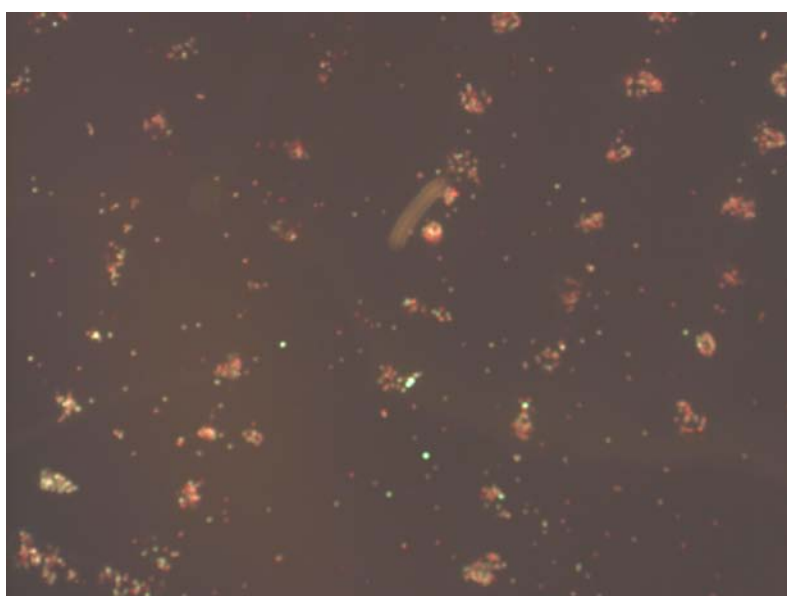


*FIGURE 72: By using high energy (98mJ) the cells that are transferred are breaking up*

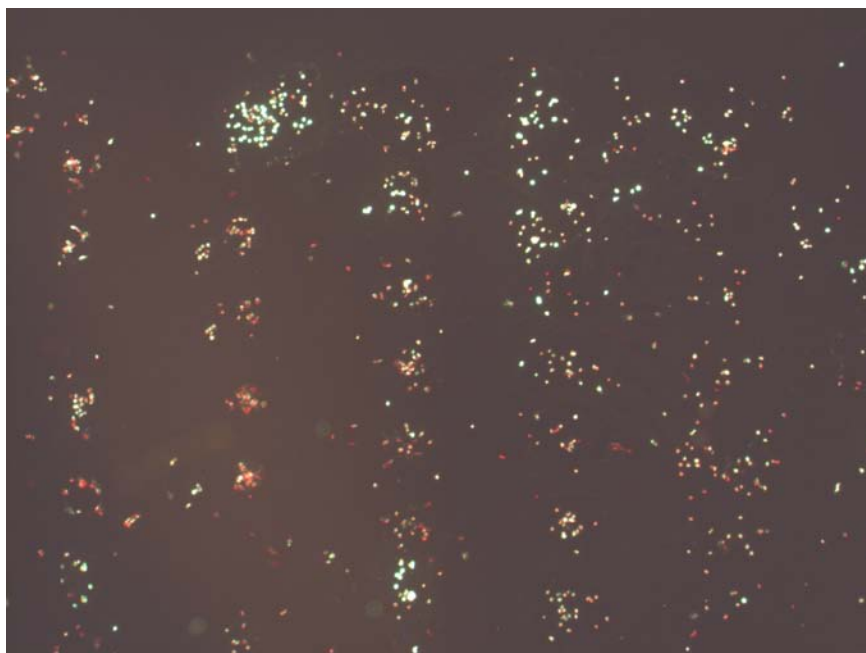


*FIGURE 73: Pattern with fibroblasts rattle cells, finding the energy threshold, the lines in the middle, by using energy  $\sim 85\text{mJ}$*

#### **5.2.4.1.2 2D Deposition of Fibroblasts 3T3 NIH Cells**

We continue to make patterns with spots of fibroblasts 3T3 NIH cells, and we study again the dependence of the energy threshold and the viability of the cells after the transfer by using the L.I.F.T. technique. The patterns that were made were again: the first line has the smallest energy of the transfer  $\sim 82\text{mJ}$ , and the last line has the biggest energy of the transfer  $\sim 98\text{mJ}$ . The energy change between the lines was approximately  $5\text{mJ}$ . Finally the pictures were taken by using a fluorescent microscope, so again the alive cells are expected to be green and the dead ones to be red respectively.

##### **5.2.4.1.2.a 2D Deposition of Fibroblasts 3T3 NIH Cells on glass substrate**

In this part we create patterns of fibroblasts 3T3 NIH cells on glass substrate, and again we study their viability dependence on the energy of the transfer. The first pattern was made by using energies around  $\sim 89\text{mJ}$  (Fig.74), we saw that some of the cells were alive after the transfer, so we decrease the energy and we had patterns of alive transferred cells (Fig.75- Fig.77) by using laser energy  $\sim 84\text{mJ}$ .

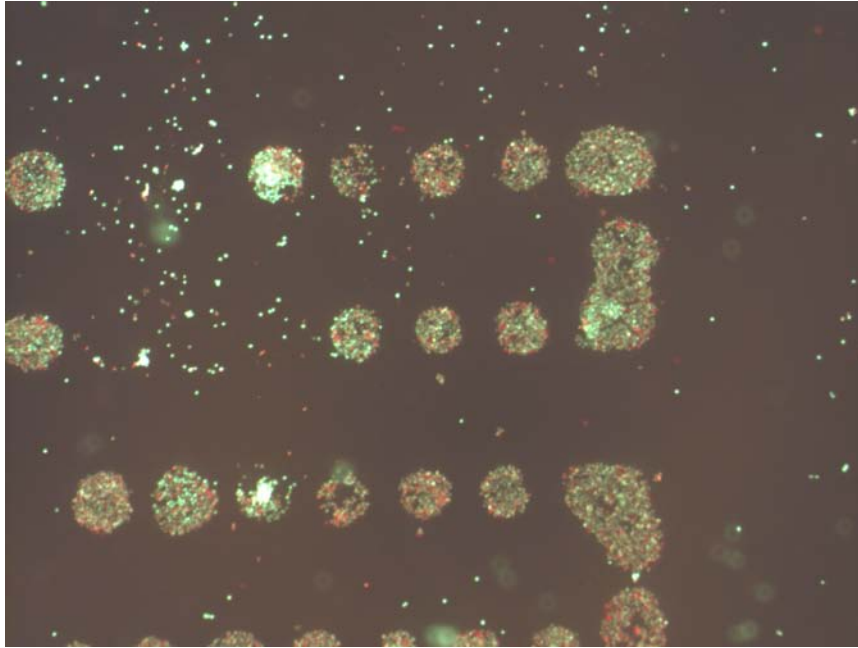


*FIGURE 74: Pattern of spots of fibroblast 3T3 NIH cells with different energies  $\sim 89\text{mJ}$*

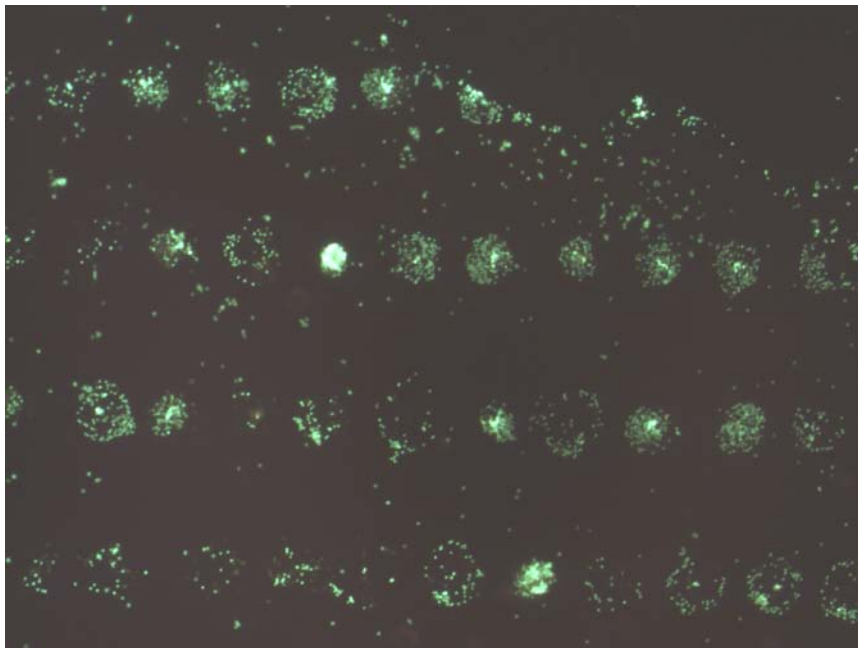


*FIGURE 75: Pattern of spots of fibroblast 3T3 NIH cells with energy  $\sim 84\text{mJ}$*

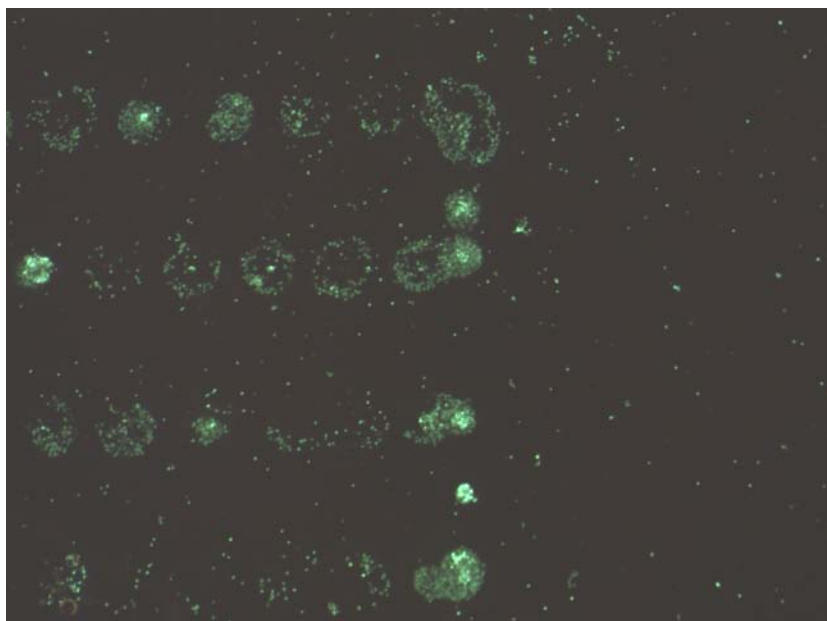


*FIGURE 76: Pattern of spots of fibroblast 3T3 NIH cells by using the threshold energy ~84mJ, the beginning of the spots line*

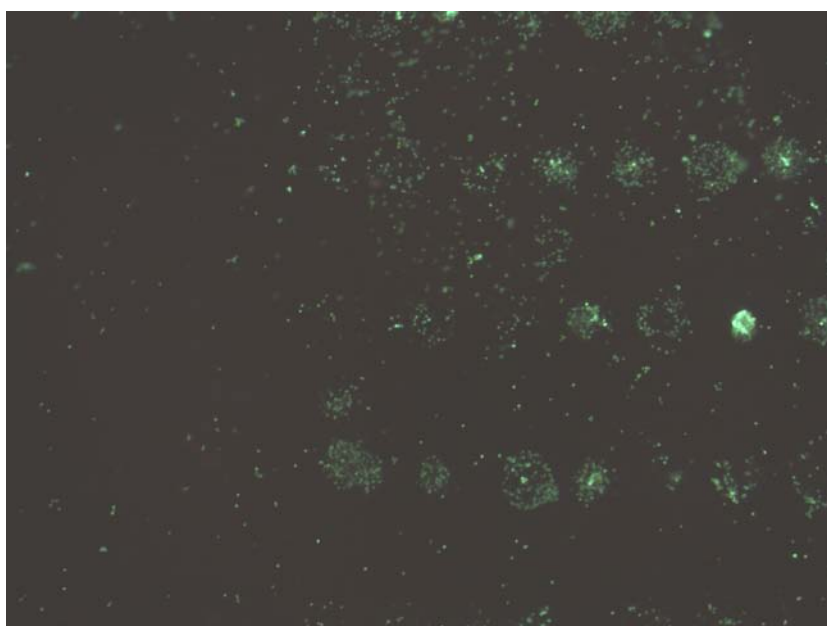


*FIGURE 77: Pattern of spots of fibroblast 3T3 NIH cells by using the threshold energy ~84mJ, the end of the spots line*

The pictures were taken by using a fluorescent microscope, while the substrate on which the cells were transferred was inside the solution of the fluorescent substances, and this is the reason why at some spots of the cells are not looking so clear, cause some cells seems to travel inside the solution and not be attached at the glass substrate. The dependence of the cells viability on the laser energy is clearly represent at the following Figures 78-79.

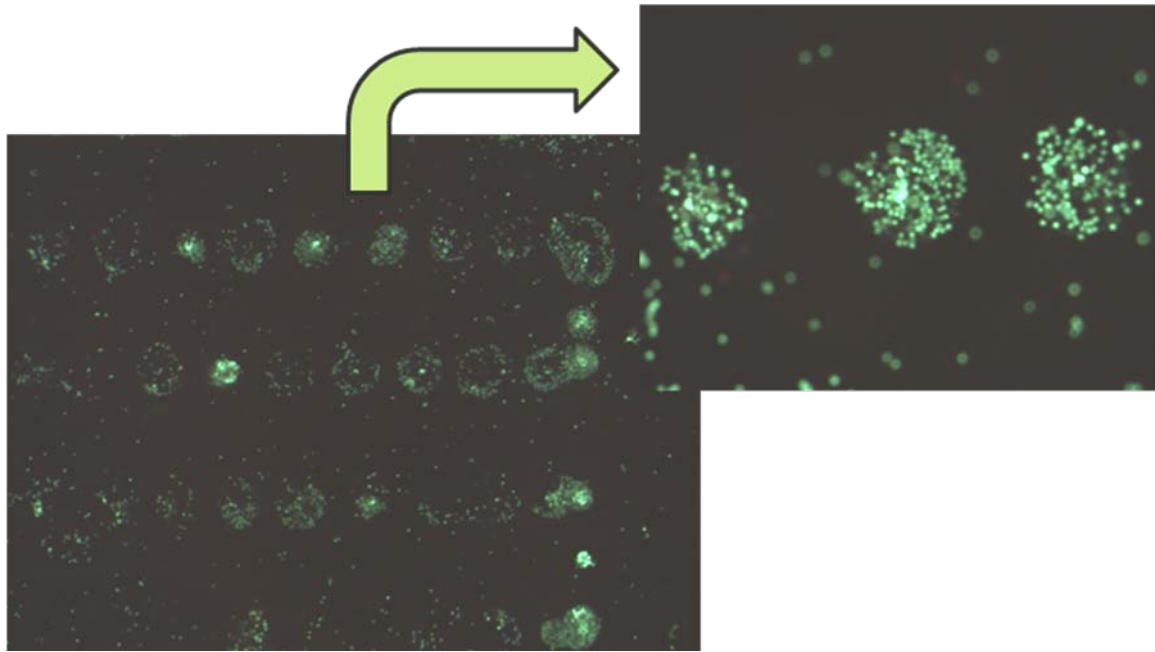


*FIGURE 78: Pattern of alive fibroblast 3T3 NIH cells by using energy  $\sim 84\text{mJ}$*

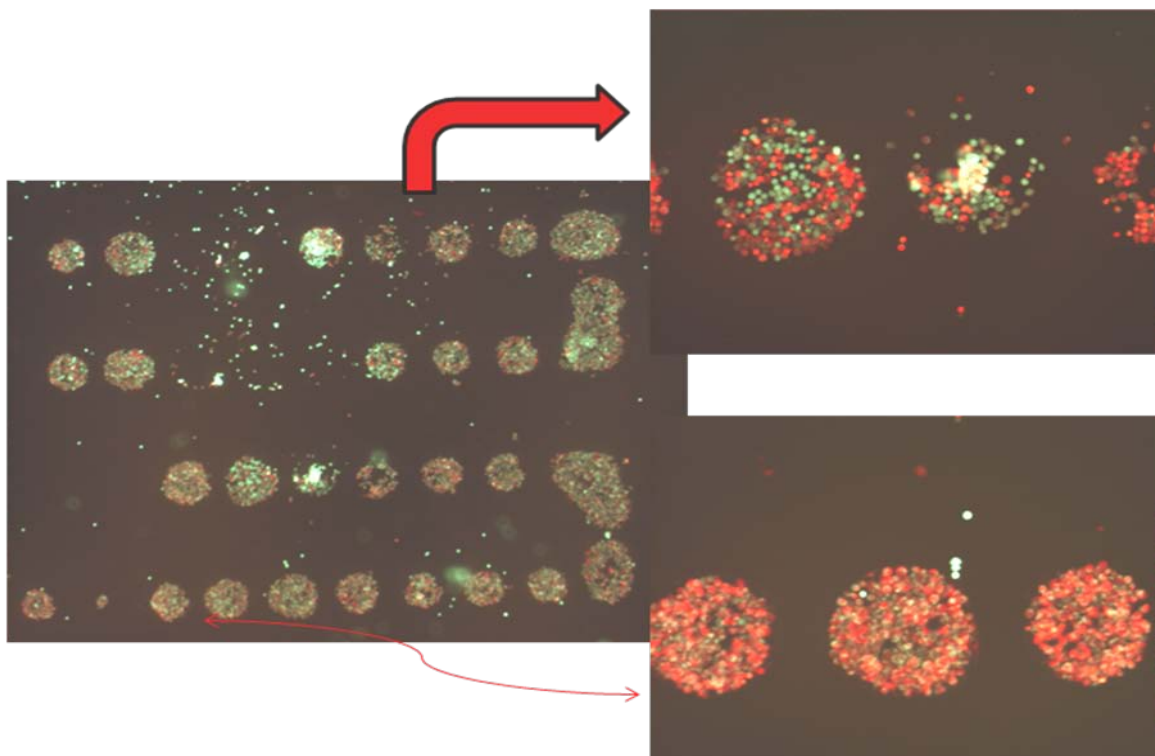


*FIGURE 79: Pattern of dead fibroblast 3T3 NIH cells by using energies  $\sim 89\text{-}98\text{mJ}$*

#### 5.2.4.1.2.b 2D Deposition of Fibroblasts 3T3 NIH Cells on gel substrate

In this part patterns of fibroblasts 3T3 NIH cells were made by L.I.F.T. technique as before, but on a gel substrate. This substrate was made by spreading the gelatin solution on a clean glass slide. We worked as before, studying the cells viability dependence on the energy of the transfer and of course the energy threshold was found. The first pattern was made by using energies around  $\sim 90\text{mJ}$  (Fig.80), we saw that some of the cells were alive after the transfer, so we increase the energy and we made a pattern of different energies for each line, started by using energy  $\sim 85\text{mJ}$ , then at each line we were increasing the energy  $\sim 5\text{mJ}$  (Fig.81).

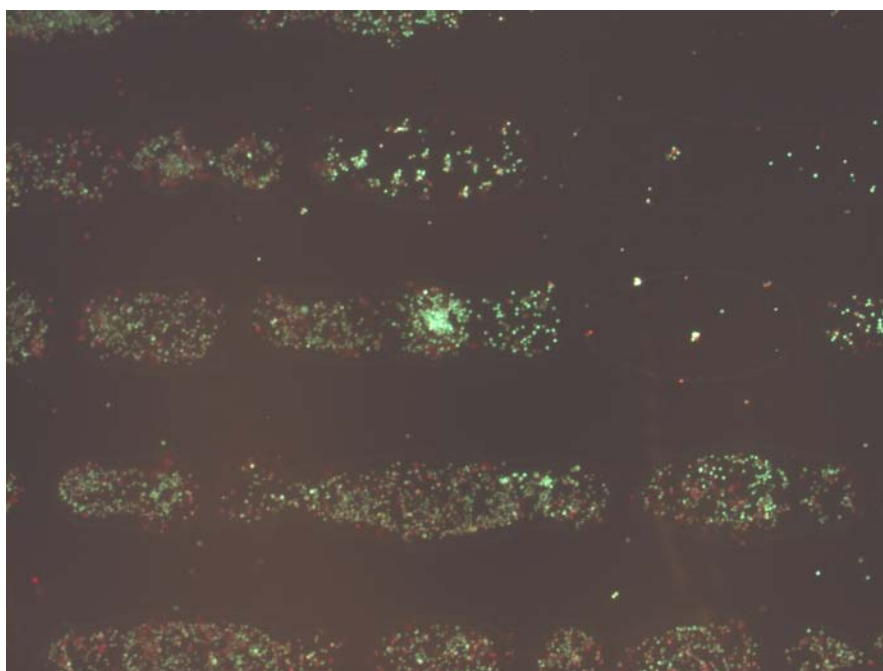


*FIGURE 80: Pattern of spots of fibroblast 3T3 NIH cells by using energies  $\sim 90\text{mJ}$*

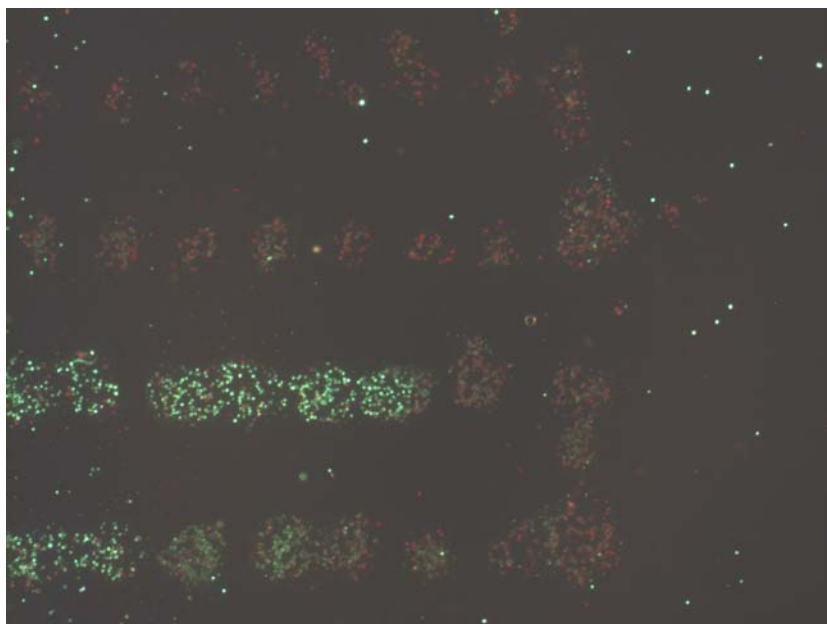


*FIGURE 81: Pattern of spots of fibroblast 3T3 NIH cells by using energies 85~98mJ*

So the energy threshold was found to be approximately around 86mJ, and the next pattern was made by using this laser energy (Fig.82). We can also assume that when we are using in this part a gel substrate, and by keeping the same distance between the spots as before, we can see that the spots of the transferred cells are spreading on the gel substrate and at the end we are not having a clear pattern with spots as before, but we are having a pattern of lines (Fig.83-Fig.84).

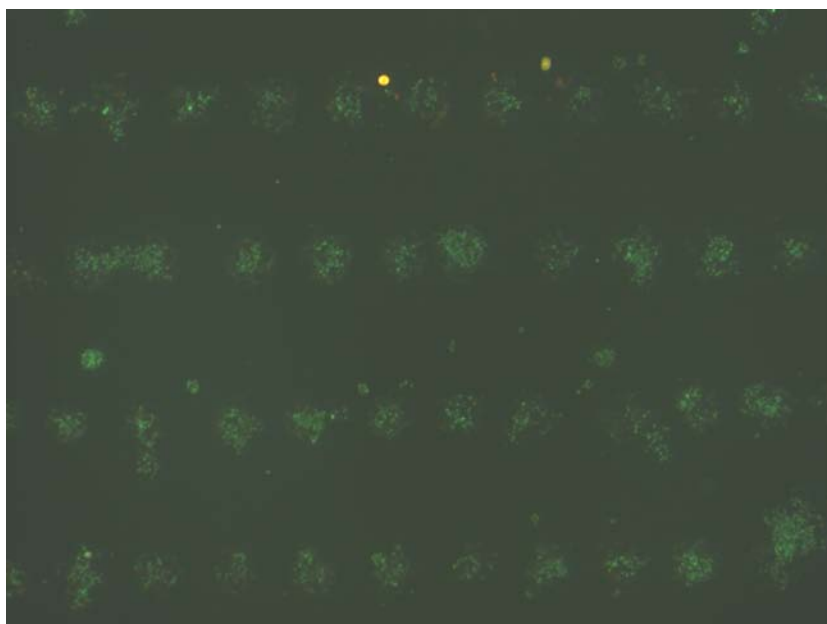


*FIGURE 82: Pattern of spots of fibroblast 3T3 NIH cells by using the threshold energy~86mJ*

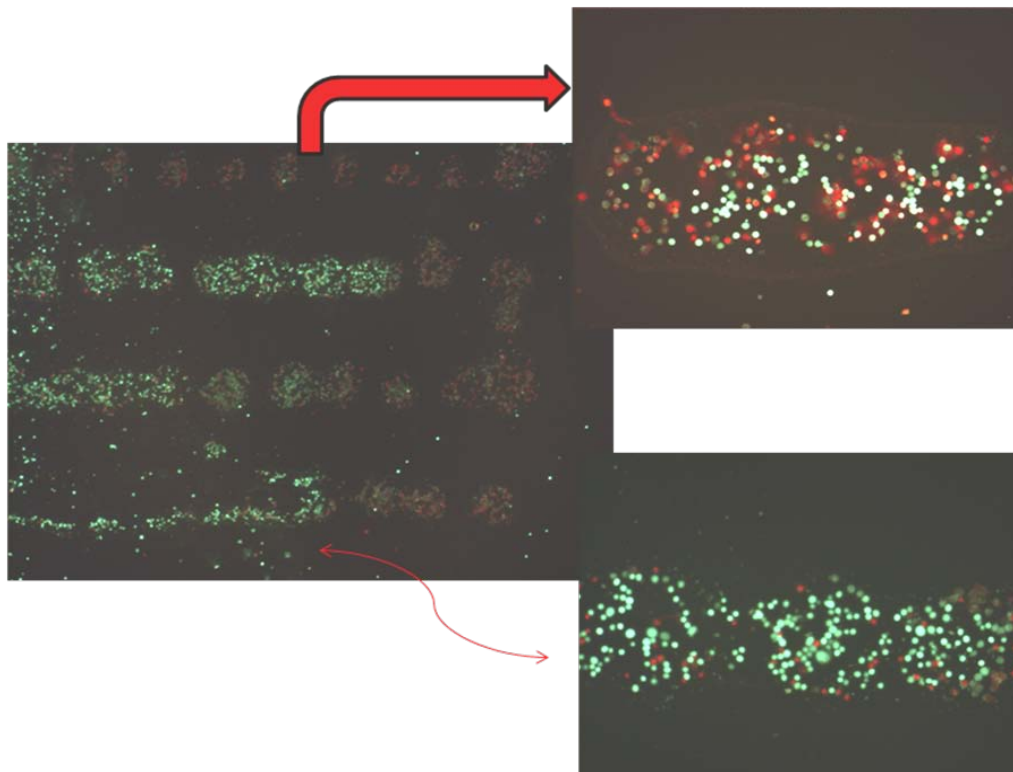


*FIGURE 83: Pattern of dead and alive fibroblast 3T3 NIH cells on a gel substrate by using energies  $\sim 85-98\text{mJ}$*

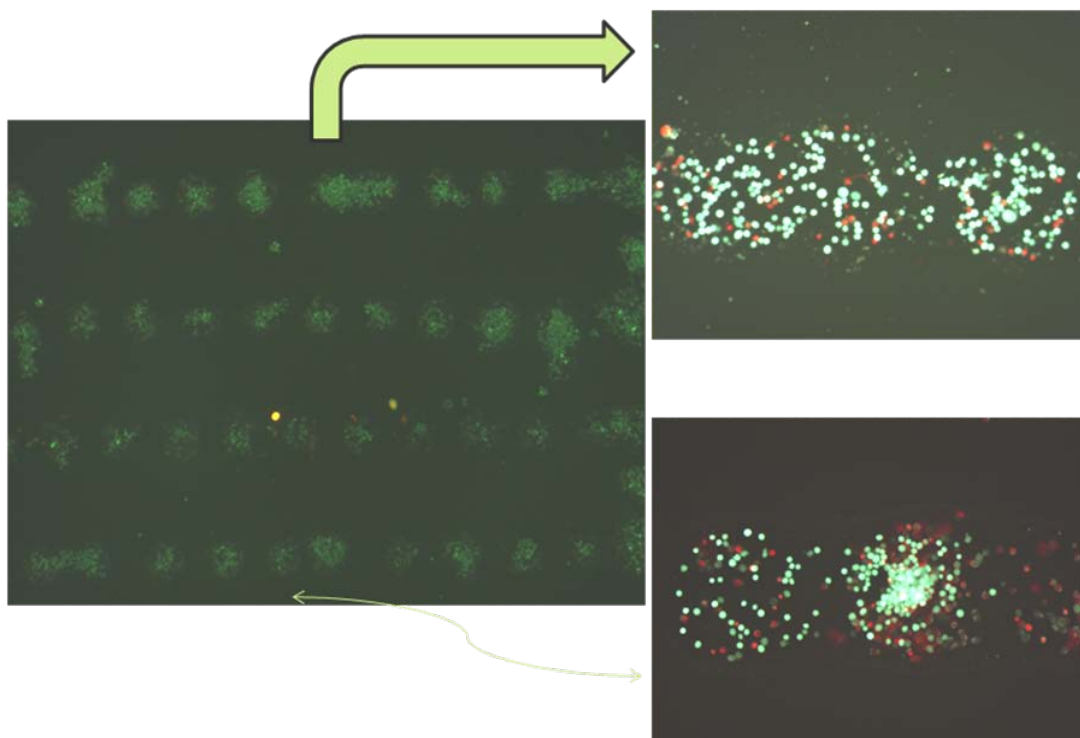


*FIGURE 84: Pattern of alive fibroblast 3T3 NIH cells on a gel substrate by using the threshold energy  $\sim 86\text{mJ}$*

### 5.2.4.1.3 2D Deposition of Granulosa Cells GFS-HR17 on glass substrate

In this part we create patterns of Granulosa cells on a glass substrate, and we worked as before, studying their viability dependence on the energy of the transfer and of course we found the energy threshold for the transfer. The first pattern was made by using energies around  $\sim 88\text{mJ}$  (Fig.85), we saw all the cells were alive after the transfer, so we continued the transfer by using this energy (Fig.86).

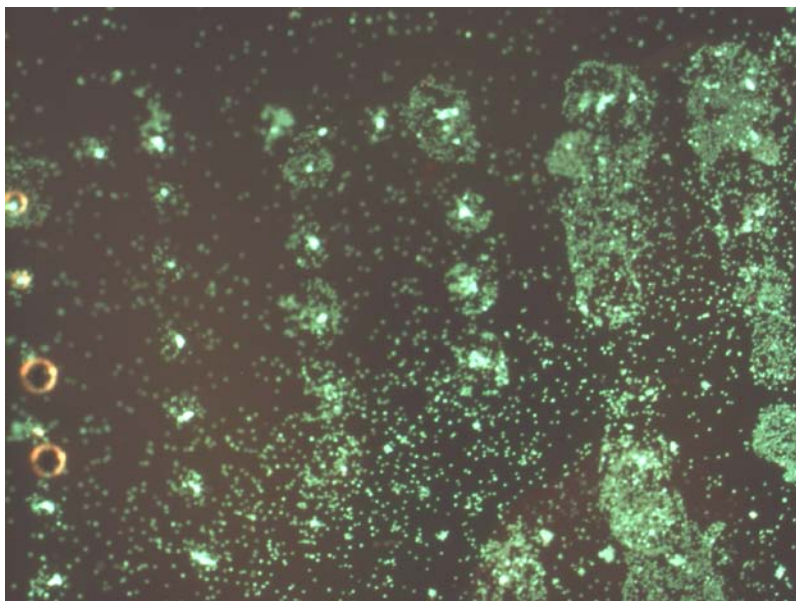


*FIGURE 85: Pattern of spots of granulosa cells by using energies  $\sim 88\text{mJ}$*

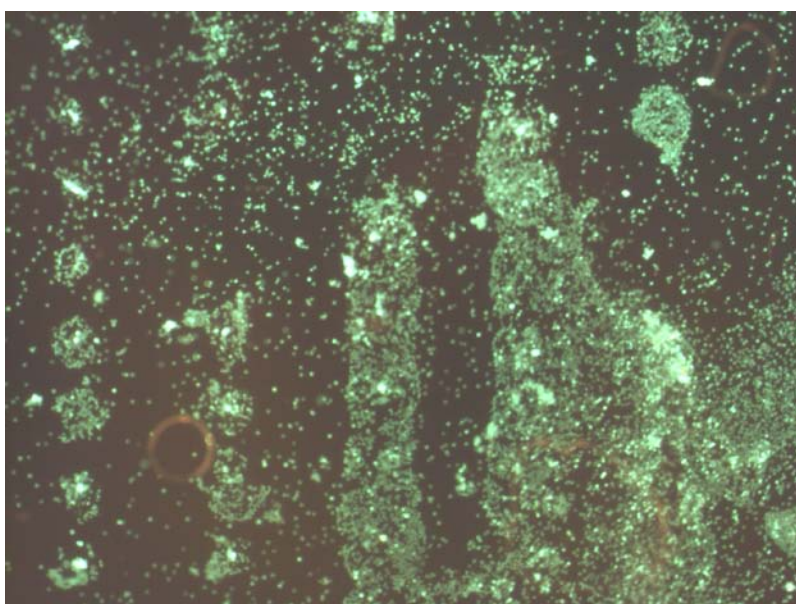


*FIGURE 86: Pattern of spots of granulosa cells by using energies  $\sim 88\text{mJ}$ , all the transferred cells are alive!*

All the pictures in this study of the cells transfer by using the L.I.F.T. technique, were taken by using a fluorescent microscope, and as it was mentioned before the substrate on which the cells were transferred, after the transfer we were placing it inside the solution of the fluorescent substances, due to this reason some spots of the alive cells after the transfer are not looking so clear, cause some cells seems to travel inside the solution and not be attached at the glass substrate (Fig.87). The dependence of the cells viability on the laser energy is clearly represent at the following Figures 88-89.

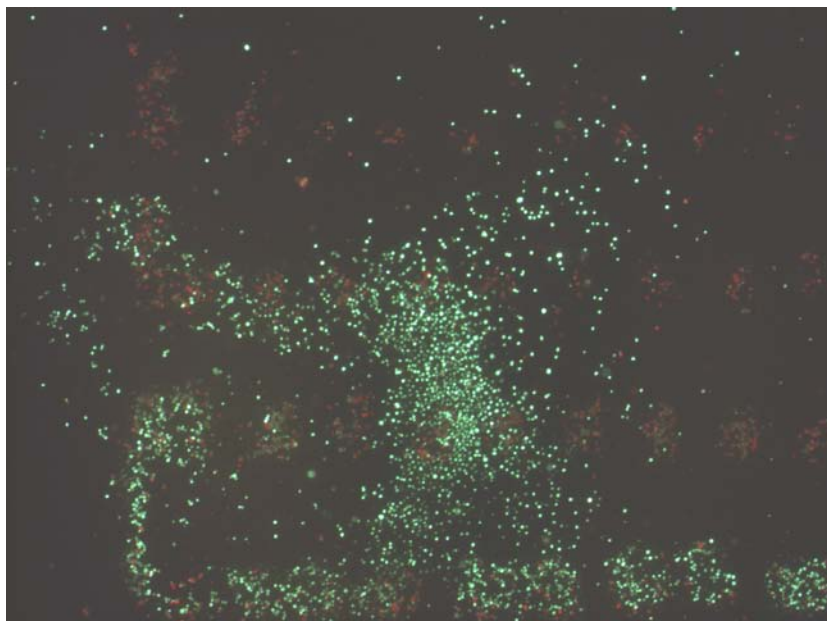


*FIGURE 87: Pattern of spots of granuloosa cells on a glass substrate by using energies 85~98mJ, some alive cells seems those are not attached at the substrate and are raveling inside the dye solution*

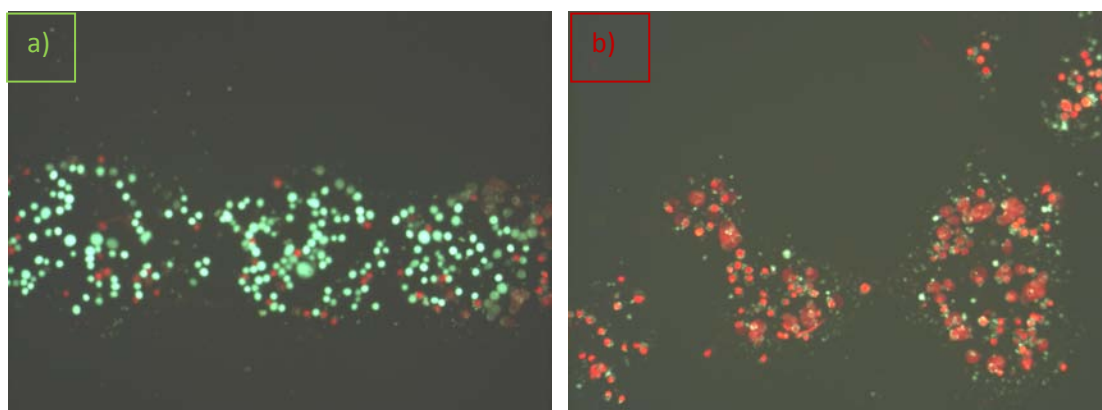


*FIGURE 88: a) Alive granuloosa cells by using energy ~88mJ, b) Dead granuloosa cells by using energies ~96mJ*

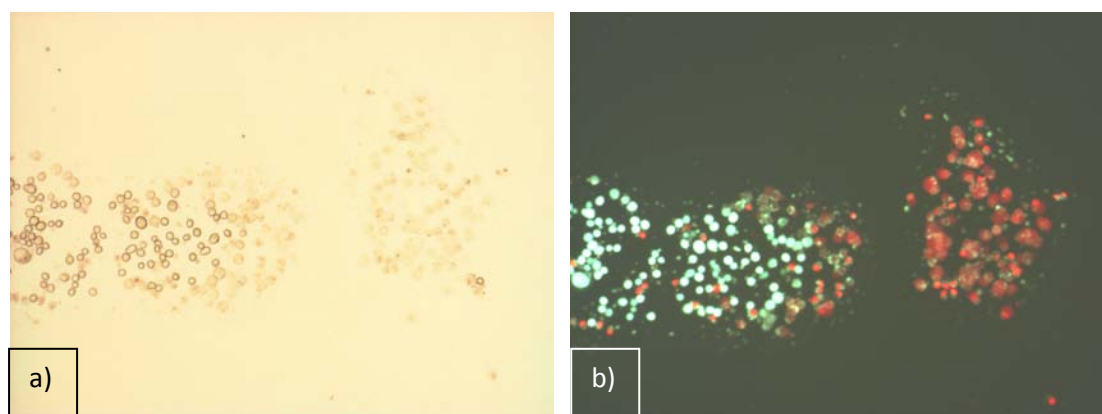


FIGURE 89: a) Alive and dead granulosa cells by using energy  $\sim 90\text{mJ}$  by an optical microscope, b) Alive and dead granulosa cells by using energies  $\sim 90\text{mJ}$  by using a fluorescent microscope

### 5.2.5 Construction of calcium alginate gel scaffolds

The first step of the construction of the calcium alginate gel scaffolds was to build the calcium alginate gel matrix. We worked as before and we made a 3D matrix of three layers of sodium alginate gel and three layers of calcium acetate in  $5\text{mm} \times 5\text{mm}$  scale. So we built a three layer 3D calcium alginate gel matrix, which height was approximately about  $10\ \mu\text{m}$  (Fig. 90.a.-Fig. 91.a). The whole process was performed in air and at room temperature and the laser energy was varied from 100 to 180 mJ per pulse. The distance between the receiving surface and the target was kept constant at 500 mm. Finally the second step of the construction of the calcium alginate gel scaffold was to transfer cells in each square of the matrix. So granulosa cells were transferred inside each the calcium alginate gel matrix by using the threshold energy for their transfer that was found before and was  $\sim 88\text{mJ}$  (Fig. 90.b.-Fig.91.b), so alive cells were transferred inside the matrix in order to have a scaffold (Fig.92).

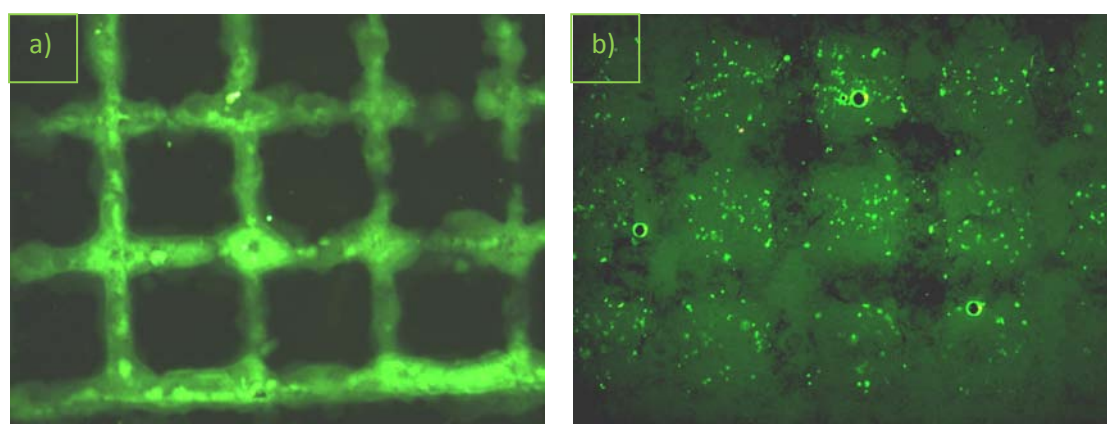
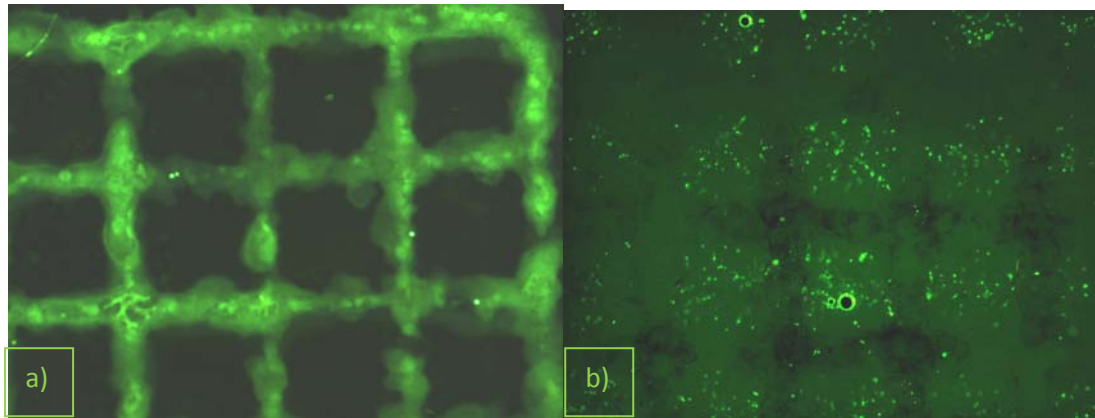
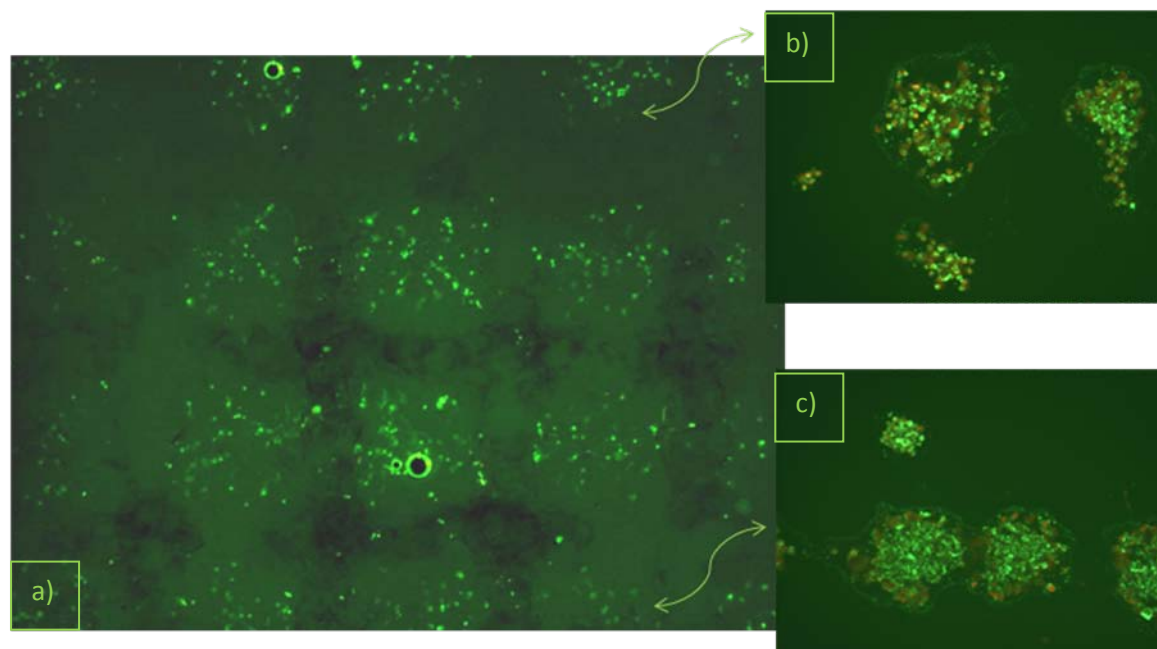


FIGURE 90: Fluorescent images of a) calcium alginate gel 3D matrix its each square of is  $1\text{mm} \times 1\text{mm}$ , b) granulosa cells transferred inside each square of the 3D matrix



*FIGURE 91: Fluorescent images of a) calcium alginate gel 3D matrix its each square of is 1mm\*1mm and the whole matrix is 5mm \*5mm b) granulosa cells transferred inside each square of the 3D matrix*



*FIGURE 92: Fluorescent images of a) the granulosa cells transferred inside each square of the 3D calcium alginate gel matrix, b),c) where we study the viability of the cells, and all of the transferred cells where alive by using the energy threshold during their transfer ~88mJ*

## **B. Results after using the Multi-Photon Polymerization technique**

An innovative technique, the 3PP of an acrylate composite, was developed for built 3D structures bottom up layer by layer using an infrared femtosecond laser at 1028nm and a Ti:Sapphire femtosecond oscillator operating at 800 nm. The composite consisted of an acrylate monomer, a free-radical co-initiator and a photo-sensitizer. The material was transparent to infrared laser radiation and absorbed strongly in the visible spectrum. Scanning the tightly focused laser beam, we achieved polymerization and solidification of the material. Due to their versatile optical and chemical properties and their ability of mixing with active molecules, the materials described in this work are particularly useful for a variety of applications such as photonic devices, actuators, micro-fluidic devices and self-assembled biomolecular structures. Molecular self-assembly is emerging as a viable “bottom-up” approach for fabricating nanostructures. Self-assembled biomolecular structures are particularly attractive, due to their versatile chemistry, molecular recognition properties, and biocompatibility. Among them, amyloid protein and peptide fibrils are self-assembled nanostructures with unique physical and chemical stability, formed from quite simple building blocks; their ability to work as a template for the fabrication of low resistance, conducting nanowires has already been demonstrated. The precise positioning of peptide-based nanostructures is an essential part of their use in technological applications, and their controlled assembly, positioning, and integration into microsystems is a problem of considerable current interest, as it was briefly described in chapter3 at the previous part A.. Here, we propose a new method for the precise, three dimensional patterning of amyloid fibrils. The technique, which combines femtosecond laser technology and biotin-avidin mediated assembly on a polymeric matrix, can be applied in a wide variety of fields, from molecular electronics to tissue engineering.

### 5.3 3D structures of Ormocer by three photon polymerization

The material was prepared following the reference formulation. We placed a drop of Ormocer in the middle of a coverslip and on the sample holder. Most important, we had to find the interface glass – substrate and this was achieved moving the laser beam at the z axis and detecting the second reflection of the focal spot (Fig.93). The structures were built bottom up layer by layer by repeating the pattern according the sketch over several layers depending on the desired thickness. As Ormocer was very viscous and the build process lasted less than a minute, material drifting was not an issue.

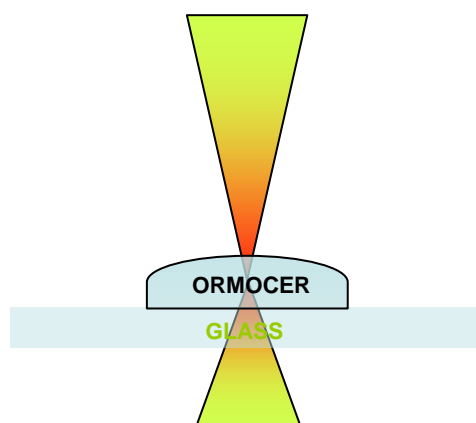


FIGURE 93: Laser focusing into the material

The fabrication was controlled by three parameters, the number of loops for each layer, i.e. the number of times the scanning is repeated at a same z value, the galvo mirror scanning speed and the power of the laser regulated by filters. Several structures were built with varying these parameters.

The first component built by three-photon polymerization and by using the Amplitude Systems t-pulse laser femtosecond oscillator operating at 1028 nm, is a porsche car-3D structure. The component was built layer by layer over 37 layers with a 1  $\mu\text{m}$  separation thickness. The objective 20X was used. The separation thickness was smaller than the lateral focal length of the lens therefore the adhesion between the layers was adequate (fig.94).

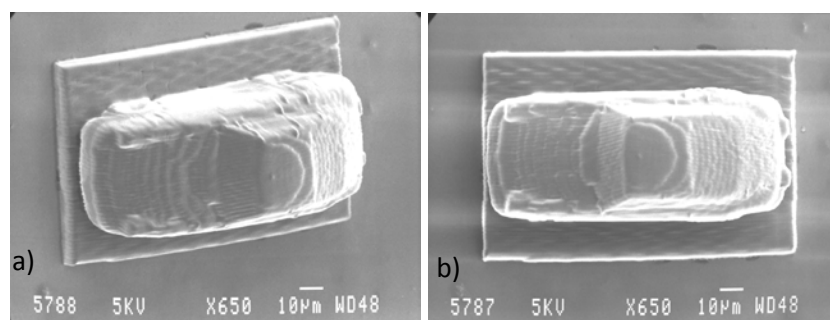


FIGURE 94: SEM image of the porsche car-3D structure built by two-photon polymerization (650xmagnification)

The galvo scanning speed used in this case was 7mm/s. For the same galvo speed, several laser powers were investigated. The lowest laser energy per pulse that appeared to polymerize the material was found to be 2.5 nJ, which corresponds to a laser fluence of 0.13 J cm<sup>-2</sup>. The components were made using this minimum laser pulse energy. After the completion of the component building process, the sample was developed for approximately 3 min in 50-50 solution of isopropanol, 4-methyl-2-pentanone and also rinsed in isopropanol. Moreover a cow 3D structure (Fig.95-Fig.97) was built with the following parameters: the galvo scanning speed used in cases was 7mm/s, and the structure was built by repeating the same pattern over 37 layers with a 1 μm separation thickness and the laser source was a Ti:Sapphire femtosecond oscillator operating at 800 nm.

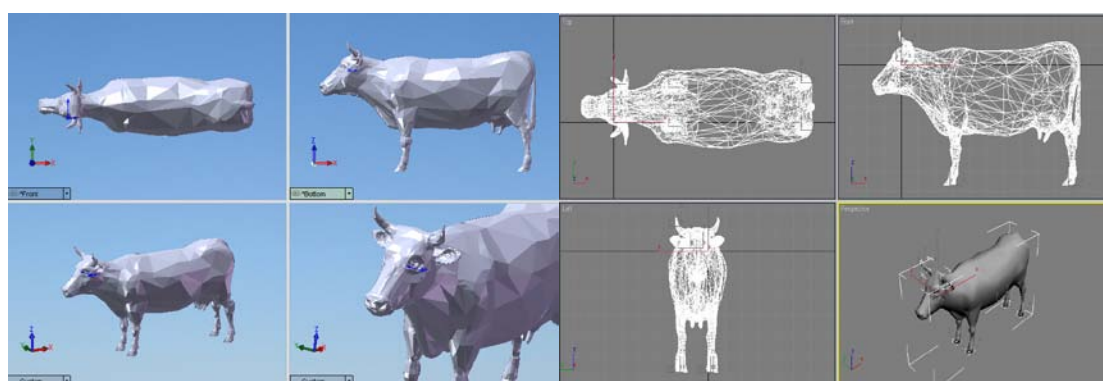


FIGURE 95: 3D sketch of ormoecr structure of a cow

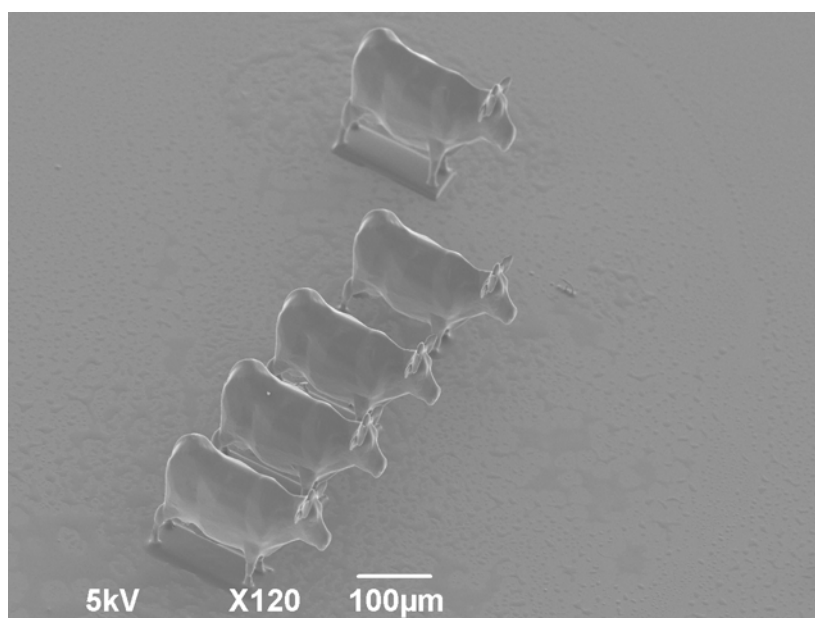
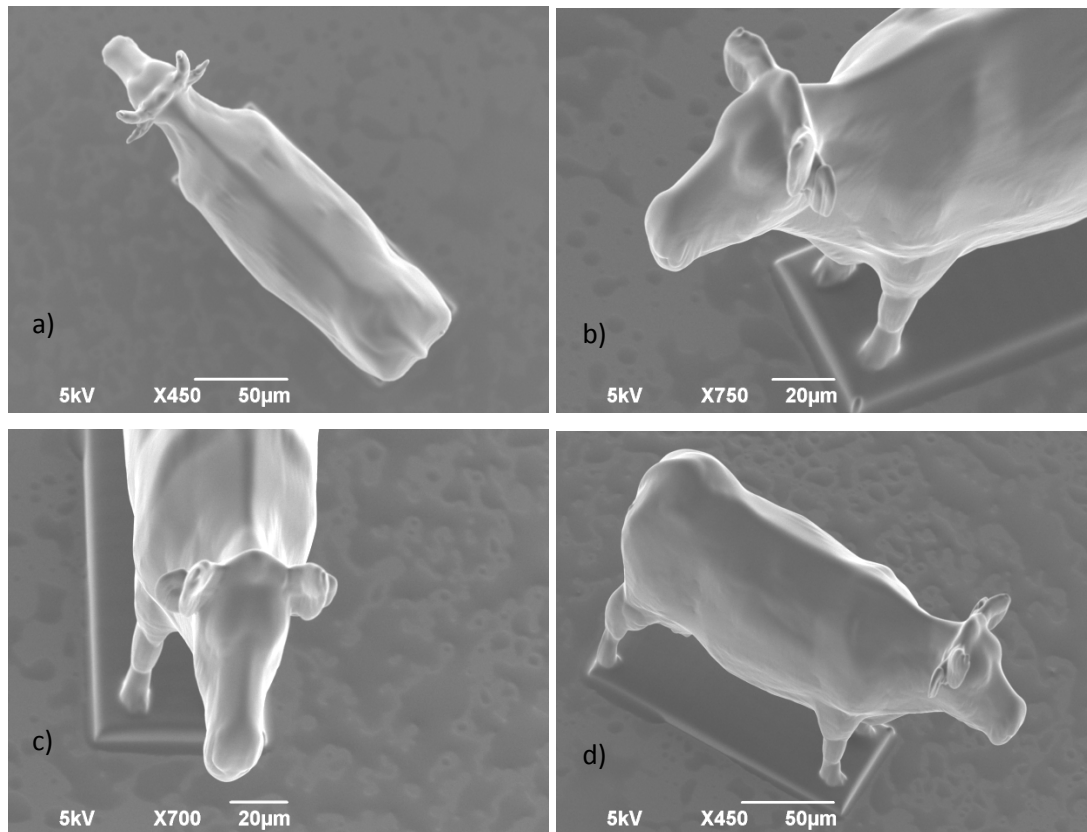


FIGURE 96: SEM image of 3D structures of a cow array built by two-photon polymerization.

The dimensions of these structures are: 244μm length, 152μm height, 68μm width  
(120xmagnification)



*FIGURE 97: SEM images of the cow-3D structure built by two-photon polymerization in different angles. a),d) 450xmagnification, b) 750xmagnification, c) 700xmagnification*

We continue by building a 3D structure of a penguin (Fig.98-Fig.101), that was built with the following parameters: the galvo scanning speed used in this case was 7mm/s, and the structure was built by repeating the same pattern over 37 layers with a 1  $\mu\text{m}$  separation thickness and the laser source was a Ti:Sapphire femtosecond oscillator operating at 800 nm.

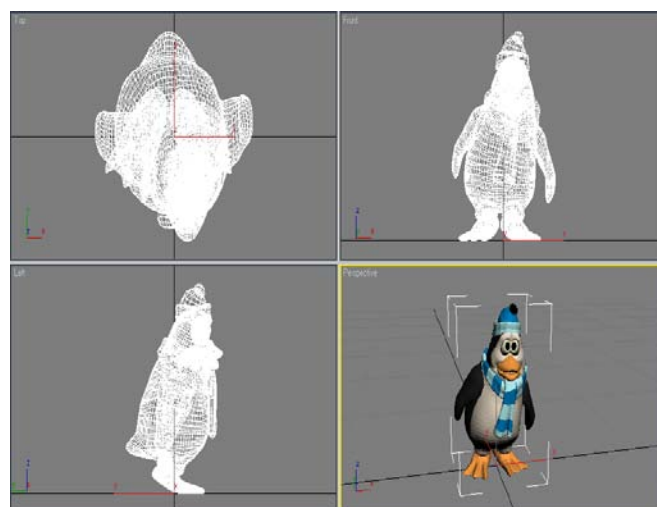


*FIGURE 98: 3D sketch of ormozer structure of a penguin*

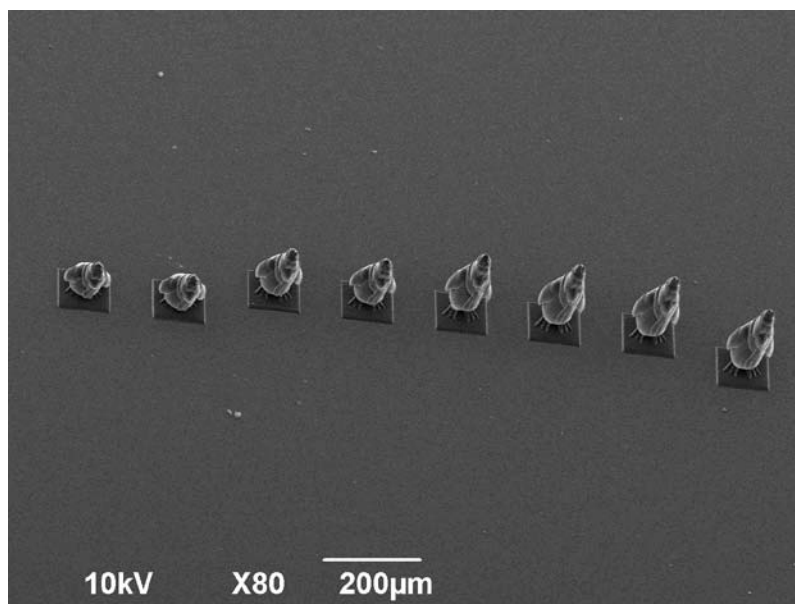


*FIGURE 99: SEM image of 3D structures of a penguin array built by two-photon polymerization. The dimensions of these structures are: 114μm length, 150μm height, 104μm width (80xmagnification)*

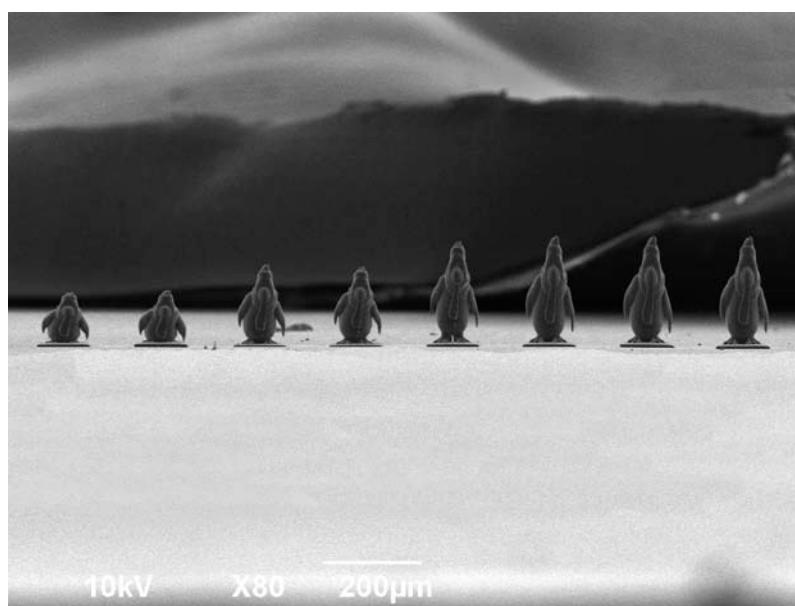


*FIGURE 100: SEM image of 3D structures of a penguin array built by two-photon polymerization*

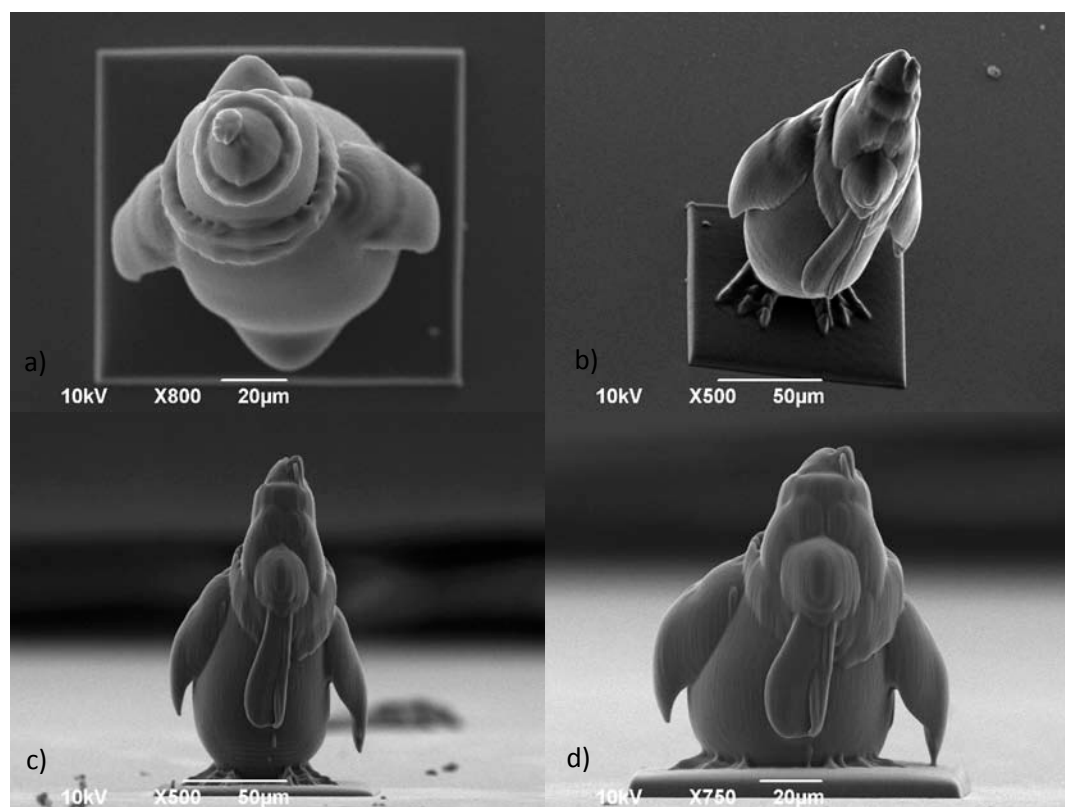


*FIGURE 101: SEM images of the penguins-3D structures built by two-photon polymerization in different angles and by using different speeds during polymerization. a) top view, b) side view, c) by using 7mm/s galvo scanning speed d) by using 9mm/s galvo scanning speed*

### 5.3.1 Directed Three-Dimensional Patterning of Self-Assembled Peptide Fibrils

The process of Functionalization of Ormocer for peptide fibril growth is illustrated in Figure 6. First a thin layer of photobiotin is deposited on the Ormocer surface. When this layer is exposed to UV light (Figure 102a), it is immobilized irreversibly on the Ormocer surface<sup>15</sup>. The samples are washed thoroughly to remove the nonimmobilized photobiotin, and they are subsequently functionalized further with avidin (Figure 102b) and finally with the iodoacetamide- functionalized biotin (Figure 102c). The next step is peptide attachment on the functionalized surfaces (Figure 102d); this is achieved through the thiol group of the peptide that will react with the biotin-conjugated iodoacetamide group. A thin layer of peptides will form on the structures; this layer will act as an “anchoring point”, which, under the right conditions, will trigger the further assembly of the peptide nanostructured fibrils into micron-sized “bridges”.

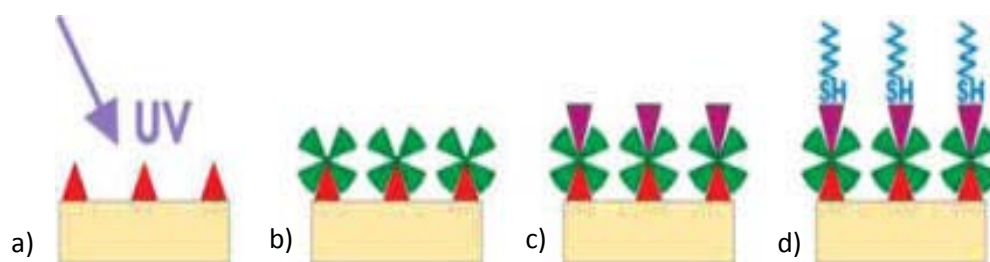


*FIGURE 102: Functionalization of Ormocer for peptide fibril growth. A thin layer of photobiotin (red triangles) is deposited on the Ormocer surface and exposed to UV light a) before being further functionalized with avidin (green crosses, b) and iodoacetamide-functionalized biotin (purple triangles, c). The final step is the attachment of the cysteine-containing peptide through the SH-iodoacetamide reaction d).*

Finally, the 3D structures of Ormocer are immersed in an aqueous solution of peptides that contain a cysteine residue. The peptide solutions have been “aged” so that self-assembled fibrils are already formed in solution. It is generally accepted that formation of amyloid fibrils in solution follows a classical nucleation and growth mechanism; small oligomers first form slowly and subsequently serve as nuclei for fibril elongation and development<sup>16</sup>. The term “aged” refers to solutions where, according to previously determined kinetic conditions<sup>17</sup>, mature amyloid fibrils reaching the order of microns in length have been formed. The self-assembly of the peptide fibrils into bridges on the structures is initiated through the controlled evaporation of water. However, in order for this to occur between two specific positions, there is a seed, or “anchoring point”, required. This is provided by the covalent bond formation between the iodoacetamide group in the biotin derivative and the thiol group in the cysteine. The requirement for the “seeding”, and therefore the selectivity of the technique, is demonstrated with the use of peptides that do not contain cysteine. In this case, self-assembled peptide fibrils are formed in solution, as shown in Figure 7b, but there is no peptide fibril attachment on the functionalized structures. Transmission electron microscopy (TEM) images of fibrils of cysteinecontaining as well as the fibrils of the serine containing peptide are shown in Figure 103, panels a and b, respectively.

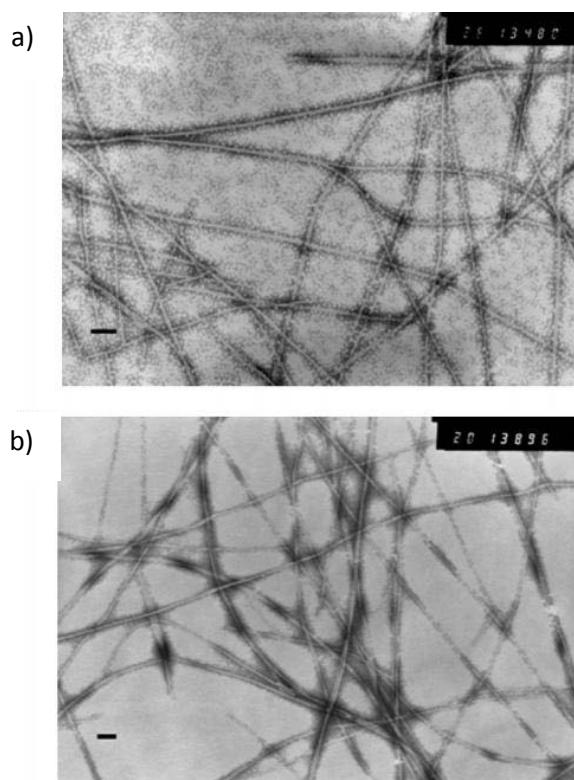


*FIGURE 103: a) TEM image of fibrils of the cysteine-containing peptide (CNGAITIG, bar 150 nm) and b) TEM image of fibrils of the peptide that does not contain cysteine (NSGAITIG, bar 150 nm).*

Peptide fibrils were visualized either with scanning electron microscopy (SEM) or using the well established diagnostic test of fluorescence emission of the dye Thioflavin T that binds specifically to amyloid fibrils and gives blue fluorescence when excited at 440 nm. A thioflavin fluorescence image and a SEM image of the directed 3D assembly of the peptide fibrils is shown in Figure 104, panels a), b) and c), respectively. In this case, a series of 3D columns is fabricated using multiphoton polymerization; the columns are subsequently functionalized as described earlier.

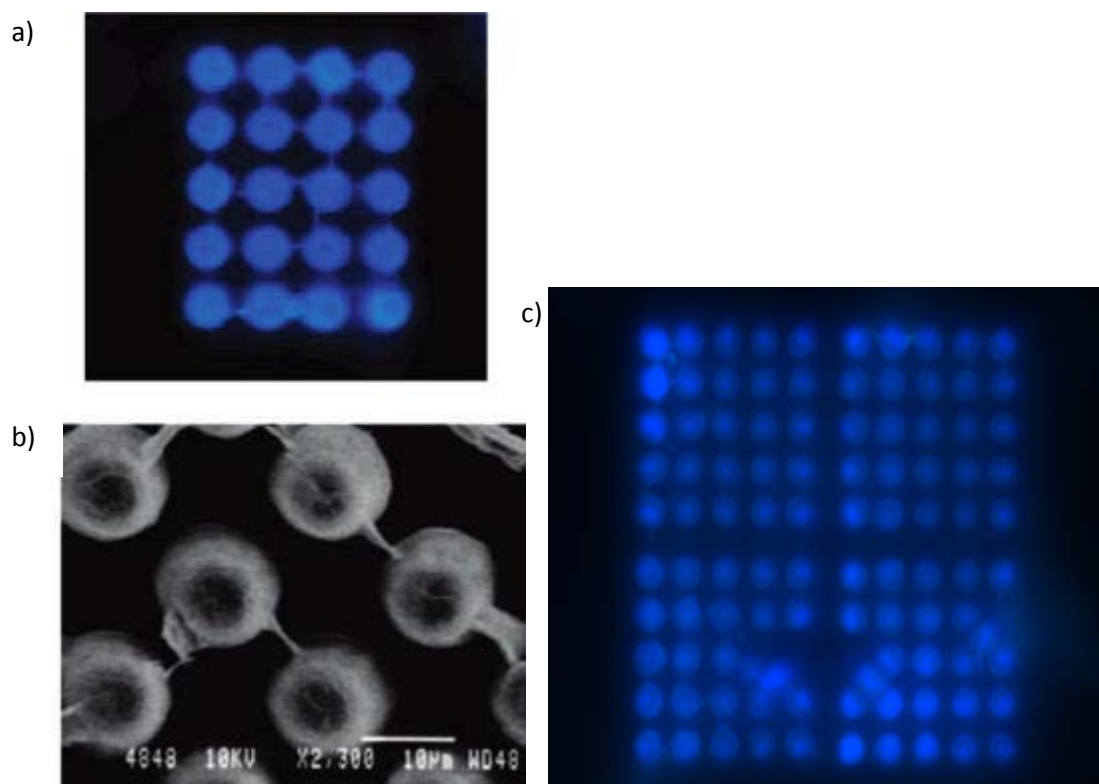


*FIGURE 103: a) Thioflavin fluorescence image, b) SEM image of a 3D column array, with peptide bridges self-assembled between the columns and c) Thioflavin fluorescence image of 3D column arrays with the peptide bridges self-assembled between the columns.*

Then the structures are immersed in the cysteine-containing peptide solution and they are left to dry slowly. The peptide bridges form during the drying process. The length and the diameter of the peptide fibrils will depend on the design of the 3D structures, i.e., the distance between them and the diameter of the fibril support. So we built by using three photon polymerization 3D structures of the following sketch (Figure 104, panels a), b), c) and d)). The peptide bridges appear to form over the shortest distance, as it can be seen in fig. 105.

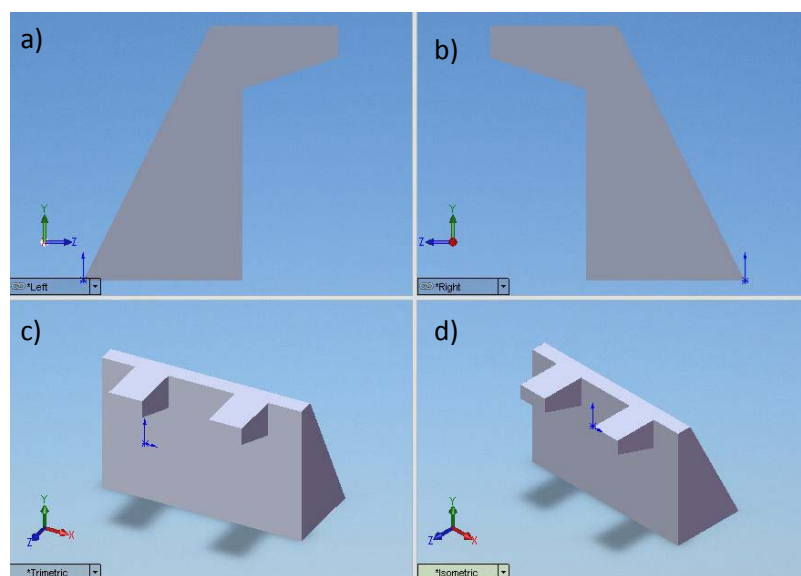


FIGURE 104: 3D sketch of 3D structure of Ormocer, which was used for an array, with different distances between the structures

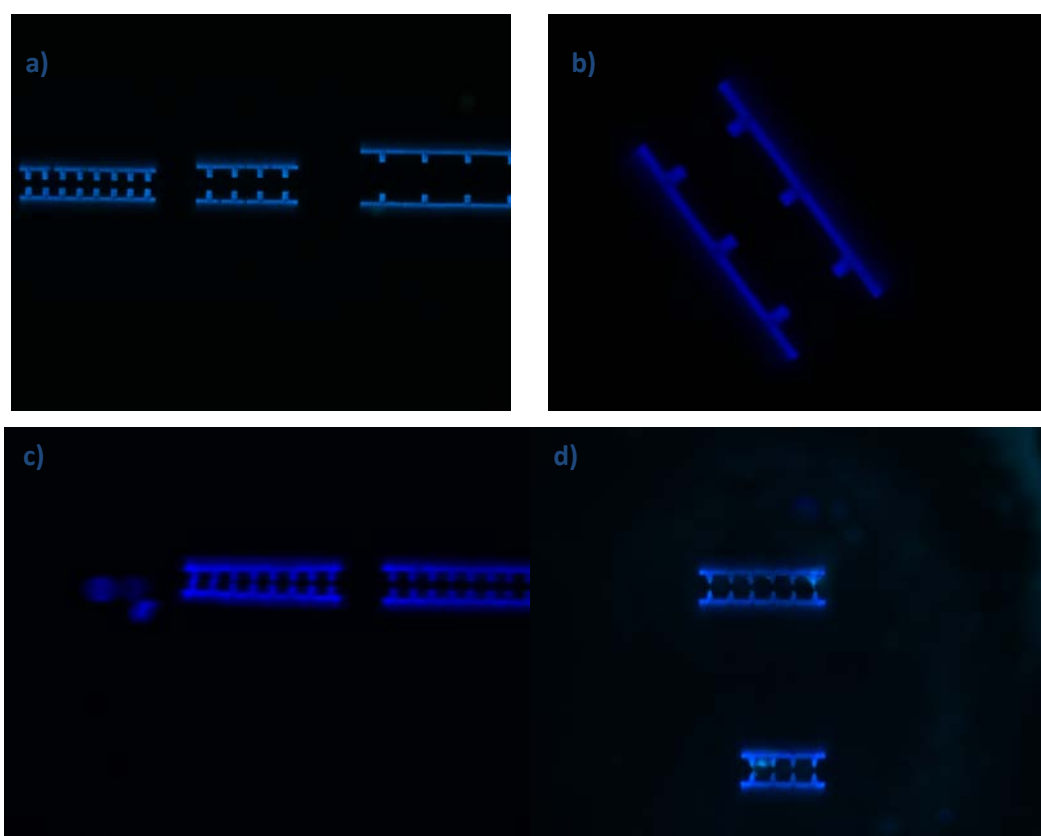
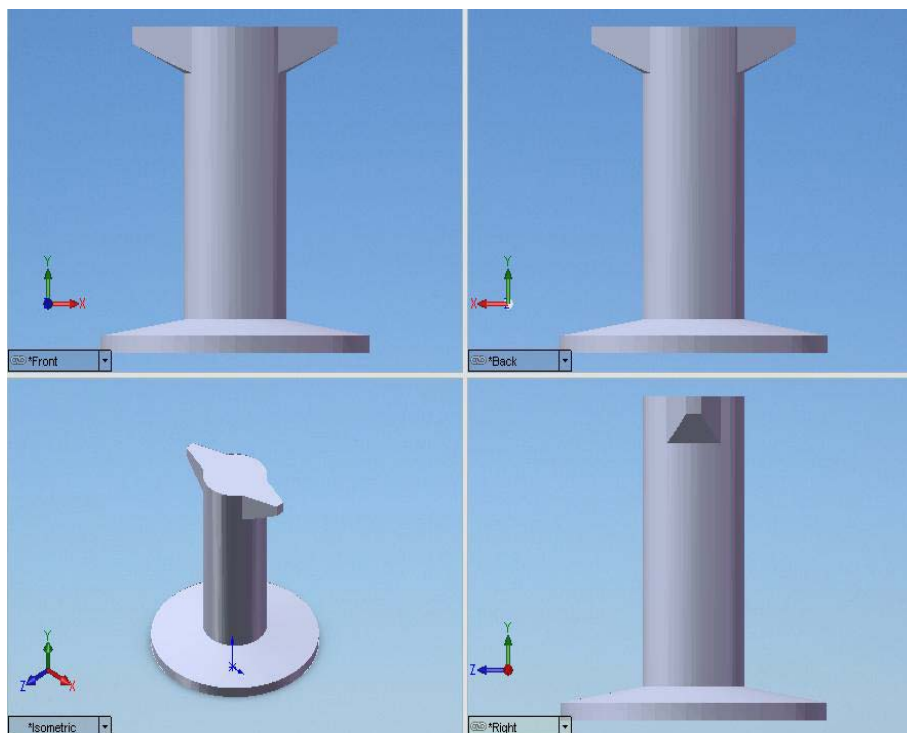
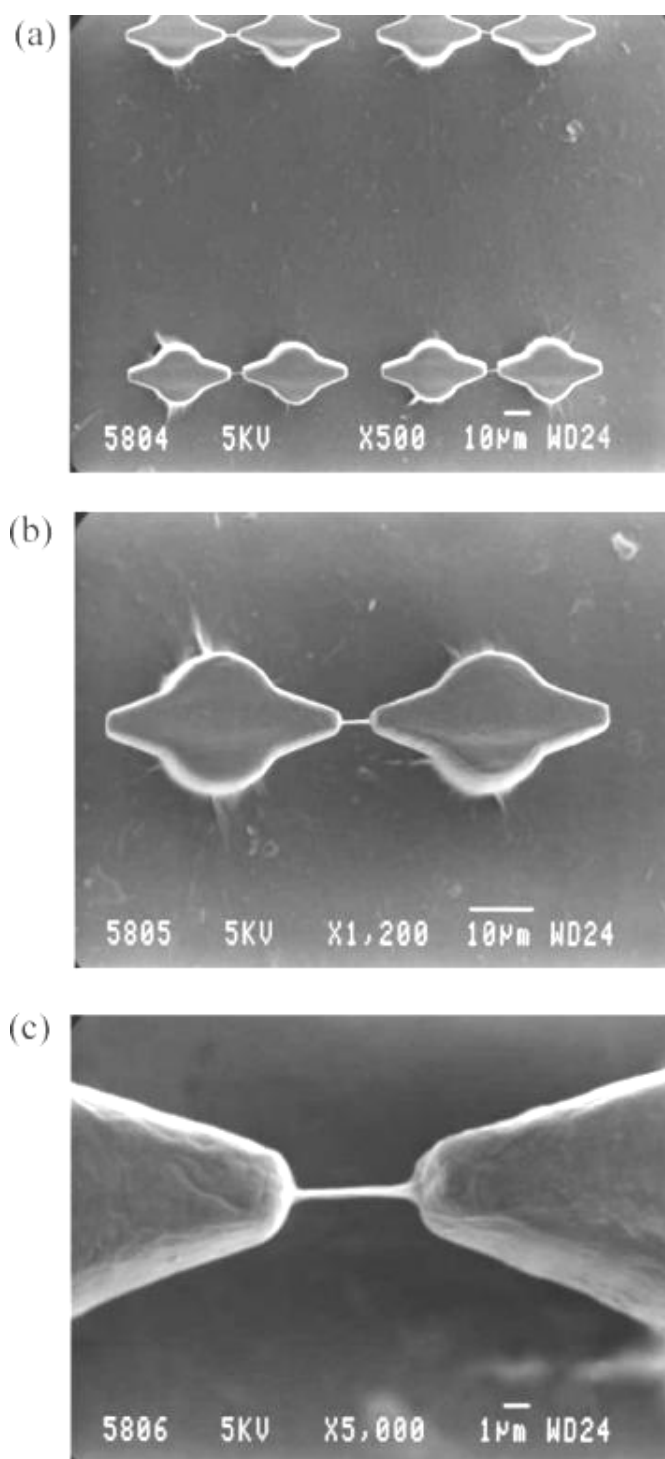


FIGURE 105: a) Thioflavin fluorescence image of an array of 3D structures in different distances between them, b), c), d) peptide bridges form over the shortest distance

Then we continue making arrays of 3D columns that had the shape that is presented in the following figure 106. Again the structures are immersed in the cysteine-containing peptide solution and they are left to dry slowly, while the peptide bridges form during the drying process. It is obvious that the length and the diameter of the peptide fibrils depend on the distance between the columns of the array and on the diameter of the fibril support too.



*FIGURE 106: 3D sketch of 3D column of Ormocer, which was used for an array, with different distances between the columns*



*FIGURE 107: (a) SEM image of a series of 3D ORMOCER columns, with peptide fibril bridges self-assembled between them. (b) One pair of 3D ORMOCER columns, with peptide fibril bridges self-assembled between them. (c) Detail of the self-assembled fiber bridge.*

Once the fibril bridges form, they remain at their position even when the sample is immersed in water for as long as 24h. However, for the fibril bridges to form, it is essential that there is a trigger; we believe is provided by a thin layer of peptides formed on the 3D structures, due to the iodoacetamide-thiol reaction. This thin layer is clearly visible in Figure 108a. When the peptide used does not contain cysteine, then there is no formation of peptide thin layer of fibrils as shown in Figure 104b and subsequently no bridges.

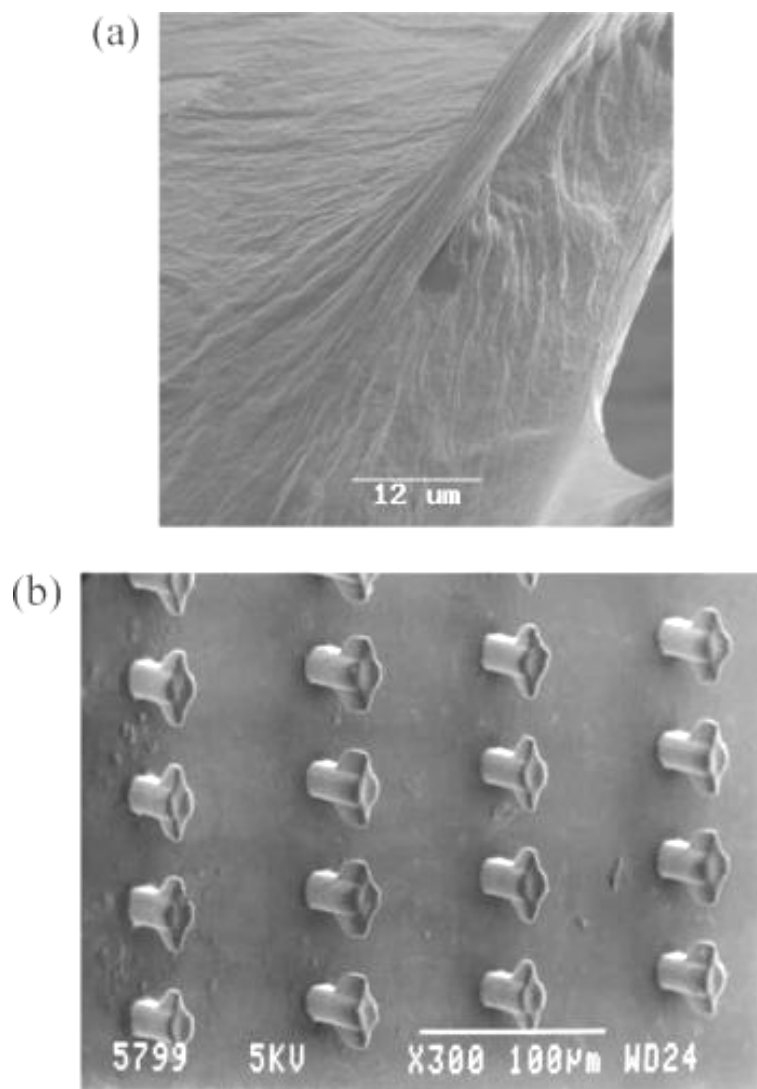


*FIGURE 108:(a)Thin layer of peptide fibrils embedded on the Ormocer structure. (b)Ormocer structures functionalized as described in the text; the peptide used does not contain cysteine and therefore no bridges are formed.*

### 5.3.2 Conclusions

To conclude, we have demonstrated a new method for the controlled self-assembly of peptides in three dimensions. The method is based on biotin-avidin and thiol chemistry and Ormocer is used as a substrate. Thiolfunctionalized biomolecules can be easily produced in the laboratory scale and can even be commercially available, so this method should be applicable not only to peptides, but to other self-assembling biomolecules as well. In a pioneering work, metal and semiconductor binding peptides were displayed at the surface of filamentous bacteriophages and were used for the fabrication of conductive and semiconductive nanowires<sup>18,19</sup>. A natural continuation of the work presented here will be the use of mineralized peptide fibers, since cysteine is a metal-binding amino acid. The use of peptide building blocks functionalized with semiconductor-binding sequences can also be foreseen. This will enable the direct self-assembly of nanoscale electronic circuits and devices. Another domain where our methodology would be particularly applicable in tissue engineering. Peptide networks are already investigated as cell supports in the form of injectable hydrogels<sup>20,21</sup>. A combination of larger scaffolds with well-defined biodegradable peptide supports in a “scaffold on scaffold” format could possibly be used as a support to allow the directed growth of several cell types into ordered arrays of functional biological units. Microstructures with dimensions of tens of microns have been built with polymer composite with a lateral resolution of 1  $\mu\text{m}$ . It has been shown that the axial resolution enables the building of more complicated structures by scanning layers with different patterns. More experience on this technique and on the materials has to be acquired in order to build structures with a design giving rise to a concrete application. The material and the innovative method of two-photon polymerization are promising for the incorporation of active molecules that are sensitive to UV radiation.

## REFERENCES

1. K. Papanikolopoulou, G. Schoehn, V. Forge, V.T. Forsyth, C. Riekel, J.F. Hernandez, R.W.H. Ruigrok, A. Mitraki, *J. Biol. Chem.* 280 (2005) 2481.
2. V. Dinca, M. Farsari, D. Kafetzopoulos, A. Popescu, M. Dinescu, C. Fotakis, Thin solid films, 2007, in press.
3. M. Nilson, *Methods* 34 (2004) 151.
4. M. Reches, E. Gazit, *Science* 300 (2004) 625.
5. I. Karaiskou, I. Zergioti, C. Fotakis, M. Kapsetaki, D. Kafetzopoulos, *Appl. Surf. Sci.* (2003) 208.
6. P. Serra, J.M. Fernánde z-Pradas, M. Colina, M. Duocastella, J. Domínguez, J.L. Morenza, *J. Laser Micro/Nanoeng.* (2006) 236
7. E. Gazit, *FEBS J.* 272 (2005) 5971.
8. M.T. Pastor, A. Esteras-Chopo, M. Lopez de la Paz, *Curr. Opin. Struct. Biol.* 15 (2005) 57.
9. G.M. Whitesides, B. Grzybowski, *Science* 295 (2002) 2418.
10. G.M. Whitesides, J.P. Mathias, C.T. Seto, *Science* 254 (1991) 1312.
11. T. Hamada, D. Hasegawa, H.Y. Naiki, *J. Biol. Chem.* 278 (2003) 16462.
12. D. Hamada, I. Yanagihara, K. Tsumoto, *Trends Biotechnol.* 22 (2004) 93.
13. M. Cretich, F. Damin, G. Pirri, M. Chiari, *Biomol. Eng.* 23 (2006) 77.
14. Drakakis, T. S.; Papadakis, G.; Sambani, K.; Filippidis, G.; Georgiou, S.; Gizeli, E.; Fotakis, C.; Farsari, M., Construction of three dimensional biomolecule structures employing femtosecond lasers, *Appl. Phys. Lett.* 2006, 89, 144108.
15. Gilead, S.; Gazit, E., Self-Organization of Short Peptide Fragments: From Amyloid Fibrils to Nanoscale Supramolecular Assemblies, *Supramol. Chem.* 2005, 17, 87-92.
16. Papanikolopoulou, K.; Schoehn, G.; Forge, V.; Forsyth, V. T.; Riekel, C.; Hernandez, J.-F.; Ruigrok, R. W. H.; Mitraki, A., Amyloid fibril formation from sequences of natural  $\alpha$ -structured fibrous protein, the adenovirus fiber., *J. Biol. Chem.* 2005, 280, 2481-2490.
17. Mao C.; Solis D. J.; Reiss B. D. et al. Virus-based toolkit for the directed synthesis of magnetic and semiconducting nanowires. *Science* 2004, 303, 213-217.
18. Lee, S. W.; Mao, C.; Flynn, C. E.; Belcher, A. M. Ordering of quantum dots using genetically engineered viruses. *Science* 2002, 296, 892-895.
19. Haines-Butterick, L.; Rajagopal, K.; Branco, M.; Salick, D.; Rughani, R.; Pilarz, M.; Lamm, M. S.; Pochan, D. J.; Schneider, J. P. Controlling hydrogelation kinetics by peptide design for three dimensional encapsulation and injectable delivery of cells. *Proc. Natl. Acad. Sci.* 2007, 104, 7791-7796.

## PUBLICATIONS

1. V. Dinca, J. Catherin, A. Mourka, S. Georgiou, M. Farsari and C. Fotakis, “2D and 3D biotin patterning by ultrafast lasers”, Int. J. Nanotechnol., Special Issue on "Nanotechnology in Greece", Vol. 6, Nos. 1/2, pp.88-98, (2009)
2. V. Dinca, E. Kasotakis, A. Mourka, A. Ranella, M. Farsari, A. Mitraki, and C. Fotakis,” Fabrication of Amyloid Peptide Micro-Arrays using Laser-Induced Forward Transfer and Avidin-Biotin mediated Assembly”, Phys. Stat. Sol. (c) 5, No12, 3576-3579 (2008)
3. V. Dinca, E. Kasotakis, J. Catherine, A. Mourka, A. Ranella, A. Ovsianikov, B. N. Chichkov, M. Farsari, A. Mitraki and C. Fotakis, “Direct two- and three- dimensional patterning of self-assembled peptide fibrils”, Nanoletters 8, 538 (2008)
4. V. Dinca, E. Kasotakis, J. Catherine, A. Mourka, A. Mitraki, A. Popescu, M. Dinescu, M. Farsari and C. Fotakis, “Development of peptide-based patterns by laser transfer”, Applied Surface Science, 254 , 1160-1163 (2007)